Direct imaging of planetary mass companions and circumstellar debris disks

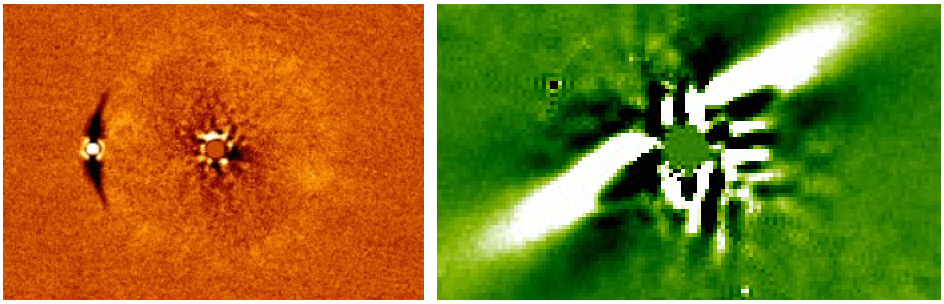

Elisabeth C. Matthews

Submitted by Elisabeth Christina Matthews to the University of Exeter as a thesis for the degree of Doctor of Philosophy in Physics, June 2018.

I certify that all material in this thesis which is not my own work has been identified and that no material has previously been submitted and approved for the award of a degree by this or any other University.

Signed: .....

Elisabeth Matthews

Date: .....

Abstract

Gas giant planets at the widest separations can only be identified via high contrast imaging. Studying these planets allows us to understand the full architecture of exoplanetary systems, and to probe whether these objects are formed via a core accretion or a disk instability process. The high contrast imaging method is also unique in that stellar and planetary light are spatially separated, allowing detailed spectroscopic analysis of detected companions with a comparatively low observational cost.

It has long been predicted that giant planets and circumstellar debris dust are linked, with planets such as β-Pictoris b and HD 106906 b residing in highly dusty systems. Of particular interest are those systems where the dust morphology is suggestive of the presence of planets: for example, in both the HR 8799 and HD 95086 systems one or more planets have been found in the gap between two belts of debris dust. Even the solar system is in this configuration, with the Asteroid and Kuiper belts enclosing the four gas and ice giants.

In this work we carry out two surveys, where we search for planets using high contrast imaging. We survey both (a) 24 targets with the highest levels of circumstellar debris dust and (b) 20 targets with circumstellar disks, where infrared analysis suggests that the debris disk is carved into two distinct belts. For the second group of targets, the gap between the debris belts indicates the expected position of a giant planet within the system. Even further, we place constraints on the mass of the inferred planets in the system, based on the measured properties of the debris dust: the time taken to clear a gap in a debris disk is related to the mass of planets present. We can therefore calculate a minimum expected mass for planets in any particular system, based on the properties of the debris gap and the age of the system. These dynamical limits are complementary to observational limits we place on each system using high contrast imaging at the Very Large Telescope (VLT). These high contrast imaging surveys are carried out with the SPHERE instrument, a state-of-the-art high contrast imager, and we are typically sensitive to planets of a few Jupiter masses. These observational limits, along with the dynamical reasoning,

allow tight constraints to be placed on the inferred planetary systems even when no planets are detected.

While undertaking these surveys, we have made several new discoveries. Three of the debris disks were imaged in scattered light: two of these had never previously been resolved, while the third had been resolved with the Hubble Space Telescope at lower resolution and larger spatial scales. We detected two M-type companions to dusty targets, and a stellar binary with a moderate mass ratio. Finally, we identified a complex hierarchical quadruple stellar system, in which two of the four stars host debris disks based on their infrared excess.

Contents

List of Figures

List of Tables

Declaration

The majority of the research presented here was performed by myself, and was carried out in collaboration with several collaborators - in particular, Sasha Hinkley, Grant Kennedy and Arthur Vigan. I provide a chapter-by-chapter list of contributions to this work below. All figures reproduced from other works are clearly marked.

Chapter 3: for this chapter, which is based on the paper Matthews et al. (2018), the target selection was done jointly by myself and Sasha Hinkley. SED fitting and interpretation of disk radii was performed by with Grant Kennedy and Farisa Morales.

All of the data were post-processed by me, with advice and a subset of the code used provided by Arthur Vigan. The candidates were then identified and astrometry measured by myself and three Exeter summer students, namely Ben Sutlieff, Dawn Wickenden and Sam Treves. I calculated absolute magnitudes and colours for all candidates, to aid in their determination as companions or background objects. I calculated the contrast curves for each target and converted these to mass limits, using interpolated models provided by Isabelle Baraffe.

I performed a literature search for ages, and Trevor David provided useful discussion and assistance in determining the age of the targets. I calculated dynamical lower mass limits for these systems following useful discussion with Grant Kennedy and Andrew Shannon. Additionally Tiffany Meshkat, Dimitri Mawet and Karl Stapelfeldt provided useful discussion. The entire text of this paper was written by me and I made all of the figures in this chapter.

Chapter 4: this chapter includes data from three VLT/SPHERE proposals, lead respectively by Dimitri Mawet, Sasha Hinkley and myself. The target selection was performed by Dimitri Mawet and Sasha Hinkley, based on work from Deborah Padgett and Karl Stapelfeldt, and I chose which targets to follow up. All of the data were processed by me, with assistance and a subset of the code provided by Arthur Vigan. The candidates were identified and the astrometry measured by myself. I calculated contrasts curves and

converted these to mass limits, using interpolated models provided by Isabelle Baraffe.

Chapter 5: for this chapter, which is published as Matthews et al. (2017), the target was selected by Sasha Hinkley with input from Aaron Rizzuto. Interpretation of the infrared data was carried out by Grant Kennedy and Christine Chen, and Grant Kennedy created the SED (Figure 5.1). Mark Booth and Hannah Jang-Condell additionally contributed useful discussion of the infrared spectrum and ALMA data for this target. The data were processed by me, with assistance and a subset of the code provided by Arthur Vigan. I carried out the visual interpretation and GRaTeR fits, including implementation of a negative injection technique using GRaTeR code provided by Jean-Charles Augereau. The interpretation in the context of the field was performed by me with useful inputs from Karl Stapelfeldt, Grant Kennedy, Sasha Hinkley and Dimitri Mawet, and I wrote the entire text of this paper.

Chapter 6: I reduced all of the data presented in this chapter, and identified all of the objects presented. HIP 67497 was also identified by Bonnefoy et al. (2017), and I discuss their results in this chapter. Mickaël Bonnefoy and I independently observed and reduced data for HIP 63439, which hosts a faint circumstellar disk, and I performed the interpretation of my data on this target. The proposal for follow-up data was lead by Bonnefoy as part of a larger SPHERE program, and I contributed to this proposal and will lead analysis of the follow-up data. I identified the quadruple nature of the HD 223352/HD 223340 system, and Grant Kennedy realized that this system contained two debris disks. I provided interpretation of this system following discussion with Grant Kennedy, and led HST and ALMA proposals to follow-up the system. Grant Kennedy provided the SEDs presented in Figure 6.6. Finally, I identified the companions to HD 133778, HD 18378 and HD 19257. Trevor David and Eric Mamajek provided age analysis of HD 133778, and Arthur Vigan performed spectral extraction of HD 133778B from the IFS data. I performed the remainder of the data analysis and interpretation for these three companions.

Telescope, Software & Funding Credits

This work was supported financially by the University of Exeter, in the form of a PhD studentship.

This work is based on observations made with ESO Telescopes at the La Silla Paranal Observatory under programme IDs 095.C-0426, 095.C-0549, 095.C-0838, 097.C-0949, 097.C-1019, 097.C-1042, 099.C-0734.

This work has made use of data from the European Space Agency (ESA) mission *Gaia* (http://www.cosmos.esa.int/gaia), processed by the *Gaia* Data Processing and Analysis Consortium (DPAC, http://www.cosmos.esa.int/web/gaia/dpac/consortium). Funding for the DPAC has been provided by national institutions, in particular the institutions participating in the *Gaia* Multilateral Agreement.

This research has made use of NASA's Astrophysics Data System and of the SIMBAD database, operated at CDS, Strasbourg, France.

With thanks to Arthur Vigan for providing a SPHERE/IFS reduction pipeline, Jean-Charles Augereau for providing the GRaTeR code and Isabelle Baraffe for providing interpolated DUSTY and COND luminosity models.

Acknowledgements

There are so many people to whom I owe a great deal of thanks, and this page certainly doesn't do justice to how grateful I am.

First and foremost, of course, Sasha: none of this would have been possible without you. You always made time and always believed in me even when I didn't believe in myself. Thank-you for supporting me throughout, even when I was getting lost down various rabbit holes and when came up with proposal ideas only a few days before the deadline. Thank-you also for allowing me to explore avenues beyond research and supporting my adventures in science communication and in trying to make the department a more inclusive place to be.

Thank-you to my parents, who allowed me to grow up exploring, and encouraged me to believe I could achieve anything. And Oma and Opa, who bought me my first star chart and took me to see a meteor shower. And to the rest of my family, for the many ways you have supported me.

Thank-you to all the people who I have had the pleasure of sharing office 407 with at various points: Jon, Tom, Damian, Florian, Ahmad, Sally, Andy: we've laughed, we've cried, we've moaned, we've bickered, we've looked after each other. I'll miss you all.

Thank-you to the Tom-Tom hive collective, and to Laura and Aarynn and Matt and Louis and all the other people around the department who made it a great place to be.

Thank-you to Joe, for everything.

Finally, thank you to all the people who have helped me achieve some semblance of the mystical "work-life balance": the pit band musicians, the folkies, the parkrunners, the climbers, and to everyone else who I've interacted with in Exeter. It's been a pleasure.

Elisabeth Matthews

1st June 2018

Chapter 1

Introduction

1.1 Exoplanet science in the 21st century

Exoplanet science is a comparatively young field, and has grown remarkably since the detection of the first pulsar planet (Wolszczan & Frail 1992) and the first planet around a main-sequence star (Mayor & Queloz 1995). The field has advanced from only a few planet detections each year in the 1990s, to the present decade where new planet detections are published almost every day, with a single paper (Morton et al. 2016) presenting 1284 new planet detections at once. Figure 1.1 shows the number of planets detected each year as reported on the site exoplanet.eu, and stratified by detection method.

Not only have a huge number of planets been detected, but these planets span a huge range of properties. The known exoplanets have orbital periods from a few hours to hundreds of years, exoplanets have been found that are as light as Mercury and as heavy as tens of Jupiter masses, and many species including carbon monoxide (e.g. Snellen et al. 2010; Brogi et al. 2012; Brogi et al. 2014), water (e.g. Deming et al. 2013; Huitson et al. 2013), sodium and potassium (e.g. Redfield et al. 2008; Jensen et al. 2011) have been identified in their atmospheres. Figure 1.2 shows the mass and semi-major axis of the ~40% of known exoplanets for which masses have been determined.

Figure 1.2 is color-coded by detection method, and it is immediately obvious that

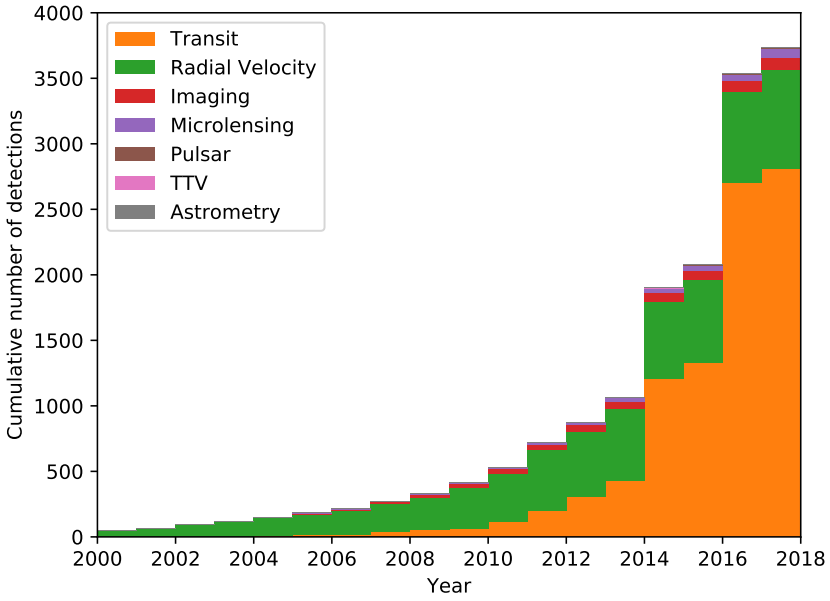

Figure 1.1: Histogram of the number of known planets by year, with the planets colour-coded by detection method. The field is showing exponential growth. Data are from exoplanet.eu and are correct as of 23rd May 2018.

(a) there is a wide range of detection methods available and (b) these detection methods complement each other in accessing different areas of the parameter space. This plot only shows two parameters: not shown is that these planets also span a huge range of ages stellar types, and planet obliquities and each detection method brings a unique angle. For example, microlensing is the only technique able to detect planets at several kiloparsecs, and thus the only technique able to probe the frequency of planets towards the galactic bulge. Over the next decade, this plot will dramatically change again with the *TESS* and *Gaia* missions each predicted to detect thousands of new exoplanets (Barclay et al. 2018; Perryman et al. 2014).

In recent years, it has become possible to not just detect these exoplanets, but also characterise them in detail. Sing et al. (2016) presented spectra of ten hot Jupiters, demonstrating a diverse range of atmospheres showing a continuum from clear to cloudy objects. Spectroscopic studies like this allow us to probe the compositon, surface gravity and temperature of exoplanets, and eventually understand their formation and habitability. Missions such as CHEOPS, JWST and eventually ARIEL will revolutionise our ability to characterise exoplanets by providing spectra of far more exoplanets, and at far better

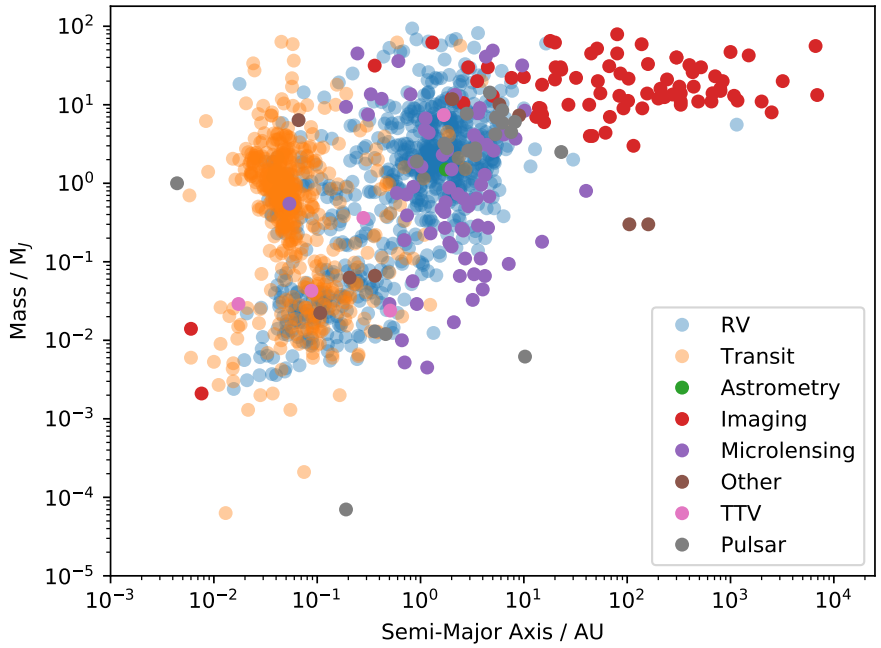

Figure 1.2: Mass vs semi-major axis for the 1483 planets for which masses have been determined. The objects are color-coded by detection method, and due to the large number of transiting and RV planets, these objects are shown with semi-transparent points. The planets span a wide range of parameter space, and the constraints on this plot are predominantly due to the limitations of current detection methods. Data are from exoplanet.eu and are correct as of 23rd May 2018.

resolution than is currently possible.

1.2 Exoplanets at the widest separations

The vast majority of the detected planets are found within a few AU of their host stars. High Contrast Imaging, meanwhile, gives access to another population of planets at the very widest separations from their host stars. These objects bridge the gap between brown dwarfs and small, rocky planets, and their formation and classification as planets or brown dwarfs is often debated.

Understanding the occurrence, or lack thereof, of planets at these very wide separations is a key ingredient in being able to probe and understand the complete architecture of exoplanetary systems. The large numbers of exoplanets discovered at close separations provides a framework for addressing the frequency of exoplanets around nearby stars. The frequency of planets at close separations is relatively well constrained, with Howard

et al. (2010) finding that $11.8^{+4.3}_{-3.5}$% of stars have planets with mass 3-10$M_\oplus$ and orbital period up to 50 days using an RV sample, and Fressin et al. (2013) finding an occurence rate of 16.5 ± 3.6% for planets with radii between 0.8 and 1.25 $R_\oplus$ and orbital period up to 85 days. The population of giant, wide-separation planets is smaller, with both Bowler (2016) and Vigan et al. (2017) finding occurence rates of a few percent.

Such objects are inaccessible with the transit and radial velocity methods, due to the very long time baselines required to observe multiple transits or a characterisable RV trend, and the low probability that a planet at these wide separations will transit. Indeed, high contrast imaging is the *only* method that allows these wide-separation objects to be studied and characterised. However, high contrast imaging with current instruments is only sensitive to the most massive planets. Figure 1.3, from (Bowler 2016), shows the median sensitivity of the NICI instrument (see Biller et al. 2013), along with scaled curves that demonstrate the effect of telescope efficiency, stellar age and stellar distance on the parameter space accesible to high contrast imaging. Even in the best cases, i.e. the best possible instruments, the best weather conditions and the youngest target ages, only planets with mass $\gtrsim 1\,M_J$ can be imaged.

Planet formation necessarily requires gravitational concentration of a large amount of matter, which generates significant quantities of latent heat. Very young planets are therefore very warm and very bright, and the planets radiate heat and cool throughout their lifetimes. Figure 1.4 shows age-luminosity relations for stellar (orange), brown dwarf (green) and planetary (blue) objects. Stars, which are sustained by hydrogen fusion, show an almost constant luminosity beyond a few million years, planets are not internally heated and so cool throughout their lifetimes: companions at less than 10 Myr are only a few orders of magnitude fainter than the sun, while at old ages, even large planets with mass $\sim 1 - 10\,M_J$ have $T_{\rm eff} \sim 100 - 500\,K$, and absolute magnitudes in the near-infrared of ≤ 18 mag (Dupuy & Kraus 2013), making these objects increasingly inaccessible to direct imaging.

So far, only a handful of planets have been detected with high contrast imaging. The exact number is often debated, since many objects sit near the planet/brown dwarf boundary. The census of objects near this boundary for which there are age and bolo-

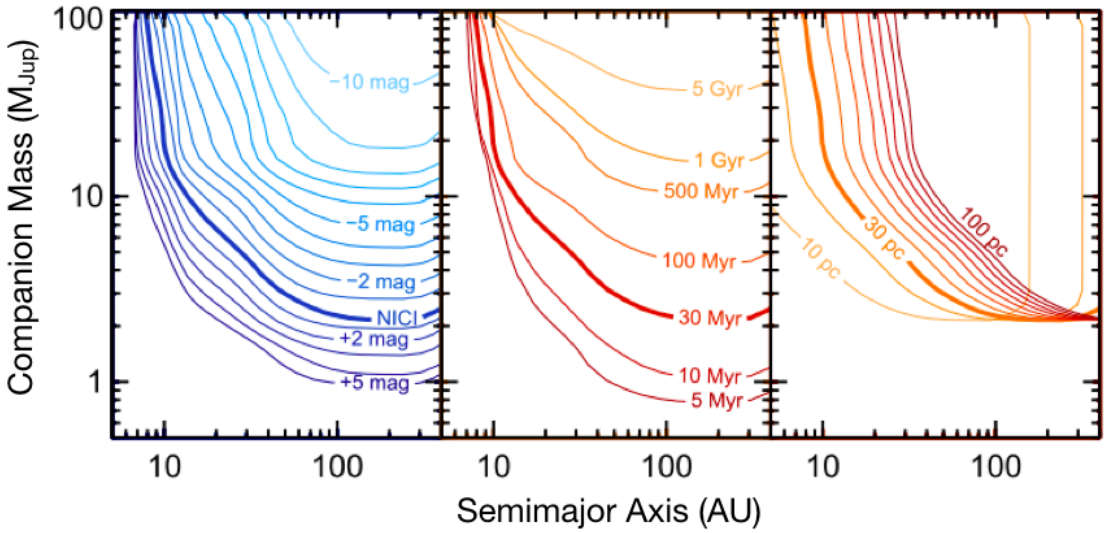

Figure 1.3: Mass and separation limits for typical direct imaging surveys. In each panel, the bold curve is the 50% sensitivity curve of the NICI survey in Biller et al. (2013) for a 30 Myr K1 star at 30pc, and additional lines indicate the effect of changing the limiting contrast, stellar age and stellar distance on the physical parameters that can be probed. Since the absolute magnitude of the planet depends steeply on its mass and age, a small gain in contrast in the brown dwarf regime corresponds to a large gain in limiting mass, but the same contrast gain in the planetary regime translates into a much smaller gain in mass. The mass limit is particularly sensitive to stellar age, while closer distances mean smaller physical separations can be studied. Figure adapted from Bowler (2016).

metric luminosity measurements are overplotted on Figure 1.4. Many of these objects span the planet/brown dwarf boundary, and more accurate determination of their ages might alter their designation. The occurrence rate and distribution with mass and radius of these objects allows us to probe how they form and migrate to wide separations, and to differentiate between various formation routes. Giant planets at wide separations might be formed by turbulent fragmentation (Boss & Bodenheimer 1979; Boss 1986; Bate et al. 2003), disk instability (Durisen et al. 2007; Kratter & Lodato 2016), pebble accretion (Lambrechts & Johansen 2012), or planet-planet scattering (Veras et al. 2009), and each of these formation pathways should form a unique mass/radius distribution of giant planets.

With only a small number of wide-separation planets known, it remains difficult to differentiate these pathways, and to find correlations with host star properties (e.g. stellar type, presence of debris dust, etc.). Wide-separation planets are certainly rare, with the two biggest statistical analyses to date both finding occurrence rates ~1% (Bowler 2016; Galicher et al. 2016). Tentative evidence has been found that there might be a correlation

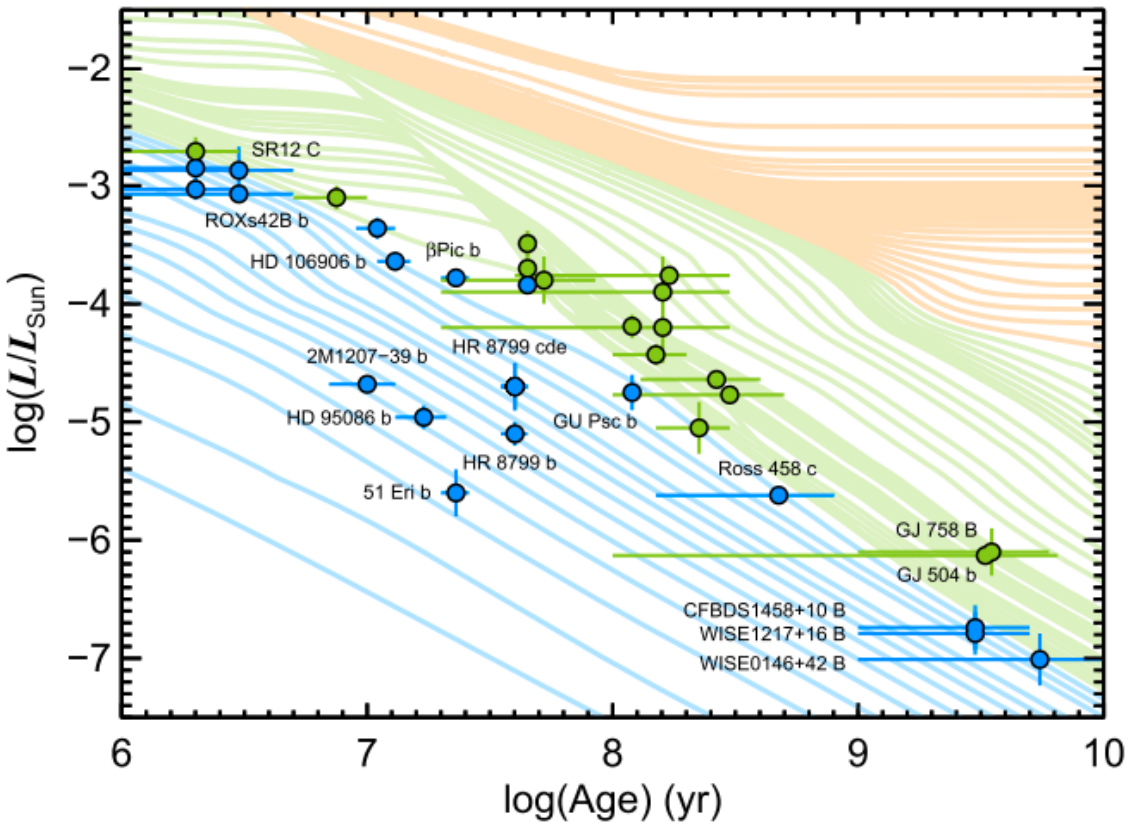

Figure 1.4: Age-luminosity tracks for objects at a range of masses. Orange, green and blue tracks represent masses >80 M_J, 14−80 M_J and <14 M_J, and therefore loosely correspond to stellar, brown dwarf and planetary objects. The tracks shown are hot-start evolutionary models taken from Burrows et al. (1997). Overplotted are the known low mass planetary companions and candidate planets (as of 2016) for which age and bolometric luminosity have both been determined. Many of these objects lie close the the boundary, and an updated age determination could easily change their current designation as either a planet or a brown dwarf. Figure from Bowler (2016).

of occurrence rate with stellar type (see Lannier et al. 2016), but this was not confirmed by Bowler (2016).

Beyond using the occurrence rate and mass/radius relationship of these planets to probe formation, high contrast imaging holds a particular advantage in that any planets that are detected can then also be studied spectroscopically. High contrast imaging is the only exoplanet detection method for which stellar and planetary light are spatially separated, which offers a clear advantage in spectroscopic analysis, without some of the biases and systematic errors present in transit spectroscopy. Spectroscopic observations of wide-separation planets allows a unique insight into the formation, migration and atmosphere of gas giant planets. Example spectroscopic analyses of two low-mass companions are shown in Figure 1.5: the two spectra are taken with the VLT/SPHERE long-slit spectroscopy mode and the Keck/OSIRIS instrument respectively. The later is particularly notable since at high resolution ($R \sim 4000$) individual molecular absorption lines can be detected.

1.3 Survey Optimisation

Radial Velocity, transit and microlensing surveys all demonstrate that at close separations (less than a few AU), super Earths and small rocky planets are far more common than giant gas planets. Although it is not clear if this trend continues to wider separations, it is certainly obvious that the occurrence rate of giant planets at the widest separations is low. In a meta-analysis of several deep imaging surveys, Bowler (2016) found an overall occurrence rate of $0.6^{+0.7}_{-0.5}$% for companions in the range 5-13M_J and $30 - 300$ AU.

Given this low occurrence rate and the difficulty in detecting exoplanets via direct imaging as discussed above, surveys must be carefully designed so as to have a high chance of detecting objects and allowing meaningful scientific conclusions to be drawn. Several groups of targets are of particular interest when designing surveys, and some of these target types are described below.

Planets become cooler and fainter as they age (e.g Chabrier et al. 2000; Baraffe et

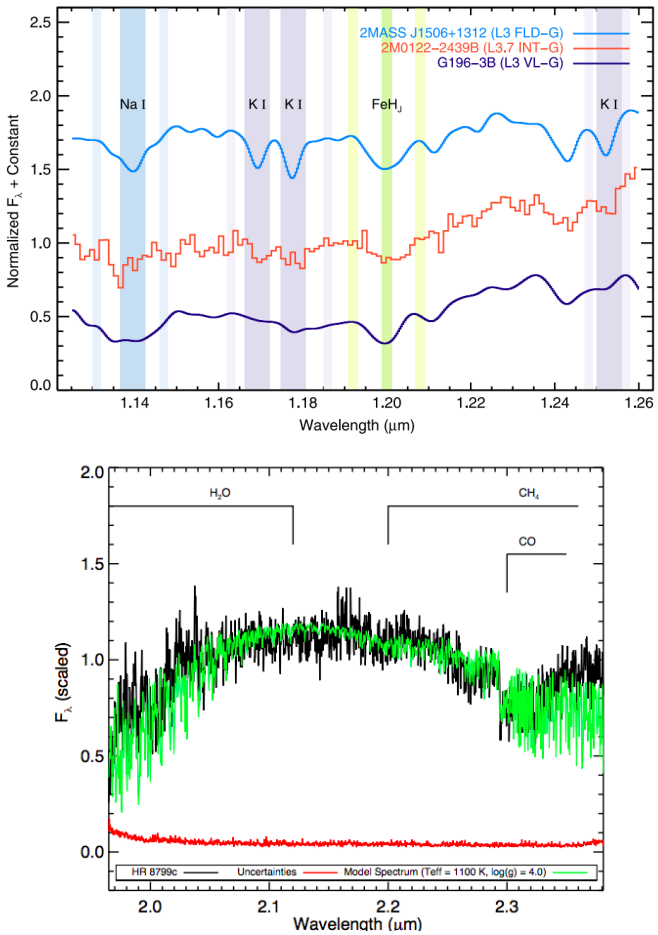

Figure 1.5: Two examples of spectroscopy of directly imaged low-mass companions. *Top:* A spectrum 2MASS 0122-2439 B, an object on the planet/brown-dwarf boundary with a similar contrast to the HR 8799 planets. The spectrum is taken with SPHERE and with an integration time of ~1 hour and has a resolution $R \sim 350$. The spectrum is in red, and is presented alongside a young object (in light blue) and a field age object (dark blue) of a similar spectral type. Gravity-sensetive absorption features are highlighted. Figure from Hinkley et al. (2015a). *Bottom:* A Keck/OSIRIS spectrum of HR8799c (in black) at $R \sim 4000$. Uncertainties are shown separately in black, and the bext fit model spectrum is in green. Individual absoprtion lines can be seen, with the CO absorption being particularly pronounced, although the broad CH_4 features are not easily detected. Figure from Konopacky et al. (2013).

al. 2003; Helling et al. 2008; Allard et al. 2011; Allard et al. 2012), and so observing the youngest planets allows for the lowest mass planets to be detected (see Figure 1.3 above). A very common tactic therefore is to select targets in young moving group: these nearby groups of stars have precise ages (e.g. Bell et al. 2015; Herczeg & Hillenbrand 2015) based on lithium depletion boundaries and isochrone fitting, and are close enough that survey telescopes are sensitive to planets within a few tens of AU. Mamajek (2016) lists a total of 14 moving groups within 100pc, and with ages between 10 ± 3 Myr (TW Hya; Bell et al. 2015), and 750 ± 150 Myr (the Hyades; Brandt & Huang 2015). The moving groups of particular interest are those with ages $\lesssim$ 100 Myr, such as β Pic, Tuc-Hor, and Columba.

Although outside this constraint, AB Dor has an older age of 150^{+50}_{-30} Myr (Bell et al. 2015), but a very close distance of 20.1 ± 1.6pc (Barenfeld et al. 2013) and so is also of interest. *Gaia* will undoubtedly reveal new members of these moving groups, and possibly new moving groups altogether, which will likely be excellent targets for future high contrast imaging surveys.

Similarly, the Scorpius-Centaurus (Sco-Cen) association is the focus of many surveys, especially with the newest generation of instruments which have better sensitivity at very small angular resolution. This extra sensitivity allows for planetary mass objects to be detected at the slightly further distance of Sco-Cen (~140pc, de Zeeuw et al. 1999). This region is very young (~10 – 16 Myr, Pecaut & Mamajek 2016) and so planets shortly after the period of active planet formation can be observed. This allows for the best constraints to be placed on the radial locations at which planets form, and on the very early thermal histories of young planets which are particularly relevant in differentiating the hot- and cold-start models of planet luminosity (Ireland et al. 2011; Janson et al. 2013a; Lafrenière et al. 2014; Hinkley et al., 2015b). A key benefit of Sco-Cen over nearer groups of stars is that it has hundreds of members (de Zeeuw et al. 1999; Rizzuto et al. 2011), a significant benefit in designing a uniform survey and in studying a group of objects at very similar age.

Another area of interest is understanding the occurrence rate of planets in binary star systems. This is technically challenging: if multiple bright objects are present in the field of view, the performance of adaptive optics correction is reduced. Additionally, since only one star can be placed behind the coronagraph, the second star will quickly saturate. However, such systems are of key interest from an architecture point of view: the presence of a binary companion should inhibit planet formation since the protoplanetary disk is truncated or even completely cleared (Cieza et al. 2009; Duchêne 2010; Kraus et al. 2012), but both circumprimary and circumbinary planets have been detected, and understanding the formation of these planets is a key area of interest. The SPOTS survey (Thalmann et al. 2014; Bonavita et al. 2016) avoid the challenges of high contrast imaging in binary systems by looking at binaries that are either so close that the two stars are spatially unresolved, or so wide that only one appears within the field of view. Rodigas et al. (2015)

presents a novel post-processing method where two binary stars are imaged simultaneously and used as reference stars for each other, and another avenue is to explore methods of wavefront control that are effective even when there are two bright objects in the field of view (see e.g. Thomas et al. 2015; Sirbu et al. 2017).

The PALMS survey (e.g. Bowler et al. 2012; Bowler et al. 2017) searches specifically for planets around low mass stars. Planets should be harder to form around very low mass stars since the proto-planetary disks are less massive (Andrews et al. 2013; Mohanty et al. 2013), but the relatively faint magnitudes of these stars mean that the same contrast allows a deeper absolute magnitude to be probed in the speckle-dominated region close to the host star. Many of these objects have masses that are a large fraction of the host mass (typical mass ratios are 0.2-0.5), leading to speculation that they form similarly to binary stars.

For a number of targets, long-term RV trends exist that hint at the presence of a companion: if RV monitoring over a number of years indicates that a star is accelerating, then the star is presumably orbited by either a giant planet or brown dwarf, or a more massive companion at wider separation. High-contrast imaging in these cases can rule out massive, wide-separation objects (see e.g. Luhman & Jayawardhana 2002; Kenworthy et al. 2009), and possibly even detect the companion responsible for the RV trend (e.g. Crepp et al. 2012; Crepp et al. 2014). If planets are found in these cases, the radial velocity data allows independent constraints to be placed on the mass of the planet, and thus independently verify the luminosity models that are normally used to calculate masses.

Finally, many surveys have targeted and continue to target stars that host debris disks, as described in detail in the next section.

1.4 The role of debris dust

Debris disks are the long-lived clouds of planetesimals and second-generation dust within a stellar system. Such disks can be identified by the thermal emission of the dust components of the disk, which appears as an excess emission above the stellar photosphere

in the infrared. 20% of A-stars host dusty debris disks (Rhee et al. 2007). The first such debris disks were identified with *IRAS* (Aumann 1985), and the majority of known disks have been identified with *Spitzer*, *Herschel* and *WISE*. Dust within a stellar system is short lived, since it is either blown out by stellar winds, or falls onto the star via the Poynting-Robertson effect, and so for the dust to be observed it must continuously be produced by planetesimal collisions. These planetesimals, in turn, must be stirred so as continually collide and replenish the dust within the system. Several causes of this stirring have been suggested: the dust could be pre-stirred by process during the protoplanetary stage of disk evolution (Wyatt 2008), stirred by an external influence such as a stellar flyby (Kenyon & Bromley 2002), self-stirred if the planetesimals are of sufficient size (Kenyon & Bromley 2010; Kennedy & Wyatt 2012), or stirred by exoplanets (Mustill & Wyatt 2009).

The link between planets and debris has long been inferred, both because the presence of a debris disk implies that at least some level of coagulation has occurred between the initially micron-sized dust grains in a stellar system, and because the planetesimals producing the debris dust might be stirred by exoplanets. Wyatt et al. (2007) predicts a correlation between planets and debris disk brightness, although Raymond et al. (2012) predicts an anti-correlation between eccentric Jupiters and debris dust, but a correlation between terrestrial planets and debris. In the case of radial velocity planets, Moro-Martín (2013) found that disks were more common around systems known to host low-mass planets. Several studies have also attempted to explore the link between directly imaged planets and debris, by searching for planets in systems known to host circumstellar dust (see e.g. Janson et al. 2013a; Rameau et al. 2013; Wahhaj et al. 2013; Meshkat et al. 2015). It is worth noting at this point that many of the known directly imaged planets reside in highly dusty systems: HR 8799 bcde, 51 Eri-b, HD 95086 b, β-Pictoris and HD 106906 all belong to this category. However, since many survey samples are biased towards debris disk targets, this face-value correlation does not itself imply a statistically sound link between directly imaged planets and debris dust. Meshkat et al. (2017) was the first work to find a statistically significant excess (at the 88% confidence level) of planets around debris hosting stars, relative to a control sample.

The occurrence and architecture of debris disks gives clues as to the formation of

exoplanets in these systems: for example, correlations of dust with spectral type might indicate that planets also form more or less easily around stars of certain spectral types. Multi-disk systems give a unique insight into the formation of planets under the influence of external perturbers: planets are known to exist in binary star systems (e.g. Correia et al. 2005; Doyle et al. 2011), and are known to exist on highly oblique orbits (Campante et al. 2016). Although some work has looked at whether such oblique planets might be formed by wide separation binaries (see e.g. Knutson et al. 2014; Ngo et al. 2015), observing the debris disks themselves can shed light on whether the planets form in a tilted disk, or migrate onto their eventual oblique orbits. However, only a few systems are known which host multiple debris disks (notably the quadruple star system δ Sculptoris, see Matthews et al. 2014, and the tertiary Fomalhaut system, see Kennedy et al. 2013).

A particularly interesting subset of debris disk targets is those stars with additional dynamical hints that there are planets present: those that show signs of sculpting, for example when sharp edges have been imaged, or when the debris dust is sculpted into two distinct components. Apai et al. (2008) was the first work to target specifically such sculpted dust systems, and both Meshkat et al. (2015) and Lazzoni et al. (2018) survey specifically two-belt debris disk systems. Both HR 8799 and HD 95086 host such two-belt debris disks, and the planets in these systems are sandwiched in between these dust rings (see Reidemeister et al. 2009; Su et al. 2009; Matthews et al. 2014 for HR 8799 and Su et al. 2015 for HD 95086). Although this is a tantalising correlation, no statistical trend has yet been confirmed between directly imaged exoplanets and sculpted debris disks.

The presence of sculpted dust can reveal additional clues about the exoplanets in a system, whether or not these exoplanets have been detected. For example, N-body simulations of the system evolution can be used to probe the mass an orbit of exoplanets that might have shaped the debris, based on the distribution of an observed debris disk (see e.g. Thilliez & Maddison 2017). More generally, several theoretical works have used simulations to place limits on the masses of planets between two belts of debris at known radius: Nesvold & Kuchner (2015) and Morrison & Malhotra (2015) both investigate the single planet case, while Shannon et al. (2016) calculates the mass and expected number of planets between two debris belts for multi-planet systems. In dusty systems where a

directly imaged planet has been identified, N-body simulations can be used to calculate dynamical masses. The HR 8799 planets have been shown to have masses $\lesssim 10\,M_J$ so as to be dynamically stable to the age of the host star (e.g. Goździewski & Migaszewski 2014; Fabrycky et al. 2012; Currie et al. 2011; Sudol & Haghighipour 2012; Goździewski & Migaszewski 2014). In the case of HD 106906, meanwhile, Rodet et al. (2017) used N-body simulations to conclude the planet is likely being ejected from the system and on an eccentric orbit, based on the debris disk morphology.

It is well studied that the rate of stars hosting a debris disk excess decreases with age (Su et al. 2006; Trilling et al. 2008; Carpenter et al. 2009; Chen et al. 2011; Chen et al. 2012; Urban et al. 2012), a result that has been shown to hold regardless of spectral type. Selecting debris disk stars therefore applies an automatic bias towards young stars to any survey: this is beneficial for direct imaging, where targeting the youngest stars allows for the best detection limits.

To understand the interaction of debris disks and planets in detail, it is important to obtain resolved images of the debris. However, this is technically challenging since debris disks are typically at least ~100 times fainter than protoplanetary disks (Matthews et al. 2014), and are within a small angular separation of their host star (typically extending to fewer than a few hundred AU, or a few arcseconds for a star at 100pc). Although some success has been had resolving the thermal emission of disks with *Herschel* (e.g. Morales et al. 2013) and ALMA (e.g. Lieman-Sifry et al. 2016), to date only ~40 debris disks have been imaged in scattered light (Choquet et al. 2016) and only a small subset of these at the high resolution that 8m-class, ground-based telescopes can provide.

Such resolved images of debris disks are vital in fully understanding the debris disk extent, morphology and grain properties. Although an approximate radial extent of the debris can be inferred by fitting the SED and using the assumption that the dust is emitting as a blackbody and in equilibrium, Pawellek & Krivov (2015) found that debris disks are generally further from their host than this equilibrium would imply. Morphological features (warps, rings and spirals), meanwhile, might hint at the dynamical influence of a planet on the debris. Finally, in a resolved disk the grain properties can be understood: polarisation probes the typical grain properties within the disk (see e.g. Hinkley et al. 2009;

Graham et al. 2007), and it is sometimes possible to extract chemical composition from the spectral features of the disk (Lisse et al. 2012), although this has rarely been achieved in practice. The most valuable systems are those were multi-wavelength observations have been obtained: in these cases, the radial and temperature distribution of grains, and their size and composition, can be probed and the resulting advanced understanding of the disk sheds light on how these systems form and evolve.

1.5 Methods for High Contrast Imaging

1.5.1 Challenges of High Contrast Imaging

1.5.1.1 Intrinsic Faintness

Planets are faint (see Figure 1.4 above). Jupiter, the brightest planet in the Solar System, is 10^9 times fainter than the Sun at visible wavelengths, and the Earth is an order of magnitude fainter again. This intrinsic faintness can be partially overcome by choosing an appropriate observational wavelength: the spectral energy distribution (SED) of a sun-like star peaks at visible wavelengths, while an exoplanet will have a much cooler temperature, and consequently an SED that peaks in the near- or mid-infrared, well into the Rayleigh-Jeans tail of the stellar SED. A schematic of this is shown in Figure 1.6 in the context of the solar system, as viewed from 10pc. At 0.5 μm the Sun is 9 orders of magnitude brighter than Jupiter, and 10 orders of magnitude brighter than the Earth, but at a longer wavelength of 50 μm the contrast barrier is less prohibitive, with Jupiter and the Earth being 5 and 6 orders of magnitude fainter than the Sun respectively.

There are also drawbacks to observing at these much longer wavelengths: firstly, at longer wavelength the same telescope aperture provides a lower resolution. This is problematic, since obtaining sufficient angular resolution is a key challenge in direct imaging (as detailed below). Secondly, one would ideally like measurements of the planet at a broad range of wavelengths so as to characterise both the reflected and emitted light from the planet, and as such fully explore its properties including atmosphere, weather and

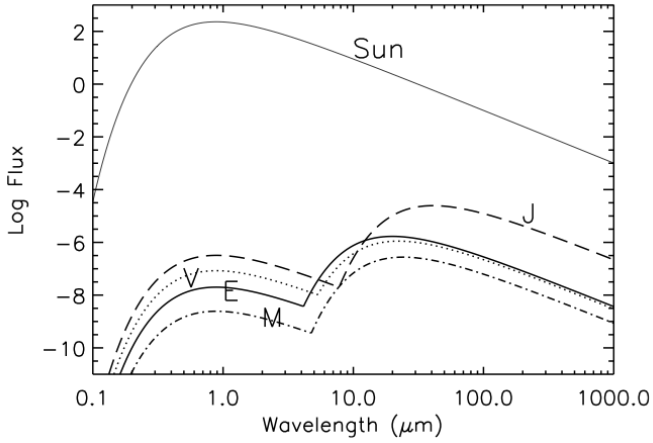

Figure 1.6: Idealised spectral energy distributions (SEDs) for Solar System bodies viewed from 10pc. Jupiter, Venus, Earth and Mars are shown and labelled as J, V, E and M respectively. In each case there are two peaks: at low wavelengths, below a few microns, the planets are primarily reflecting stellar light, while at longer wavelengths the planets emit thermally. While the contrast at any wavelength is a challenge to direct imaging, this challenge is less extreme when observing at longer wavelengths: at 1 μm the contrast of Jupiter is 10^9, at 10 μm it is $10^{7.5}$ and at wavelengths $\gtrsim$140 μm it is just 10^4. Figure from Seager (2003).

composition. Finally, ground-based observations are limited to the wavelengths of light at which the atmosphere is transparent for ground-based observations. Ground-based high contrast instruments tend to use near-infrared wavelengths, in the ~1-5 μm range.

As detailed above in Section 1.3, targets can also be carefully selected to partially overcome this contrast barrier. The youngest stars, the nearest targets, and targets with circumstellar dust can all be target in direct imaging surveys so as to reduce the extreme contrast barrier faced and increase the expected detection rate.

1.5.1.2 Angular Resolution

Although planets are very faint, these objects are well above the limiting magnitudes of 10m-class telescopes. The real technical challenge comes from imaging an object that is simultaneously very faint and very close to a much brighter object, namely its host star. To put the scales into context, the separation between Jupiter and the Sun as viewed from a distance of 100pc subtends an angle of 0.052″: this is the same angle as would be subtended by a grain of sand, viewed from a distance of 1km. Not only do objects at these tiny separations need to be spatially separated and resolved, but this needs to be done when one is a million or more times brighter than the other.

The angular resolution problem can be partially overcome by observing with telescopes in the 8-10m range, such as Keck, the VLTs and Gemini. Not only are these large instruments far more efficient at collecting light, which is important in allowing the faint apparent magnitudes of planets to be reached, but crucially they allow the best possible angular resolution to be reached. Even with these world-class facilities, the planets we aim to detect are separated by a few times the diffraction limit, and so careful control and suppression of the stellar light is vital.

1.5.1.3 Quasistatic speckles

Imagine a single point source, which in the diffraction-limited case produces an Airy ring in the image plane. An idealised sinusoidal phase aberration applied to the telescope pupil would create offset copies of this Airy ring in the image plane, formed by the convolution of the Fourier transform of a single point source (an Airy pattern) with the Fourier transform of a sinusoid (a pair of delta functions with separation set by the frequency of the phase aberration). Since any distortion on the telescope can be decomposed into a linear combination of sinusoidal phase aberrations, a complex set of distortions creates a complex pattern of faint, offset images of the central pattern. This light in the image plane is referred to as quasi-static speckle noise, and the complex pattern of quasi-static speckles is one of the key factors limiting the imaging contrasts achievable. As well as being an additional source of noise in the final image plane, these speckles by their very nature have the same full-width half maximum (FWHM) and are often similar in brightness to the low-mass companions that we hope to detect, and so in a single image can appear identical to a real, on-sky companion.

1.5.2 Starlight Control & Suppression

1.5.2.1 Extreme Adaptive Optics

For starlight to be removed as effectively as possible, that light should ideally be as concentrated as possible. However, 8-10m class telescopes have resolutions well above the seeing

limit at near-infrared wavelengths. In a typical image without adaptive optics correction, stellar light is spread across the central ~0.5 – 1.0" of the image, in a highly unpredictable and constantly varying manner since it is scattered by the turbulent atmosphere.

Extreme adaptive optics can be used to overcome this problem by concentrating the light into a tight, diffraction-limited core, which can be effectively blocked by use of a coronagraph. The effect is shown in Figure 1.7: on the left is an image taken with the Keck telescope and with the AO system turned off. The stellar light is scattered throughout the image. The right hand side of Figure 1.7 shows an image once the AO has been turned on, and the starlight is concentrated into a small circle in the centre of the image.

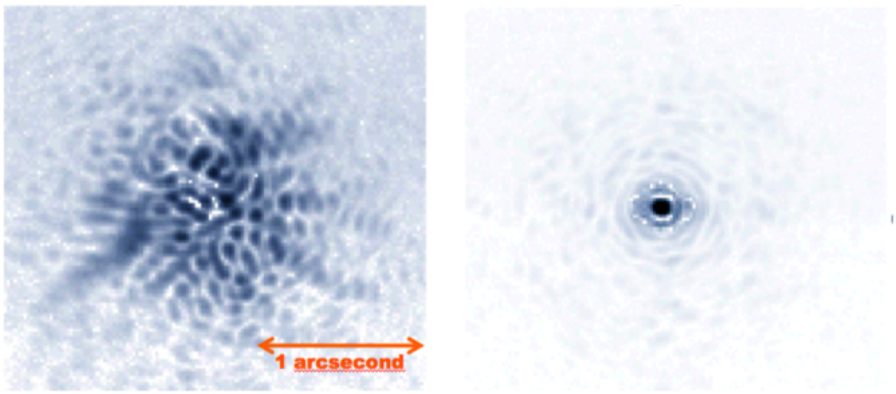

Figure 1.7: Example image of a bright star, taken without (left) and with (right) an adaptive optics system in place. On the right, the light is far more concentrated into the central Airy disk and surrounding rings, increasing the angular resolution achievable. As such the adaptive optics allows far greater starlight control, enabling easier subsequent starlight subtraction. Figure provided by Sasha Hinkley with data from Remi Soummer and James LLoyd.

To carry out this AO correction, a bright guide star is used to measure the abberrated incoming stellar wave front. In most cases, the stars around which a planet search is being conducted are sufficiently bright to serve as their own reference stars: this is the case for all of the targets in this thesis. By monitoring light from this reference star, the atmospheric distortions can be measured and removed. To do this, a portion of the telescope light is redirected to a wavefront sensor, and the distortions to the wavefront are monitored. This is then relayed to a deformable mirror which is distorted opposite to the distortions the atmosphere is imposing, thus smoothing out these distortions and leaving a flat plane wave. This correction must be repeatedly looped to account for the constantly changing atmosphere: the time period for which the atmosphere can be assumed unchanging is the coherence time, which for visible wavelengths is typically a few milliseconds (Davies &

Kasper 2012), and the correction must be run at least once every coherence time. There are technological limitations to this process since the corrective loop takes a finite time to run, and the actuators controlling the deformable mirror have some finite spacing, so very high order deformations and very quick changes to the deformation cannot be taken into account.

Adaptive Optics is more effective at longer wavelengths: the typical scale length of atmospheric distortions, known as the Fried parameter r_0, scales as $\lambda^{\frac{6}{5}}$ (Davies & Kasper 2012). The distortions have a larger typical scale at long wavelengths, and so are more easily compensated with the deformable mirror. However, observations at longer wavelength also have inherently lower resolution (since $\theta \sim \lambda/D$), and so a compromise is required. Typically, ground-based high contrast imaging survey are carried out in the near infrared, between ~1-5 μm.

1.5.2.2 Coronagraphy

The basic idea behind coronagraphy was first proposed by Lyot (1939) in his studies of the solar corona, and the goal is to block light from on-axis bright source using a mask, to allow a far dimmer off-axis target to be observed. A traditional coronagraph uses two optical stops: firstly an occulting stop in the image plane and secondly a Lyot stop in the pupil plane. The idea was optimized for use with modern adaptive optics by Sivaramakrishnan et al. (2001). A one-dimensional representation of the process, from the same paper, is shown in Figure 1.8. Note that between the initial image (b) and the final output (h) 98% of the stellar light is removed.

The technology for coronagraphs has significantly developed recently, and perhaps the simplest improvement to this technique is the use of Apodized Pupil Lyot Coronagraph (APLC). Here, the sharp edges of the telescope pupil are softened, thus reducing the numerous resulting Airy rings in the final image. There are many additional methods for coronagraphic suppression of light, detailed for example in Guyon et al. (2006). For the moment at least, APLC is proving to be the most efficient, since it provides a good balance between suppression of stellar light and throughput of planetary light.

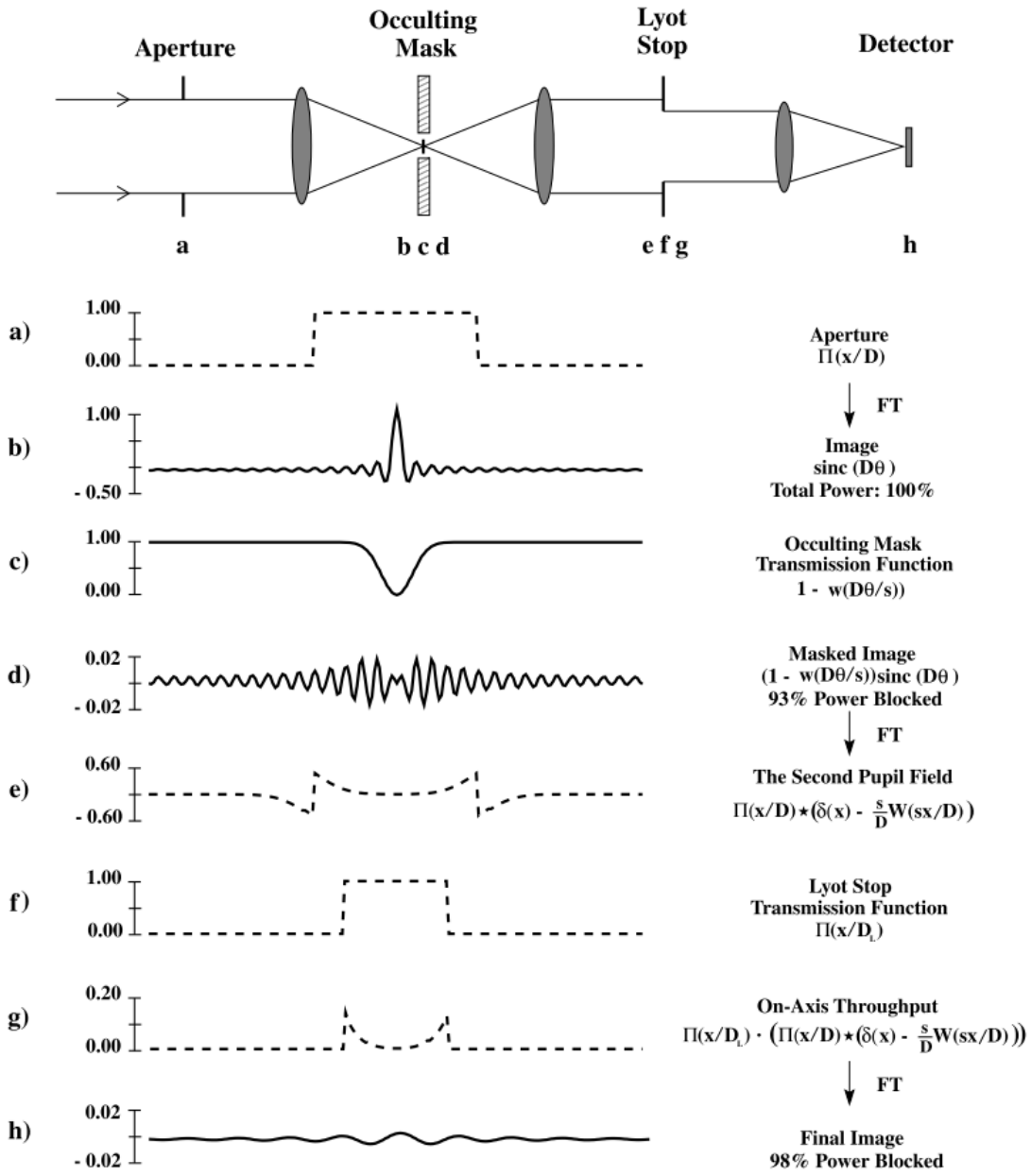

Figure 1.8: Demonstration of Lyot Coronagraphy in one dimension. The schematic shows the locations of lenses and optical stops, and the plots below show the intensity at different planes in the coronagraph: dotted lines indicate pupil plane while solid lines are in the image plane. The initial aperture gives the wave the form of a top-hat function, which Fourier transforms into a sinc-squared pattern in the image plane. Multiplying this by an occulting mask significantly reduceds the central intensity. A second mask, the 'Lyot stop', in the pupil plane further reduces the intensity, such that in the final image 98% of the power is blocked. Figure from Sivaramakrishnan et al. (2001).

1.5.3 Data post-processing

As described in Section 1.5.1.3, tiny defects on the telescope mirror give rise to quasi-static speckles in the image plane. Since some of these speckles are correlated over thousands of seconds (Hinkley et al. 2007), it is impractical to remove these speckles by increasing the

exposure time, as could be done for stochastic noise. Image post-processing requires that the speckle noise and the real astrophysical sources to be disentangled so that the speckles can be effectively subtracted without real planetary or debris disk signal being removed. Speckle noise changes with time, wavelength and orientation in ways that are unphysical for real astrophysical sources, and are in general unpolarised. By exploiting these various differences between planet signal and speckle noise, the two can be differentiated and genuine planets detected, as detailed below.

1.5.3.1 Reference Differential Imaging

Perhaps the simplest method for removing speckle noise is simply to image another star to measure the shape of the point spread function (PSF) and speckle noise. This image can be subtracted from images of the target star, so as to remove the majority of the stellar light and preserve any companion signal. This method relies on the PSF being static, whereas in reality the speckles have a wide range of lifetime between tens and thousands of seconds (Hinkley et al. 2007). Only the broad shape of the PSF, and speckles that are common between the reference and the target observation, will be removed. In fact, the very act of moving the telescope between the reference and the target star will cause slight changes to the tensions present in the telescope mirror, and as such tiny deformations present on the mirror surface will evolve as the telescope moves. This causes the speckles to evolve, making the reference PSF imperfect. To minimise this effect, it is vital that observations use a reference star close to the science target. In addition, the reference star must ideally be color-matched, especially if observations are carried out with a wide filter, to account for the wavelength dependency of the PSF.

The best reference star, therefore, is one that is as close as possible in spectral type to the target star and is observed as close as possible in time to the science observations. An ideal reference would therefore be images of the target star itself, taken during the science observation sequence. That is indeed possible, as described in the next section.

1.5.3.2 Angular Differential Imaging

The stellar PSF and speckle noise are formed by tiny imperfections in the telescope mirror and optical path, and so if the mirror is rotated these retain their orientation relative to the image. The plane of the sky, meanwhile, appears to rotate relative to the image as a result of this mirror rotation. Scattered starlight speckles therefore appear in the same place between each image, and astrophysical sources (planets, debris disks, and background stars) appear at different locations in each image. Angular Differential Imaging (ADI, first developed by Marois et al. 2006) makes use of this angular diversity to separate speckle noise and astrophysical signals. The method is demonstrated in Figure 1.9: stellar speckle noise is first modeled by median combining several images taken at different rotation angles. This median image is subtracted from each individual frame, to removed the majority of the speckles. The images are then derotated so that the planetary signal is aligned, and co-added to improve the planet flux and reduce the stellar speckle noise further. A median combination is used since this removes outlier values, and so the stellar noise is modelled with minimum contamination from the planet signal. A bright planet will nonetheless shift this median value to brighter fluxes, and so when the median is subtracted faint images of the planet appear as negative flux shadows.

In the case of space-based observations (e.g. with the Hubble Space Telescope), this process is typically carried out with only a few distinct angles: for consecutive orbits, the telescope is rolled by typically 20-30°, and the final image is similar to that in Figure 1.9 panel (e). For ground-based observations, the process makes use of the natural movement of the sky relative to the Earth. Through the course of a night, the Earth rotates under the sky, and for an alt-azimuth telescope the sky appears to rotate in the image frame as the telescope tracks the motion of an individual star. In this case, negative flux arcs appear either side of the planetary signal, which is itself slightly weaker than a pure co-add (see Figure 1.9 panel (f)). This self-subtraction effect must be taken into account when measuring planets and debris disks detected with ADI.

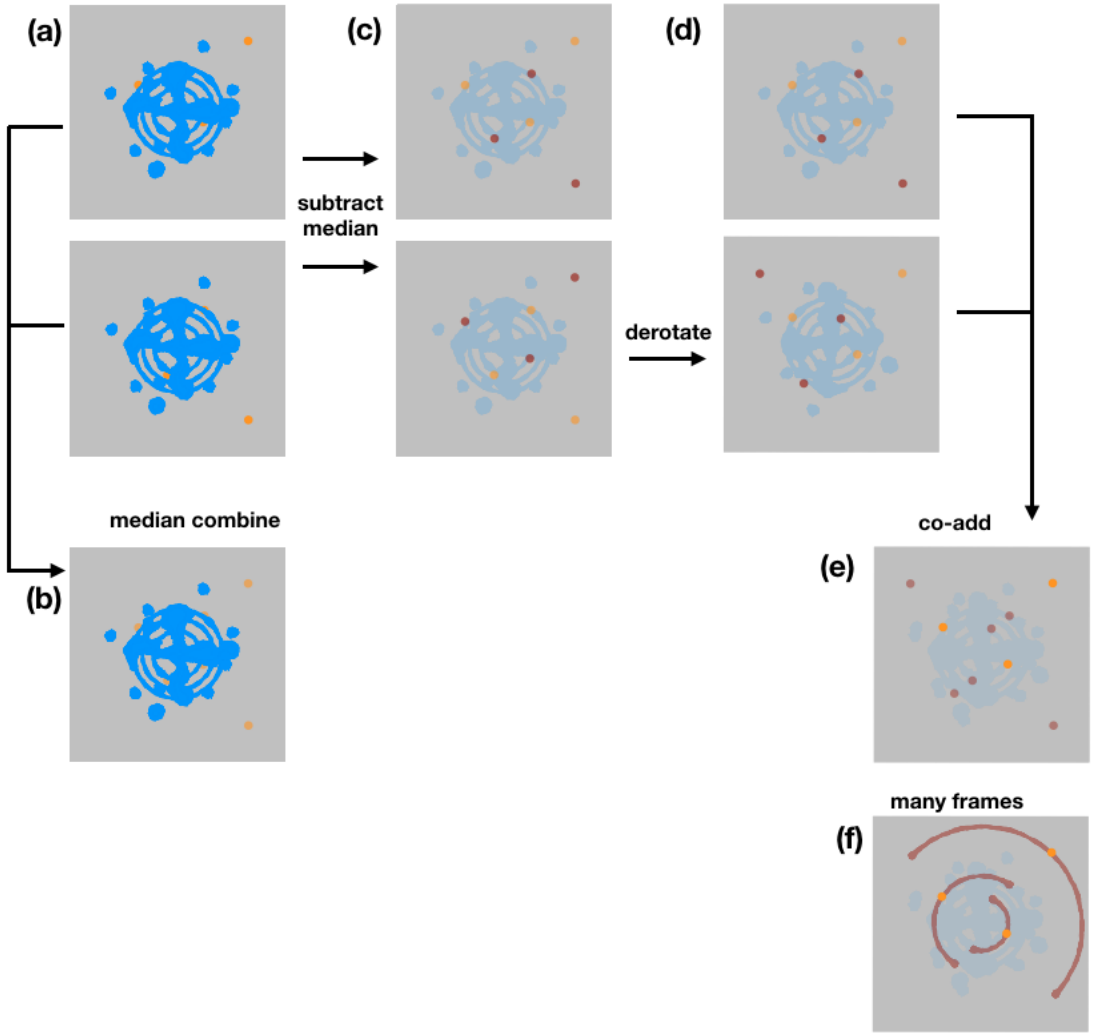

Figure 1.9: Schematic of the angular differential imaging (ADI) technique. For clarity, starlight is shown in blue and planets are shown in orange in this diagram, with negative images of the planets in brown. Raw images taken at different telescope angles show the stellar PSF and speckle noise in the same orientation, and on-sky objects rotated (a). These images are median combined (b), and in this way the stellar speckle noise is accurately modelled and the planetary signal is diluted. This median is then subtracted from each individual frame (c), and the majority of the stellar noise is removed. Some planet signal is also self-subtracted, and shadows of the planet appear at rotations where a dilute planet signal was captured in the median image, i.e. at the positions that planets are present in the other raw image. Images are then aligned to the same physical orientation, so that the planets are aligned between frames and the stellar speckles are misaligned (d). These images are finally co-added (e), boosting the planetary signal and diluting the stellar signal further since it is now misaligned between planes. The shadows of the planets are still present, but are fainter since their signal is not aligned between images. If this process is carried out for a smoothly rotating sequence of images, then instead of individual planet shadows a smooth arc of negative flux forms between the initial and final positions of the planet (f).

1.5.3.3 Spectral Differential Imaging

If observations are taken at more than one wavelength simultaneously, it is additionally possible to separate speckles and astrophysical signals via the chromatic dependence of

speckle noise. The speckle pattern occurs due to the diffraction of light on the mirror, and any defects or imperfections on its surface. The spatial scale of this diffraction pattern scales as $\theta = 1.22\frac{\lambda}{D}$, with λ the observing wavelength and D the diameter of the telescope. The PSF for an observation at a longer wavelength therefore has a larger characteristic scale. The image of an astrophysical source, meanwhile, appears at the same spatial position independent of wavelength. This spectral diversity can be used to separate speckles and astrophysical signals in the same way that angular diversity is used in ADI, and the process is shown in Figure 1.10.

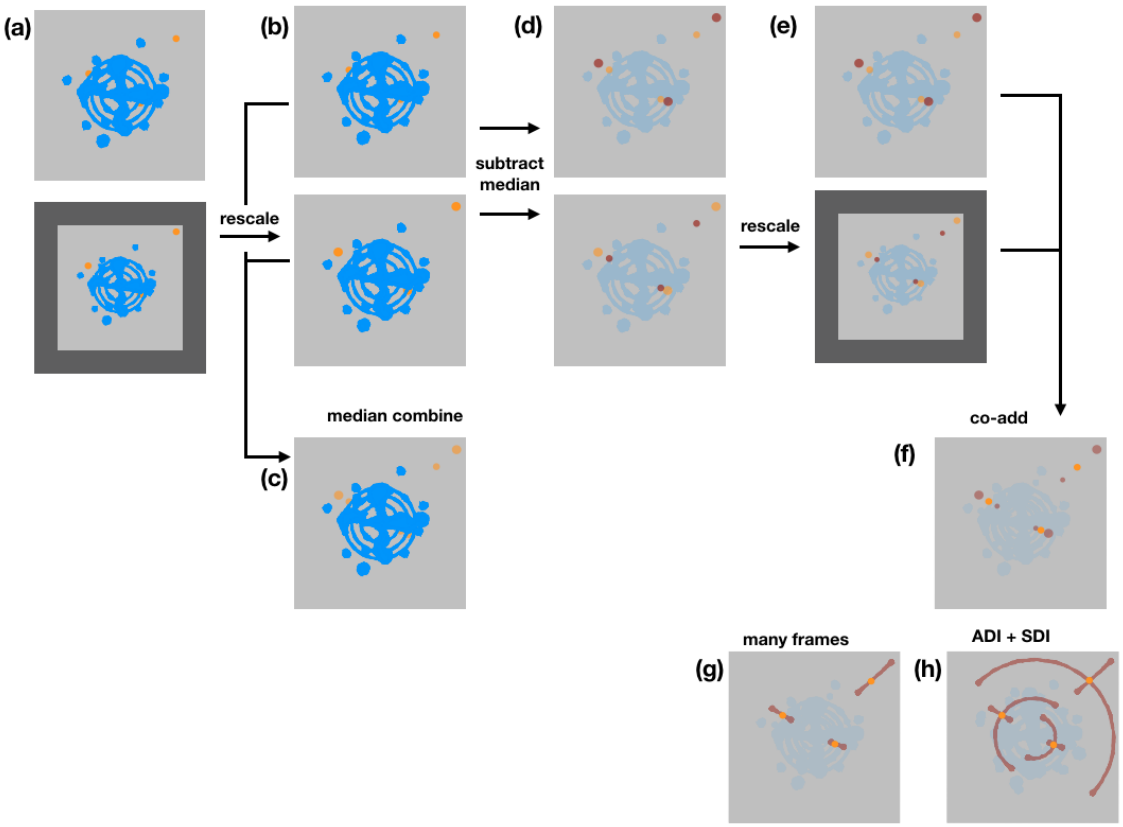

Figure 1.10: Schematic of the spectral differential imaging (SDI) technique. Starlight and planet light are shown in blue and orange respectively, as for Figure 1.9, and the same example system is used in this demonstration. For two images taken at different wavelengths, the stellar PSF and the characteristic scale of speckles is different, while the position of any on-sky objects is consistent regardless of wavelength (a). These images can be rescaled, so that the stellar PSF and speckle noise matches between frames, and planets are displaced (b). The frames are then median combined (c) so as to capture the stellar speckle noise, and dilute the planetary signal. This median is subtracted from each frame, removing the majority of the stellar noise (d). As is the case for ADI, the planet signal is also diluted, and self-subtraction shadows appear. In SDI these shadows are radially displaced from the planet signal. The images are then rescaled back to their original scale, so that the planet signal is once again aligned and the stellar noise is misaligned (e) and the frames finally co-added (f). In this co-add, self-subtraction shadows of the planet appear radially inner and outer to the planetary signal. If this process is carried out on IFS data with many simultaneous wavelength images, the self-subtraction forms a smooth radial trace. SDI is usually carried out in conjunction with ADI (h), and in this case both the angular and radial self-subtraction traces are formed, appearing as a cross centred on the planet signal.

Spectral Differential Imaging is the most effective when images with narrow $\Delta\lambda$ and similar λ are used, so as to avoid any chromatic effects in the PSF. The technique is traditionally used with an integral field spectrograph (IFS), where images across a range of wavelengths are collected simultaneously and as such the PSF is well modelled: a larger number of images allows the stellar PSF to be captured more accurately and reduces the extent to which self-subtraction occurs. A unique mode of SPHERE/IRDIS collects data through two narrow-band imaging filters simultaneously, meaning that SDI can also be used for these images, although the contrast improvement is not as dramatic as for an IFS imaging at many wavelengths simultaneously.

SDI is normally carried out in conjunction with ADI. In this case, the spectral and angular diversity of the images can in fact be exploited simultaneously: first, the images are scaled such that speckles have the same characteristic scale. There then exists a library of images with similar stellar noise and planet position varying both radially due to the image rescaling and rotationally due to the telescope movement. This stellar noise can be modelled and removed from each frame. The frames are then rescaled, de-rotated and co-added to give a single, broadband reduced image of the target, which shows traces of both angular and radial self-subtraction, as shown in Figure 1.10 panel (h).

1.5.3.4 Polarimetric Differential Imaging

Starlight is unpolarized, while the light from planets, protoplanetary disks and debris disks is polarized to various degrees and this can be used to differentiate companions and disks from the stellar halo. The polarimetric differential imaging process is shown in Figure 1.11. In this schematic an artificial companion is present to the right of the star, and is 80% polarized. Light is split into orthogonal polarisation states, and the unpolarized stellar light is very similar between each frame, while the polarized companion signal is far stronger in the vertical than the horizontal polarization state in this case. Subtracting these images gives a difference image, where the majority of the speckle halo is removed and the companion signal preserved. In this schematic the process is additionally repeated at a second polarisation state (LCVR Configuration 2): this configuration allows a negative difference image to be created, and combining the two images removes non-common path

aberrations.

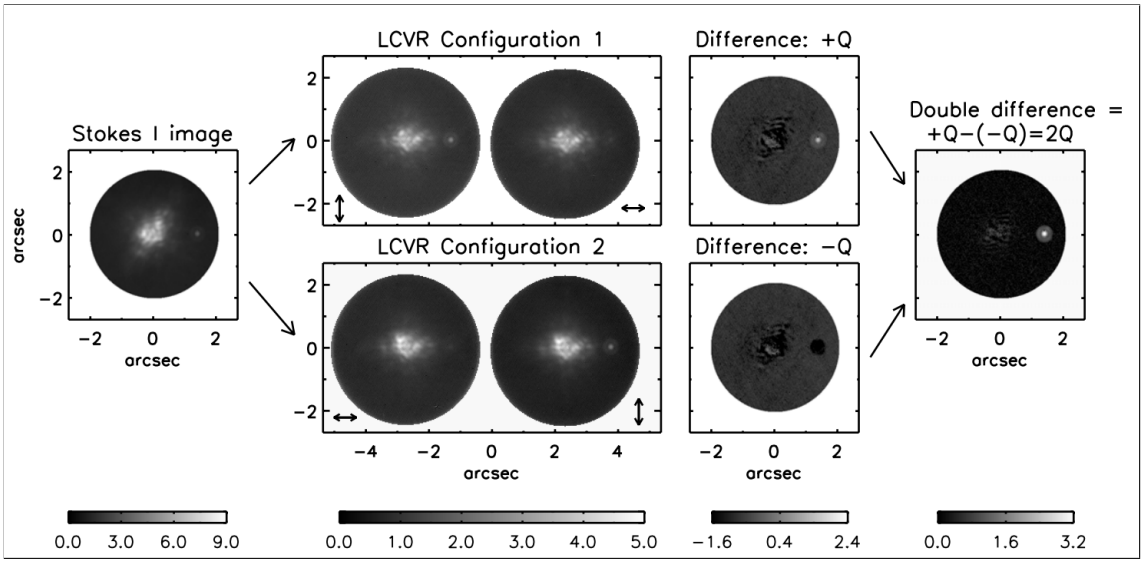

Figure 1.11: Schematic of differential imaging using polarimetry. A faint, 80% polarized artificial companion is inserted to the right of the star, and a total intensity (I) image is shown on the left. Light is split into orthogonal components which can be subtracted from each other: this removes the majority of the unpolarized speckle halo common to the two polarization channels, and produces a Stokes +Q difference image (top row of the figure). The process is repeated with polarization modulated by 90°, creating a negative (-Q) image as shown in the bottom row, with any astrophysical signal appearing as negative counts in this image. Combining these two images removes aberrations unique to each path. The process can be repeated with different polarization modulations applied so as to obtain the Stokes U and V polarization vectors. Figure from Hinkley et al. (2009).

As well as allowing stellar light to be removed, observing companions and disks in polarized light gives a unique insight into their physical properties. Light emitted deep within a planet is scattered from clouds and hazes high in the planetary atmosphere (Sengupta & Marley 2009; Sengupta & Marley 2010), and observing the degree of polarization allows the extent of cloud cover, and even the oblateness of the planet, to be probed (de Kok et al. 2011; Marley & Sengupta 2011). In the case of disks, observations in polarized light can allow the front and back edge of the disk to be differentiated, and can even give an insight into the optical thickness and grain properties of the dust (e.g. Graham et al. 2007; Perrin et al. 2015).

1.5.3.5 Algorithmic approaches

The above sections all describe various methods by which images can be collected in which speckle noise is diverse from the planetary or debris disk signal in a dataset. Once such a library of images characterising the PSF has been build, this speckle noise must be sub-

tracted from the science images in such a way that the maximum possible speckle noise in each science image is subtracted, but the companion signal is preserved.

The simplest method to achieve this is a straight-forward PSF subtraction, as referred to above: a single reference image is subtracted from the science image, or a set of reference images are median combined and subtracted from one or more science images. This is sometimes referred to as classical ADI, and this method gives a contrast improvement of a factor ~5-10 over unprocessed science images (Debes et al. 2016).

For improved speckle subtraction, it is possible to use a tailored set of science images that best captures the speckle variance in each individual science image as the reference. Such a tailored reference image can be created either by minimising the residuals between the science image and a combination of images from the PSF library, or by minimising the residuals between the science images and a combination of eigenimages from the PSF library: these approaches are known as the Locally Optimised Combination of Images (LOCI) and Principal Component Analysis (PCA) respectively, and a variety of codes exist for both approaches (see e.g. Lafrenière et al. 2007; Marois et al. 2010a; Soummer et al. 2012; Amara & Quanz 2012; Amara et al. 2015)). For these methods the detection limits are typically a factor of 10-20 improved over a classical ADI approach Debes et al. (2016), depending on the noise statistics of the specific images used.

Some additional gain might be achieved by careful selection of which frames are used as reference images: it might, for example, be beneficial to remove the nearest neighbours in an ADI or SDI sequence, so as avoid self-subtraction. The image plane can also be split into smaller regions and to match the speckles in each region seperately: this is often performed in concentric annuli, and in general improves the sensitivity to planets but removes disk signal. An alternative approach is that of the ALICE project (Soummer et al. 2014; Choquet et al. 2016; Choquet et al. 2017; Choquet et al. 2018), which uses a reference library approach whereby the best-matched PSF images from the entire observing history of HST are selected and subtracted from each individual science target.

Novel post-processing algorithms are currently being developed: in the LLSG technique (Gomez Gonzalez et al. 2016) the signal in each image is decomposed into three

components (low-rank, sparse and gaussian-noise), such that the planetary signal is captured in the spare term, while the ANDROMEDA algorithm (Cantalloube et al. 2015) uses a statistical approach to understand the typical signature of a planet versus a speckle in post-processed ADI data.

Several of these algorithms will cause at least some of the planetary or disk flux to be removed, as well as the stellar speckle noise. Such self-subtraction and over-subtraction of signal in the process images can alter both the apparent morphology of disks and the photometry of disks and planets in the final processed image, causing incorrect conclusions to be drawn. To account for this, forward modelling approaches are generally used so as to accurately capture the effect of the post-processing on the companion or disk signal that is being observed. This can be done either by negative model injection (Lagrange et al. 2010), where the many models are injected into the raw data which is reprocessed and the residuals minimised, or using an analytical approach to understand the effect of post-processing on the data (see e.g. Milli et al. 2012; Pueyo 2016). Finally, it is important to account for the fact that at very small radii there are only a few resolution elements present, and if pixel variance is used to model noise this can give biased results as described in Mawet et al. (2014), who provide a contrast correction term to account for this statistical bias.

1.6 Aims of my research in this context

In this thesis, we present data from 57.5 hours of VLT/SPHERE observations collected by our team, where we studied 45 targets to carry out two surveys. I have led the data reduction and analysis for both of these surveys.

Firstly, we surveyed 24 targets with debris disks that show evidence of being carved into two debris belts. The infrared excess of these targets shows two distinct temperatures, believed to correspond to two belts of dust at different radii (Kennedy & Wyatt 2014b), with a deep gap in between these rings of dust. For these targets, the gap between the debris belts indicates the expected position of a giant planet in the system. Even further, it is

possible to place constraints on the mass and number of planets in the inferred planetary systems, based on the measured properties of the debris dust. Shannon et al. (2016) found a relationship between the mass of planets and the time they take to clear a debris disk, and this can be inverted to find the minimum mass that is expected for planets in a particular system, so as to have carved the observed gap in the debris. Our aim in this survey was both to image low mass companions and debris disks orbiting these targets, and to place tight constraints on the mass/radius parameter space that the companions orbiting these targets should occupy. This work is similar to that of Meshkat et al. (2015), but with a significantly larger sample size and with improved detection limits. The survey is the first to present high contrast imaging limits against the dynamical limits of Shannon et al. (2016), and establish how the tightly parameter space can be constrained with current instruments. We established that very young targets are the best in terms of placing these tight constraints on parameter space, since the dynamical limits are much higher, even though these young targets are generally more distant (Sco-Cen is ~140pc from Earth) and so resolution and absolute sensitivity are sacrificed. This survey is presented in detail in Chapter 3.

Secondly, we surveyed 20 of the dustiest debris disk systems, as identified with WISE. The role of dust has been discussed extensively in Section 1.4 above, but at the time that this survey was started there was no conclusive evidence that planets are more common in highly dusty systems (see e.g Wahhaj et al. 2013; Rameau et al. 2013). Meshkat et al. (2017) has subsequently demonstrated a statistically significant excess of planets orbiting dusty targets. By observing newly identified debris disk targets, many of which had never been observed with high contrast imagers, with VLT/SPHERE we aimed to (a) detect low mass companions and debris disks in scattered light and (b) improve future statistical calculations of planetary occurrence rates in systems with and without debris dust. This survey is presented in detail in Chapter 4.

1.7 Contributions of my work to the field

My work on this topic is an important step in understanding directly imaged planets, debris dust, and their relationship to each other.

Firstly, these targets will contribute to future statistical calculations of occurrence rates in highly dusty systems and in systems with sculpted dust. Huge target lists are required to place tight constraints on the small frequencies of directly imaged planets, and the targets presented here contribute to that work. Although we do not carry out a detailed statistical analysis of occurrence rates at this point, my survey will contribute to future analyses of the frequencies of planets in dusty systems, and in those with sculpted dust.

Our first survey, of two-belt systems, is larger than previous similar surveys (e.g. that of Meshkat et al. 2015), and is the first time that high contrast limits are directly compared to the dynamical arguments of Shannon et al. (2016) for real data. In some cases we can place very tight limits on the inferred planetary systems, and my work demonstrated that selecting very young targets ($\lesssim 50$ Myr) is vital for such studies, so as to place the tightest constraints on parameter space. In some of these cases, where the dynamical mass limit is relatively high, we expect that JWST will be sensitive to planets at this mass limit. In these cases, therefore, future JWST observations will either find the planets inferred in Shannon et al. (2016) and other works, or indeed will fail to find them and so demonstrate that either planetary mass objects clear debris mass more efficiently than predicted, or that these disks are not in fact caused by planets, as is usually assumed, but by some other mechanism.

Our second survey, where we study stars hosting the highest volumes of circumstellar dust, will not only improve the community's understanding of planet frequencies in general, but might eventually also allow for planet frequencies to be calculated as a function of target infrared excess, i.e. as a function of the extent of dustiness in the system. As described above, we would expect the presence of giant planets to perturb planetesimal orbits and thus elevate the rate of dust production, and so one might expect a higher planet frequency in highly dusty systems than in moderately dusty systems. Although

our relatively small survey will not itself answer this question, the target list will be useful to future statistical works on this topic, and eventually it will be possible to calculate frequencies in a sample stratified by dustiness.

Over the course of these two surveys we have also identified several new targets of particular interest. Firstly, we imaged three debris disks in scattered light. One of these (HD 129590) is published as Matthews et al. (2017), and a second (HIP 63439) will likely lead to another paper in the next year, once more data have been collected (see Section 6.2 for more details). Only a handful of debris disks have been detected from the ground, and GPI and SPHERE combined with the most up-to-date speckles subtraction techniques are for the first time allowing the study of a larger number of debris disks in scattered light at infrared wavelengths, which in turn allows detailed study of their morphology. We also identified 3 new stellar-mass companions in our survey of highly dusty systems, and work on these companions is ongoing.

In the course of my surveys, it became clear that the improved sensitivity of these objects also means there are hugely more background objects detectable in any observation. For example, HD 182919 was observed with Keck as part of Hinkley et al. (in prep) and 8 background objects were detected. When observing the target with SPHERE for Matthews et al. (2017), however, we detected 40 background objects. This increased number of background objects can be beneficial: as discussed in Chapter 3 and presented in my paper, we can for the first time start to use comparative astrometry between candidates to verify and improve the calibration of the stellar proper motion and position behind the coronagraphic mask. There is also a drawback to the large number of objects: there are physically more candidates to vet and rule out as genuine companions for each target. Additionally, as instruments improve even further and even more background objects are detected, these objects will increasingly contaminate observations of bona fide companions and debris disks. Future instruments and surveys will have to take this into account, perhaps by observing at very red wavelengths where background stars are fainter, or by excluding targets near the galactic centre. This will be important in the design and execution of future surveys.

1.8 Statement of contributions to co-authored papers

During my PhD, I have first authored one accepted and one submitted paper, and co-authored two additional papers. My contributions to these papers are as follows:

- For the paper "Early Results from VLT SPHERE: Long-slit Spectroscopy of 2MASS 0122-2439 B, a Young Companion Near the Deuterium Burning Limit" (Hinkley et al., 2015a), I used an extracted spectrum to calculate a bolometric luminosity of the companion 2MASS 0122-2439 B, and compare this to previous literature values. We found good agreement with the luminosity values found in Bowler et al. (2013). That work is not included in this thesis.

- For the paper "The unseen planets of double belt debris disc systems" (Shannon et al. 2016), a relationship was found between the mass of planets in a debris gap and the debris clearing time. This gives a theoretical minimum mass of planet present in an observed debris gap, such that the observed gap can be cleared within the lifetime of the system. For this paper I used our SPHERE data to simulate observational upper limits for HD 38206, an example target with a wide debris gap, and compare these to the theoretical lower limits presented in the paper. I created Figure 5 and wrote the text for section 3.2 of the paper. My work on that paper is not directly included in this thesis, but the results are applied to our two-belt disk survey, presented in Chapter 3

- I led the paper "The First Scattered-light Image of the Debris Disk around the Sco-Cen Target HD-129590" (Matthews et al. 2017), where we presented the first resolved images of the HD 129590 debris disk. For this paper, I processed the raw SPHERE data, identified the disk, used the images to deduce spatial constraints on the disk, coupled our PCA pipeline with the GRaTeR debris disk code and `emcee.py` so as to use MCMC injection modelling and find a debris structure, and drew broader conclusions about this target in the context of imaged debris disks in the Sco-Cen association. I wrote the entire text of this paper, which is included as Chapter 5 in this thesis.

- I lead the submitted paper "Constraining the presence of giant planets in two-belt debris disk systems with VLT/SPHERE direct imaging and dynamical arguments", where we presented a VLT/SPHERE survey of 24 objects with evidence of multi-belt debris dust, to search for planets and place meaningful constraints (both upper and lower mass limits) on the possible planetary mass companions that could be responsible for sculpting the dust into multiple rings. For this paper I jointly selected the targets with Sasha Hinkley, performed all of the data reduction including developing my own SPHERE/IRDIS pipeline and calculating contrast curves for each observation, performed astrometry for a number of the candidate companions and made the final determination for each candidate as either a companion, a background or an unknown, found literature ages for all of the targets, and designed the final parameter space plots and interpreted our results. I wrote the entire text of this paper, which is included as Chapter 3 in this thesis.

1.9 Chapter Overview

In this thesis, I first present our observational and data reduction methods in Chapter 2. Chapters 3 and 4 detail the two surveys that we have run: the first of targets hosting two-belt debris disks and the second of targets with the dustiest targets identified with WISE. In Chapter 5, I present the first scattered light images of HD 129590, a debris disk in our two-belt survey, and our modelling of this system, and in Chapter 6 I present the other objects of interest identified in our two surveys: two further debris disks, three low mass companions, and a fascinating hierarchical quadruple star system. Finally, I conclude in Chapter 7.

Chapter 2

VLT/SPHERE Observations and Data Reduction

2.1 SPHERE as a high contrast imager

SPHERE (Spectro-Polarimetic High-contrast Exoplanet REsearch) is the latest ESO direct-imaging instrument (Beuzit et al. 2008). The instrument had its first light on 2014 May 04 and became available to the community from December 2014. SPHERE is mounted at the VLT, and therefore makes use of an 8.2m mirror, and benefits from an extreme AO system. The instrument consists of three sub-systems: IRDIS, a dual-band imager with a variety of filters in the YJHK bands (970 – 2340nm), an Integral Field Spectrometer (IFS), which collects simultaneous images at 39 wavelengths across YJ (0.95 – 1.35 μm) or YJH (0.95−1.65 μm), and ZIMPOL, a visible wavelength polarimeter. The IRDIS mode can also be used in Long-Slit Spectroscopy (LSS) configuration, where a slit is placed across the star and the companion, and light from the split is then spread by wavelength. Long-Slit Spectroscopy can be carried out at low resolution (R~50), over a wide range of wavelengths (0.95 to 2.32 μm), or at medium resolution (R~350) between 0.95-1.65 μm.

A unique advantage of SPHERE is that the IRDIS and IFS modes can be used simultaneously in the "IRDIFS" mode via the use of a dichroic filter. This filter passes different

wavelengths of light to the IFS and the IRDIS subsystems, meaning that the throughput of each subsystem is unaffected. This mode is ideal for survey observations: such observations benefit from the wide field of view (11″×12.5″) and relatively simple data processing of the IRDIS instrument, and the superior speckle suppression of the IFS. In addition, if a companion is detected within the IFS field of view (1.73″ × 1.73″), we have immediate access to data across a wider wavelength range and as such better SED coverage, and can carry out spectroscopy within the IFS wavelength range.

2.2 Observational Strategy

For this thesis, SPHERE survey data are consistently collected in this IRDIFS mode. We used IRDIS in dual-band imaging mode (DBI; Vigan et al. 2010) with the H23 filter pair ($\lambda = 1588.8$ nm, $\Delta\lambda = 53.1$ nm and $\lambda = 1667.1$ nm, $\Delta\lambda = 55.6$ nm), and the IFS was used in the YJ mode, which spans the range $0.95 - 1.35\ \mu$m and has 39 wavelength channels (Zurlo et al. 2014; Mesa et al. 2015a).

Initial observations for each target were structured following the recommended standard procedure. The first observation of each target consisted of a 1hr observing block (OB), the maximum normal period available for Service Mode observations at the VLT. Service mode is used since this allows data to be collected in the best possible weather conditions and additionally allows each target to be observed close to the zenith, where field rotation is maximised. In these OBs, IRDIS and IFS data were collected simultaneously. Observations were carried out in pupil-stabilized mode to allow angular differential imaging analysis, and the blocks were broken down as follows, with each frame being collected by both sub-systems:

1. **Target acquisition**, for which we are typically charged ~12 minutes of time. This accounts for the time spent slewing to the target and for the AO system to lock on.

2. **A "waffle" center calibration frame (C):** for this frame, sinusoidal pattern is applied to the deformable mirror. This creates four starspot images, with equal displacements from the central star, in each corner of the frame. Together these allow the

star position to be accurately measured to ~0.1 pixels (1.2mas, Vigan et al. 2016) behind the occulting mask. The waffle frame is always taken immediately before the science sequence, to ensure the calibration is accurate, and with the same exposure time as the science frames. An example waffle frame for the SPHERE/IRDIS data is shown in Figure 2.1.

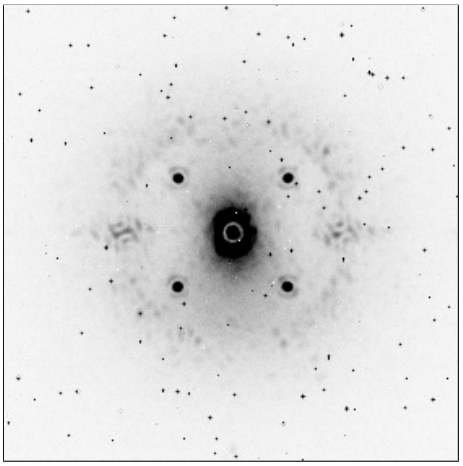

Figure 2.1: The "waffle" frame, where four images of the host star are created in each corner. These can be used to accurately locate the star behind the coronagraphic mask. This image shows the raw data in inverted color.

3. **Several "science" frames (S):** these have exposure times between 2s and 64s, depending on the target brightness (for bright targets, shorter exposure times are required to ensure that the central region does not become saturated) and the target zenith angle (a target higher in the sky causes the telescope to rotate more quickly, and we wish to avoid "smearing", an effect where the PSF is elongated due to the rotation of the telescope. Exposures are set to avoid objects moving by more than λ/D in a single image). Science frames for these 1 hour OBs typically covered a field rotation of ~20-30°. Example raw science frames are shown in Figure 2.2 and 2.3 for the IRDIS and IFS subsystems respectively.

4. **A second "waffle" frame**, immediately after the science frames, is usually collected. This can be used to test the stability of the telescope over the OB.

5. **A flux calibration frame (F)**: for this frame a tilt is applied to the deformable mirror, so that the stellar PSF is displaced from the coronagraph by 707mas in the image. This frame allows for the PSF shape to be measured, and for contrast limits and pho-

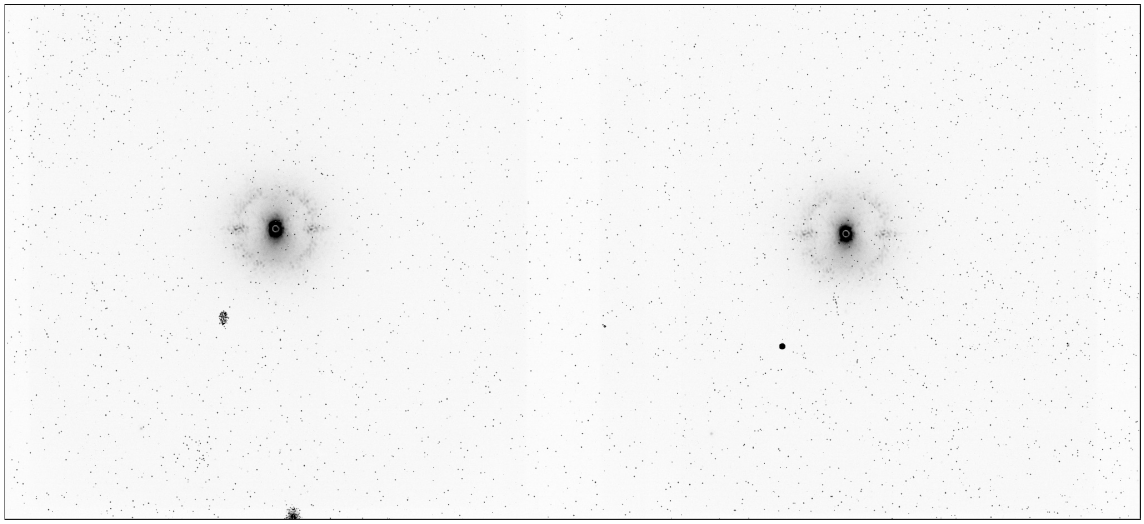

Figure 2.2: Raw SPHERE/IRDIS data, shown in inverted color. Two images with two different filters can be clearly seen, and occulted target star appears in the centre of each image. A ring of starlight at the edge of the AO control radius is also apparent. Additionally, the background is littered with badpixels and in particular a chip deformation can be seen to the lower left of the star in both images.

tometry of point sources to be calibrated. The frame is taken with one of the three neutral density filters in place. The exposure time is tailored for each target based on its apparent magnitude and the choice of neutral density filter. In some of our early observations, these flux calibration frames were taken immediately before the C and S frames, but we found that Exposure Time Calculator[1] sometimes overestimated the exposure times, and so the flux calibrations would be saturated. These flux calibrations can be retaken, but some detector persistence would nonetheless be visible in the first few science frames. Although the latest version of the exposure time calculator is more accurate, taking this frame at the end of the sequence nonetheless avoids the risk of detector persistence affecting the science frames. Once the flux frames have been taken, there is sufficient time during slew and acquisition of a new target that any detector persistence fades before the next science observation.

We choose not to take sky background frames, since the sky emission is not the dominant form of noise in the YJH bands where our data are collected. Since there is no significant improvement in using immediate sky backgrounds over of daytime calibrations, the additional time these frames require is better spent improving the integration time on the target itself.

1. https://www.eso.org/observing/etc/

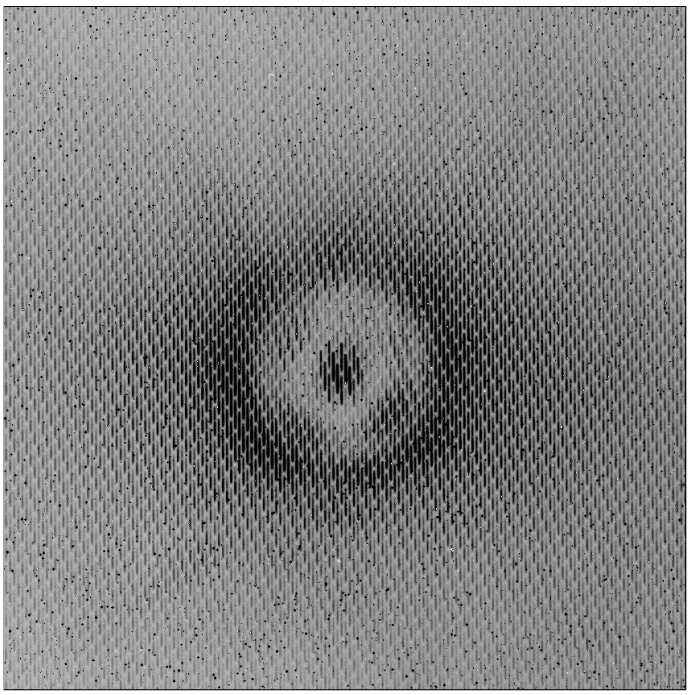

Figure 2.3: Raw SPHERE/IFS data, shown in inverted color. The individual spectra corresponding to each pixel are visible as short, almost vertical lines. Only the central region of the frame is shown: in the very centre of the image the target can be seen through the coronagraph, and a dark ring of spectra shows the position where starlight spills around the edge of the coronagraph. Each individual spectrum in this data must be extracted and separated into 39 distinct wavelengths, to build a datacube as shown in Figure 2.4.

Follow-up observations were taken for the subset of our stars for which we identified candidates that had not previously been reported in the literature. These follow-up observations are tailored to the specific candidates that are being redetected: integration times are chosen as the minimum time for the specific candidates in the field of view to be redetected. In this way we ensure the most efficient use of telescope time. Details of all the observations (both initial and follow up) used in this work, including individual choices of exposure and integration times, are given in Table 3.3 and Table 4.2.

In addition to these frames, a series of day-time calibrations and more infrequent calibrations are collected each of the IRDIS and IFS subsystems. For IRDIS, the calibrations we use are as follows:

- **Dark frames** with exposure times matched to the exposure times used on-sky for the science and flux frames.

- **Flat frames** with a variety of exposure times so that detector response can be modelled

- Periodically, **astrometric calibration frames** are collected and processed by the SPHERE instrument team. For these frames the a variety of calibrators (globular clusters and long-period binaries) are imaged so as to calibrate the true north and plate scale of the instrument. Values are provided by the SPHERE instrument team (see Maire et al. 2016 and the ESO SPHERE User Manual[2]) and we use these values rather than independently reducing the data.

For the IFS, the following day-time calibrations are used:

- **Dark frames** with exposure times matched to the exposure times used on-sky for the science and flux frames.
- **Flat frames:** are collected under white light illumination, and at several specific laser wavelengths, to calibrate the detector response.
- **A spectral position frame** is used to determine where on the chip the individual spectra fall.
- **A wave calibration frame** allows the wavelength at each pixel to be calibrated.
- As for the IRDIS data, periodic **astrometric calibration frames** are collected and processed by the SPHERE instrument team, and we use the values provided in the ESO SPHERE User Manual.

2.3 Initial data reductions

2.3.1 IRDIS sub-system

Initial reduction of the IRDIS data is carried out using the ESO data reduction and handling pipeline (DRH, Pavlov et al. 2008). The raw dark and flat frames are first used to create a 'master' dark and flat frame, and a map of badpixel positions. A point finding routine is then applied to the waffle (C) frame, so as identify the four star spots. By interpolating the positions of these four spots, the star center is found and subsequent frames

2. 6th & 7th release, see https://www.eso.org/sci/facilities/paranal/ instruments/sphere/doc.html

are transposed so that the star is positioned in the exact centre of the image. At this stage, I manually check that the correct starspots have been identified, and the star is centered to the correct position. Then, each science and flux frame is independently reduced by applying the master dark and flat frames and realigning based on the measured star center position and the dither of each individual image. The images are additionally split into two halves, so as to separate the part of the chip behind each wavelength filter. The cubes are then stacked using a custom code and normalised based on exposure time, so as to create a single datacube to which Principal Component Analysis (PCA) can be applied.

2.3.2 IFS sub-system

The initial cleaning and alignment of the IFS data frames is carried out with the code presented in Vigan et al. (2015). This code first creates basic calibrations (dark fields, master flat-fields, IFS spectra positions, initial wavelength calibrations and an IFU flat) using the DRH. A custom routine is then used to calculate an accurate parallactic angle and time for each image, and to normalise the data based on its exposure time. Bad pixel and cross-talk corrections were applied as detailed in Vigan et al. (2015). The DRH is then used to interpolate these frames both spectrally and spatially. A sigma-clipping routine is applied to remove remaining bad pixels which deviated from their neighbours by more than 3.3σ. Finally, the wavelengths for each image is recalibrated, due to small systematic errors in the DRH pipeline, as described in Vigan et al. (2015). The final product is a 4-dimensional datacube, with the four dimensions being x-y position, time and wavelength. An example of this cleaned data is given in Figure 2.4 .

2.4 Principal Component Analysis

In this work, we use Principal Component Analysis (PCA) to create the model PSF that is subtracted from each individual image (see e.g. Soummer et al. 2012; Amara & Quanz 2012). PCA is a technique that allows a tailored reference image to be created so as to model the speckle noise in each science image as accurately as possible. This is done

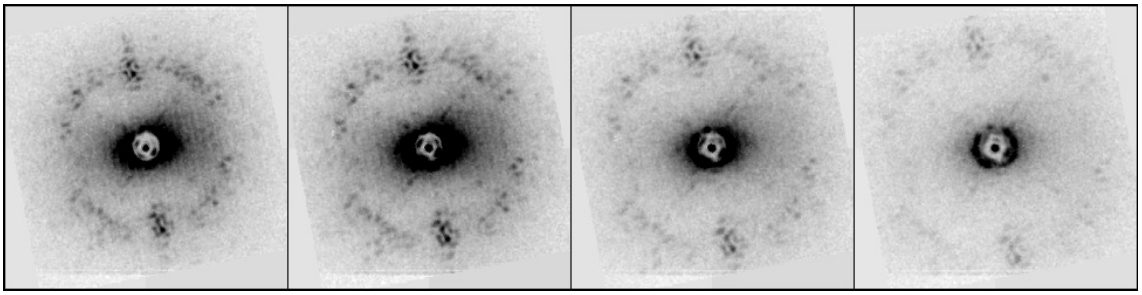

Figure 2.4: SPHERE/IFS data after the initial processing stages: the badpixels have been removed, and the individual spectra extracted to create images at 39 wavelengths. In the above frames we show four of these 39 wavelength slices (at λ = 0.97 μm, 1.08 μm, 1.20 μm, 1.31 μm), and in each case the data is shown in inverted color. In the very centre, the target is bright enough to be seen through the coronagraph, and a ring of starlight surrounds the edge of the coronagraph. The speckle pattern has a wider characteristic scale in the images at longer wavelengths, shown on the right hand side.

using a matrix decomposition: the entire set of reference images are transformed into a two-dimensional matrix holding vectorized versions of each individual image. This matrix therefore has dimensions M×N, where N is the number of pixels in each image and M is the number of images being used. This matrix is then decomposed onto a set of M orthogonal bases, giving a number of distinct PCA modes that together capture all of the structure within the data. Subtracting all of these modes from a science image would leave only random, gaussian noise. Instead, some small number of these modes are subtracted: the first few contain the majority of the highly structured stellar light which is similar between frames. As more modes are subtracted, the stellar light is more effectively subtracted but the planetary signal is also more strongly removed (see Figure 2.5).

Speckle subtraction for both IRDIS and IFS data is carried out in the same way, using a custom PCA code to perform both ADI and SDI simultaneously. Images are first scaled relative to their wavelength so that speckles have the same characteristic scale between images. The code then uses both the spatial and spectral similarity of the images to find principal components (or modes) that are subtracted, thus removing the stellar light. The images are then rescaled back to their physical wavelength, and rotated so that the sky rotation is aligned between frames. Finally, the images are combined across time and optionally also across wavelength. The collapsed “broadband" image offers the best sensitivity to companions, while the non-collapsed “ifs" image allows the flux of detected objects to be measured across a range of wavelengths.

During this PCA process, we optimise the balance between removing sufficient

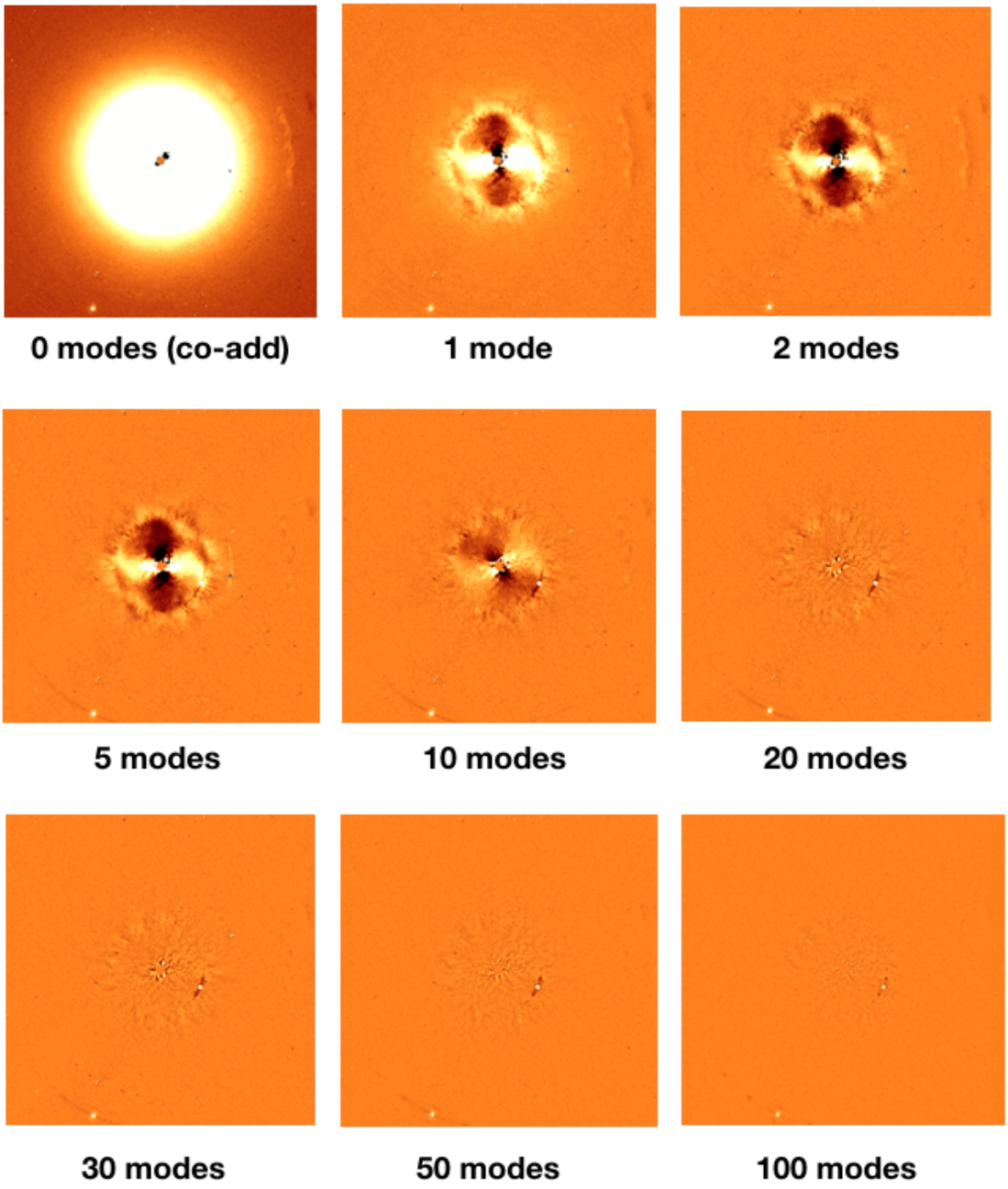

Figure 2.5: Example SPHERE/IRDIS data reductions, with between 0 and 100 PCA modes subtracted. All of the images are shown with the same colorbar. This dataset includes 96 timesteps at two wavelengths, i.e. a total of 192 distinct images. The "0 modes" image is a simple co-add of the data. As the first few principal components are removed, the stellar halo and dominant speckles are removed. Between 20 and 50 modes, little change is seen in the data, and once a large fraction of the modes are removed ($\gtrsim 1/3$ of the available modes), the planet flux starts to be strongly removed.

starlight without subtracting too much planetary flux. To do this, we calculate and store reductions with between 0 and $\sim 1/3$ of the available principal components removed. In the first few frames, significant stellar flux is removed, as can be seen in Figure 2.5, and once $\sim 1/3$ of the modes are removed the planetary flux is heavily subtracted. Figure 2.6

demonstrates this effect visually: the signal/noise of inserted fake planets is shown as a function of number of PCA modes removed, for planets at a variety of separations. In each case, the inserted planet is 10 magnitudes fainter than the host star. For the wide separation planets at 2° and 4°, there is very little scattered starlight and so the peak S/N is almost immediately removed. As such, removing more principal components removes planet signal but not stellar signal, reducing the S/N. For the closer planets at 0.5° and 1 °, the first few modes significantly increase the acheivable S/N. As the number of modes increases beyond this peak, the S/N is reduced as the planetary flux is strongly removed. There is never an increase in S/N after ~1/3 of available modes have been removed, and once all 192 modes have been removed the resultant S/N is zero. Instead of carrying out this text for each target, we simply use a set of reductions with between 0 and ~ 1/3 of the available modes removed. By using these reductions of different strengths, we can optimise the sensitivity in our final images: we examine images with a range of reduction strengths when searching for candidates, and use the entire range of reductions when calculating contrast limits, as described below.

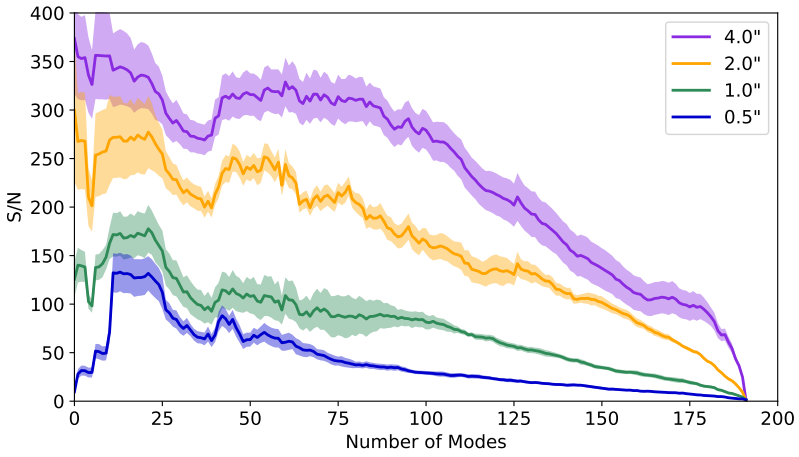

Figure 2.6: Signal to noise of fake planets versus number of PCA modes removed. Each inserted planet is 10 magnitudes fainter than the star, and the planets are injected at 0.5°, 1°, 2° and 4°. For the wide separation planets, the peak S/N is quickly reached, while the close planets show a noticeable improvement in S/N as the first few planets are removed. Beyond ~50 modes, all of the planets show a decline in S/N with increasing number of modes. Once all 192 modes have been removed, the S/N of each fake planet is 0.

2.5 Fake Planet Injection

For each target, we run a series of reductions with fake planets injected. These planets are injected in a spiral pattern, with individual fake planets separated by at least 100mas so as to avoid contamination, and with a total of 20 fake planets in each IFS frame and 60 fake planets in each IRDIS frame (see Figure 2.7 for an example). The fake planets themselves are scaled copies of the stellar PSF, and we use a range of fake planets that are between 8 and 15 magnitudes fainter than the star.

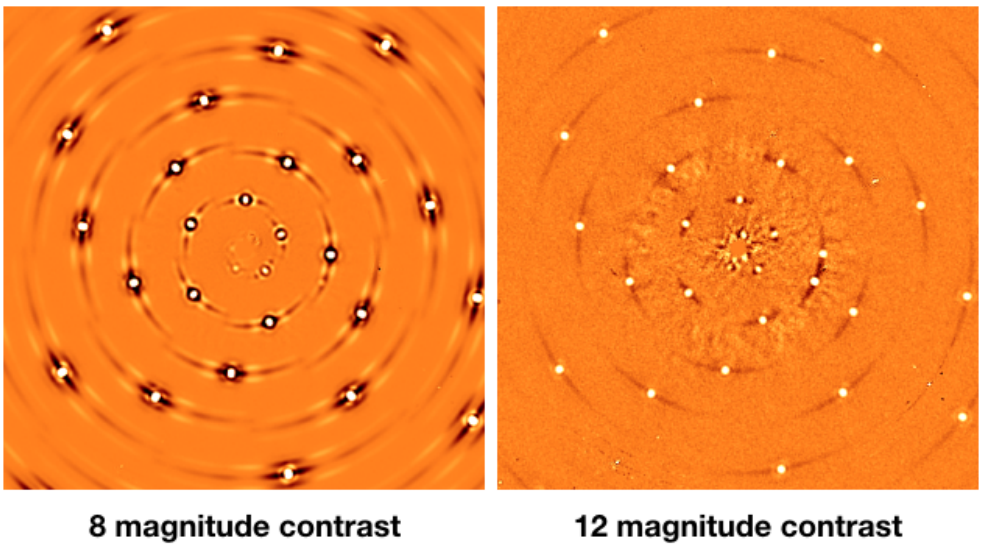

Figure 2.7: Example data reductions where fake planets have been injected, to calibrate the throughput of the PCA routine and calculate contrast curves. The two images show fake planets 8 and 12 magnitudes fainter than the star. These fake planets are injected in a spiral pattern, and the reduced throughput near to the star can clearly be seen in the images above.

These fake planets are used to calculate detection limits. For each fake planet, we measure the planet signal and also measure the noise as the statistical variance of pixels near the injected planet, in a frame with no injected planets. We then pick the best signal-to-noise for that planet across all of the reductions with varying numbers of PCA modes subtracted. These signal-to-noise values are averaged by angle, and then interpolated against magnitude to find a precise magnitude value at which a planet would be detected at 5σ. This contrast can then be plotted against radius for each target. We additionally apply the correction term presented in Mawet et al. (2014) so as to account for the small number of resolution elements at small separations from the star. In a small number of cases, a very bright candidate planet affects our contrast calculation: if the candidate is

within the region of pixels we use to measure the noise, then the measured noise value is artificially raised, and the signal-to-noise consequently reduced. In these cases, we mask out the bright candidate and the affected fake planet is not included in the contrast calculation.

In the IRDIS data, injected planets are also used to calibrate the throughput of the PCA routine. As can be seen in Figure 2.7, the planets close to the star appear significantly fainter than those further away, since the PCA routine removes some of the flux from these planets as it removes the starlight, and the self-subtraction is stronger. To account for this, the fractional throughput of each injected planet is measured, and a curve is fitted to throughput versus radius. For each candidate, the signal is measured and then scaled based on the throughput at the candidate radius, so as to accurately calculate the contrast of each candidate. We calculate contrasts in the H2 and H3 filters separately, and by converting these values to absolute magnitudes, the H2-H3 color can be used to differentiate planets and stars for sufficiently faint targets. In a small number of cases we are unable to retrieve contrasts in the two filters, either since the target is too faint to be identified in each individual filter or because the target is off-screen in one of the two filters, and in these cases color cannot be used to differentiate companions and background objects.

Chapter 3

Survey of Two-Belt Debris Disk Systems

This chapter is based on the paper "Constraining the presence of giant planets in two-belt debris disk systems with VLT/SPHERE direct imaging and dynamical arguments", which has been accepted for publication in MNRAS. Some of the text concerning HD 223352 from the paper, including one table, is included in Chapter 6 of this thesis.

3.1 Introduction

Directly imaged planets are rare. This has been demonstrated by numerous surveys over the last decade: NaCo (Chauvin et al. 2015), the Lyot project (Leconte et al. 2010), GDPS (Lafrenière et al. 2007), IDPS (Galicher et al. 2016), SEEDS (Brandt et al. 2014), NICI (Biller et al. 2013; Nielsen et al. 2013; Wahhaj et al. 2013) and others. In a meta-analysis of several deep imaging surveys, Bowler (2016) found an overall occurrence rate of $0.6^{+0.7}_{-0.5}$% for companions in the range 5-13M_J and 30-300 AU. Galicher et al. (2016), meanwhile, use a slightly wider parameter space of 0.5-14M_J and 20-300 AU, and find an occurrence rate of $1.05^{+2.80}_{-1.70}$%. Directly imaged planets are rare in the modest region of parameter space that can be probed, i.e. the most massive planets at the widest of separations.

The latest generation of direct imagers (notably SPHERE and GPI, see Beuzit et al. 2008; Macintosh et al. 2014, respectively) are sensitive to lower mass wide-separation planets than were previously inaccessible to direct imaging. These instruments are proving to have excellent high contrast abilities, and the GPIES and SPHERE/SHINE surveys are initially consistent with the low occurrence rates for wide-separation planets within the region where direct imaging is sensitive, i.e. massive planets in the Jupiter-mass regime, separated by tens of AU from their host stars. Only a few planets have been identified with these instruments so far: the GPIES team detected a planet around the β-Pictoris member 51 Eridani (Macintosh et al. 2015; De Rosa et al. 2015), while a planet around the Sco-Cen star HIP 65426 has been detected by the SPHERE/SHINE team (Chauvin et al. 2017). An exoplanet PDS 70b was very recently identified with SPHERE, in a gap within the transitional disk of this object (Keppler et al. 2018).

In contrast to this relatively small number of planet detections, great success has been had with both SPHERE and GPI in detecting and characterizing debris dust systems in scattered light (e.g. Currie et al. 2015b; Kasper et al. 2015; Draper et al. 2016; Wahhaj et al. 2016; Feldt et al. 2017; Bonnefoy et al. 2017; Matthews et al. 2017). These systems are of particular interest since the presence of dust in a system may correlate with the presence of planets. Dust is transient, being blown out of systems by stellar winds or falling onto the stellar surface via the Poynting-Robertson effect. Therefore, if dust is observed to be present it must be constantly regenerated via planetesimal collisions. Planetesimals are the building blocks of planets, and so their presence is a useful indicator that planets may also have been able to form in a certain system. Even further, the presence of one or more giant planets in a system may perturb the orbits of these planetesimals, further increasing the rate of dust production (Mustill & Wyatt 2009). Those systems that host massive, wide-orbit planets might therefore also show evidence for particularly high quantities of dust.

Many of the known directly imaged planets reside in highly dusty systems. For example, the massive debris disk around β-Pictoris was first imaged by Smith & Terrile (1984), and a massive planet was subsequently detected by Lagrange et al. (2009). It is worth noting however that this correlation does not itself imply an underlying link

between debris disks and planetary systems, since many directly imaged planets have been discovered in surveys deliberately targeting a biased selection of highly dusty disks. Nonetheless, Meshkat et al. (2017) found that there is a statistically significant excess (at the 88% confidence level) of planets around highly dusty stars, compared to the occurence rates in a control sample, for early type stars.

These dusty systems also allow the study of the dynamical interactions of dust and planets. A sharp disk edge or a gap between two belts of debris dust can be formed by the gravitational influence of a giant planet. This has been observed in the HR 8799 system (Marois et al. 2008; Marois et al. 2010b) which hosts four known planets, with radii between 14 AU and 68 AU, and two distinct debris belts at ~9 AU and beyond ~95 AU (Reidemeister et al. 2009; Su et al. 2009; Matthews et al. 2014). HD 95086 shows similar system architecture, with two distinct debris belts (Su et al. 2015) and one known planet (Rameau et al. 2013) lying between them. Su et al. (2015) present possible architectures for this system with up to four planets clearing the gap between these debris belts, the inner three being below current detection limits. Even our own solar system is in this configuration, with the Asteroid and Kuiper belts enclosing four large, wide-separation gas and ice giants.

Systems in this two-belt configuration can be detected by observations of an infrared excess: if this infrared excess is best modelled as two distinct temperatures, as is the case for both HR 8799 and HD 95086, we infer that there are two temperatures of dust and therefore probably rings of dust at two radii (see e.g. Kennedy & Wyatt 2014a). These two-belt systems are unique in that there is spatial information suggesting *where* in the system planets are likely to be found. By assuming that the debris gap is formed by the gravitational clearing of one or more giant planets, we conclude that the planets in these systems should lie between the inner and outer debris belt radii, as inferred from infrared SED fitting. Under the assumption that planets are equal mass and typically separated by ~20 mutual Hill radii, it is even possible to deduce the predicted location of each individual planet in a multi-planet system, based on the number of planets we expect. The mutual Hill radius is defined as

$$R_H = \frac{a_1 + a_2}{2} \times \left(\frac{m_1 + m_2}{3M_\star} \right)^{\frac{1}{3}} \tag{3.1}$$

for planets with masses m_1 and m_2, and semi-major axes a_1 and a_2. For transiting planets observed with *Kepler*, Fang & Margot (2013) found a typical planet-planet separation of $21.7\pm9.5R_H$. While there is no guarantee that massive, wide-separation planets will behave as close-in planets do, we note that a significantly closer spacing is likely unstable. The HR 8799 planets are separated by as little as 3-4 mutual Hill radii, but the system is only stable due to the special dynamical configuration of the planets with several mean motion resonances (Fabrycky & Murray-Clay 2010; Goździewski & Migaszewski 2014).

As well as using disk structure to predict the locations of planets, it is possible to use dynamical arguments to constrain exoplanet masses. By assuming several equal mass planets spread across a debris gap, Shannon et al. (2016) found that the clearing time scales with the planet mass and the width of the debris gap. For a system with widely spaced debris belts and giant planets, this timescale is of order millions of years, and as such is similar to the lifetime of the system. By imposing that the clearing time be less than the stellar age, it is possible to calculate the minimum mass of each planet in the system that would facilitate clearing of the observed debris gap. This constraint can be combined with upper mass limits based on direct imaging analysis, so as to place tight limits on the possible planetary configurations in these multi-belt systems.

In this work, we survey 24 systems with previously published evidence for debris disks segregated into two distinct belts. We search for evidence for the planets that might be responsible for sculpting these debris disks, and test how tightly the undetected planetary systems can be constrained. Section 3.2 describes our target selection, and our observations and data reduction are discussed in sections 3.3 and 3.4 respectively. The contrast limits and candidate companion identification are given in section 3.5, and we discuss our results in section 3.6.

3.2 Target Selection

For this survey the aim was to study systems hosting the best characterized multi-belt debris disks, as determined by fitting of the infrared excess emission. To do this, targets were

selected that are presented in Chen et al. (2014) as hosting two-temperature debris disks. However, fitting the infrared excess is inherently complex, and there are often disagreements in the literature about the nature of a certain target. Many of our targets appear in the literature in Morales et al. (2011), Ballering et al. (2013), Kennedy & Wyatt (2014a) and Morales et al. (2016), and so we search for any disagreement between these literature sources. In Table 3.1 we list the literature references for each target, and specify which works find each target as having either one or two temperatures. We flag all those targets where there is disagreement in the literature as less certain. We then visually inspect the SEDs of targets for which there is only one literature source, and additionally flag the targets HD 120326 and HD 143675 as less certain. In both of these cases, no infrared excess is detected beyond the wavelength of the *Spitzer* InfraRed Spectrograph (5.2-38 μm), and so it is hard to robustly infer a two-temperature disk. Figure 3.1 shows two example SEDs, one with a good fit and one with a more uncertain fit. Our final target list includes 14 targets that host two-temperature debris disks, and 10 targets that likely host two-temperature debris disks, where this debris structure is less certain. All of the targets we observe are presented as having two temperatures in Chen et al. (2014), and so for consistency we use the temperature fits of that work in our subsequent analysis, with further details given in Section 3.5.2.

The final target list consists of 24 stars with some evidence for the presence of two belts. As part of the selection criteria, we included only stars with high parallaxes and young ages, since these targets allow the detection of planets at the closest physical separations to their host star, and at the lowest masses. The nearest OB2 association, Scorpius-Centaurus (de Zeeuw et al. 1999, hereafter Sco-Cen) is a particularly promising region for these studies since it is close (~140pc) and young (~10-16Myr, Pecaut & Mamajek 2016). A significant fraction (58%) of our targets are selected from this region. All of our targets have indicators of youth, mostly based on their association memberships, as detailed in Section 3.5.4. Target properties are listed in Table 3.1.

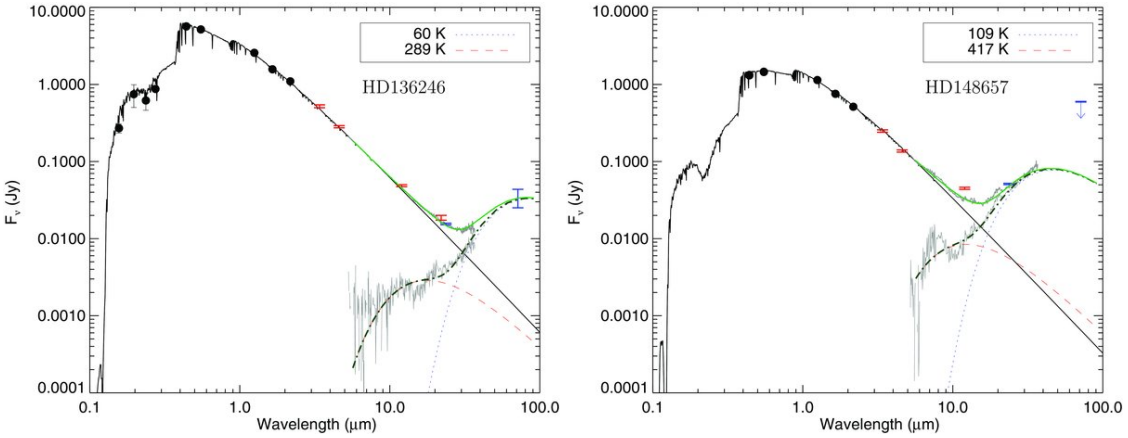

Figure 3.1: Example SEDs for the targets HD 136246 and HD 148657. HD 136246 is a clear two-belt target, and has been fit by several literature sources as such (see Table 3.2. The infrared excess with the stellar photosphere subtracted (black dot-dashed line) shows to clear peaks. HD 148657 shows more uncertainty: although the fit shows some evidence for two peaks, these are only marginally differentiated and a single belt fit provides a similarly good interpretation. Figures from (Chen et al. 2014).

3.3 Observations

Each of the targets was observed with the SPHERE planet-finding instrument on the VLT (Beuzit et al. 2008). Data were collected in the dual imaging IRDIFS mode, which splits the light into two subsystems: a differential imager and spectrograph (IRDIS; Dohlen et al. 2008), and an integral field spectrometer (IFS; Claudi et al. 2008). For this work we used IRDIS in dual-band imaging mode (DBI; Vigan et al. 2010) with the H23 filter pair ($\lambda = 1588.8$ nm, $\Delta\lambda = 53.1$ nm and $\lambda = 1667.1$ nm, $\Delta\lambda = 55.6$ nm), and the IFS was used in the YJ mode, which spans the range 0.95-1.35 μm and has 39 distinct wavelength channels (Zurlo et al. 2014; Mesa et al. 2015a). Plate scales are 12.255 mas/pix for IRDIS and 7.46 mas/pix for the IFS (Maire et al. 2016), and we use the `N_ALC_YJH_S` coronagraphic mask, which has an inner working angle of ~0.15″.

Each target was initially observed for a total integration time of ~2000s, split into individual exposures between 2s and 64s. The individual exposure times were tailored based on the brightness and zenith distance of the target stars. The observations were carried out in pupil-stabilized mode to allow angular differential imaging (ADI; Marois et al. 2006) to be performed. We also collected flux calibration frames, with the coronagraph removed, and star position calibration frames (waffle frames), where a sinusoidal pattern is applied to the deformable mirror to create four starspot images, one in each corner of

HD	HIP	Parallax[mas]	σ_{para}[mas]	Association	Age[Myr]	Refs
166	544	72.63[a]	0.52	TWA/LA/Her-Lyr[c]	8-150	6, 8, 10, 15
16743	12361	17.24[a]	0.24	Field	200	14
71722	41373	14.93[a]	0.31	Field	301^{+227}_{-100}	1, 2, 3, 11
79108	45167	10.07[b]	0.39	Field	212^{+133}_{-67}	1, 2, 3, 5
112810	63439	7.43[a]	0.26	LCC	17±1	4, 13
120326	67497	8.82[a]	0.98	UCL	16±1	4, 13
125541	70149	6.18[a]	0.24	UCL	16±1	4, 13
126062	70441	7.15[a]	0.27	UCL	16±1	4, 13
126135	70455	6.06[b]	0.60	UCL	16±1	4, 13
129590	72070	7.07[a]	0.33	UCL	16±1	4, 13
132238	73341	6.15[b]	0.51	UCL	16±1	4, 13
136246	75077	8.67[a]	0.41	UCL	16±1	4, 13
136482	75210	7.34[b]	0.51	UCL	16±1	4, 13
138965	76736	12.53[a]	0.40	Field	348^{+39}_{-54}	1, 3, 11
143675	78641	8.12[a]	0.42	UCL	16±1	4, 13
146606	79878	7.70[a]	0.54	USco	13±1	4, 13
148657	80897	6.04[b]	1.15	UCL	16±1	4, 13
151109	82154	4.96[a]	0.91	UCL	16±1	4, 13
153053	83187	19.30[b]	0.35	Field	539^{+276}_{-268}	1, 2, 3
182919	95560	13.72[b]	0.34	Field	198	2, 16
196544	101800	17.26[b]	0.35	Field	280^{+256}_{-98}	1, 3, 11
215766	112542	10.27[b]	0.46	Field	73^{+115}_{-33}	1, 2, 3
223352	117452	23.73[b]	0.22	AB Dor	150^{+50}_{-30}	9, 17
225200	345	8.01[b]	0.46	Blanco I	90±25	7, 12

Table 3.1: Target stars. Distances are from *Gaia* (Gaia Collaboration et al., 2016b; Gaia Collaboration et al., 2016a) where available, and Hipparcos (Perryman et al. 1997) otherwise. USco, UCL, LCC indicate the Upper Scorpius, Upper Centaurus-Lupus, and Lower Centaurus-Crux regions of Sco-Cen respectively, while LA is the local association. Age determination is discussed in Section 3.5.4.
Note. [a] *Gaia* distance, [b] Hipparcos distance, [c] There is conflicting literature for this target, discussed in Section 3.5.4.
References. (1) Brandt & Huang 2015; (2) Chen et al. 2014: (3) David & Hillenbrand 2015; (4) de Zeeuw et al. 1999; (5) Gerbaldi et al. 1999; (6) López-Santiago et al. 2006; (7) Lynga & Wramdemark 1984; (8) Maldonado et al. 2010; (9) Mamajek 2016; (10) Nakajima & Morino 2012; (11) Nielsen et al. 2013; (12) Panagi & O'dell 1997; (13) Pecaut et al. 2012; (14) Rhee et al. 2007; (15) Tetzlaff et al. 2011; (16) Zorec & Royer 2012a; (17) Zuckerman et al. 2011.

the image. These allow the stellar position to be accurately measured behind the occulting mask. Flux and center calibrations were collected for each target, immediately before or after the main science observations.

For a subset of our target stars, follow-up observations were collected. These allow differentiation between background stars and co-moving companions based on whether the candidate shows common proper motion with the host. Follow-up observations generally had shorter exposure times, tailored to the specific candidates we were aiming to re-detect. Details of all observations (both initial and follow-up) used in this work are

HD	One-Temp	Two-Temp	Uncertain?
HD 166		1, 2, 5	
HD 16743		2, 3	
HD 71722		1, 2, 3, 5	
HD 79108		1, 2, 3, 5	
HD 112810		1, 2	
HD 120326	1	2	yes
HD 125541		2	yes
HD 126062		2	
HD 126135	1, 5	2	yes
HD 129590	1	2	yes
HD 132238	5	2	yes
HD 136246		1, 2, 3, 5	
HD 136482		1, 2, 3, 5	
HD 138965		1, 2, 3, 5	
HD 143675	1	2	yes
HD 146606		2	
HD 148657		2	yes
HD 151109		2	
HD 153053		1, 2, 3, 5	
HD 182919	1, 4	2, 3	yes
HD 196544		1, 2, 5	
HD 215766	5	1, 2	yes
HD 223352	5	1, 2	yes
HD 225200		1, 2, 3, 4	

Table 3.2: Literature SED fits of each target as either one or two temperature disks. Since Morales et al. (2011) and Morales et al. (2016) use similar methodology we do not count these as independent, but use Morales et al. (2016) where available and Morales et al. (2011) otherwise. Note also that Kennedy & Wyatt (2014a) do not present any one-temperature SED fits. In the final column, we list the targets for which we consider the two-belt nature to be more uncertain.
References. (1) Ballering et al. 2013; (2) Chen et al. 2014; (3) Kennedy & Wyatt 2014a; (4) Morales et al. 2011; (5) Morales et al. 2016.

given in Table 3.3.

		IRDIS			IFS		
Target	UT Date	N_{images}	T_{sep}[s]	Rot[deg]	N_{images}	T_{sep}[s]	Rot[deg]
HD 166	2015 Jul 19	768	2	11.2	180	4	8.9
HD 16743	2016 Sep 19	64	32	17.8	63	32	17.8
HD 71722	2015 Apr 25	192	8	15.1	82	16	13.1
HD 79108	2015 Apr 09	240	8	19.2	94	16	18.5
HD 112810	2016 May 02	80	32	21.8	40	64	22.9
HD 120326	2016 Jun 04	80	32	21.6	40	64	22.6
HD 125541	2015 Apr 16	64	32	29.9	62	32	29.7
	2016 Jun 04	16	32	6.9	8	64	6.7
HD 126062	2016 Jul 23	80	32	23.9	40	64	25.2
HD 126135	2016 Apr 07	512	4	34.0	448	4	35.2
	2018 Mar 17	64	32	24.8	32	64	26.5
HD 129590	2016 May 04	80	32	35.1	40	64	36.9
HD 132238	2016 Apr 07	128	16	29.1	124	16	29.3
	2018 Mar 17	64	8	7.6	17	32	8.1
HD 136246	2015 Apr 14	192	8	88.3	228	8	97.8
	2016 Apr 03	256	4	25.7	228	4	26.8
HD 136482	2015 Apr 15	96	16	35.1	67	16	24.9
HD 138965	2015 Apr 15	240	8	12.2	31	32	6.2
HD 143675	2015 Jul 11	96	16	36.8	91	16	35.6
HD 146606	2016 Jul 02	304	8	15.8	150	16	17.7
HD 148657	2015 Apr 20	96	16	34.5	89	16	33.3
	2016 Jun 05	16	32	8.6	8	64	8.4
HD 151109	2015 Apr 15	96	16	31.9	91	16	30.8
	2016 Jun 04	16	32	8.0	8	64	7.9
HD 153053	2015 Apr 23	96	16	13.6	45	32	13.0
	2016 Apr 09	64	32	15.4	64	32	15.7
HD 182919	2016 Apr 14	128	16	12.1	64	32	12.2
	2017 Jul 15	48	32	8.3	24	64	8.9
HD 196544	2015 May 29	48	32	11.0	69	8	13.7
HD 215766	2015 Jun 20	192	8	28.1	228	8	38.0
HD 223352	2015 Jul 16	320	4	65.1	196	8	82.9
HD 225200	2015 Jul 18	64	24	31.3	60	32	35.3

Table 3.3: SPHERE observations of target stars. The rotation column (Rot) indicates the total rotation of the field, between the first and the last images. Note that the listed exposure times refer to each individual science image in the observation sequence.

3.4 Data Reduction

3.4.1 Pre-processing

3.4.1.1 IRDIS

Pre-processing of the SPHERE/IRDIS data was performed using the CPL (Common Pipeline Library) provided by ESO. Master dark and flat frames were created, and the star position behind the coronagraph was calibrated using the center calibration frames. Each data frame was independently reduced by applying the master dark and flat frames, and then realigned taking into account the star center position calibration and the dither position for each frame.

3.4.1.2 IFS

Integral Field Spectrograph (IFS) data reduction was performed following Vigan et al. (2015). Basic calibrations were first created using the ESO data reduction and handling pipeline (DRH, Pavlov et al. 2008): master dark and flat fields, IFS spectral position calibrations, initial wavelength calibrations and an IFU flat-field were all created. We then used a custom pipeline to calculate accurate time and parallactic angles for each image, and to normalise the data based on the direct integration time and neutral density filters for each observation. The pipeline also performs bad pixel correction and cross-talk correction, and the DRH is then used to interpolate these frames spectrally and spatially. To complete the initial cleaning and calibration of the frames, we finally perform a sigma-clipping routine to remove remaining bad pixels, and a correction of the wavelength calibration. Full details of these cleaning and calibration steps are given in Vigan et al. (2015).

3.4.2 Principal Component Analysis

After the initial cleaning and calibration of the data, we use Principal Component Analysis (PCA, see e.g. Soummer et al. 2012; Amara & Quanz 2012, our own implementation) to

remove stellar speckle noise. The same process is carried out on both the IRDIS and the IFS data. We perform a full-frame PCA, taking into account each timestep (typically ~90) and each wavelength channel (2 for IRDIS data, 39 for the IFS) independently. First, each wavelength channel is rescaled proportional to its wavelength, such that the characteric scale of speckles is equal between images. Then, the PCA algorithm is applied to remove stellar speckles based on the similarities between each individual image: speckles appear at the same location in each scaled image, while on-sky signals (planets, debris disks or background stars) appear at different positions with time since the field is rotating, and with wavelength due to the image scaling. The PCA processed images are then rescaled back to their original plate scales, and the parallactic angle for each image is used to align the North axis of each time step. The individual images are finally co-added to give a single, broadband reduced image for each target. Following the same process but co-adding by time only, we also create a cube of reduced images at each individual wavelength. This allows a comparison of H2 and H3 magnitudes in the case of IRDIS data, and spectral extraction across the YJ bands in the case of IFS data.

The aggressiveness of the PCA algorithm is tuneable: removing more principal components before co-adding the images removes more of the scattered starlight, but also reduces the throughput of the planetary signal. We aim to achieve the optimum balance between removing starlight and preserving companion signal, so as to detect the faintest possible planets and place the most stringent contrast limits. To do this, we perform several PCA reductions with the same code, where we remove between 1 principal component and approximately one-third of the total available principal components, at which point a planetary signal is almost entirely removed. Each of these different reductions is used in our subsequent analysis when identifying candidate companions and calculating contrast curves.

3.4.3 Candidate Companion Identification & Verification

Candidate companions were identified by visual inspection of both the IRDIS and the IFS data, and each target was visually inspected by at least two individuals to confirm that

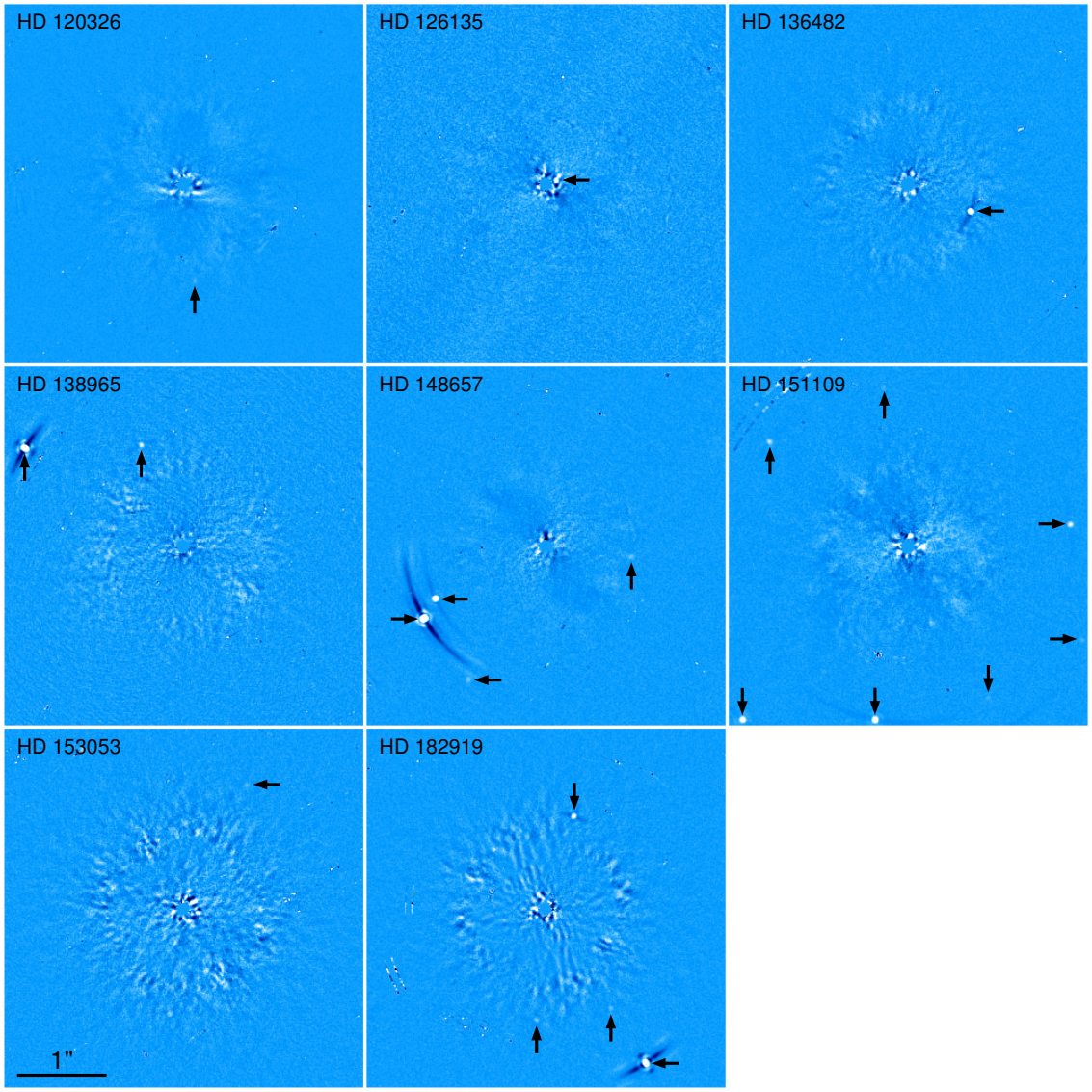

Figure 3.2: PCA reduced images for a selection of targets from the survey. All survey targets with candidates closer than 2″ are shown. Each image is 4″ square, and candidates within this field of view are highlighted with arrows. The HD 126135 candidate is a likely speckle, as detailed in Section 3.5.5. The arcsecond scale bar applies to all images, the colorbar is identical for each thumbnail, and North is oriented upwards in each case.

no candidates were missed. Candidates within a 2″ square, centred on the host star, are shown in Figure 3.2.

IRDIS observations are used to calculate astrometry of each candidate companion relative to its host star. To do this, the pixel position of each candidate and the stellar position behind the occulting mask are measured, and we assume an error of 0.2 pixels in the determination of each. Following the ESO User Manual[1], we use a plate scale

1. 6th & 7th release, see https://www.eso.org/sci/facilities/paranal/ instruments/sphere/doc.html

of 12.255±0.021mas/pix and a true north correction of -1.700±0.076° for data before December 2015, and -1.75±0.08° for data after February 2016. The additional pupil IFS offset (135.99±0.11°) is also applied, as well as an additional 'epsilon' correction, due to a missynchronisation problem at the telescope (see the User Manual for details). For our data, we find that this correction is consistently smaller than 0.1°. We also correct for the anamorphic distortion of the chip before performing astrometry. The epsilon and anamorphic distortion corrections are applied to each individual frame, before the images are combined. The measured separation and position angle of each candidate are listed in Table 3.4.

We use several methods to distinguish between genuine companions and background objects: we refer to previous literature, use common proper motion testing where there are multiple epochs of SPHERE data, and study the H2-H3 colors for candidates with an absolute magnitude fainter than 15 in the H2 filter. A negative H2-H3 color indicated the presence of methane, which we expect for sufficiently low mass companions but not for distant background stars. For the remaining candidates, it is not possible to make a conclusive determination, but we use separation from the host star to determine likely background objects. In this survey we detect 178 candidates of which 2 have been previously published as companions, and 13 have been previously published as background objects. A further 124 are found to be background objects based on their common proper motion between two epochs, and 20 are background objects based on their H2-H3 colors. The final 18 are likely background objects based on their relative faintness and wide separations from their respective host stars. The final designation of each candidate is given in Table 3.4. One additional candidate to HD 126135 is detected close to the coronagraph in a first epoch of data, but not redetected and we conclude the object is likely to be a speckle.

For the 13 candidate companions that have been previously determined to be background objects, we plot relative astrometry against the published astrometry in Figure 3.3. We consistently see close agreement with the predicted positions for candidates in Nielsen et al. (2013), and in each case confirm their conclusion that these are background objects. For the candidate around HD 125541 that was previously published in Janson

et al. (2013b), we note a systematic offset of ~80mas in the candidate astrometry between their work and our measurements. It is not immediately clear what the cause of this difference is, but since the candidate is relatively bright (ΔH2=8.6 mag) we suggest that it is a non-infinite background object with non-zero proper motion. The 7 candidate companions to HD 120326 were previously detected in Bonnefoy et al. (2017), but due to the short time baseline between their observations and ours we do not attempt to create CPM plots for this target. Two candidate companions to HD 223352 have been previously detected in several works (De Rosa et al. 2011; Rameau et al. 2013; Galicher et al. 2016), and confirmed to be co-moving. These companions are discussed in more detail in Section 6.3.

For 6 targets, we have multiple epochs of SPHERE data. In these cases we create multi-candidate common proper motion plots (see Figure 3.4), where the motion of each candidate relative to its host is presented simultaneously. A reference track, demonstrating the predicted motion of an infinitely distant background star relative to the primary is also plotted. HD 148657 and HD 153053 demonstrate the expected outcome for a target with a large number of candidate companions: the final positions of the various candidates (in red) are clustered around the predicted final position (dark blue), with some statistical spread. In these cases it is clear that each of the plotted companions shows a good match to the background hypothesis. In the case of HD 151109, however, the measured final positions of candidates are clustered around a point in between the initial (light blue) and predicted final (dark blue) positions. This is indicative of some systematic error: either (a) the host star position is incorrectly calibrated behind the coronagraphic mask, (b) there is a slight error in calibration of the telescope angle or (c) the proper motion and parallax of this object in the *Gaia* catalog (Gaia Collaboration et al., 2016b; Gaia Collaboration et al., 2016a) are not accurate. This systematic uncertainty can be probed by considering the candidates simultaneously, since *all* the candidates show this shift from the expected final position, and it is clear that not all the candidates are genuine companions. We suggest instead that any candidates with significantly outlying proper motion relative to the other candidates should be considered as co-moving companions, rather than any candidates which show a small proper motion between the two epochs. For HD 151109, therefore, all the candidates appear to be background objects. For a subset of targets with faint enough M_{H2} for the H2-H3 colors to differentiate between companions and background objects,

Star	Epoch Date	No.	ΔH (mag)	Sep(″)	σ_{sep}	PA	σ_{PA}	Reference	Status
HD 71722	2015-04-25	1	11.4	2818.2	6.0	260.37	0.15	N13	BG
HD 71722	2015-04-25	2	11.2	5915.2	10.8	3.47	0.14	N13	BG
HD 79108	2015-04-09	1	13.3	5248.5	9.7	89.50	0.14	–	?BG
HD 122810	2016-05-02	1	14.6	3512.9	7.0	262.04	0.15	–	?BG
HD 122810	2016-05-02	2	7.8	5682.9	10.4	311.36	0.14	–	?BG
HD 122810	2016-05-02	3	11.3	5788.2	10.6	357.93	0.14	–	?BG
HD 122810	2016-05-02	4	13.8	5859.7	10.7	126.75	0.14	–	?BG
HD 122810	2016-05-02	5	–	6188.0	11.2	284.11	0.14	–	?BG

Table 3.4: Candidate companion astrometry and magnitudes for the survey. A total of 178 candidates were detected, of which 157 are background (BG) and a further 18 are likely background objects (?BG) based on their separation from the host star and color analysis. 2 objects are previously detected companions (C) and one object is a likely speckle (S?). Further detail on candidate designation is given in Section 3.4.3. Only a portion of the table is shown here, with the full table is included in Appendix C.
Note. TF = candidate too faint to be redetected, OS = candidate off-screen in this epoch.
References. (B17) Bonnefoy et al. 2017; (dR11) De Rosa et al. 2011; (G16) Galicher et al. 2016; (J13) Janson et al. 2013b; (N13) Nielsen et al. 2013; (R13) Rameau et al. 2013.

we find H2-H3 colors close to zero, further supporting this conclusion. In cases like this the entire set of candidates reveals additional information about systematics: although an individual CPM diagram might suggest a co-moving companion, comparing the entire set of candidate in this way allows more accurate conclusion to be drawn about the true nature of candidates.

3.4.4 Contrast Limits

For each of the targets, contrast limits are calculated via injection of fake candidates. Several scaled images of the PSF calibration frame are inserted into the raw data at a variety of offsets and position angles, and the full reduction process repeated. A total of 20 scaled PSF images are inserted into each IFS frame, and 60 into each IRDIS frame. In each case, the minimum separation between fake planets is 100mas, to avoid contamination between the separate injections. The injections are repeated at five different position angles, and at several different magnitudes. The contrast quoted in this work is the mean 5σ detection across the five fake planet candidates at each separation. To account for the small number of resolution elements at small inner working angles, the correction term presented in Mawet et al. (2014) is applied. By using this method we ensure the planetary throughput of the algorithm is accurately captured.

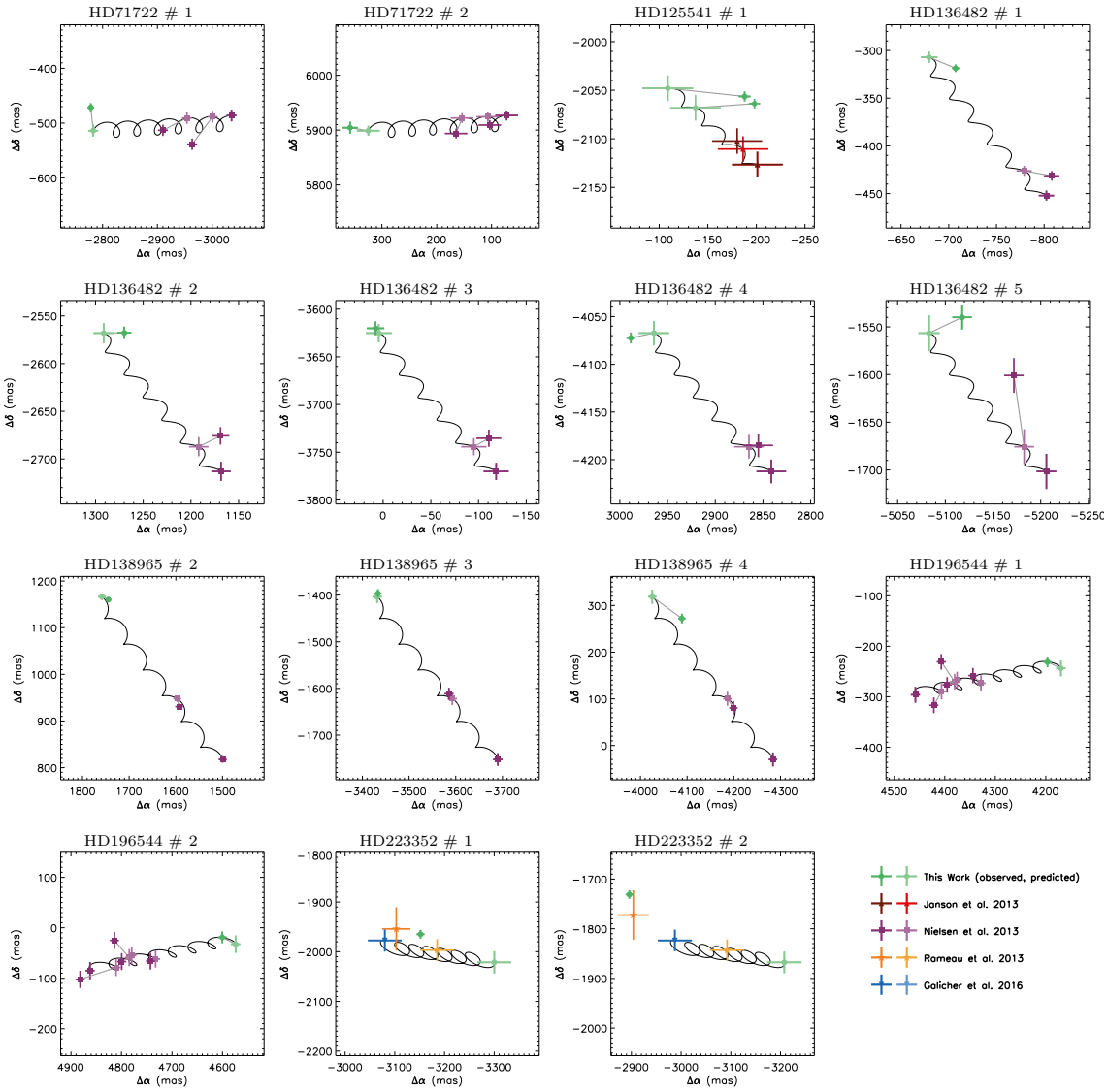

Figure 3.3: Astrometry for all candidates with archival data. Archival data are taken from Nielsen et al. (2013), Janson et al. (2013b), Rameau et al. (2013), and Galicher et al. (2016). Darker points are measured, and lighter points show the predicted position for a background object at each epoch, with the black lines showing the path a stationary background object would take. In several cases there is imperfect agreement with the background hypothesis, possibly due to non-zero motion of the background objects. Although we see a systematic offset between Janson et al. (2013b) and our astrometry for HD 125541, discussed further in Section 3.4.3, we agree with their conclusion that this is a background object. For HD 223352, we only plot a subset of archival astrometry for clarity, and the two candidates are previously confirmed companions, as discussed in Section 3.5.5 and Table 6.2.

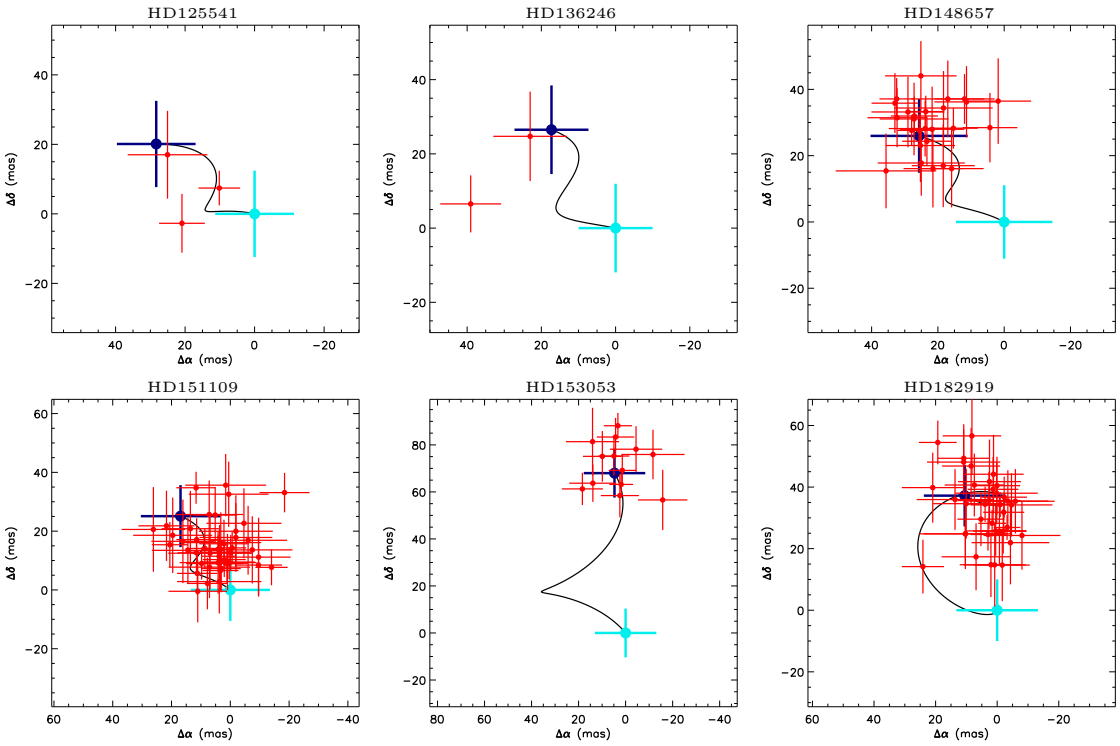

Figure 3.4: Multi-candidate common proper motion plots for targets where we have multiple epochs of SPHERE data. The predicted background motion for a candidate in each case follows the black line from the light to the dark blue point, and the measured final positions of each candidate are plotted in red relative to the light blue point. The complete astrometry is included in Table 3.4 and individual common proper motion plots for each candidate are included in Appendix A.

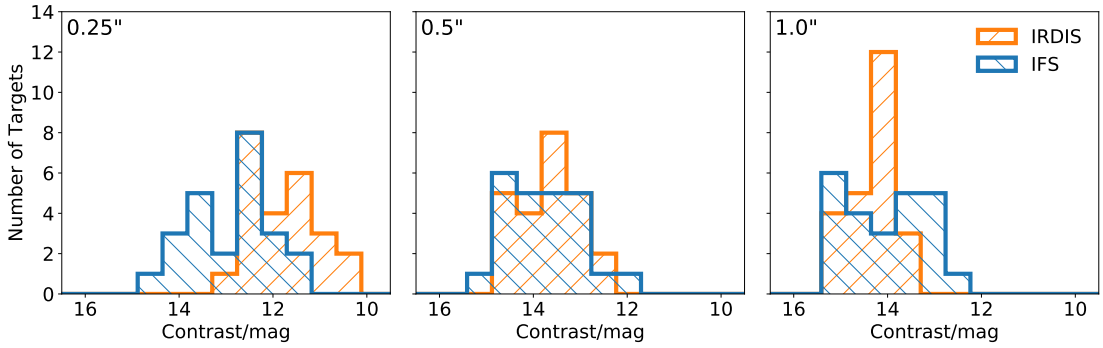

Figure 3.5: Histograms of our survey contrast, at a separation of 0.25″, 0.5″ and 1.0″. Orange and blue lines represent the IRDIS and IFS data respectively.

This process is performed for each of our PCA reductions with different numbers of PCA components removed, and the contrast quoted is that of the most favorable reduction. By testing the contrast at a variety of reduction strengths, we ensure that we remove the optimum number of PCA modes to balance removing sufficient starlight, while minimizing the extent to which the planetary signal is self-subtracted for each individual dataset.

We convert these contrast limits into mass limits by using the COND models (Baraffe et al. 2003) for temperatures below 1700K and DUSTY models (Chabrier et al. 2000) otherwise (as in e.g. Janson et al. 2013b). For simplicity, we use only the SPHERE/IRDIS data in calculating these mass limits. The majority of conversions use the COND models, due to the high sensitivity of the SPHERE instrument.

3.5 Results

3.5.1 Achieved contrast

Our achieved contrast as a function of separation for both the IRDIS and IFS instruments is presented in Figure 3.5. Mean and best contrasts as a function of separation are given in Figure 3.6 and individual contrast curves for each dataset are presented in Appendix B. We are able to reach contrasts of ~15 magnitudes at 0.5″ in the most favorable systems.

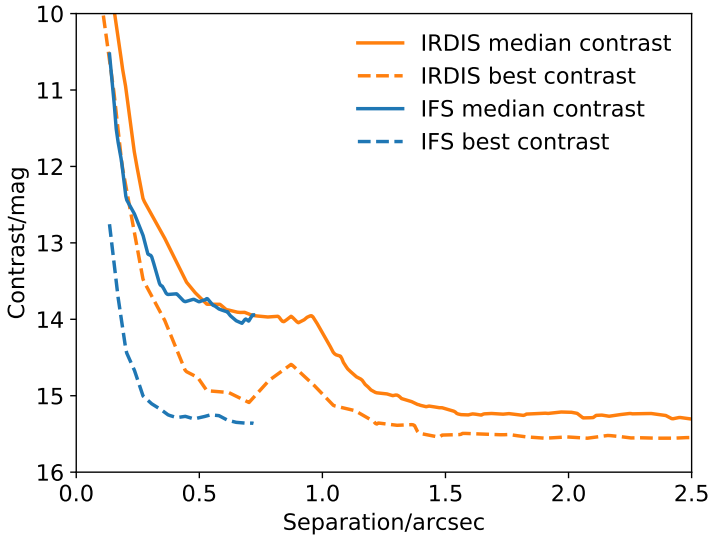

Figure 3.6: Median and best contrasts achieved by our survey, for both the IFS and IRDIS subsystems. Only the initial observation (durations ~1h) of each target is included in this plot.

3.5.2 Disk Radii

14 of the targets in this work show strong evidence for hosting two-temperature debris disks, based on the available literature and our examination of the SEDs as described in Section 3.2. The remaining 10 targets are less certain: these target SEDs can be modelled almost as well with a single temperature excess as with two temperatures. For the purposes of this thesis, we proceed under the assumption that these two-temperature systems host two debris belts and discuss the planetary configurations for this case. If these are in fact single debris belt systems, there are clearly a range of additional planetary configurations which are not considered in this work.

For consistency, we use the temperature values found in Chen et al. (2014) to calculate radii for all of our targets. We calculate updated radii following Pawellek & Krivov (2015) and using the “50% astrosilicate + 50% ice" dust composition.

3.5.3 Resolved Disk Radii

For six of the targets in this survey, resolved disk images exist, and these targets are listed in Table 3.5. This allows some verification of the calculated radii. Four of the targets have

Target	λ	r_R / AU	r_C / AU	Reference
HD 166	70 μm	29±3	76^{+12}_{-10}	Morales et al. 2016
	100 μm	36±3		Morales et al. 2016
HD 71722	100 μm	139±27	128^{+20}_{-16}	Morales et al. 2016
HD 138965	100 μm	187±6	191^{+38}_{-30}	Morales et al. 2016
HD 153053	100 μm	186±12	306^{+81}_{-68}	Morales et al. 2016
HD 120326	1.6 μm	58.6±3, 130±8	$33.0^{+2.8}_{-2.4}$, 134^{+24}_{-19}	Bonnefoy et al. 2017
HD 129590	1.6 μm	59.3±0.2	$60.2^{+1.3}_{-1.3}$, 103^{+451}_{-3}	Matthews et al. 2017

Table 3.5: Measured and calculated radii (indicated r_R and r_C respectively) for disks where at least one belt of debris has been resolved. The upper group of targets have been resolved with the *Herschel* space telescope, and for these we list only the calculated outer radius, which corresponds well for two targets and is a factor of 2 off for two targets. The lower group have been resolved with VLT/SPHERE. In this case we list both calculated radii: for HD 129590 the resolved disk is likely the inner band of dust, while for HD 120326 both bands of dust are tentatively detected in Bonnefoy et al. (2017), with the outer closely matching the calculated value. Note that only the outer disk radius is used in the calculation of a lower mass limit.

been resolved with *Herschel* (see Morales et al. 2016), and in two of these cases, namely HD 71722 and HD 138965, we see close agreement with the calculated values. For the other two targets, there is a factor ~2 difference between the measured and calculated radii, which changes our calculated lower mass limits (see below) by a factor ~2.8.

Two of the targets, namely HD 120326 and HD 129590, are resolved with VLT/SPHERE at ~1.6 μm. For HD 129590, the resolved radius shows very close agreement with the calculated radius for the inner dust belt. Given that Matthews et al. (2017) found a very soft external power law for the dust ring, we suggest that the resolved disk corresponds to the inner dust belt, and that the soft power law is caused by an additional, fainter ring of dust at wider separation. For HD 120326, Bonnefoy et al. (2017) found evidence for both dust belts in scattered light, and both radii are listed below. The outer radius matches closely with the calculated value, and the inner radius is within a factor of 2. We note at this point that the calculated lower mass limits (see Section 3.6) depend only on the radius of the outer disk, although the position of the inner disk determines the number of planets at this mass that are required to fill the gap.

3.5.4 Age Determination

Where available, we use cluster membership to determine the ages of each target. 14 of the 24 targets are members of the Scorpius-Centaurus association, as determined by de Zeeuw et al. (1999), and we use the Pecaut et al. (2012) ages for each Sco-Cen subgroup. There is some disagreement about the membership of HD 166: it is listed as a member of either Hercules-Lyra (150-300 Myr; López-Santiago et al. 2006), the Local Association (20-150 Myr; Maldonado et al. 2010) or the TW Hydrae association (8 Myr; Nakajima & Morino 2012). Tetzlaff et al. (2011) also find a very young age of 20.1±6.4 Myr for this target using pre-main sequence evolutionary models. We choose to assign this target a range of ages, namely 8-150 Myr, to reflect this range of literature ages, and in subsequent calculations represent this range as an age of 79±71Myr. HD 223352 is a member of the AB Dor moving group (Zuckerman et al. 2011), which has an age of 150^{+50}_{-30} Myr (Mamajek 2016). HD 225200 is a member of Blanco I (Lynga & Wramdemark 1984), which has an age of 90±25 Myr (Panagi & O'dell 1997).

The remaining targets are field stars, and so ages are harder to determine accurately. Each is nonetheless likely to be young, given the presence of high volumes of circumstellar dust. For these targets we use previously performed age determinations. HD 71722, HD 79108 and HD 196544 all show close agreement between several literature sources (see Table 3.1), and in these cases we use the Bayesian ages from David & Hillenbrand (2015, here on DH15). For HD 138965 and HD 215766, there is some slight discrepancy between DH15 and Brandt & Huang (2015), with the best fit ages varying by a factor of ~3. For consistency, we use the DH15 ages here too, but note that there is more uncertainty. For HD 153053, the DH15 Bayesian age appears discrepantly lower than both the DH15 interpolated age and the ages presented by Brandt & Huang (2015) and Chen et al. (2014), and so we use the Brandt age. Finally, there is limited literature for both HD 16743 and HD 182919 and so we use Rhee et al. (2007) and Zorec & Royer (2012b) respectively, but note that these age designations are more uncertain. In these two cases, no uncertainties are quoted with the literature ages.

3.5.5 Candidate Companions to Individual Targets

HD 166: This target was previously studied by Lafrenière et al. (2007) as part of the GDPS, and no candidates were identified. Even with our improved contrast limits, we do not find any candidates around HD 166.

HD 16743: No candidates are identified around HD 16743.

HD 71722: Both the candidates presented in Nielsen et al. (2013) as background stars are redetected in this work, and our astrometry is consistent with that of Nielsen et al. (2013) for the background hypothesis. No further candidates are identified.

HD 79108: For this target, we identify a single candidate at a separation of 5.25″ and M_{H2}=14.5. This is too bright for H2-H3 color analysis to be conclusive, but the physical projected separation of 521 AU strongly suggests a background object.

HD 112810: Five widely separated candidates are identified (>3.5″). All are likely background objects based on their separation. Additionally, the disk was detected in scattered light for the first time (Matthews et al., in prep).

HD 120326: A debris disk was imaged around this target in Bonnefoy et al. (2017). We redetect this debris disk, and detect seven of the ten candidate companions found in that work. An eigth candidate appears on the very edge of the detector where astrometric measurements are no longer reliable, and we choose to ignore this candidate. The final two candidates listed in Bonnefoy et al. (2017) are off the edge of our detector, due to the camera rotation. Our data were collected two months after those in Bonnefoy et al. (2017), a short time baseline in which a background object would move 11.2mas relative to the host star. Although this number is larger than the nominal SPHERE astrometric accuracy of 5mas, it is too small to allow us to clearly differentiate the companion and background hypotheses, and we do not create common proper motion plots for this target. Bonnefoy et al. (2017) conclude that all of these candidates are background objects based on their colors, and on previous detections of several of the candidates in HST/STIS data (Padgett & Stapelfeldt 2016).

HD 125541: This candidate was observed twice, with four candidates detected in the first epoch, and three of these redetected in the second epoch. Candidate #1 was previously detected in Janson et al. (2013b) and confirmed to be a background object. We detect significantly less than the expected proper motion between our two observational epochs. Given the systematic differences with Janson et al. (2013b) and the relative brightness of the candidate, this is likely a nearby background object, with non-zero proper motion. Candidates #2 and #4 both show significant motion between our two observational epochs, suggesting that they are background objects. Candidate #3 is only detected in one epoch, at M_{H2}=16.1. At this very faint magnitude, an H2-H3 color of 0.08 and a separation of 4.86″=786 AU imply that this is a background object.

HD 126062: Three faint, wide separation candidates are identified around this target. With only one epoch of data, we are unable to use proper motion to confirm whether the candidates are genuine companions or background objects. Based on the wide separation, faint absolute magnitude and low H2-H3 color of each candidate, all three are assumed to be background objects.

HD 126135: In a first epoch of data, we find a bright candidate very close to the coronagraph edge (separation 137mas, see Figure 3.2). At this close separation it is hard to distinguish companions and speckle noise, but the candidate is resilient to the number of principal components subtracted, and appears to have self-subtraction wings. The candidate appears in the IRDIS but not the IFS data, suggesting that it is either an extremely red object or a speckle.

In a second epoch of data the candidate is not recovered. Although it is possible that this is a genuine low-mass companion, it is most likely a particularly persistent speckle, and further follow-up is required to confirm the nature of this object.

HD 129590: The debris disk around this target was detected in scattered light for the first time (see Matthews et al. 2017). In addition, one candidate was identified at 5.67″, corresponding to a physical projected separation of 752 AU. At this wide separation, the candidate has a low probability of being associated with the host star. The candidate is positioned North of the debris disk, which has a position angle of 122° and an inclination of

75° (Matthews et al. 2017). A bound candidate in this position would either be significantly further than this 752 AU separation, or significantly misaligned with the disk, further supporting our assumption that this is a background star and not a bound companion.

HD 132238: A single candidate is observed at a separation of 4.29″. The candidate has M_{H2}=15.3 and H2-H3=0.05, and shows good agreement with the predicted motion of a background object between two epochs, and so we conclude that it is a background object.

HD 136246: Two candidates are identified, and both are redetected in a second epoch of data. Although the astrometric measurement of candidate #1 is displaced from the predicted position in epoch 2, the candidate moves significantly from the initial position. Since a companion would show almost no motion relative to the host in this period, this is likely a background star with non-zero proper motion. As such, we conclude that both candidates are background stars.

HD 136482: Six candidates are identified around HD 136482. Five of these have been previously identified by Nielsen et al. (2013), and an additional candidate at 5.95″ is found below the contrast limit in that work. Based on the projected separation and H2-H3 color of this candidate, it is a background object. We do not detect the 6th candidate listed in Nielsen et al. (2013) since it is outside the SPHERE field of view.

HD 138965: Four candidates are detected, three of which are also listed in N13 as background objects. Our candidate #1 is below the detection limit of N13, with M_{H2}=15.2. For this candidate H2-H3=0.05, and so the candidate is a likely background object.

HD 143675: 4 candidates are detected around HD 143675. Since all are faint (contrast 11.2 mag or higher) and at wide separation (>3.89″=468 AU), each candidate has a low likelihood of being bound, and so we did not collect follow-up data for this candidate. Candidates #1, #2 and #3 are all fainter than 15th magnitude in H2 and have H2-H3 colors of 0.21, -0.11 and 0.34, and so we conclude all three are background objects. Candidate #4 is too bright for H2-H3 color to differentiate between a background and a companion, but at a projected separation of 5.39″= 664 AU this object is highly likely to be a background star.

HD 146606: A single, faint candidate is identified at a separation of 4.7″, and at this wide separation is a likely background object.

HD 148657: This target is just 6.8° from the galactic plane, and so there is a rich field of background objects. We identify a total of 29 candidates in our first epoch of data, 26 of which are redetected in a second epoch, and confirmed to be background objects based on CPM and color analysis. The remaining three candidates are too faint to be identified in the second epoch. These three candidates are at relatively wide projected separations (161, 547 and 799 AU), and based on their faint H2 magnitudes and small H2-H3 colors, we conclude that all three are background objects.

HD 151109: We detect a total of 49 candidates around HD 151109, which is 4° from the galactic plane. 44 of these are redetected in a follow-up observation, and the remaining 5 are too faint to be detected in the second epoch. As discussed in Section 3.4.3 above, the candidates we detect are systematically shifted by a smaller distance than would be expected based on the proper motion of this target. Based on the systematically similar motion of the set of candidates we conclude they are all likely background stars. The subset of candidates faint enough that H2-H3 color can be used to differentiate companions and background objects all have colors close to zero, confirming this assumption. The 5 candidates detected only in the first epoch are also highly likely to be background objects, based on their wide separation, faint absolute magnitude and small H2-H3 colors.

HD 153053: For this target, 14 candidates are identified and 13 of these are redetected in a second epoch of data and confirmed to be background objects. The final candidate, at a separation of 5.60″, is outside the field of view in the second epoch of data, due to the orientation of the ccamera. Based on the wide separation of this candidate, it is a likely background object.

HD 182919: A total of 40 candidates are detected around this target, which is 1.7° from the galactic plane. In a second epoch of data, we redetect 38 of these 40 candidates. As can be seen in Figure 3.4, there is some scatter in final position relative to the predicted final positions for each candidate. We nonetheless conclude based on the proper motion, absolute magnitude, color and separation of each candidate that these are all background

objects. The two candidates that appear only in the first epoch are also assumed to be background objects, based on their wide separation, faint absolute magnitude and small H2-H3 colors.

HD 196544: The two background objects identified in Nielsen et al. (2013) are redetected, and no new candidates are found.

HD 215766: No candidates are detected around this target.

HD 223352: This target was first identified as a tertiary system in De Rosa et al. (2011), and redetected by Rameau et al. (2013) and Galicher et al. (2016). We detect the companions HIP 117452Ba and HIP 117452Bb as listed in De Rosa et al. (2011), but do not find any evidence for additional companions orbiting the primary, even with our improved contrast limits. A more detailed discussion of these candidates is presented in Section 6.3.

HD 225200: No candidates are detected around this target.

3.6 Analysis

The mass/radius parameter space for planets orbiting these 24 systems discussed in this work can now be tightly constrained by combining our VLT/SPHERE observations with dynamical arguments. Is is therefore possible to make inferences about the putative planetary systems hiding within the debris gaps.

Mass limits are calculated using the SPHERE/IRDIS contrast limits as described in Section 3.4.4: the COND models (Baraffe et al. 2003) are used for temperatures below 1700K and the DUSTY models (Chabrier et al. 2000) otherwise. These mass limits are shown in Figures 3.7 and 3.8. For these mass limits, the confidence interval is calculated based solely on the age of the system. As discussed above in Section 3.5.4, for two targets (HD 16743 and HD 182929) we were only able to find literature ages without uncertainties quoted, and as such are also unable to calculate uncertainties in our mass limits. For the 14 Sco-Cen targets in our sample, the ages are well determined (Pecaut et al. 2012) and so our uncertainties in mass limit are small.

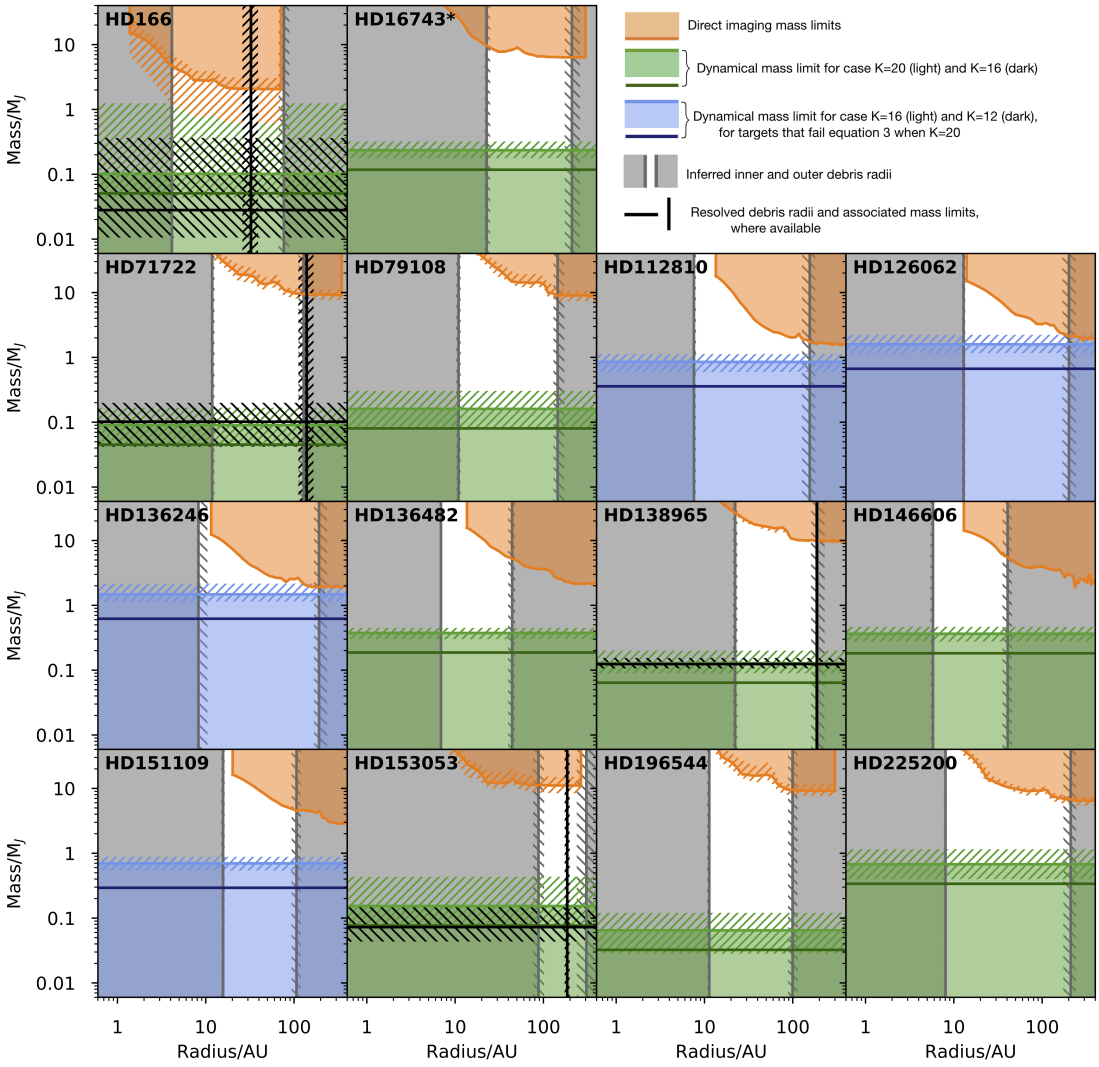

Figure 3.7: Constraints on the planetary systems for each of the targets in our survey. Since we do not detect companions, we expect the planetary systems to be within the white area of each subplot. The positions of the inner and outer debris belts are indicated in grey, with the regions inside the inner and beyond the outer shaded. Our direct imaging contrast limits based on SPHERE/IRDIS are shown in orange, with the region above this shaded, and dynamical mass constraints from Shannon et al. (2016) are indicated in green, with masses below this value shaded. The uncertainty on this lower limit is calculated based on the age of host and the uncertainty in debris belt temperature, and indicated with hatching. Dark green lines indicate the lower limits for a slightly closer planet spacing of 16 mutual Hill radii. Errors are the same size as those on the light green lines but are not shown for clarity. For a small number of targets the inferred planetary mass from Shannon et al. (2016) is too great to allow an interplanetary spacing of $20R_H$. In these cases we instead show the $16R_H$ case in blue, with an inferred $12R_H$ limit shown in navy. In each case, a spacing of $12R_H$ between each planet fulfils equation 3.3. Additional black lines show the outer debris radius, and associated lower mass limit, for the subset of systems where the outer disk has been resolved (see Table 3.5). As mentioned Section 3.5.4, for two of the targets (HD 16743 in this figure and HD 182919 in figure 3.8) the literature ages have no uncertainties, and we indicate these targets with asterisks.

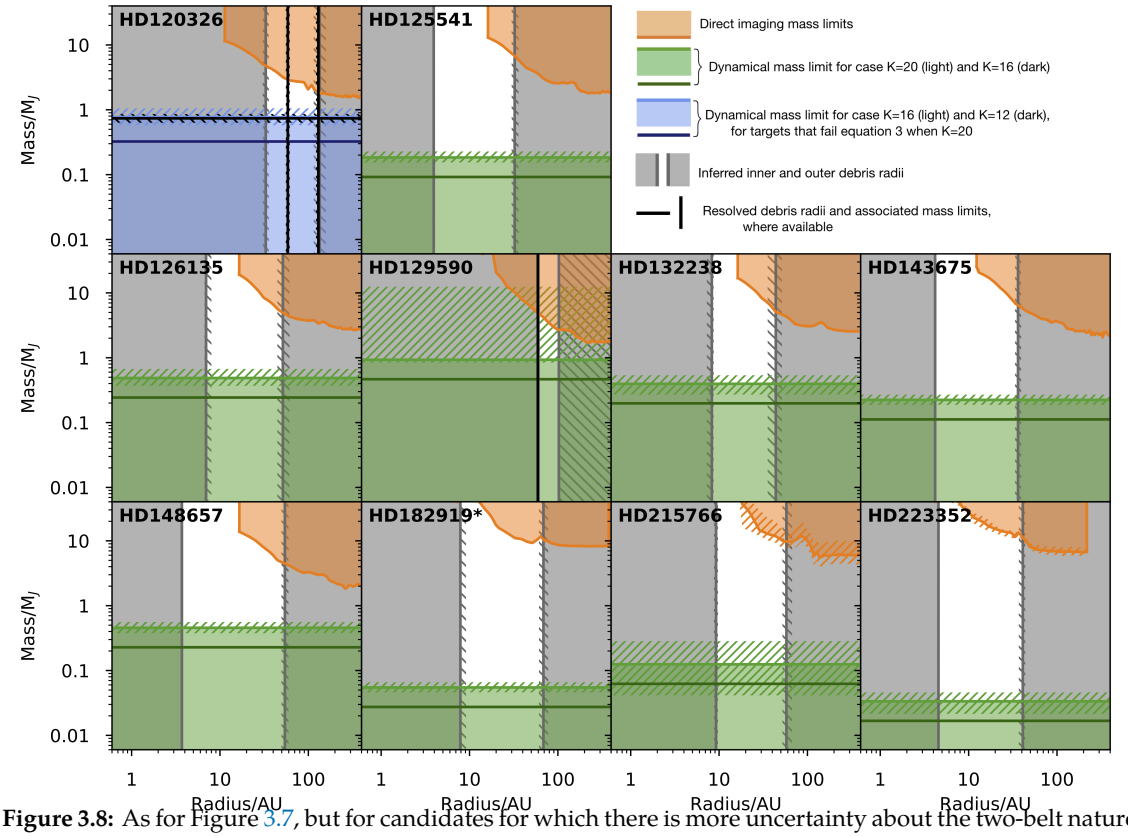

Figure 3.8: As for Figure 3.7, but for candidates for which there is more uncertainty about the two-belt nature of the disks. In these cases we only present the two-belt planetary constraints.

Also plotted in Figures 3.7-**??** are the minimum masses of planets required to clear the inferred debris gaps, based on the N-body simulations of Shannon et al. (2016). The quoted mass is the minimum mass *per planet*, with uncertainties calculated based on the age of the system and the uncertainty in the disk radius. In all cases except for HD 129590, we infer that the system must be in a multi-planet configuration: the theoretical mass for a single planet to clear the gap is large ($\gtrsim$50 M_J in each case, Quillen 2006; Morrison & Malhotra 2015). Quillen (2006) found this clearing mass to be consistent for eccentricities $\lesssim$0.3. Nesvold & Kuchner (2015) predicts slightly lower masses for a single gap-clearing planet, but still requires a single planet to have $\gtrsim$25 M_J to have cleared the observed gap.

The minimum mass calculation relies on the assumption that planets are spaced by ~20 mutual Hill radii. To demonstrate the impact of this choice of spacing, we additionally plot the lower mass limits for a spacing of $16R_H$, as given in Shannon et al. (2016). The number of Hill radii between each planet has a relatively small effect on the dynamical constraints. For a planet spacing >$20R_H$, the predicted mass for each planet is higher than in the $20R_H$ case, and so the lower limits that we plot remain valid.

In a small number of cases, the planet masses inferred from Shannon et al. (2016) are sufficiently high that the value of R_H approaches a significant fraction of the star-planet spacing. In this case, for planets to be spaced by KR_H, the second planet will be at semi-major axis $a_2 = a_1 + KR_H$. Substituting for equation 3.1, the semi-major axis is given by

$$a_2\left(1-\frac{K}{2}\left(\frac{m_1+m_2}{3M_\star}\right)^{\frac{1}{3}}\right) = a_1\left(1+\frac{K}{2}\left(\frac{m_1+m_2}{3M_\star}\right)^{\frac{1}{3}}\right), \tag{3.2}$$

which only gives a positive value for the semi-major axis when

$$m_1 + m_2 < \frac{24M_\star}{K^3}. \tag{3.3}$$

At this point, the very definition of mutual Hill radii means that for a specified planet mass, there is a certain maximum value of K, the number of R_H between each planet. Alternatively, for a given K, there is a maximum mass of planets that fulfils equation 3.3. For a solar mass star, and equal mass planets with K=20, this condition is reached at a planet mass of 1.43 M_J.

For a small number of the targets in this work, the masses inferred from Shannon et al. (2016) are sufficiently high that this limit is reached, and equal-mass planets cannot be separated by 20 mutual Hill radii. For these targets, we instead calculate the lower limits for a spacing of $16R_H$. These are highlighted in blue in Figure 3.8. When the number (K) of Hill radii between each target is changed, the clearing time appears to scale as K^3, so we tentatively also calculate a clearing time limit for a $12R_H$ spacing as 0.42× the limit for $16R_H$. This is an unusually close inter-planet spacing, and for all of the targets in our survey a value of K=12 predicts a clearing mass that satisfies equation 3.3, and so a spacing of $12R_H$ is reasonable.

We separate the targets for which there is doubt about the two-belt nature of the debris, and plot these in Figure 3.8. Our analysis is only valid if these are genuine two-belt systems.

By combining the observational upper and theoretical lower mass constraints in this way, only a small region of parameter space is left unconstrained. In some cases the region between the upper and lower mass constraints is less than an order of magnitude, with lower mass limits exceeding 1 M_J for systems with the widest debris disks and at the youngest ages. For all targets except HD 129590, we infer a multi-planet system based on the large theoretical clearing masses. In such a multi-planet system, the widest separation planet will have a physical separation close to that of the outer debris belt, where our direct imaging limits are relatively tight. Geometrical arguments mean that the planet will only appear at such a wide projected separation in a subset of cases, but this outermost planet is nonetheless constrained to a relatively small mass range, especially for targets where ALMA or *Herschel* data constrains the system inclination.

In our survey of 24 targets, no exoplanetary mass companions were detected. For context, Meshkat et al. (2017) found occurrence rates of 6.27% (68% confidence interval 3.68-9.76%) in a debris disk sample of planets between 5-20M_J and 10-1000 AU. Although our sample is too small for a detailed statistical analysis to be instructive, a non-detection in a sample of 24 stars is not inconsistent with the debris disk occurrence rate found in that work, since one would expect some companions might be geometrically unfavorably aligned, or below our detection limits. Our non-detections are also consistent with

the lower occurrence rate of ~1% found in unbiased samples by both Bowler (2016) and Galicher et al. (2016). The results of this survey are not incompatible with the theory that planets are carving wide debris gaps, since in each case our direct imaging upper mass limits are higher than the theoretical lower mass limits that we calculate. However, in several cases there is only a small mass range remaining where the planets could be massive enough to clear the observed gap, and yet sufficiently small and faint to remain undetected.

It is possible that the inferred gaps in these systems are not in fact caused by the presence of planets. An alternative cause of such a two-belt debris structure is that the belts form at the positions of molecular snow lines (see e.g. Ballering et al. 2017; Matrà et al. 2018), with the inner belt positioned at a water snow line and the outer belt at a CO snow line. The correlation found in Kennedy & Wyatt (2014a) between the outer disk temperature and the stellar luminosity suggests that the dust location does not consistently match with a condensation temperature. However, in an optically thick disk the snow line positions would be determined by the mid plane temperature and so this correlation does not exclude the possibility of a more complex relationship between condensation positions and the formation of two-belt debris disks, and more work is needed to understand this possibility. It is also possible that the two temperatures in these debris disks do not correspond to two distinct radii of debris, as addressed in detail in Kennedy & Wyatt (2014a). However, the existence of the HR 8799 and HD 95086 systems where planets are known to reside in two-temperature debris disks and the solar system where planets are known to reside between two belts of debris implies that planets are a valid explanation for the formation of this debris structure in at least a subset of cases.

The very youngest systems are clearly the most effective targets for a study like this one: in these cases the parameter space can be most tightly constrained. The ratio between the upper and lower limits for the younger, more distant Sco-Cen stars in this survey is much smaller than that for the older, closer targets. For these younger, more distant targets, exoplanets are more luminous (see e.g. Chabrier et al. 2000; Baraffe et al. 2003), although at these further distances the same absolute magnitude corresponds to a fainter apparent magnitude. Crucially, though, the lower limits inferred from Shannon

et al. (2016) are significantly higher in the case of younger targets, where gaps have only a limited time to form. This effect is so significant that even in the cases where the direct imaging mass limit is higher, constraints on the planetary system are still tighter for the youngest targets.

3.7 Conclusions

In this work, we have imaged 24 debris disk hosting stars using the VLT/SPHERE instrument in IRDIFS mode. These targets were specifically selected as those that are likely to host multiple, segregated debris belts enclosing a debris gap. It is inferred that a system of one or more planets is responsible for the clearing of this wide debris gaps, as is the case for the solar system and for exoplanet hosts HR 8799 and HD 95086. We identify a total of 178 candidates. Two of these have been previously identified as companions, and the remainder are found to be background or likely background objects based on previous literature, common proper motion analysis, and the magnitude, color and separation of each candidate. Our survey reaches a typical contrast of ~13 mag at 0.25″ and ~15 mag at 1.0″. These contrasts are converted to mass limits for each target. We additionally calculate the *minimum* required mass for planets in the system to have cleared the observed debris gap. Combining our upper and lower mass limits, we are able to tightly constrain the unexplored parameter space around these systems: typically, planets must be at least ~0.2 M_J to clear the observed gap based on dynamical arguments, and in some cases the dynamical limit exceeds 1 M_J. Direct imaging data from VLT/SPHERE, meanwhile, is sensitive to planets of ~3.6 M_J for a typical target in our survey, and 1.7 M_J in the best case. Several of the inferred planetary systems will likely be detectable with the next generation of high contrast imagers.

Chapter 4

SPHERE/VLT survey of the dustiest stars identified with WISE.

4.1 Introduction

The role of dust has already been extensively discussed in this work: dust is produced by the collision of planetesimals, and the presence of a giant planet or low mass star will cause these planetesimals to collide more often and increase the rate of dust production. As such, giant planets should be found more often in systems with debris dust than in systems without, and a preliminary link was demonstrated by Meshkat et al. (2017). Additionally, we would expect planets to be the most common in the most dusty systems (Wyatt et al. 2007), and with a sufficient sample size it will eventually be possible to test this prediction.

For this survey, we therefore studied 20 of the dustiest known debris disk systems with VLT/SPHERE, and aimed to both detect the low-mass companions responsible for elevating the rate of dust production in these systems, and image the dust itself in scattered light. All of the targets were selected to be young, early-type stars, with a previously unknown 22 μm excess indicating that warm debris dust is present.

4.2 Target Selection

To select targets with the highest volumes of circumstellar dust, the all-sky WISE catalog (Wright et al. 2010) was merged with the *Hipparcos* catalog and ~520 stars with a mid-IR excess > 4σ, and within 125pc of Earth, were identified. Of these, 348 were not previously known to host debris disks (Padgett et al., in prep). For this survey we picked newly identified, nearby debris disk hosting targets with the largest excess at 22 μm: all of these targets have an infrared luminosity $L_{\rm IR}/L_\star > 2 \times 10^{-4}$. Targets were additionally selected to be early type, with the majority of the final target list being BAF stars.

Our target list is given in Table 4.1, along with target distances (from *Gaia* Data Release 2, Gaia Collaboration et al. 2016b; Gaia Collaboration et al. 2018; Lindegren et al. 2018), and the WISE W1-W4 excess, which demonstrates the high quantity of dust around these objects. All of our targets have an excess of at least 5σ, and the best targets have an excess over 20σ. For context, HR 8799 has W1 - W4 = 0.34 ± 0.22, and the extremely dusty β Pictoris has W1 - W4 = 3.5 ± 0.4. In our survey 20 targets were observed, and 11 of these were subsequently followed up to look for common proper motion. No explicit selection was made based on the target ages, but we note that young stars tend to have a larger infrared excess than old targets (Rieke et al. 2005; Su et al. 2006; Carpenter et al. 2009) and so this survey is likely biased towards the younger targets for which high contrast imaging achieves the best detection limits.

4.3 Observations and Data Reduction

For each target in this survey, observations and data reductions were carried out as detailed in Chapter 2 and performed for the survey of two-belt systems (Chapter 3). Details of each observation are given in Table 4.2.

HD	HIP	SpT	Distance[pc]	W1-W4
18378	—	K2(III)	520.7 ± 5.4	1.27 ± 0.09
19257	14479	A5	76 ± 6*	2.10 ± 0.08
24966	18437	A0V	114.9 ± 0.5	1.73 ± 0.07
94893	53484	F0V	106.5 ± 0.4	2.21 ± 0.04
98363	55188	A2V	138.6 ± 0.7	2.73 ± 0.03
113902	64053	B8/9V	100.4 ± 1.2	0.81 ± 0.13
119152	66837	F0V	81.2 ± 0.3	0.62 ± 0.08
122802	63376	F3/5V	105.6 ± 0.9	1.49 ± 0.05
123247	69011	B9.5V	98.8 ± 0.7	2.08 ± 0.05
133778	73976	G2V	163.6 ± 1.9	0.89 ± 0.08
138564	76234	B9V	102.6 ± 0.7	1.15 ± 0.08
138923	76395	B8V	134.2 ± 2.2	1.32 ± 0.27
151012	82069	B9.5V	108.6 ± 0.6	1.10 ± 0.08
151029	81971	A3/5V	109.5 ± 0.6	0.86 ± 0.08
157728	85157	A7V	42.8 ± 0.1	1.16 ± 0.18
158815	—	G1V	144.3 ± 1.2	1.39 ± 0.08
176638	93542	B9.5V	57.5 ± 1.2	1.00 ± 0.21
182681	95619	B8.5V	71.4 ± 0.7	1.10 ± 0.17
192544	99892	A0III	81.6 ± 0.3	0.82 ± 0.09
207204	107585	A0V	95.3 ± 1.4	0.90 ± 0.09

Table 4.1: Target stars for this survey. Spectral types are as quoted on SIMBAD, and all distances are from *Gaia* data release 2 (Gaia Collaboration et al., 2016b; Gaia Collaboration et al. 2018; Lindegren et al. 2018), except for HD19257 for which *Gaia* find a poor fit and so the *Hipparcos* distance (Perryman et al. 1997) is quoted. This target distance is marked with an asterisk. W1-W4 excesses are calculated from the WISE all-sky survey catalog (Wright et al. 2010).

4.4 Methods & Results

4.4.1 Candidate Companion Identification & Verification

Thumbnails for each target are shown in Figure 4.1, and candidates were identified by visual inspection. We identified a total of 162 candidates, with 98 of these candidates associated with the target HD 158815, which is very close to the galactic plane. Of the 162 candidates identified, 3 are confirmed to be co-moving companions in the stellar mass regime (namely HD 18378B, HD 19257B and HD 133778B), and 115 are found to be background objects based on their motion relative to the host. For the remaining 44 targets, only one epoch exists since the target was only observed once or the candidate is too faint or off the detector in a second epoch, or in the case of HIP 82069 the common proper motion testing is inconclusive, and in these cases further work is required to determine if the candidates are genuine companions. Combined common proper motion plots for all targets with more than one candidate are shown in Figure 4.2, with individual CPM plots

		IRDIS			IFS		
Target	UT Date	N_{im}	T_{exp}[s]	Rot[°]	N_{im}	T_{exp}[s]	Rot[°]
HD 18378	2016 Sep 15	80	32	15.7	40	64	16.5
	2017 Aug 29	32	64	12.6	32	64	13.4
HD 19257	2015 Aug 26	48	32	8.0	49	32	8.4
	2017 Sep 01	32	16	2.7	34	16	3.0
HIP 18437	2016 Sep 19	70	32	32.6	70	32	34.0
HD 94893	2015 Apr 11	48	32	16.9	49	32	17.5
	2018 Jan 07	16	16	3.1	17	16	3.4
HD 98363	2015 Apr 11	48	32	11.5	45	32	11.0
	2018 Mar 24	16	64	6.3	16	64	6.7
HIP 64053	2016 Jun 06	80	32	19.4	80	32	21.0
	2017 Jun 23	64	32	15.9	32	64	16.9
HIP 66837	2016 May 01	144	16	48.2	72	32	53.8
HD 122802	2016 Jul 25	288	8	9.1	144	16	10.6
	2018 May 15	192	8	26.8	180	8	27.3
HD 123247	2015 Apr 06	48	32	17.5	49	32	18.1
	2018 Mar 22	32	32	9.6	16	64	10.2
HD 133778	2016 May 16	320	8	91.3	160	16	97.8
	2017 Jun 22	256	2	28.5	136	4	30.7
HIP 76234	2016 May 07	144	16	34.0	72	32	35.6
	2018 Mar 17	64	16	13.5	32	32	14.4
HIP 76395	2016 May 03	144	16	53.0	72	32	56.1
HIP 82069	2016 Jun 04	320	8	21.0	160	16	25.5
	2017 Jul 15	512	2	14.0	396	2	15.5
HIP 81971	2016 May 17	80	32	20.9	80	32	22.5
HIP 85157	2016 May 01	160	16	13.3	44	64	17.7
HD 158815	2016 May 03	240	8	20.7	263	8	20.0
	2017 Jun 29	256	8	37.3	248	8	39.4
HIP 93542	2016 Jun 04	80	32	31.3	40	64	32.9
	2017 May 28	128	16	26.0	32	64	26.9
HIP 95619	2016 May 15	288	8	80.0	144	16	85.0
HIP 99892	2016 May 16	144	16	50.5	72	32	53.8
HIP 107585	2016 Jun 30	80	32	26.5	81	32	29.0

Table 4.2: VLT/SPHERE observations of each target. In each case, the listed exposure time refers to each individual science. Initial observations include ~35-45 minutes of integration, and followup observations are often shorter depending on the candidates we aim to redetect.

given in Appendix D and astrometry for each candidate at each epoch given in Appendix F.

4.4.2 Contrast curves

Contrast curves are calculated as detailed in Chapters 2 and 3: fake planets are inserted into each cleaned dataset at a variety of position angles, separations and magnitudes. A PCA reduction is then carried out, and the fake planets measured for reductions with a

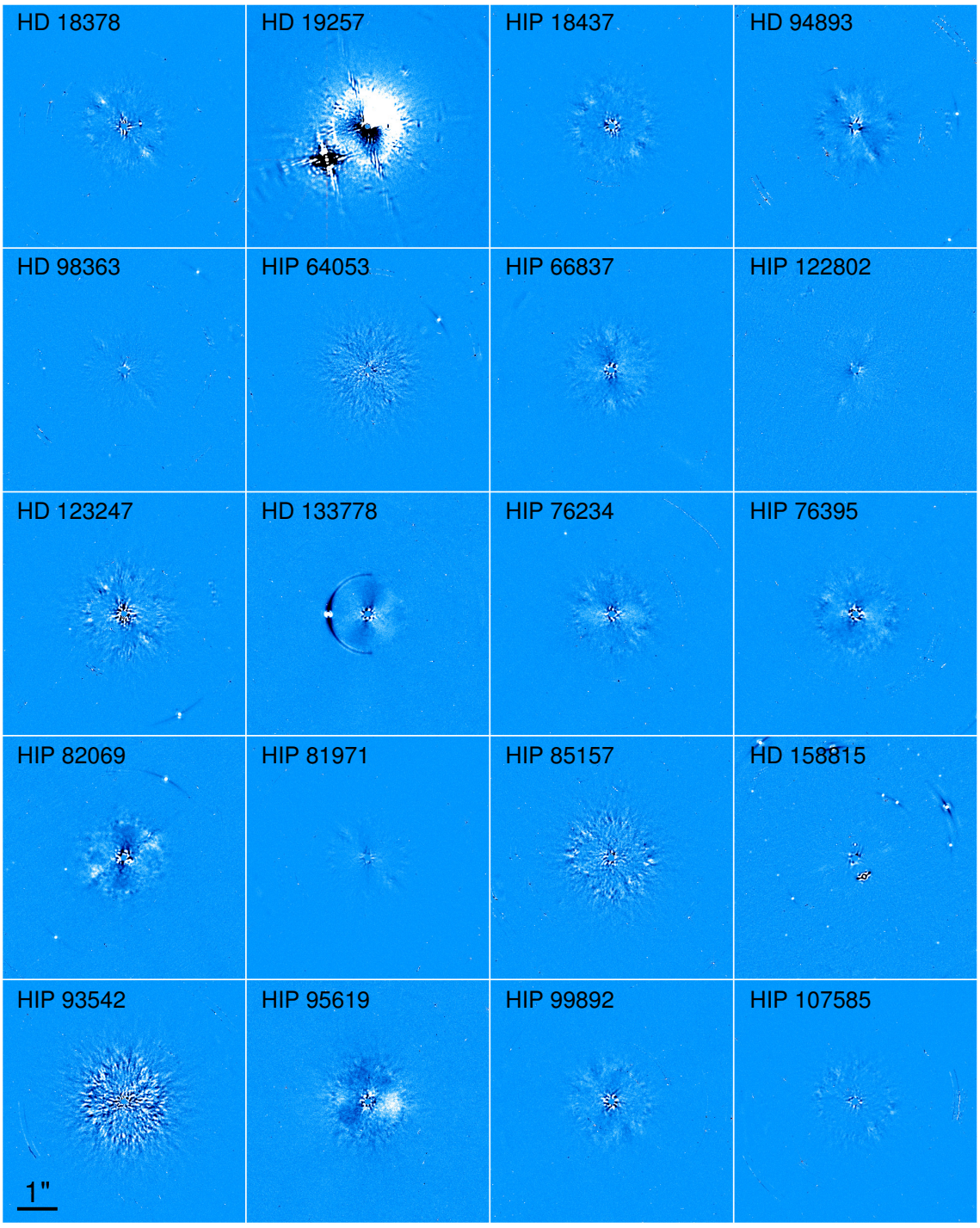

Figure 4.1: Thumbnail images of each of the targets in this survey. In each case, the central $6'' \times 6''$ of the field of view is shown, with North oriented up. This is the region where we expect the most exciting targets to be found. In this survey we find a total of 161 candidates companions, and do not detect any debris disks in scattered light.

range of numbers of modes subtracted, so as to ensure the best possible contrast is quoted. Additionally, the contrast correction term from Mawet et al. (2014) is applied.

In this survey we reach typical contrasts of 13.8 mag at 0.5″ with both subsystems,

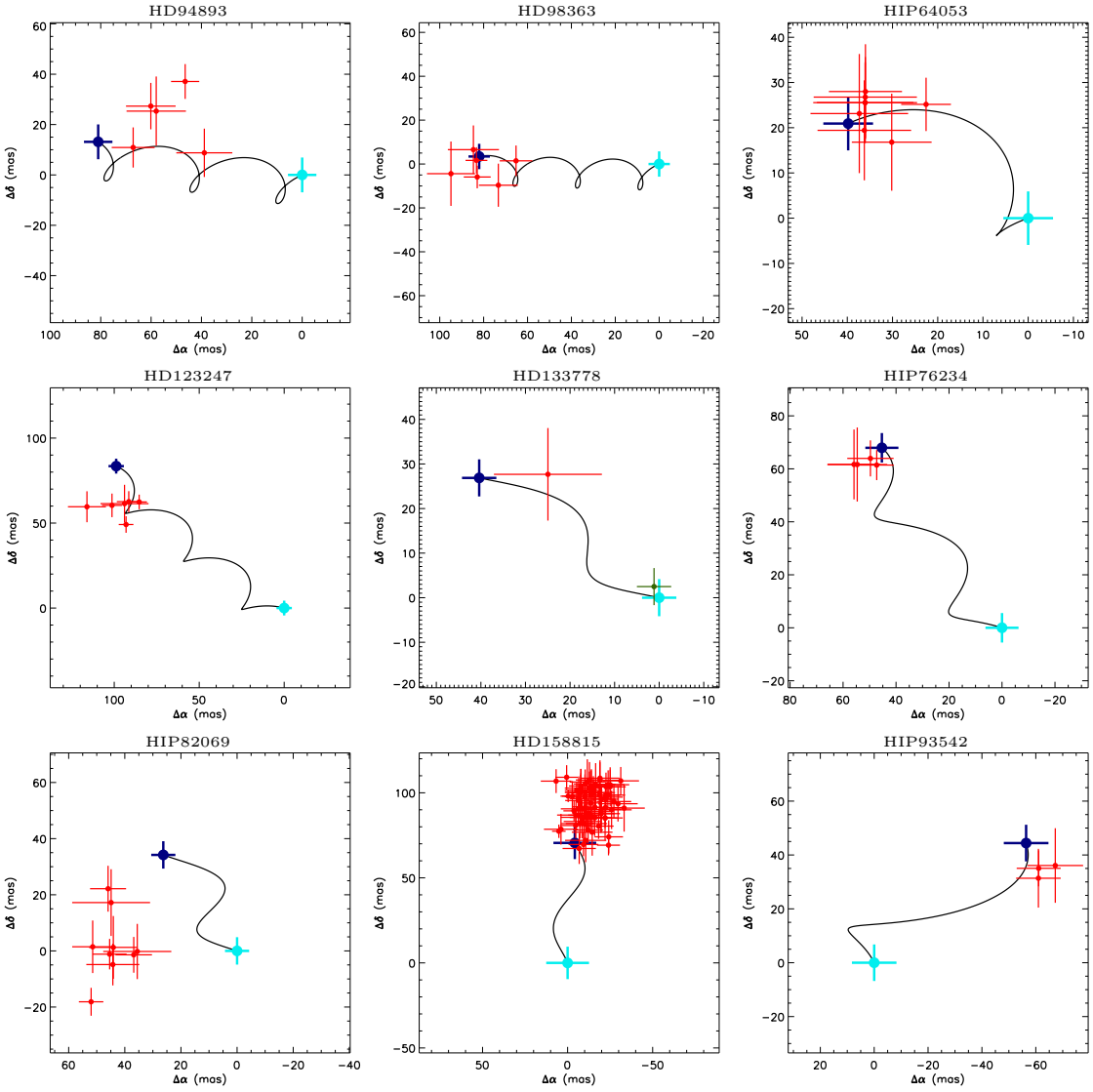

Figure 4.2: Combined common proper motion plots for the nine targets with two data epochs where we identify background objects. Not shown are the common proper motion plots for HD 18378 and HD 19257: for each of these targets we identify a single candidate and show that it is a companion, and common proper motion plots for these stars are given in Figures 6.10 and 6.11. Candidate companions are shown in red, while the confirmed companion to HD 133778. In all cases except for HIP 82069, we conclude that the objects are backgrounds, while for HIP 82069 there is a clear calibration error with the spread of data points being greater than the motion of the star between the two epochs. As such, these objects remain undetermined and more data is required. Individual common proper motion plots for each candidate are given in Appendix D, and astrometry is given in Appendix F.

and 15.4 mag in the wide field at a separation of 4″ with IRDIS. A plot of the median contrast of our survey is presented in Figure 4.3: for this plot we only include the first observation of each target, since subsequent observations often had shorter exposure times. For HD 98363, the first observation was taken in poor weather and at rank C, and so for this target we instead use the second observation, taken in better weather conditions, when calculating mean and best contrasts. Individual contrast curves for each initial observa-

tion are given in Appendix D, except in the case of HD 98363 where we also include the contrast curve of the follow-up observation.

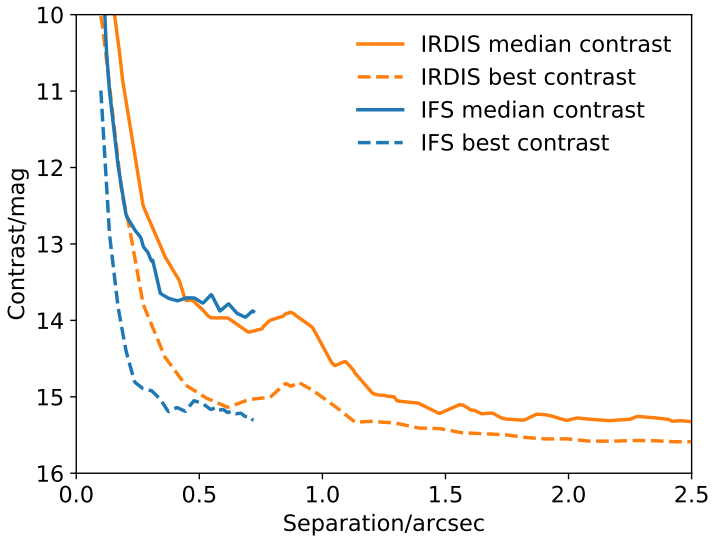

Figure 4.3: Median and best contrasts for initial observations in this survey, with the performance of the SPHERE/IRDIS subsystem given in orange and that of SPHERE/IFS in blue. Although the IFS slightly outperforms IRDIS in the very near-field, the instruments perform similarly beyond $\sim$ 0.5″. We reach typical contrasts of 13.8 mag with both systems at 0.5″

4.4.3 Individual Target notes

In this section we discuss the candidate companions to each target in the survey, and their designation as co-moving companions or background objects.

HD 18378: a single candidate is found, and confirmed to be co-moving. This object is discussed in detail in Section 6.5.

HD 19257: a single, bright candidate is found, and is likely a co-moving companion as discussed in Section 6.6.

HIP 18437: no candidate companions are detected for this target.

HD 94893: five candidates are detected. Although the motion of some of these candidates is discrepant with a stationary background, they all move significantly more than a companion would between out two epochs of data, and so we conclude they are all background objects.

HD 98363: this target was observed in poor weather in 2015, and six candidates detected. A follow-up observation in significantly better weather conditions was carried out in 2018. The six candidates from the 2015 observation were all recovered and confirmed to be backgrounds based on their proper motion, and an additional 12 candidates were detected. Further work is required to determine if any of these additional 12 objects are companions.

HIP 64053: eight candidates are detected, and all show good agreement with the background hypothesis between our two epochs of data.

HIP 66837: no candidate companions are detected for this target.

HD 112802: one wide separation candidate is margnially detected on the very edge of the detector, at a separation of 6.3″ from the host star. Both astrometry and photometry are biased this far from the target star, and so we do not include this candidate in our work.

HD 123247: six candidates are identified in two epochs of data, and common proper motion testing suggests that all of these candidates are background objects.

HD 133778: two candidates are detected, at 970mas and 5.2″. The close candidate is confirmed to be co-moving, and is discussed in detail in Section 6.4 and the wide separation candidate moves as a background object.

HIP 76234: four candidates are detected, and all move as stationary objects relative to the foreground star, and so are confirmed to be background stars.

HIP 76395: a single candidate is detected in one epoch of data, and further work is required to confirm if this object is a companion.

HIP 82069: This candidate is observed twice: twelve candidates are found in the first epoch and ten are recovered in a second epoch of data. As demonstrated in Figure 4.2, there appears to be some calibration issue and these motion of these candidates is discrepant with that of an infinite background object. Since the spread of candidate positions is larger than the expected motion of a background star, more work is required to determine whether any of these objects are companions.

HIP 81971: no candidate companions are detected for this target.

HIP 85157: no candidate companions are detected for this target.

HD 158815: this object is observed twice and 98 candidates are detected: 82 in both epochs, 14 only in the first epoch and 2 only in the second epoch. All of the candidates that are detected twice are clear background objects (see Figure 4.2), and further work is required to determine if any of the 16 candidates that are only detected once are companions.

HIP 93542: 3 candidate companions are detected, and all are clear backgrounds based on astrometry at two epochs of data.

HIP 95619: One candidate is detected. Since the target is only observed once, more work is required to determine if the candidate is co-moving.

HIP 99892: no candidate companions are detected for this target.

HIP 107585: no candidate companions are detected for this target.

4.5 Discussion

In this small survey of 20 targets, we have identified 3 wide binary systems (described in detail in Chapter 6). Although we have not performed a detailed statistical analysis, the fraction of binaries (~15%, bearing in mind that we have not searched for close, spectroscopic binaries) appears to be in broad agreement with previous works: Rodriguez & Zuckerman (2012) find that $25 \pm 4\%$ of debris disk systems are binary or triple star systems while Thureau et al. (2014) found similar rates of debris disk occurence around A-star with and without stellar companions ($26 \pm 7\%$ and $24 \pm 6\%$ respectively). These works both find a lack of binaries with intermediate separations between $1-100$ AU, and the three binaries discovered here are consistent with that finding, with projected separations of 99 ± 8 AU, 159 ± 2 AU, and 227 ± 3 AU.

In Chapter 3, three of the twenty-four disks were imaged (=13%), and we might expect similar results in this survey where targets were specifically selected to have the

highest volumes of circumstellar dust. For context, the three debris disks imaged in chapter 3 have W1-W4 excess of 2.893 ± 0.040, 2.628 ± 0.039 and 0.945 ± 0.073: although two of these are very bright, several objects in this survey have comparable brightness and most are brighter than the relatively faint HIP 63439 disk. We might expect some of the targets to be poorly oriented for high contrast imaging or have radii too small to be detectable, but would still expect at least some to be accessible in scattered light.

No planets are detected in this survey, although this result is in line with the relatively low occurrence rate of planets accessible to high contrast imaging. To probe the occurrence of planets in highly dusty systems, in future we will calculate an accurate occurrence rate combining these targets with other, similar surveys so as to create a sample sufficiently large that robust statistical conclusions can be drawn. A continuation of this work will generate a physically-motivated synthetic debris disk population with a high infrared excess, such that a selection of 20 objects drawn from this population would be consistent with the infrared excess of the targets in this work. Using estimates of the SPHERE sensitivity to diffuse disk structures we will ascertain if a detection of zero disk structures is consistent with the starting population of disks.

Chapter 5

Scattered Light Imaging of the HD 129590 Debris Disk

This chapter is based on the published paper "The First Scattered Light Image of the Debris Disk around the Sco-Cen target HD 129590" (Matthews et al. 2017)

5.1 Introduction

Observing the youngest stellar systems, shortly after planet formation has ceased, provides a glimpse of nascent circumstellar environments. However, only a small handful of stars ($\lesssim$3-5) with ages $\lesssim$10-20 Myr, just after dissipation of the gaseous primordial disc, are found within 100 pc (Sacco et al. 2014). The Scorpius Centaurus Association (de Zeeuw et al. 1999, hereafter Sco-Cen) is the nearest OB2 association, with a mean distance of 140 pc, making it perhaps the most promising collection of young stars which can be observed shortly after the period of active planet formation. This region, containing stars with ages ~ 10-16 Myr (Pecaut & Mamajek 2016) allows the best constraints to be placed on the orbital zones of planet formation, and on the early thermal histories of young planets (Ireland et al. 2011; Janson et al. 2013a; Lafrenière et al. 2014; Hinkley et al., 2015b).

Furthermore, such young systems often possess bright circumstellar debris disks,

belts of planetesimals analogous to the Edgeworth-Kuiper belt in our own solar system. The presence of dust in these systems suggests that planetesimals are responsible for the dust generation (Wyatt 2008). The dust that is generated through planetesimal collisions in these debris disks is inherently transient, being either blown out by stellar winds, or spiralling towards the host star via Poynting-Robertson drag. The persistence of dust in these systems implies that it is constantly being regenerated. Although populations of planetesimals may stir themselves in some cases (e.g. Kennedy & Wyatt 2010), this dust regeneration may be enhanced by perturbations from massive planets, dynamically exciting the planetesimals onto eccentric orbits, thus causing them to collide. As well as revealing the presence of massive planetary perturbers, the location of these large quantities of dust may hint at the location of giant planets in the system: gaps between dust belts may highlight where planets lie (Su & Rieke 2014), and sharp edges to debris rings can constrain the masses of planets shepherding these edges (e.g. Quillen 2006; Chiang et al. 2008; Mustill & Wyatt 2012).

One Sco-Cen system with a known circumstellar debris disk is HD 129590 (HIP 72070, T_{eff} = 5945 K, 1.3 $M_{\odot}$ 2.8 $L_{\odot}$, Chen et al. 2011). While not originally catalogued in the de Zeeuw et al. (1999) or Rizzuto et al. (2011) catalogs of Sco-Cen stars, HD 129590 has been listed as a G1V member of the Sco-Cen subgroup Upper Centaurus Lupus (Hoogerwerf 2000; Chen et al. 2011). HD 129590 has an estimated distance of 141±7 pc (Astraatmadja & Bailer-Jones 2016; Gaia Collaboration et al., 2016a; Gaia Collaboration et al., 2016b) and a high infrared luminosity L_{IR}/L_{star}~5×10^{-3}, twice the value observed for β Pictoris (Jang-Condell et al. 2015; Mittal et al. 2015), as can be seen in Figure 5.1. Although Chen et al. (2014) fit the SED as two distinct belts, Jang-Condell et al. (2015) suggest the system likely contains a single belt of dust. This is in agreement with the predictions of Ballering et al. (2013) (see Section 5.4.1 for further details).

The high fractional luminosity of HD 129590 makes it an extremely promising target for scattered light imaging of circumstellar material (Currie et al. 2014; Draper et al. 2016). ALMA data have previously been obtained for this object (Lieman-Sifry et al. 2016), with the disk being marginally resolved along the major axis. Lieman-Sifry et al. (2016) constrain the inclination angle to $> 50^{\circ}$ with a best fit value of 70°, and the position angle to

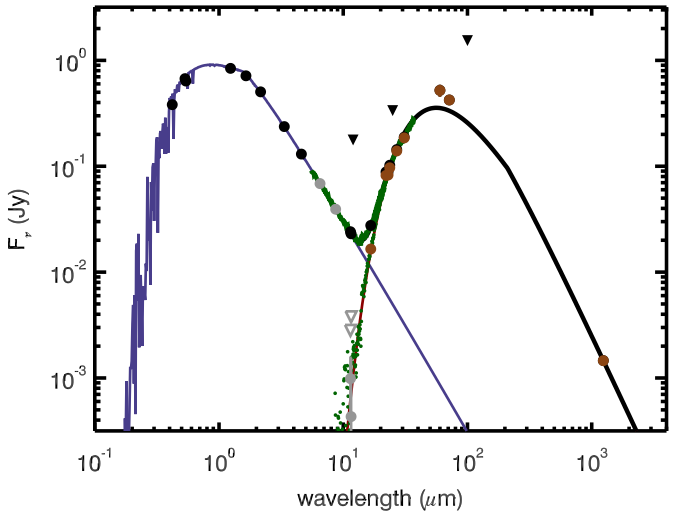

Figure 5.1: Spectrum of HD 129590. Black dots show photometry from *Hipparcos*, 2MASS, WISE, IRAS, *Spitzer* and ALMA (Høg et al. 2000; Cutri et al. 2003; Wright et al. 2010; Helou & Walker 1988; Chen et al. 2014; Lieman-Sifry et al. 2016). Triangles show IRAS upper limits, and small green dots show the *Spitzer* IRS spectrum. The lines show a 5850K PHOENIX stellar model (blue, Brott & Hauschildt 2005) and a 91K modified blackbody (black). Brown and green dots show star-subtracted measurements (which cover the black dots in some cases). Grey open triangles indicate where star-subtracted values are consistent with zero.

-59^{+17}_{-12} °. The ALMA data finds a best-fit grain size of $3.2^{+0.6}_{-0.5}$ μm, and at this size find the outer edge to be 110^{+50}_{-30} AU and the inner edge to be < 40 AU. No gas was detected in that work, and so we do not expect gas to have a strong influence on the dust dynamics in this disk.

In this letter, we present the first scattered light image of the debris disk around HD 129590, using the SPHERE instrument on the VLT. The observations and data post-processing are presented in Section 5.2 and Section 5.3 respectively. In Section 5.4 we describe our modelling of the disk, where we use an optically thin disk model to conclude that the disk has a radius of $\sim$ 60-70 AU. Finally, we conclude in Section 5.6.

5.2 Observations

HD 129590 was observed on 2016 May 4 with the SPHERE instrument at the VLT (Beuzit et al. 2008), as part of a larger planet-finding survey within Sco-Cen. The data were taken in the IRDIFS mode, whereby light is split through a dichroic beamsplitter, and passed simultaneously to both the differential imager and spectrograph instrument (IRDIS; Dohlen et al. 2008), and the integral field spectrometer (IFS; Claudi et al. 2008). A total of 2560s

on-sky integration was collected by each instrument, with the `N_ALC_YJH_S` coronagraph in place. The sequence consisted of 80×32s individual exposures for the IRDIS data and 40×64s exposures for the IFS data. We used IRDIS in dual-band imaging (DBI; Vigan et al. 2010) mode with the H23 filter pair, at wavelengths $\lambda = 1588.8$ nm, $\Delta\lambda = 53.1$ nm and $\lambda = 1667.1$ nm, $\Delta\lambda = 55.6$ nm, while the IFS instrument (Zurlo et al. 2014; Mesa et al. 2015b) was used in the `YJ` mode, which spans the range 0.95-1.35 μm. Platescales of the instruments are 12.25 mas/pix for IRDIS and 7.46 mas/pix for the IFS (Maire et al. 2016), and the inner working angle of the coronagraph is 0.15".

In addition to these science observations, flux calibration images were collected with the target displaced from the coronagraph. Star center calibration frames (waffle frames) were also collected, by imposing a sinusoidal pattern on the deformable mirror. This creates four starspot images, with equal displacements from the central star, in each corner of the frame. Together, these allow the star position to be accurately measured to ~0.1 pixels (1.2 mas) (Vigan et al. 2016) behind the occulting mask. The observations were carried out in pupil-stabilized mode to allow angular differential imaging analysis (ADI; Marois et al. 2006). The entire sequence of observations, including acquisition and calibration, lasted 59 minutes spanning an airmass range of 1.037 to 1.042. The primary science frames covered a total field rotation of 36 degrees, and included the meridian crossing of the target.

5.3 Data Post-Processing

Our data post-processing was carried out following the process described in Vigan et al. (2015). We used both the ESO data reduction and handling pipeline (DRH, Pavlov et al. 2008) and the publicly available code described in Vigan et al. (2015), as well as some custom routines.

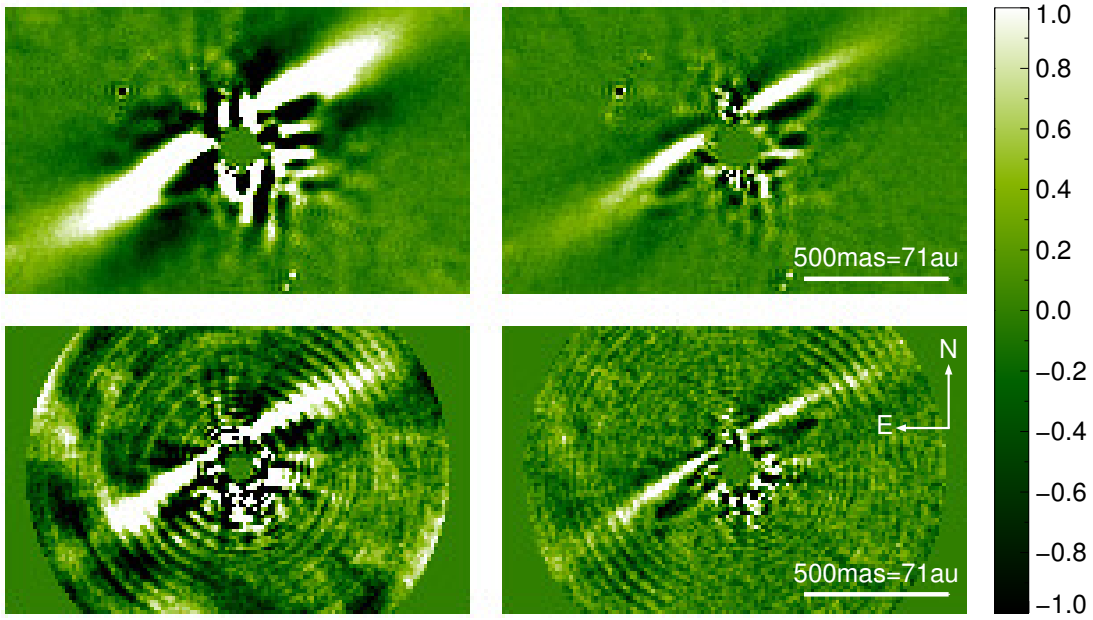

Figure 5.2: SPHERE detections of a scattered light debris disk around the target HD 129590. Data from the IRDIS (1.6 μm) and IFS (0.95-1.35 μm) subsystems are shown on the top and bottom rows respectively. In each case, the image is a co-add of the entire wavelength range of the subsystem. The left hand images have 6 principal components subtracted, while on the right hand side a more aggressive reduction is presented, where 20 principal components have been removed. In both cases, the reduction is full-frame treatment, where the entire field of view is considered simultaneously. The ringed structure observed in the IFS images is an artifact of the fast Fourier transform process used to rescale the various wavelength observations.

5.3.1 IFS

For the IFS data, basic calibrations were first created using the DRH: dark fields, master flat-fields, IFS spectra positions, initial wavelength calibrations and an IFU flat were all generated. We then used a custom routine to calculate an accurate parallactic angle and time for each image, and to normalise the data based on its exposure time. Bad pixel and cross-talk corrections were also applied. The DRH was then used to interpolate these frames both spectrally and spatially. A sigma-clipping routine was applied to remove remaining bad pixels which deviated from their neighbours by more than 3.3σ. Finally, the wavelengths for each image were recalibrated, due to small systematic errors in the DRH pipeline, as described in Chapter 2. This process results in a set of calibrated images in the x-y plane, at 39 wavelengths spanning 0.95-1.35 μm and at 40 distinct timesteps. No

frame selection was performed, although each individual frame was visually inspected to confirm there were no data issues.

Speckle subtraction was performed using a custom PCA code (e.g. Soummer et al. 2012; Amara & Quanz 2012). This code simultaneously uses the spectral and temporal (parallactic angle) diversity of speckles to remove starlight scattered within the image plane by the telescope optics, but not genuine astrophysical sources. A disk feature was revealed, as shown in Figure 5.2. We tested reductions with between 2 and 100 principal components subtracted, and the feature is robust to the number of principal components removed.

5.3.2 IRDIS

Initial pre-processing of the IRDIS data was performed using the ESO SPHERE pipeline. Master dark and flat frames were created, and a waffle frame was used to calibrate the position of the star centers. Each frame was then independently reduced by applying the master dark and flat frames, and realigned using the star center calibrations and the dither positions so that the central star position was consistent between images.

The 160 individual images (80 timesteps, 2 wavelengths) were then input into a PCA algorithm (e.g. Soummer et al. 2012; Amara & Quanz 2012) to remove stellar speckle noise. For this process we used a custom code, described in Chapter 2. A clear disk feature was observed, as demonstrated in Figure 5.2. This disk feature closely matches that observed in the IFS data. As with the IFS data, we tested a range of reductions with between 2 and 100 principal components removed and found the disk feature to be robust.

5.4 Disc Structure & Modelling

5.4.1 SED fitting

The infrared excess of HD 129590 is well-studied. Ballering et al. (2013) fit a single cold dust component at a temperature of 89 K, while Jang-Condell et al. (2015) find a best fit with

grain temperature 93.7±0.1K. Chen et al. (2014), however, fit two separate components at 94 K and 72 K. The evidence for the second, cold belt comes from a single photometric point at 70 μm (see SED in Figure 5.1), which might be equally well explained by a dust model that is more complex than a simple blackbody. We conclude that the SED is best and most simply described by a single blackbody, with a best-fit temperature of 91 K (and radius 16 AU assuming blackbody absorption/emission). Small dust grains emit poorly at wavelengths significantly longer than their physical size, which we parametrise by modifying our blackbody fit by a factor $(210\mu\text{m}/\lambda)^{\beta}$ at wavelengths longer than 210μm (Wyatt 2008). This extra parameter is required by the ALMA observations, and $\beta = 0.5$ yields the best fit.

5.4.2 Spatial Constraints

The debris disk is highly symmetric in both the IFS and the IRDIS data. In the IRDIS data, there is a clear dark hole within 0.32″ of the star. The brightest emission extends to 0.67″, but there is evidence of extended emission as far as 1.03″ from the star, in line with the debris disk. Both lobes of the disk can be clearly seen. The disk signal in the IFS data is fainter, with only the front lobe visible. This has a spatial extent of 0.57″. As in the IRDIS data, there is extended, faint emission to the edge of the the field of view (0.87″).

5.4.3 Disk Modelling

We then use injection modelling to characterise the disk more rigorously. We choose to take a Bayesian MCMC fitting approach, as performed in Wahhaj et al. (2014).

Synthetic disk images are created using the GRaTeR radiative transfer code (Augereau et al. 1999).GRaTeR uses a parametric approach, assuming an axisymmetric grain density $n \propto R(r)Z(r,z)$, with $R(r)$ and $Z(r,z)$ the radial and vertical distributions respectively. The vertical distribution is chosen to have an exponential falloff with height, following Artymowicz et al. (1989), while the radial distribution is a smooth combination of two power laws: this represents a peak dust density at a chosen radius, which smoothly falls

off in either radial direction. The density is defined as:

$$\rho = \frac{\rho_\circ \exp\left(\left[\frac{-|z|}{\xi_\circ}\left(\frac{r}{r_\circ}\right)^{-\beta}\right]^{\gamma}\right)}{\sqrt{\left(\frac{r}{r_\circ}\right)^{-2\alpha_{\text{in}}} + \left(\frac{r}{r_\circ}\right)^{-2\alpha_{\text{out}}}}} \tag{5.1}$$

where r is the radial distance from the disk center, z is the vertical distance from the disk midplane, and $\rho_\circ$, α_{in}, α_{out}, $\xi_\circ$, β and γ are free parameters. The exponential term defines the disk vertical profile, while the denominator expresses a radial profile which rises as α_{in}, peaks at $r_\circ$ and then falls as α_{out}.

At each point in the disc, the scattered light contribution is calculated as:

$$F \propto \frac{\rho \times \mathrm{p}(\theta)}{d^2} \tag{5.2}$$

where θ is the scattering angle, namely, the angle through which light from the star is scattered so that it reaches the Earth. d is the distance from the star to the grid point. The measured flux is influenced by several factors, such as the stellar luminosity, stellar distance and the telescope gain. We fold these into a single overall normalization by modifying the $\rho_\circ$ parameter and denote this updated parameter as $\rho'_\circ$.

The phase function, $\mathrm{p}(\theta)$, is the standard Henyey-Greenstein scattering function:

$$\mathrm{p}\left(\theta\right) = \frac{1}{4\pi}\frac{1-g^2}{\left[1-2g\cos\theta+g^2\right]^{\frac{3}{2}}} \tag{5.3}$$

Since we assume an optically thin disc, scattered light contributions are added along each line of sight to create a synthetic disk image.

These synthetic images were convolved with a Gaussian to mimic the effects of the point spread function. Each model in turn was then rotated and subtracted from each frame of the raw IRDIS data, and the PCA sequence was repeated with six modes subtracted to generate a residual image. By injecting negative disk images, we accurately

take into account the throughput of the PCA post-processing, which varies with separation from the star. This process is akin to a forward modelling procedure. In the interests of computational efficiency, we use only a subset of the data for our modelling: images are trimmed to the central 240×240 pixels (~3″), and only every fourth individual exposure is included.

The goodness of each model is assessed using the normal χ^2 statistic: each pixel in the residual image is divided by its local sigma value and squared. Values for σ are calculated as in Wahhaj et al. (2014): we first convolve the PCA processed image of the disk with a Gaussian with FWHM of 2 pixels. This is then subtracted from the image to remove extended spatial components, to leave an image containing only noise information. The rectangular test region is divided into annuli, and in each annulus the standard deviation of the noise image is found, so as to capture the variance of noise with distance from the star. As noted in Wahhaj et al. (2014), some disc signal still contributes to the standard deviation. This is inevitable, and will lead to conservative error calculations on our parameters.

We initially use a downhill minimization routine to find a best fit. We then use these best fit parameters to initiate a Metropolis Hastings MCMC, using the `emcee.py` package (Foreman-Mackey et al. 2013). The MCMC chain generates a sampling of our parameters space, with probabilities assigned as $\exp\left(\frac{-\chi^2}{2}\right)$. We use uniform priors in this work. 510,000 random samplings are generated for each fit, and the first 10,000 are discarded to ensure that the results are independent of our starting position. The best fit and error values are calculated from the remaining 500,000 samples. For each parameter, the best fit given by the median value of the marginalized distribution and the 1-σ uncertainties chosen to enclose 34% of the samples on either side of the median. In addition, we calculate the best fit parameters for each third of the random samplings, and find them to be consistent. This confirms that the initial parameters do not affect the results, and that they are a genuine sample of the probability distribution.

We initially fit a single ring of dust. For this model, we have five free parameters: the overall scaling of the model $\rho'_\circ$, the forward scattering parameter g, the radius $r_\circ$, the inclination angle and the position angle of the disk. We fix the radial profile to $\alpha_{\rm in} = 3.5$

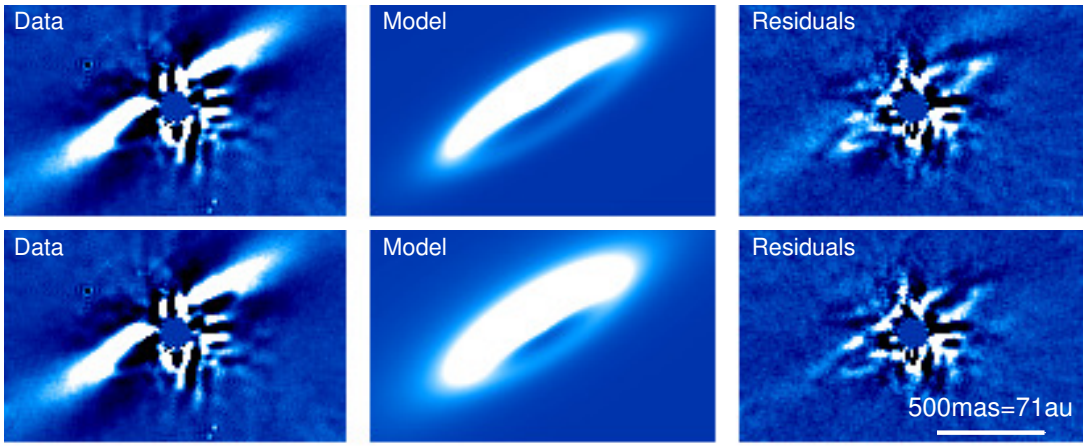

Figure 5.3: *Top:* The initial debris disk fit, where the Henyey-Greenstein parameter g, the disk radius, and the position and inclination angles of the disk have all been allowed to vary. A residual halo of light is observed. *Bottom:* Here the parameter $\alpha_{\rm out}$ has also been allowed to vary. As such, the residual halo is better modelled. Fit parameters for both models are given in Table 5.1. In both cases, IRDIS data is shown with 6 PCA modes subtracted.

and $\alpha_{\rm out} = -3.5$ and fix the stellar distance to 141 pc. The parameters defining the vertical profile, namely $\xi_\circ$, β and γ, are fixed to values of 1, 0 and 2 respectively.

This fit is presented in the top row of Figure 5.3 with parameters shown in Table 5.1. The residual image for this model shows a clear halo outside the ring, and as such we fit the data again, but this time we also fit the values of $\alpha_{\rm in}$ and $\alpha_{\rm out}$. The best fit in this case is a smaller ring, with softer power law edges - most notably on the outside, where $\alpha_{\rm out} = -1.313^{+0.011}_{-0.012}$. This is a surprisingly low value: Thébault & Wu (2008) find typical cases of either "smooth edges" with $\alpha_{\rm out}$ -3.5, or "sharp edges" with $\alpha_{\rm out}$ as steep as -8. This second fit is shown in the lower panel of Figure 5.3, with parameters given in Table 5.3. For both of these models, the Henyey-Greenstein parameter takes a relatively high value (0.52 and 0.43, respectively). Although it has been shown for cases with a wide range of viewing angles that a single component Henyey-Greenstein parameter gives a poor fit (Stark et al. 2014; Hedman & Stark 2015), the geometry of HD 129590 means that this parameter is poorly constrained: the faint edge is severely affected by speckle noise, meaning backscattering is hard to constrain.

There is some residual structure that we are unable to model with GRaTeR. In particular, we find no notable improvement in the fit when we vary the disk eccentricity or offset from the star, and the data do not place meaningful constrains on the vertical fit

Parameter	Fit 1	Fit 2	ALMA*
$\rho'_\circ$	1.106 ± 0.006	1.440 ± 0.008	
g	0.522 ± 0.002	0.4272 ± 0.0012	
$r_\circ$[AU]	73.3 ± 0.2	59.3 ± 0.2	
i_{tilt}[°]	76.87 ± 0.05	74.56 ± 0.05	> 50
PA[°]	121.58 ± 0.02	121.80 ± 0.02	121^{+17}_{-12}
α_{out}	-3.5	$-1.313^{+0.011}_{-0.012}$	
α_{in}	3.5	3.15 ± 0.03	
$\xi_\circ$	1	1	
β	0	0	
γ	2	2	
$d_{star}[pc]$	141	141	

Table 5.1: Fit parameters for the two disk models in Figure 5.3.
Note: Values for $\rho'_\circ$ are relative. PA is measured anti-clockwise of North. *ALMA fit parameters are taken from Lieman-Sifry et al. (2016) and converted to our reference system.

profile. Our position angle is in very good agreement with that found by Lieman-Sifry et al. (2016) with ALMA observations, namely $121^{+17\circ}_{-12}$, and our inclination angle is within the ALMA constraints.

5.5 Discussion

The latest generation of dedicated high resolution exoplanet imaging platforms such as GPI and SPHERE has already revealed a number of scattered light debris disc images. Sco-Cen has proved to be a particularly fortuitous region for these searches. Currie et al. (2015b) detected a dust ring around HD 115600, which was shown to be eccentric. HD 110058 has a wing-tilt asymmetry (Kasper et al. 2015), while HD 106906 appears to be misaligned with the wide planetary companion (Kalas et al. 2015; Lagrange et al. 2016). HD 111520 (Draper et al. 2016) has a dramatic brightness asymmetry, while both HIP 67497 (Bonnefoy et al. 2017) and HIP 73145 (Feldt et al. 2017) have been shown to have multiple, separate, rings of debris. Perhaps the only debris discs without complex morphology are HD 114082 (Wahhaj et al. 2016) and HD 129590.

All of these debris discs are presented in Chen et al. (2014) as hosting multiple dis-

tinct debris belts. Multiple debris belts have only been seen in scattered light around two of the above targets: either there are several very small, close in belts of disc evading detection, or two temperature discs correspond to two belt discs less often than expected. Additionally, all of the targets with debris disc images have very high excess infrared luminosity values, and all except HIP 67497 have been observed with ALMA (Lieman-Sifry et al. 2016).

As discussed in Section 4.1, the debris belt around HD 129590 is predicted to lie at ~16 AU, based on the infrared excess temperature and simple blackbody constraints. Our observations show the ring to peak at ~4 times this separation, implying an abundance of small dust at higher temperatures than the blackbody temperature. This is to be expected for a luminous star (2.8 $L_{\odot}$) where the blowout size is a few microns.

We attempt to classify HD 129590 under the categories outlined in Lee & Chiang (2016). The pronounced difference in brightness between the front and back of the disk is reminiscent of the 'moth' or 'double wing' structures simulated in that work, but we do not observe the bright, extended wings seen in e.g. HD 61005 (Hines et al. 2007). A strongly forward-scattering disk could produce only a fainter wing structure, as light will be preferentially scattered away from the viewer. In addition, an ADI based code such as that used here will self-subtract flux in regions at small angular separations to the bright disk edge, and so hide faint wing structures nearby. In Figure 5.4 contours of equal brightness are plotted, to demonstrate the full dynamic range of the disk. There is no indication of an extended wing, and indeed the self-subtraction lobes (highlighted in red in the image) show a high degree of symmetry. As such, there is no evidence for moth-like wings and it is not possible to make detailed inferences about the presence, or otherwise, of a planet in this system.

Our modelling work highlighted the presence of extended emission, at large semi-major axis. This could be a dust halo, caused by radiation pressure blowing out small grains. Alternatively, this may be a scattered disk of planetesimals, and as such more closely resemble the wings mentioned above - albeit much more compressed into the plane than Lee & Chiang (2016) find. Such a ring of planetesimals might explain our surprisingly low value for $\alpha_{\rm out}$. A higher resolution ALMA image could differentiate these two

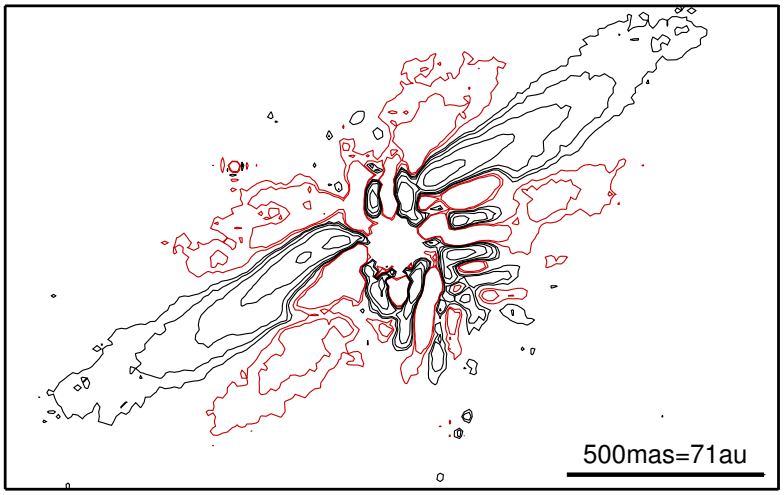

Figure 5.4: The data shown in the top left panel of Figure 5.2, but presented as a contour plot. Contours have relative brightness values of 1, 2, 4, 8 and 16, while negative contours are plotted in red, with relative flux -1 and -2. The self-subtraction wings above and below the bright ring edge are clearly visible. No attempt has been made to take the throughput of the PCA routine into account in this plot.

scenarios, while future imaging with a space facility such as the Hubble Space Telescope would allow the lowest surface brightness material (such as a dust halo) to be imaged, as well as defining the outer disk edge far better than ground based AO imaging. Polarimetric differential imaging, meanwhile, would place constraints on the dust grain size and scattering properties, and may even reveal the faint edge of the disc.

5.6 Conclusion

HD 129590 is a G1V member of the Sco-Cen association, with an infrared excess twice that observed for β Pictoris. This work presents the first scattered light images of the debris disk responsible for this infrared excess. The debris disk is revealed to be a nearly edge-on disk, with evidence for inner clearing. We use the GRaTeR radiative transfer code to model the disk as an optically thin ring, inclined to the line of sight by $\sim 75°$. Our best fitting model has a characteristic radius of $r_\circ$=59.3 AU or $r_\circ$=73.3 AU depending on the underlying model, and a forward scattering parameter g=0.52 or g=0.43. When the power law edges were freed, these were found to take values of 3.15 inside the ring and -1.313 outside the ring. These values imply a strongly forward scattering ring, with a soft outer edge. Even with this model, there is an indication in the final panel of Figure 5.3 of

some residual structure, implying that there is some morphology more complex than a simple ring present in this disk.

Chapter 6

Additional Discoveries

The two surveys detailed in Chapters 3 and 4 have uncovered a number of new disks and companions, which are described in more detail here.

In Chapter 3, we described a survey of targets hosting two-belt debris disks. Three of these debris disks were revealed in scattered light: HD 129590 (Chapter 5), and two additional debris disks presented here (HIP 67497 and HIP 63439, see Sections 6.1 and 6.2 respectively). We also establish for the first time that another survey target, HD 223352, is a member of a quadruple star system rather than a tertiary system as previously published, and that two of the four stars show evidence for circumstellar dust (Section 6.3).

In Chapter 4, meanwhile, we surveyed the dustiest targets identified with WISE. In this survey we detected three companions: two mid-M type objects (HD 133778B and HD 18378B, see Sections 6.4 and 6.5) and a stellar binary system HD 19257AB (Section 6.6).

6.1 HIP 67497: a scattered light debris disk image with evidence of multiple belts

HIP 67497 (HD 120326) is a nearby Sco-Cen target at a distance 113.9 ± 1.5pc (Lindegren et al. 2018). The target is a member of the Upper Centaurus Lupus (UCL) region of Sco-Cen

with age 16 ± 1 Myr. We observed HIP 67497 as part of our survey of multi-belt targets (Chapter 3) on 2016 Jun 04, and our processed data shows the debris disk in scattered light (see Figure 6.1). The target has a significant infrared excess and was found to have two debris temperatures in Chen et al. (2014), who find disk temperatures of 127 ± 5 K and 63 ± 5 K, corresponding to radii of 33^{+3}_{-2} AU and 134^{+24}_{-19} AU (converted using the "50% astrosilicate + 50% ice" dust composition given in Pawellek & Krivov 2015). Jang-Condell et al. (2015) offer an alternative fit of the disk as a single debris belt, with temperature 124 ± 0.4 K and radius 8.82 ± 1 AU.

The same target had been observed two months earlier on 2016 Apr 6 by another team, with SPHERE/IRDIFS and using a very similar observational setup to us. That team observed the same scattered light disk emission as we did, and published the detection as Bonnefoy et al. (2017). Their work notes the presence of two features in the disk image: a main "ring" with a visual extent of ~ 450mas (~ 50 AU) and a faint "arc" feature to the south of the ring, with a visual extent of ~ 650mas (~ 70 AU). Both of these features are visible in our data, and our images are presented alongside those of Bonnefoy et al. (2017) in Figure 6.1.

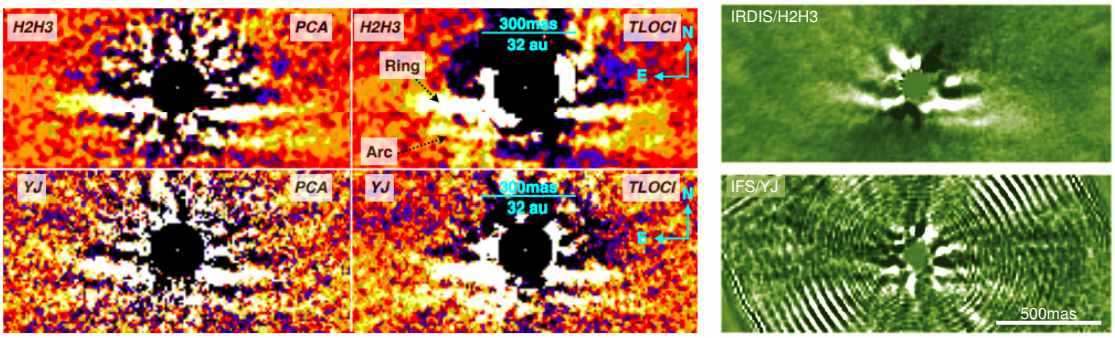

Figure 6.1: Scattered Light Images of the HIP67497 debris disk. *Left:* The reduction presented by Bonnefoy et al. (2017). IRDIS (H2H3) and IFS (YJ) images are shown, with two alternate reduction procedures (PCA and TLOCI) used and the same disk structure observed in both cases. The disk shows a prominent ring visually extending to ~ 50 AU and a fainter "arc" structure to the South of this ring, with a visual extent ~ 70 AU. *Right:* PCA processed data from our program, with the top and bottom panels showing the IRDIS and IFS data respecitvely. These data closely match the disk features of Bonnefoy et al. (2017), with both the main "ring" and faint "arc" feature visible in the data.

Bonnefoy et al. (2017) model the disk using GRaTeR (Augereau et al. 1999), and model the main disk feature (the "ring") with a peak radius $r_0 = 58.6 \pm 3$ AU and a forward scattering parameter g of 0.82 ± 0.02. This modelling is carried out using a similar negative injection technique to the one we used to model HD 129590 (described in Chapter 5), where

a disk model is subtracted from the raw data which is then re-processed and the residual image measured. The "arc" feature still appears in the residual images, confirming that this is a real feature and not a product of self-subtraction effects in the data. Bonnefoy et al. (2017) offer two interpretations of this arc: either a second sharp ring of dust (with $r_0 = 130 \pm 8$ AU), or a smooth halo of dust with a very soft power law. The model with a second ring of dust is slightly preferred.

The observation that this target does appear to host two belts of dust validates our assumption in Chapter 3 that these two-temperature disks do indeed correspond to two belts of dust in most cases. While it is not conclusive, the close agreement between the predicted radius of the outer belt (134^{+24}_{-19} AU) and that observed by Bonnefoy et al. 2017 (130 ± 8 AU) is certainly a good sign that our interpretation of these two-temperature disks is accurate, and the corresponding lower limits placed in Chapter 3 are valid.

6.2 HIP 63439: a very faint scattered light image of a debris disk

HIP 63439 (HD 112810, F4IV/V, $T_{\rm eff} = 6750$ K, 1.4 $M_\odot$, 3.5 $L_\odot$, Chen et al. 2011; Chen et al. 2014) is a member of the Lower Centaurus Crux (LCC) region of Sco-Cen with age 17 ± 1 Myr and distance 135 ± 5pc (de Zeeuw et al. 1999; Pecaut et al. 2012; Gaia Collaboration et al., 2016a; Gaia Collaboration et al., 2016b). The star has an infrared excess $L_{\rm IR}/L_\star \sim 1 \times 10^{-3}$, with both Chen et al. (2014) and Ballering et al. (2013) finding clear evidence that the debris is best fit with two distinct temperatures. As described in Chapter 3, five candidate companions to HIP 63439 were detected, with all five at projected separation >3.5"and classified as likely background objects.

We detected a debris disk around HIP 63439 in scattered light, at very low signal-to-noise (see Figure 6.2). This target was observed three times with SPHERE by different teams during the spring of 2016, and the disk is visible in two of the three IRDIS datasets, and none of the three IFS datasets. Since the observational setup (filters, integration times) is similar for each observation, it is likely that the disk is unobserved in the third dataset due to the slightly worse weather and the inherently low surface brightness of the disk.

The two disk detections are presented in Figure 6.2, with details of all three observations given in Table 6.1.

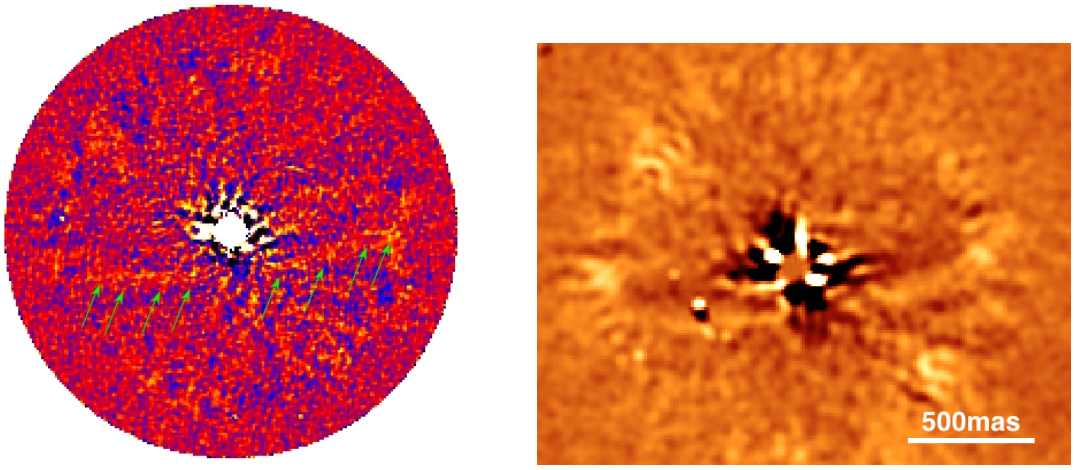

Figure 6.2: Datasets revealing a scattered light image of the HIP 63439 debris disk. Both images show the H2+H3 IRDIS data, with PCA applied. *Left:* data collected by B. Ménard and reduced by M. Bonnefoy (priv. comm.). The disk is indicated with green arrows. *Right:* Our data, my own reduction. See Chapter 2 for details of our data reduction process.

	Olofsson	Hinkley	Ménard	Planned
Date	2016-03-03	2016-05-02	2016-05-16	———
Filter	D_H23, YJ	D_H23, YJ	D_H23, YJ	BB_H, YJ
IRDIS DIT [s]	64	32	32	32
IRDIS N_{img}	32	80	128	224
IFS DIT [s]	64	64	64	64
IFS N_{img}	32	40	64	112
T_{total} [s]	2048	2560	4096	7168

Table 6.1: Planned and executed SPHERE observations of HIP 63439. Observations are denoted by the PI of each program, with the disk appearing in the Hinkley and Ménard observations. The DIT is the exopsure time per image, and T_{total} is the total integration time observed by each subsystem.

The debris disk appears as a clear, sharp ring in the data. By assuming a narrow, circular ring of dust we find the disk to be at a radius ~ 930mas or 125 AU, and to have an inclination of 14.5° from edge-on. The best fit temperatures of Chen et al. (2014) suggest radii of $7.6^{+0.4}_{-0.3}$ AU and 156^{+24}_{-28} AU for the two belts, and so the ring we observe is a good match for the outer, cold debris belt.

6.2.1 Future observations

We plan to collect further SPHERE/IRDIFS observations of HIP 63439, tailored specifically towards disk characterisation and with a significantly improved signal-to-noise. These

observations were accepted for execution during the spring of 2017 (prog. ID 099.C-0237, PI Bonnefoy) at rank B, but not executed due to weather conditions and pressure on the telescope. The proposal has been resubmitted and accepted for execution during 2018 (prog. ID 0101.C-0016, PI Bonnefoy).

These data will be collected over ~2.5 hours, using the IRDIFS mode with the IRDIS instrument observing in the broadband H filter (BB_H) and the IFS observing in YJ mode. The IRDIS data will allow a significantly improved disk image for two reasons: firstly, the broadband H filter has 5.4 times the bandpass of the previously used H23 filters, and secondly the observation block is more than twice the length of our previous observation, with a planned on-sky integration time of 7168s in each subsystem. This much longer integration time will allow a deeper observation, and a more aggressive selection of the best frames during data reduction to improve the subtraction of speckles. We will additionally take immediate sky background calibration frames: these will allow the background to be subtracted more accurately, which is important when measuring the disk surface brightness. Although the IFS data, with the same filter as previous observations, is unlikely to recover the disk there is no additional cost to recording IFS data simultaneously with IRDIS data meaning that the IRDIFS mode the best choice for these observations.

The data will be used to evaluate the dust distribution beyond ~ 100mas, including detailed modelling with GRaTeR (Augereau et al. 1999). Depending on the morphology that this modelling reveals, we may also choose to run N-body simulations to constrain the possible perturbers responsible for sculpting the observed disk morphology. An added benefit of these data is that we will be able to test the five previously identified candidate companions for common proper motion, and confirm our previous designation of these as likely background objects.

6.3 HD 223352ABab/HD 223340: a quadruple star system with evidence for two debris disks

One of the targets in our multi-belt debris disk survey (Chapter 3) was HD 223352 (del Scl, HIP 117452), a nearby A0V star at a distance of 42.1 ± 0.4pc (Perryman et al. 1997). HD 223352 is a member of the AB Doradus association (Zuckerman et al. 2011), with age 150^{+50}_{-30} Myr (Mamajek 2016). That work lists the system as a triple, with a close binary pair and a tertiary member, HD 223340, an early K-type star ~75"to the NW of the primary. De Rosa et al. (2011) resolved the close binary of Zuckerman et al. (2011) as three distinct stars: an A-type primary, and a close binary pair ~ 3.5" from the primary and ~ 300mas from each other. A schematic of the system is given in Figure 6.3.

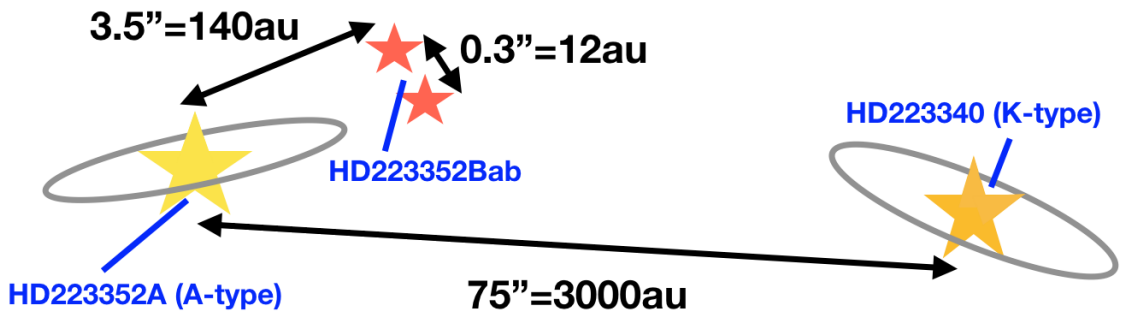

Figure 6.3: A schematic of the HD 223352ABab/HD 223340 quadruple system. An A-type star is orbited by a close binary pair at ~3.5", and a K-star at ~75". The A- and K-stars both host dusty debris disks, based on their infrared excess emission. Neither debris disk has ever been resolved, and so their mutual inclination is not known. Distance annotations are projected separations, and are therefore the minimum physical separation of the system components.

The binary pair HD 223352Bab has more recently also been resolved by Rameau et al. (2013), Galicher et al. (2016) and by our team with SPHERE, giving a total of 5 distinct astrometric measurements over 7 years. All published astrometric data for the system is collated in Table 6.2 and plotted in Figure 6.4, and Figure 6.5 shows SPHERE and *Herschel* images of the various quadruple system components. Although we do not attempt orbit fitting at this point, we find an approximate orbital period as follows: the two objects in this binary pair have a projected separation of 14.5 AU at the most recent measurement in 2015. We do not yet have mass estimates for either component, but the measured contrast relative to HD 223352A suggests that both are late-K or early-M stars, and so we assume

a combined system mass of $\sim 1\,M_\odot$. Assuming a circular orbit, an orbital separation of 14.5 AU, and a combined system mass of $1\,M_\odot$ the predicted orbital period is 55 years. Consider also that the projected separation of the pair increases from 179mas=7.5 AU on 2018-10-12 to 346mas=14.5 AU on 2015-07-18. If we assume an edge-on circular orbit, with the 2015 observation being of the projected apastron, i.e. the point 90° from the position of eclipse, the system would therefore have progressed through 0.16 of a full orbit in this period of 6.74 years, implying a total orbital period of 41 years for the system. Both of these calculations ignore any orbital eccentricity and make somewhat arbitrary assumptions about the orbital radius and system orientation: further data and detailed fitting are required to probe these properties. However, it is clear both from these calculations and from the observed motion in Figure 6.4 that the orbital period is of order 50 years, and further observations over the next years will allow the orbit to be accurately characterized.

Date	Sep (″)	σ_{sep}	PA	σ_{PA}	Reference
		HD223352Ba			
2008-10-12	3.66	0.04	237.3	–	2
2009-08-30	3.7	0.1	237.3	0.4	1
2009-12-31	3.67	0.04	237.3	–	2
2012-12-07	3.667	0.009	237.8	0.8	3
2015-07-18	3.7141	0.0073	238.06	0.14	4
		HD223352Bb			
2008-10-12	3.50	0.04	238.6	–	2
2009-08-30	3.5	0.1	238.5	0.5	1
2009-12-31	3.48	0.04	239.0	–	2
2012-12-07	3.402	0.009	238.6	0.98	3
2015-07-18	3.3738	0.0068	239.13	0.15	4

Table 6.2: Astrometry for the two close companions to HD 223352A. The third companion, an early-K star at ~75″, (Zuckerman et al. 2011) is outside the field of view for each of these observations.
References. (1) De Rosa et al. 2011; (2) Galicher et al. 2016; (3) Rameau et al. 2013, (4) Matthews et al. 2018 (submitted)

Following the identification of this system as a quadruple, it became clear that two of the stellar components host debris disks (namely HD 223352, the A-star, see Morales et al. 2011 and HD 223340, the K-star, see Phillips 2011). SEDs for both of these targets are given in Figure 6.6. The HD 223340 disk has a moderate infrared excess of $L_{IR}/L_\star = (3.6\pm0.3)\times10^{-4}$, while the HD 223352 disk is fainter but has been extensively characterised with Morales et al. (2011), Ballering et al. (2013) and Chen et al. (2014) all finding two-temperature fits for the debris disk, corresponding to two radii of dust. The multi-belt

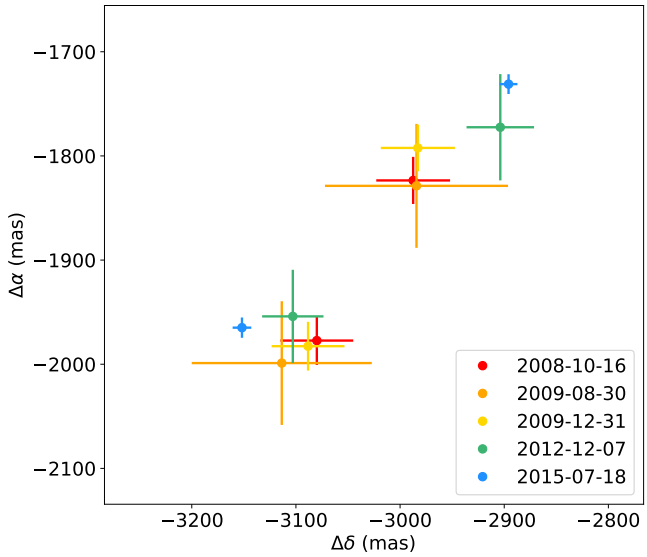

Figure 6.4: Motion of the HD 223352Bab binary relative to HD 223352A. The positions of both members of this binary are shown, and clear orbital motion of the two stars relative to eachother is visible. Orbital motion of the pair relative to the host is harder to discern. Astrometry and references are as for Table 6.2.

nature of the dust suggests one of two likely scenarios: either, there might be a planetary system present which has carved out a deep gap within the debris disk, as was discussed in Chapter 3. We do not detect such a planetary system in either the SPHERE/IRDIS or SPHERE/IFS data, but note that our contrast limits are relatively modest: at 1″ we are only sensitive to companions with mass $\gtrsim 13.9\,M_J$ in the IRDIS data. An alternative possibility is that there has been dynamical interaction with HD 223340 that has perturbed the debris disk of HD 223352. The HD 223340 disk might similarly be warped or asymmetric due to the proximity of HD 223352. Since HD 223340 is lower mass than HD 223352, its disk is more susceptible to perturbations and so we might expect a more dramatic asymmetry in that disk.

Such a system could shed light on influence of an external perturber on the evolution of both debris and planets. However, both debris disks are as yet unresolved. The HD 223352A disk does not appear in our data (Figure 6.7). HD 223340 was observed by the SPHERE GTO on 2015 Sep 24, and we independently reduce these data (see Figure 6.7), but the debris disk is not detected, and no candidate companions appear in the field of view. Additionally, neither target is resolved in *Herschel* archival data.

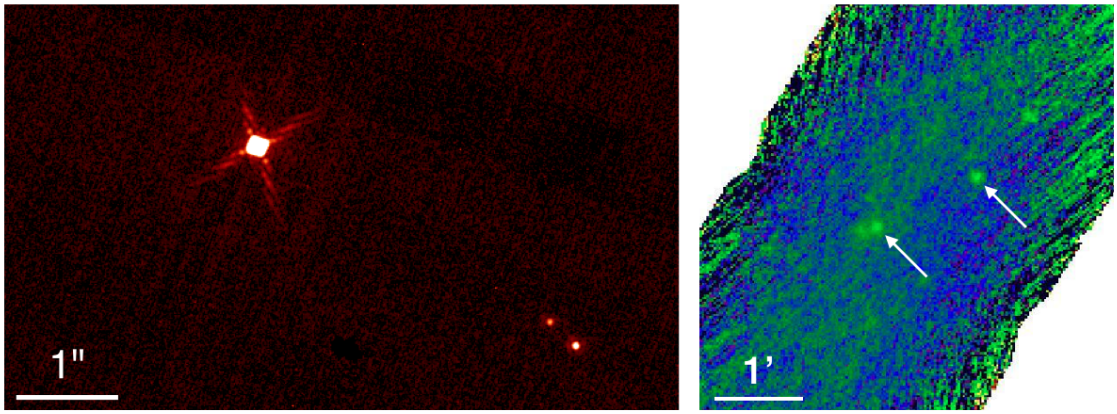

Figure 6.5: Thumbnail images of the stellar components of the HD 223352/HD 223340 quadruple system. *Left:* SPHERE flux calibration image with HD 223352A visible in the center left, and the low-mass binary pair HD 223352Bab in the lower right corner. For this flux calibration frame, taken with the H2 filter, the coronagraph is not present. *Right: Herschel* image at 100 μm with HD 223352A the lower left object and HD223340 the upper right. In both cases north is oriented upwards.

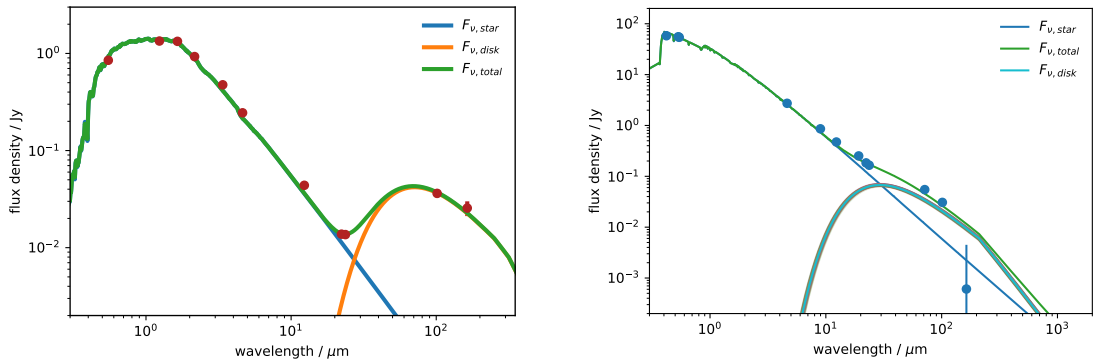

Figure 6.6: Spectral Energy Distribution of HD 223340 (left) and HD 223352A (right). In each case, the photometric measurements of the system are shown with plotted dots. A best fit for the total flux is also, along with a decomposition of this flux into a stellar and a disk component. The HD 223352A debris disk is well studied, with the SED showing clear evidence of two distinct debris belts. The HD 223340 debris disk is less well characterised but has a relatively high fractional excess of $L_{IR}/L_{\star} = (3.6 \pm 0.3) \times 10^{-4}$.

6.3.1 Future observations

To understand the system in more detail it would be beneficial to confirm the inclinations of both debris disks, and we are pursuing new data to achieve this. We will then characterise the orbit of the low-mass binary pair so that the orbital inclination and eccentricity can also be determined.

The astrometry presented in Figure 6.4 and Table 6.2 shows clear orbital motion. We plan to continue collecting astrometric measurements of this system, so as to improve orbital constraints on the HD 223352ABab subsystem. Orbital characterisation of HD 223340

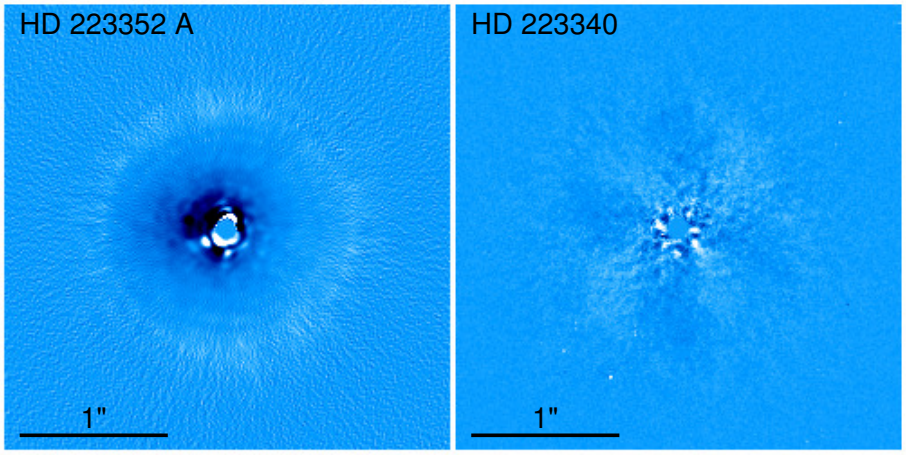

Figure 6.7: SPHERE/IRDIS images of HD 223352A and HD 223340. Each image shows a PCA-reduced square centered on the target, with side length 3″and North is oriented up in each case. Neither debris disk is detected in scattered light.

relative to HD 223352 is unfeasible, due to the very wide distance between these stars (projected separation ~ 3000 AU), and the associated very long orbital period.

Our goal is to resolve the HD 223340 debris disk, so as to determine its inclination. We have applied to observe the system with both HST/STIS in the optical and with ALMA in the millimetre. An HST detection of the disk is feasible since disks with lower fractional luminosities than HD 223340, and similar host magnitudes, have previously been resolved with HST (e.g. AU Mic, $L_{\rm IR}/L_\star \sim 2 \times 10^{-4}$, Kalas et al. 2004), although a detection will likely only be possible if the disk is relatively close to edge-on. An ALMA detection is more tentative since only a few photometric measurements exist and so the mm-flux of HD 223340 is relatively uncertain. Although the total flux of the disk (best fit values 145 μJy and 459 μJy in ALMA bands 6 and 7 respectively) is above the ALMA noise floor, the observations must be set up so that this flux spans at least a few beam elements for the disk to be spatially resolved. The more beam elements the disk covers, the lower the signal in each beam and so the less likely the disk is to be detected over the noise. As well as constraining the disk inclination, a resolved image would reveal the radial extent of dust particles. Confirming the size of the disk might demonstrate an asymmetry similar to that predicted for Fomalhaut C (Shannon et al. 2014).

The HD 223352 debris disk is very faint, and is therefore unresolvable with current instruments. A possible future project will aim to image both disks with JWST, using

MIRI for the HD 223352 disk and NIRCAM for the HD 223340 disk, based on the inferred temperature and approximate spatial scale of both disks.

6.4 HD 133778B: an M4 companion to an evolved star

A companion to HD 133778 was identified for the first time in this work (Figure 6.8). HD 133778 was observed as part of our survey of highly dusty targets (Chapter 4) and has a significant infrared excess of W1 - W4 = 0.79 ± 0.1 mag, greater than that of HR 8799, and $L_{IR}/L_{\star}$ of $3.1 \pm 0.6 \times 10^{-4}$. Infrared analysis suggests that the debris disk is compact, with a temperature ~ 190 K and a corresponding distance of ~ 3 AU.

The candidate was first identified with SPHERE/IRDIFS data collected on 2016 May 16, and confirmed to be co-moving with a second dataset a year later, on 2017 Jun 22. The companion is at a projected separation of 970mas (=164 AU at the host distance), and moves by 2.7mas relative to the host between our two datasets, less than the astrometric precision of the SPHERE instrument (nominally 5mas). For a candidate at this separation, the orbital period is >700 years and so a companion would appear stationary relative to the host, while a stationary background star would appear to move 48.4mas relative to the host due to the proper motion of HD 133778. A common proper motion plot for this target is given in Figure 6.8.

The companion is bright, with contrasts of 8.2 and 8.1 mag in the H2 and H3 filters respectively. These numbers correspond to absolute magnitudes of 9.1 and 9.0 mag in the two filters, and the companion would have a mass of ~30 M_J at an age of 10 Myr, or of ~80 M_J at 50 Myr. The companion briefly passes through the IFS field of view, and is sufficiently bright that it was possible to extract a low resolution spectrum with R~35. The spectral extracion was performed by Arthur Vigan and is shown in Figure 6.9. Based on a visual comparison, the spectrum appears to be of ~M4 type, and a field M4 object is shown for comparison in Figure 6.9.

In our survey of highly dusty objects (Chapter 4), candidates were selected solely based on their significant WISE 22 μm excesses, with all targets having $L_{IR}/L_{\star} > 2 \times$

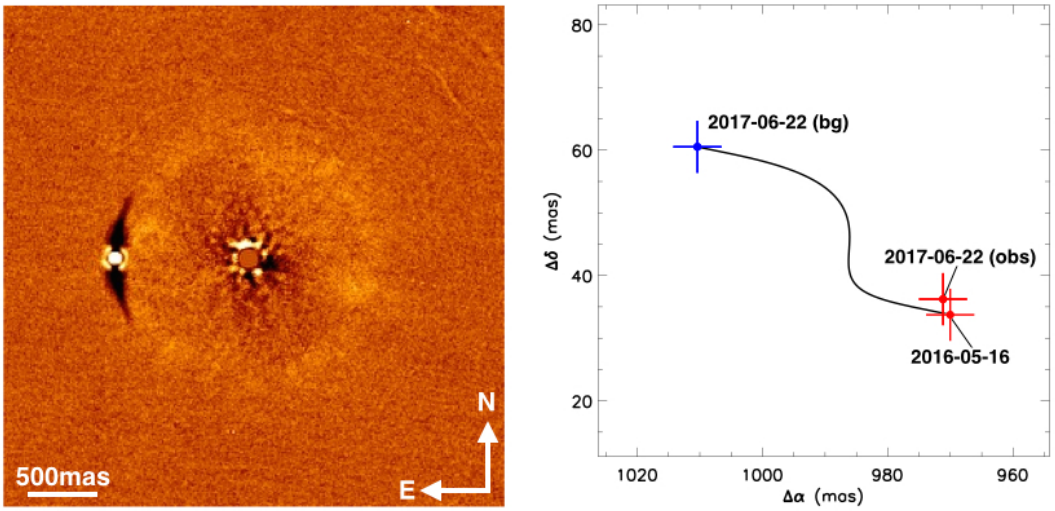

Figure 6.8: *Left:* The discovery image of HD 133778B. The host star is in the center behind the coronagraphic mask, and the companion is clearly visible to the left hand side of the image. *Right:* Common Proper Motion plot with the observed positions of the companion at two epochs shown in red. The prediction for a background object at the second epoch is shown in blue, while the prediction for a co-moving companion would be that the candidate remains stationary relative to the star. In our measurements, the companion moves by 2.7mas, which is less than the astrometric precision of SPHERE.

10^{-4}. Although targets were not explicitly selected for youth, such a high infrared excess normally indicates a young target: only 1 in 10,000 old stars have a 12 μm excess, whereas 1 in 100 young stars posess such an infrared excess (Kennedy & Wyatt 2013).

Once the candidate was confirmed to be a companion, we pursued a more accurate age determination. HD 133778 initially appeared to show signs of Sco-Cen membership based on its physical vicinity to the region and strong IR and X-ray emission and is even listed as a Sco-Cen member in de Geus et al. (1990). However, the target RV ($-37\,\mathrm{km\,s^{-1}}$, Nordström et al. 2004, Torres et al. 2006) is inconsistent with the values expected for a Sco-Cen member (typically $+5\,\mathrm{km\,s^{-1}}$, de Bruijne 1999). HD 133778 is also lithium poor (Torres et al. 2006), which would be unusual for a pre-main sequence Sco-Cen member (Chen et al. 2011).

Casagrande et al. (2011) perform isochronal analysis and find HD 133778 to have an age $\sim 1.5\,\mathrm{Gyr}$ and a mass $\sim 1.73\,\mathrm{M_\odot}$, and our work is consistent with this conclusion. This implies that the host is a ~F2-4 star which has recently left the main sequence and was previously a fast-rotating A-star. At this older age, the M4 spectral type of the companion is a good match to the absolute magnitude in the H-band, lending further support to the

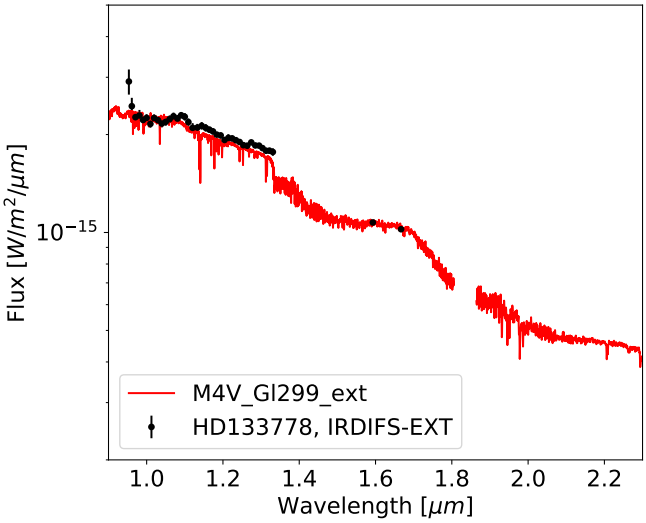

Figure 6.9: SPHERE/IFS spectrum of HD 133778 B, with resolution R~35. The IFS data are shown in black and plotted over an old M4 field dwarf (in red). Visually, these spectra are a good match. Figure provided by Arthur Vigan.

conclusion that this is an old, ~ 1.5 Gyr system.

6.5 HD 18378B: a low-mass companion to a relatively distant star

A companion to HD 18378 is detected based on two datasets, collected on 2016 Aug 26 and 2017 Aug 29. The candidate is at a separation of 440mas and a contrast of 10.9 mag (absolute magnitude 9.1 mag, and is confirmed to be co-moving with the host star (see Figure 6.10) between these epochs: the candidate moves 10mas south, whereas a background object would move ~ 35mas to the west relative to the host. We would expect this candidate to remain stationary between the two epochs, and although the observed motion is slightly larger than the nominal accuracy of the instrument it is nonetheless far closer to the companion hypothesis than to the background hypothesis. Additionally, the separations at the two epochs (435.5mas and 436.2mas) are consistent to a high degree of accuracy, while the position angle measurements (279.2° and 277.9°) are more discrepant. Given that there have been issues with North calibration for SPHERE (see the ESO User Manual[1], v7, section 8.1.4) and that the plate scale is very well calibrated (Maire et al. 2016), we conclude that this is a companion stationary relative to the host and with

1. https://www.eso.org/sci/facilities/paranal/instruments/sphere/doc.html

some astrometric error. The CPM plot and a discovery image are presented in Figure 6.10.

Using the TRILEGAL model (Girardi et al. 2005), we can predict the number of objects above a certain limiting magnitude and in a certain direction. At the co-ordinates of HD 18378, we predict that we should find just 0.1 candidates within the entire field of view (assuming that the field of view is a 6″ circle and using the contrast at 5″). This is a slight overestimate, since the contrast limits are lower in the center of the image near the stellar position. For a target where we are this unlikely to find backgrounds, finding a candidate so close to the host star is itself a sign that the object is likely a companion: this strengthens our conclusion based on the common proper motion of the target.

Although HD 18378 was initially selected as part of the our survey of highly dusty targets based on a photometric distance, in *Gaia* data release 2 (DR2; Gaia Collaboration et al., 2016b; Gaia Collaboration et al. 2018; Lindegren et al. 2018) the target is significantly further than was expected (520.7 ± 5.4pc). The star does not appear to be associated with any young moving groups, and so is likely of field age. At this age and distance, the companion is therefore likely an early-M star.

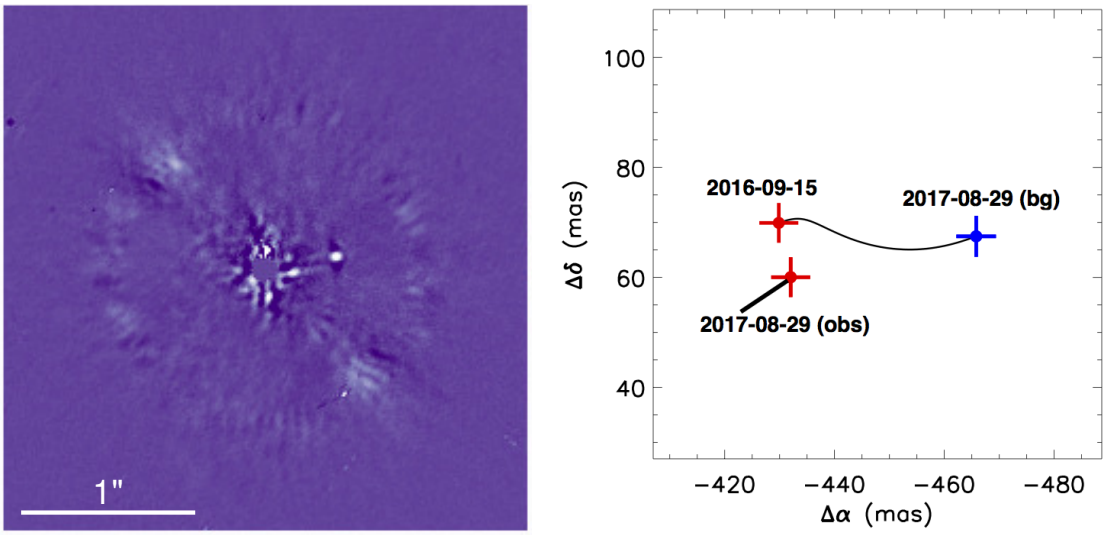

Figure 6.10: *Left:* The discovery image of HD 18378B, an early M type companion orbiting a K2 star, discovered in our survey of highly dusty targets. *Right:* Common proper motion plot, showing the two observed positions of the companion in red and the background hypothesis for the second epoch in blue, and clearly demonstrating that the companion hypothesis, where the object would be predicted to remain stationary, is a far better match to the data than the background hypothesis.

Only two literature references refer to this paper, namely the Houk & Cowley (1975) catalogue of spectral types, which lists HD 18378 A as a K2(III) type star, and Olsen (1994),

who use the same spectral type. Given this limited literature, and the discrepancy between the photometric and *Gaia* distances, the properties of this host star are highly uncertain. Ideally, a high resolution spectrum of the host needs to be collected so that the host temperature and luminosity can be calibrated and the system understood in more detail. If the host is indeed a K2(III) star and assuming the companion to be ~M3 object, the two objects have masses ~0.8 $M_\odot$ and ~0.4 $M_\odot$ based on the isochrones in Pecaut & Mamajek (2013), making this a low-mass binary system with a moderate mass ratio ~ 0.5, but more work is required to confirm this conclusion.

6.6 HD 19257B: a newly identified K-star companion to an A-star

We identify a companion to HD 19257 based on common proper motion (see Figure 6.11), at a separation of 1.3″. The object shows a discrepantly large proper motion of 28mas between the two epochs of data. We predict a companion to be stationary relative to the host, and a background object to move 129mas to the North-West. Although the companion had not been previously identified, it is sufficiently bright that it is identified in *Gaia* DR2, with a good astrometric fit and with a distance 74.4 ± 0.3pc. The host star is poorly fit in *Gaia* DR2, but quoted in *Gaia* Data Release 1 (Gaia Collaboration et al., 2016a) as having a distance 73.3 ± 2.6pc, a value in agreement with the *Hipparcos* distance of 76 ± 6pc. Since the host distance is consistent with that of the companion, we conclude that we conclude the two objects are gravitationally bound.

The object is very bright, and is visible even in the SPHERE flux calibration frames (as shown in Figure 6.11). *Gaia* DR2 photometry in the g-band gives a contrast of 4.5 mag between the objects, and using the SPHERE/IRDIS flux calibration frame we find the companion to have a contrast of 3.29 and 3.16 mag relative to the host in the H2 and H3 filters. Given this flux ratio, the candidate has an absolute magnitude of ~ 5.3 mag in the H2 filter, and is well into the stellar mass regime. Since the companion is outside the IFS field of view, it is not possible to extract a YJ spectrum from our data and assign a precise spectral type.

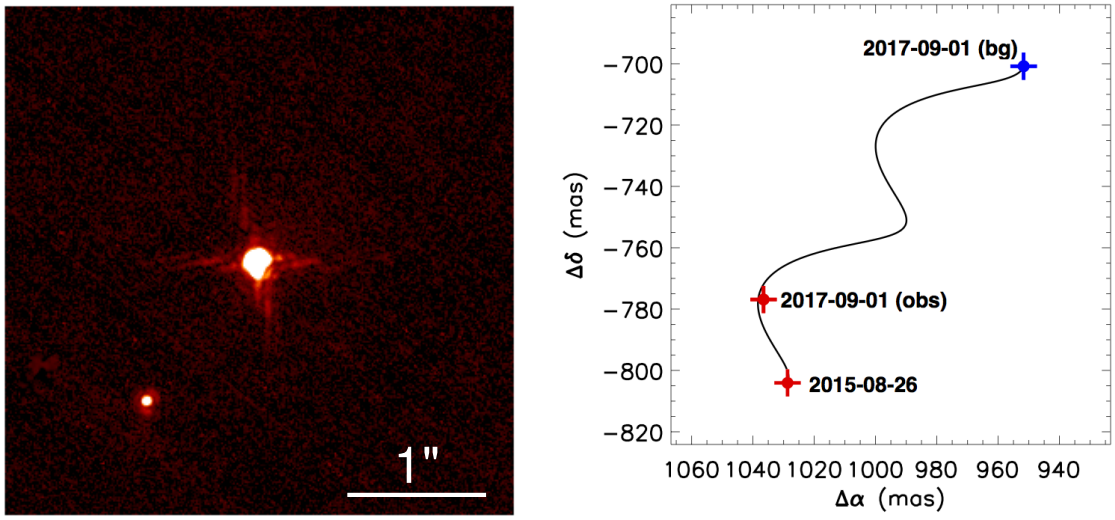

Figure 6.11: *Left:* The discovery image of HD 19257B. This is a flux calibration image taken with SPHERE/IRDIS in the H2 filter, and without the coronagraph present. HD 19257A is visible in the center and HD 19257B to the lower left. North is oriented up. *Right:* Common proper motion plot, demonstrating that the object shows motion significantly different than both the background hypothesis (upper right, indicated in blue) and the companion hypothesis (where the object would be stationary between the two epochs).

Frémat et al. (2007) recorded HD 19257 as a suspected binary due to discrepant radial velocity measurements, and in that work the target is listed as a variable star, but not identified as a spectroscopic binary. The target is listed on SIMBAD as having a spectral type A5, but subsequently by Frémat et al. (2007) as A9, which is more consistent with other literature (McDonald et al. 2012 and Kennedy & Wyatt 2013 find effective temperatures of 7227 K and 7458 K respectively). It is not clear whether any of these measurements have been affected by the presence of the binary companion. Based on the contrast between the two objects, we conclude that HD 19257 B is likely an early-K star.

6.7 Summary and conclusions

In this chapter I have described the specific objects of interest discovered in our two VLT/SPHERE surveys. The main results are:

- The debris disk of HIP 67497 was detected in scattered light, and shows evidence of two distinct belts of debris. This detection was published by another team as Bonnefoy et al. (2017).

- The very faint debris disk of HIP 63439 was detected in scattered light for the first time, and revealed to be a ring with radius ~125au. Work on the characterisation of this debris dust is ongoing.

- We identify a quadruple system, namely HD 223352ABab/HD 223340, of which two of the stellar members host debris disk. Such a complex hierarchical system with multiple debris disks is interesting from a planet formation point of view, and work on this system is ongoing.

- A companion is identified to HD 133778. Age analysis suggests that this companion is a ~M4 type star, orbiting a post main sequence ~F2-4 object.

- Two more binary systems with moderate mass ratios are identified: HD 18378B, an early-M star orbiting a K2 host and HD 19257B, an early-K star orbiting a late-A host.

Chapter 7

Conclusions and Future Work

7.1 Summary of Previous Chapters

In this thesis I have discussed our work carrying out high contrast imaging surveys of highly dusty targets, and of dusty targets with evidence that this dust is carved into two distinct belts. The specific projects described in each chapter are detailed below.

In Chapter 3, we carried out VLT/SPHERE survey of 24 targets that host two-belt debris disks, where planets are believed to be responsible for carving the deep gap between the rings of dust. We did not find any of these dust sculpting planets, but identified three debris disks in scattered light. We additionally placed tight constraints on the possible dust-sculpting planets present in these systems, calculating both upper and lower mass limits, based on our images and on dynamical arguments.

Chapter 4 presents a VLT/SPHERE survey of 20 of the dustiest debris disk targets as identified by WISE. In this survey we identified three companions, and in a future work we will undertake a thorough statistical analysis of both these and other dusty targets. This will improve our understanding of the difference in occurrence rates between targets with and without circumstellar dust.

The HD 129590 debris disk was identified in scattered light for the first time, and is presented in Chapter 5. We modelled the disk using GRaTeR and our best-fitting model

is a single, bright ring with radius 59.3 ± 0.2 AU, at a position angle 121.80 ± 0.02° and an inclination 74.56 ± 0.05° and with a moderate forward scattering parameter of ~0.4. The ring has a very soft outer slope, suggesting the presence of a dust halo, or a scattered disk of planetesimals.

Finally, chapter 6 describes the other objects identified in our two surveys. In this chapter we presented two scattered light debris disk images, three newly detected companions to highly dusty targets, and a hierarchical quadruple star system with two debris disk hosting stars, and work on these objects is ongoing.

7.2 Conclusions

The latest generation of high contrast imagers, in particular SPHERE and GPI, are performing significantly better than their predecessors. Although each instrument has only detected one new planet, the better detection limits of both instruments allow tighter constraints to be placed on the possible planetary systems present. In particular, we demonstrated in Chapter 3 that for two-belt debris disks, upper and lower mass limits can be simultaneously inferred in the same system: this tightly restricts the possible planetary configurations, and many of these inferred planets will be reachable with the next generation of high contrast imagers.

The superior detection limits of SPHERE relative to previous high contrast imagers is hugely beneficial, but brings its own set of challenges. The combination of deep detection limits and a wide field of view means that SPHERE/IRDIS is sensitive to a huge number of background stars, especially in the case that targets near the galactic plane are observed. Each of these candidates need to be carefully vetted, and this can be a time-consuming process and can require many follow-up observations: for future surveys, we recommend that targets are selected to avoid the region within a few degrees of the galactic plane. Additionally, any candidate vetting that can be performed with a single epoch of data is valuable in reducing the observational cost of surveys. In the case of SPHERE/IRDIS, this can be done for a subset of targets based on their H2-H3 color, but

is only effective for targets below a certain absolute magnitude.

GPI and SPHERE are particularly successful at allowing debris dust to be imaged in scattered light. Several debris disks have already been imaged, and in some cases complex morphology is revealed, with the two instruments: within the Sco-Cen associaton alone, at least six scattered light debris disk detections have already been made. We resolved disks around HD 129590 and HIP 63439 (Chapters 5 and 6 respectively), both of which appear to be simple rings. Both the HIP 67497 (Bonnefoy et al. 2017, presented in Chapter 6) and HIP 73145 (Feldt et al. 2017) disks have previously been imaged, but SPHERE images of these targets are the first to suggest the presence of multiple dust rings. Finally, the disks of the Sco-Cen targets HD 100546 (Currie et al. 2015a) and HD 111520 (Draper et al. 2016) were both imaged with GPI and have been shown respectively to have a spiral arm and a dramatic brightness asymmetry. Sco-Cen spans a narrow band of ages (~5-17 Myr, Pecaut et al. 2012), only shortly after the formation of giant planets has ceased, and studying disks specifically from this region is important in understanding how these disks form and evolve, and how they relate to any exoplanets in the system. It is clear even from the small sample described above that these debris disks span a range of properties and morphologies.

7.3 Future Work

The work presented in Chapter 3 can be repeated for other multi-belt targets, to place constraints on their possible planets. Additionally, future instruments such as JWST and eventually the extremely large telescopes may be sensitive to planets with masses down to the lower limits in these systems: if this is the case, these instruments should find the gap-clearing planets that are inferred here. If these planets are not detected, it will be clear that our current understanding of either wide-separation exoplanet systems themselves, or of the mechanisms by which gaps are cleared, is incomplete: perhaps the planets clear dust more quickly than in simulations, or are commonly found on eccentric orbits.

We plan to carry out a thorough statistical analysis of the targets presented in Chap-

ter 4, as well as other highly dusty targets, so as to look for a correlation between highly dusty targets and the presence of both planetary and stellar mass companions. Our initial identification of 3 binaries in the sample of 20 targets appears consistent with previous results studying whether debris disk targets are members of binary or tertiary systems, but more work is required.

Several of the objects in Chapter 6 require further work. In particular, we are awaiting new SPHERE/IRDIFS data on the HIP 63439 debris disk to allow detailed modelling of the disk structure. We are actively seeking further observations of the HD 223340 and HD 223352A disks so as to probe their inclination relative to eachother, and use the system to understand planet formation under the influence of an external perturber. The HD 129590 disk, meanwhile, has been observed in polarised light with GPI and I plan to analyse these data and carry out more thorough modelling of the system.

The Appendices

Appendix A

Common proper motion plots for two-belt targets

Here we present the Common Proper Motion plots for each candidate with multiple epochs of data. Color Schemes are as for Figure 3.3 in Chapter 3.

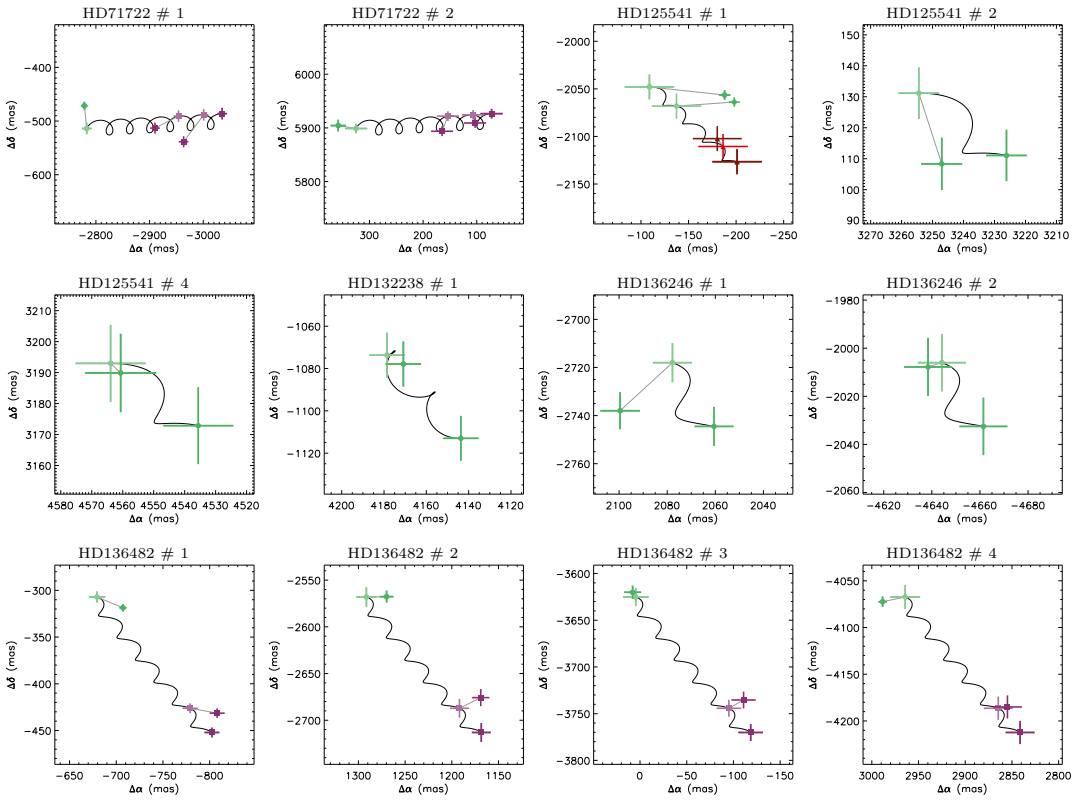

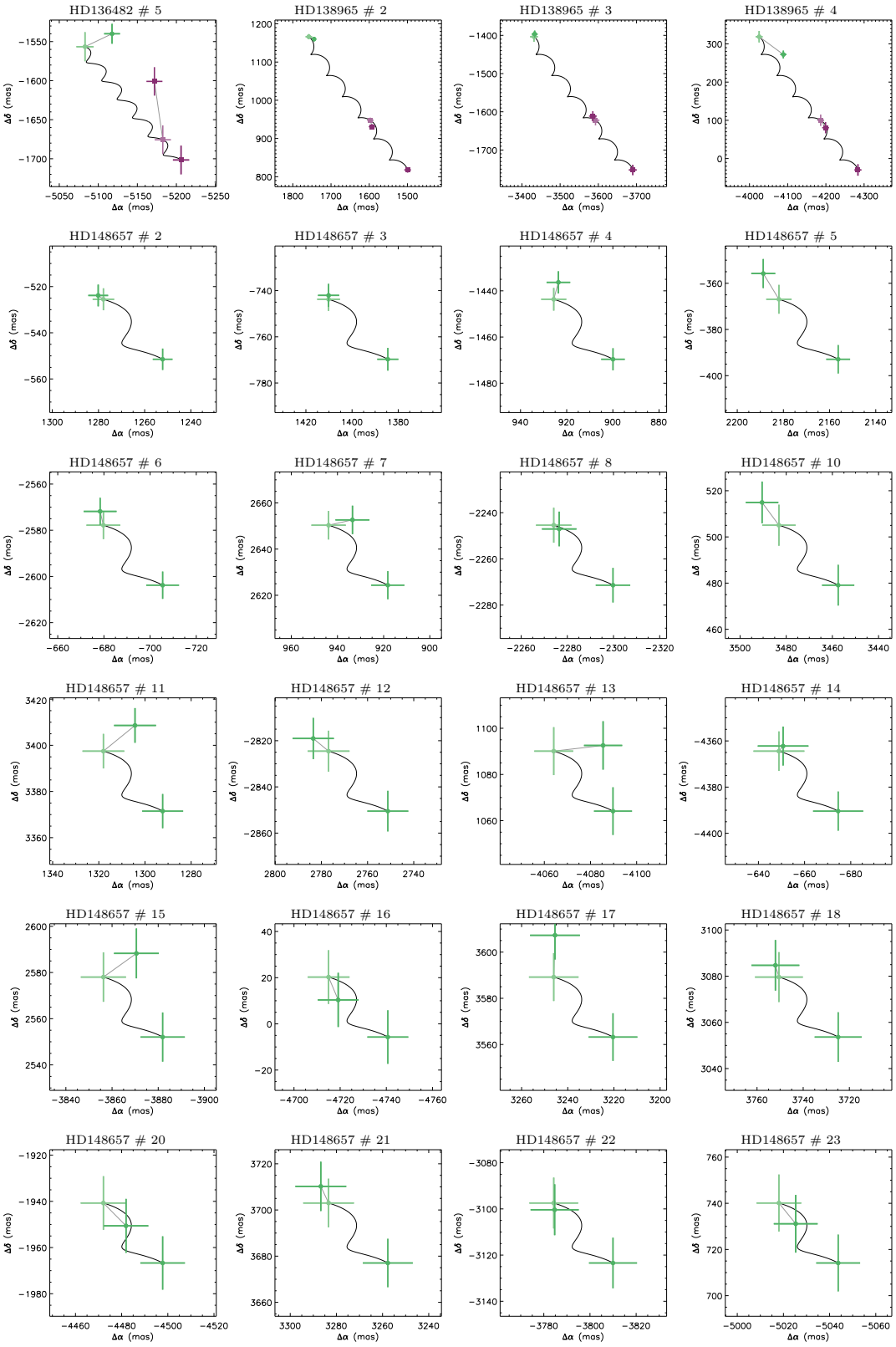
HD136482 # 5
HD138965 # 2
HD138965 # 3
HD138965 # 4
HD148657 # 2
HD148657 # 3
HD148657 # 4
HD148657 # 5
HD148657 # 6
HD148657 # 7
HD148657 # 8
HD148657 # 10
HD148657 # 11
HD148657 # 12
HD148657 # 13
HD148657 # 14
HD148657 # 15
HD148657 # 16
HD148657 # 17
HD148657 # 18
HD148657 # 20
HD148657 # 21
HD148657 # 22
HD148657 # 23
Δδ (mas)
Δα (mas)

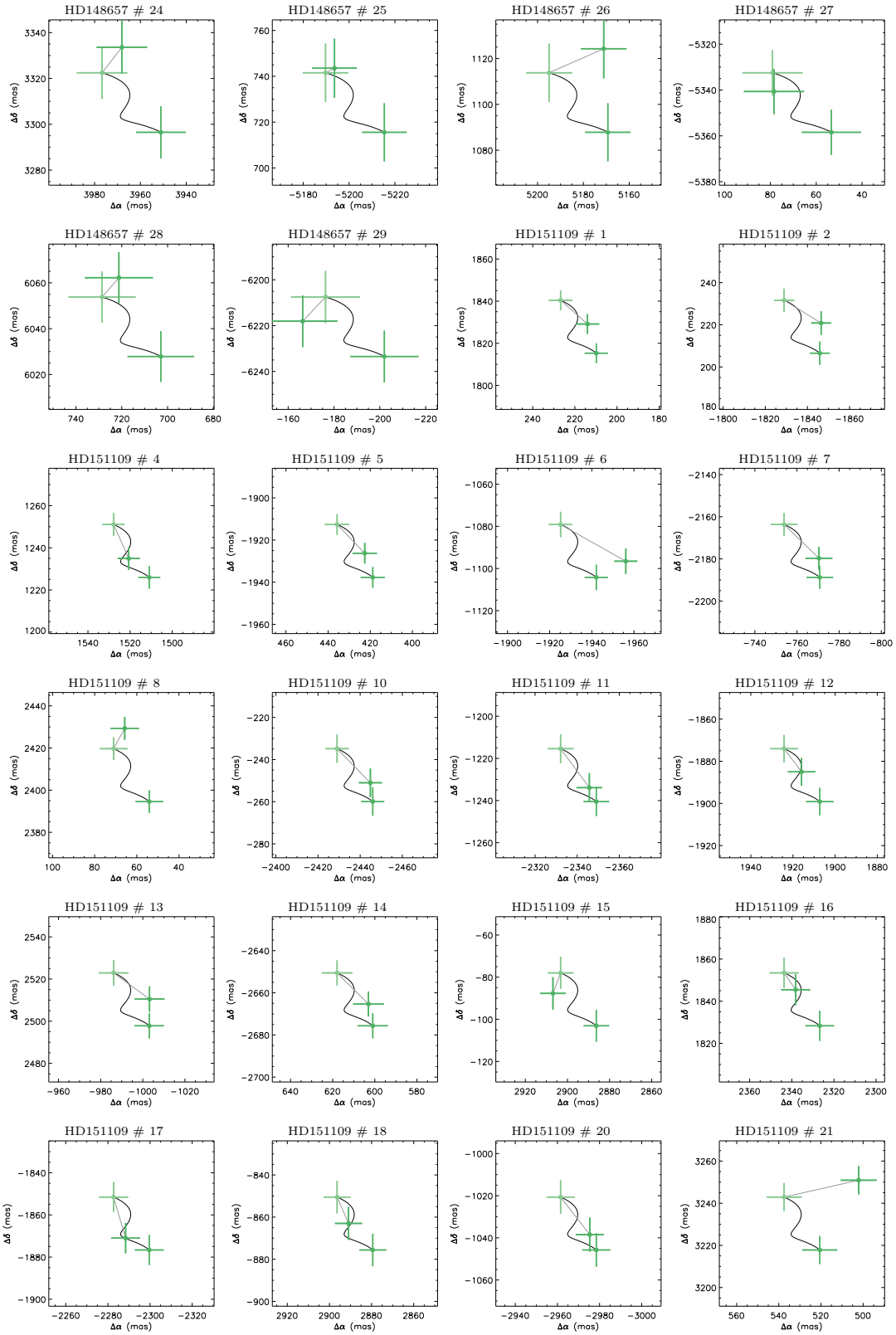
HD148657 # 24
HD148657 # 25
HD148657 # 26
HD148657 # 27
HD148657 # 28
HD148657 # 29
HD151109 # 1
HD151109 # 2
HD151109 # 4
HD151109 # 5
HD151109 # 6
HD151109 # 7
HD151109 # 8
HD151109 # 10
HD151109 # 11
HD151109 # 12
HD151109 # 13
HD151109 # 14
HD151109 # 15
HD151109 # 16
HD151109 # 17
HD151109 # 18
HD151109 # 20
HD151109 # 21
Δδ (mas)
Δα (mas)

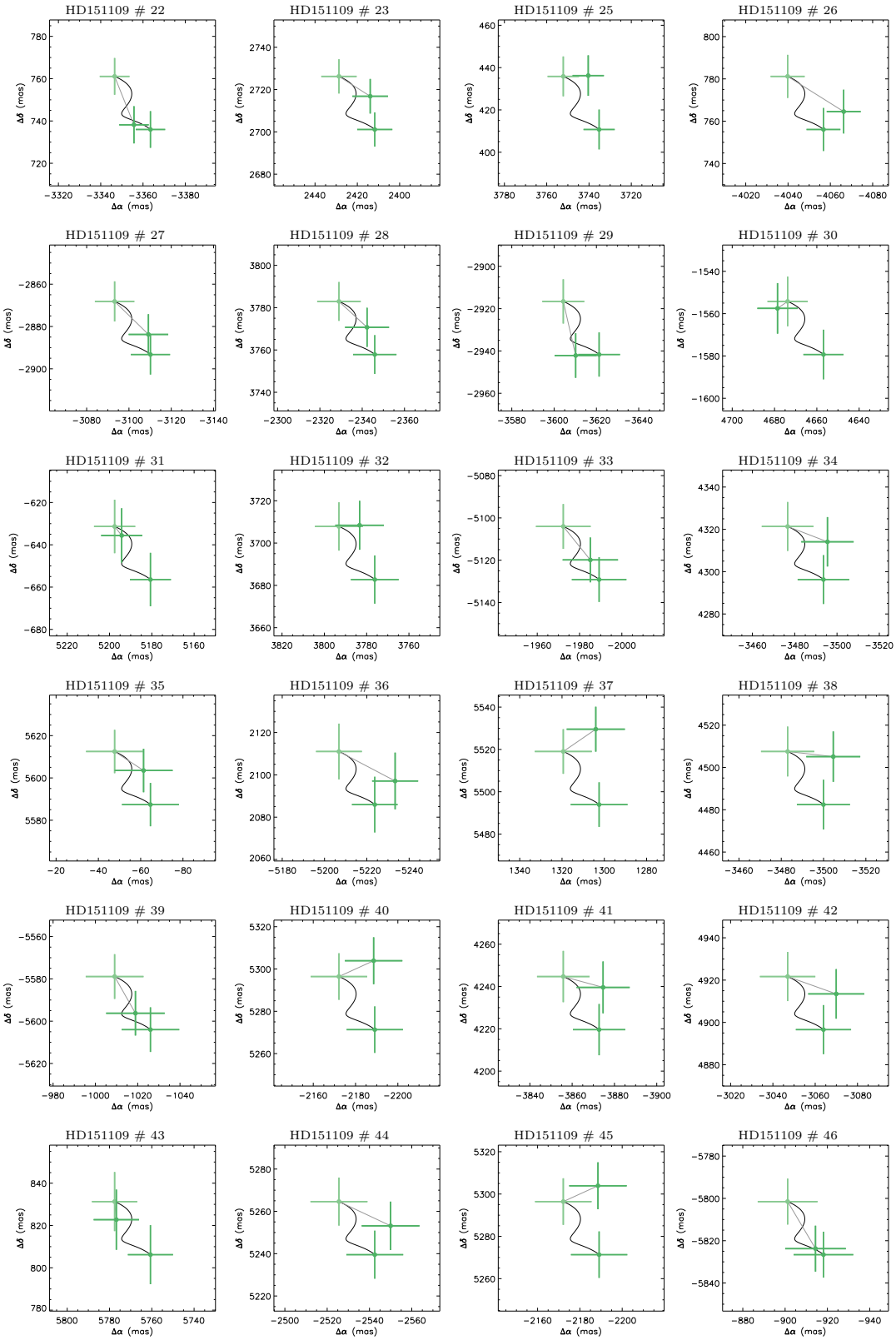
HD151109 # 22
HD151109 # 23
HD151109 # 25
HD151109 # 26
HD151109 # 27
HD151109 # 28
HD151109 # 29
HD151109 # 30
HD151109 # 31
HD151109 # 32
HD151109 # 33
HD151109 # 34
HD151109 # 35
HD151109 # 36
HD151109 # 37
HD151109 # 38
HD151109 # 39
HD151109 # 40
HD151109 # 41
HD151109 # 42
HD151109 # 43
HD151109 # 44
HD151109 # 45
HD151109 # 46
Δδ (mas)
Δα (mas)

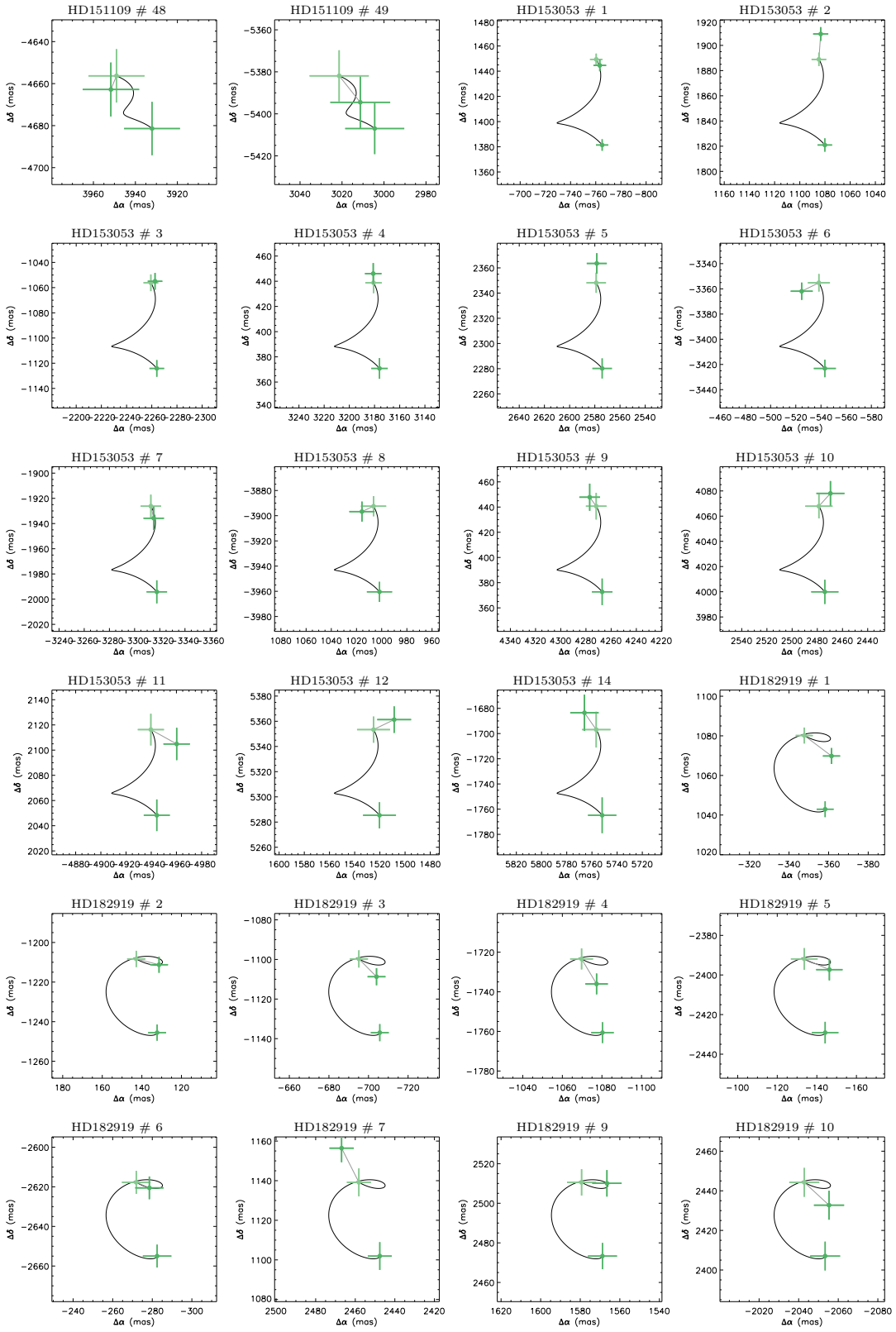
HD151109 # 48
HD151109 # 49
HD153053 # 1
HD153053 # 2
HD153053 # 3
HD153053 # 4
HD153053 # 5
HD153053 # 6
HD153053 # 7
HD153053 # 8
HD153053 # 9
HD153053 # 10
HD153053 # 11
HD153053 # 12
HD153053 # 14
HD182919 # 1
HD182919 # 2
HD182919 # 3
HD182919 # 4
HD182919 # 5
HD182919 # 6
HD182919 # 7
HD182919 # 9
HD182919 # 10
Δδ (mas)
Δα (mas)

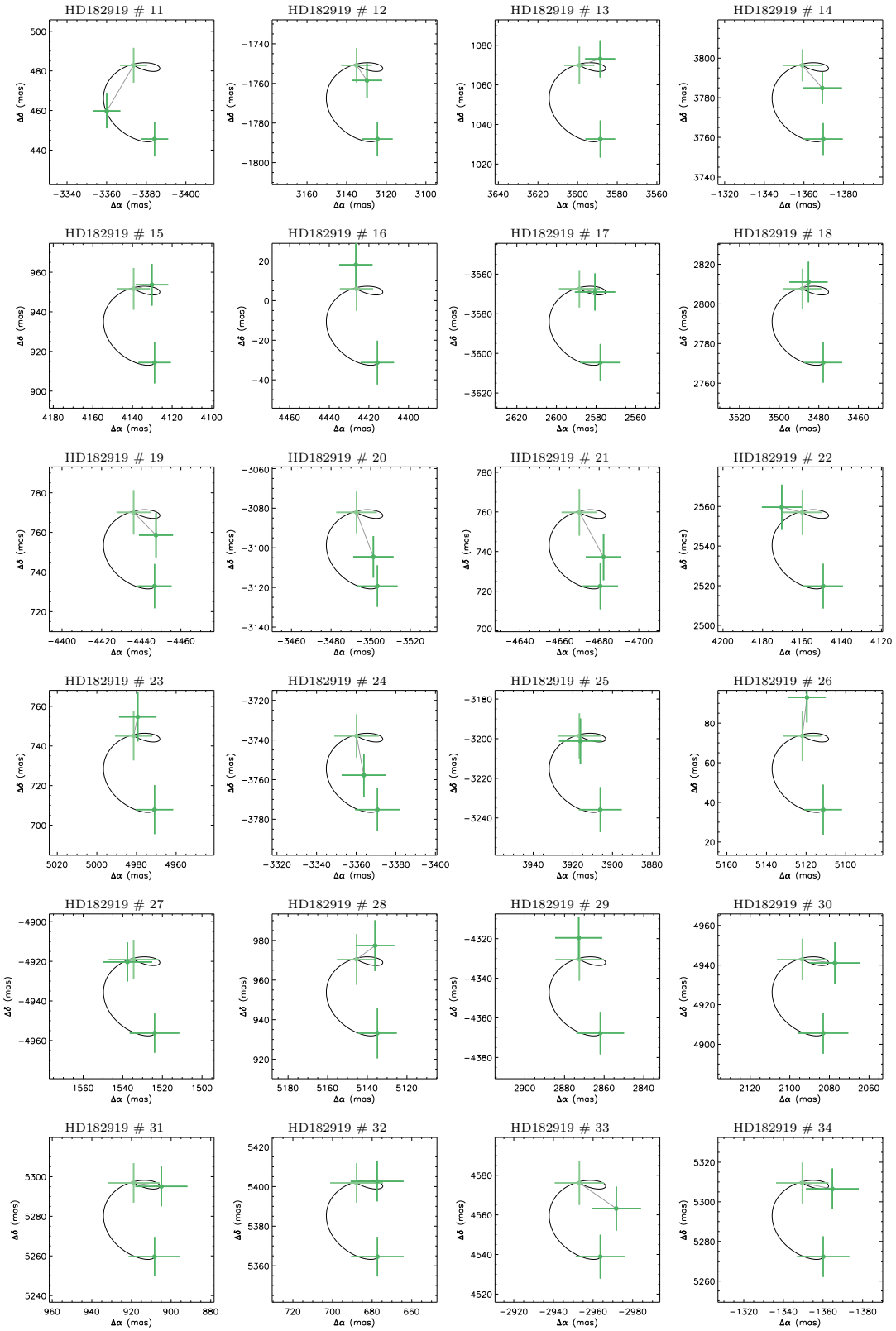
HD182919 # 11
HD182919 # 12
HD182919 # 13
HD182919 # 14
HD182919 # 15
HD182919 # 16
HD182919 # 17
HD182919 # 18
HD182919 # 19
HD182919 # 20
HD182919 # 21
HD182919 # 22
HD182919 # 23
HD182919 # 24
HD182919 # 25
HD182919 # 26
HD182919 # 27
HD182919 # 28
HD182919 # 29
HD182919 # 30
HD182919 # 31
HD182919 # 32
HD182919 # 33
HD182919 # 34
Δδ (mas)
Δα (mas)

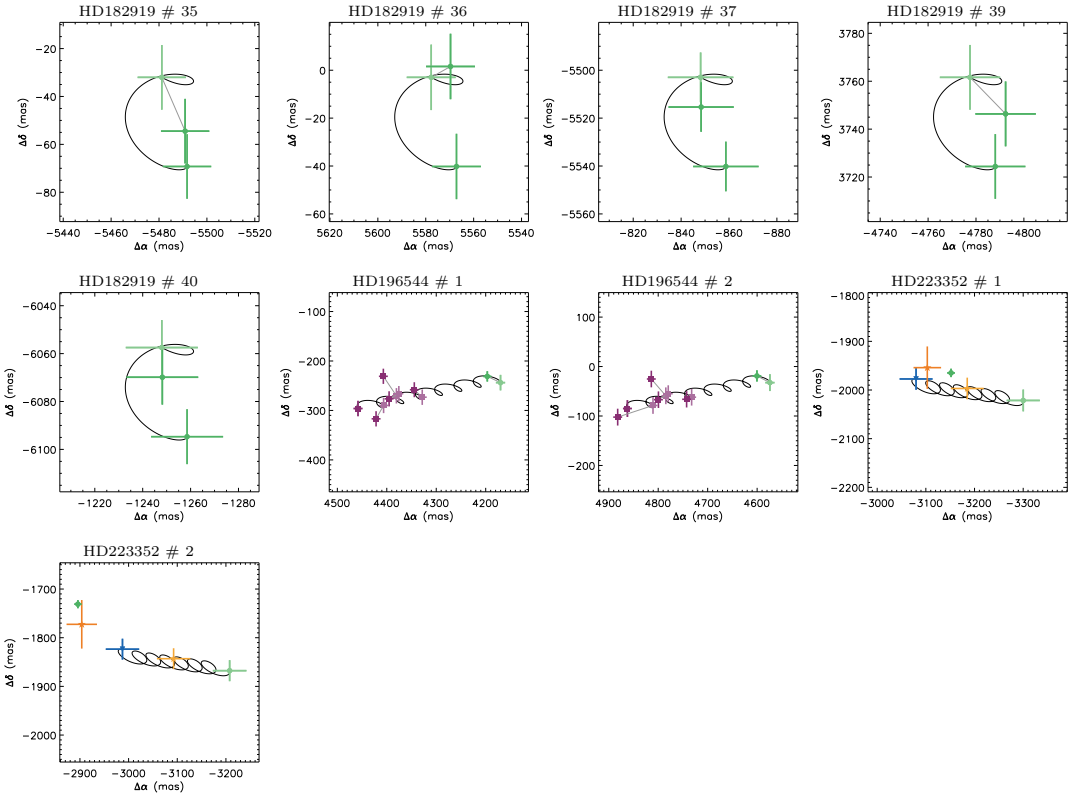
HD182919 # 35
HD182919 # 36
HD182919 # 37
HD182919 # 39
HD182919 # 40
HD196544 # 1
HD196544 # 2
HD223352 # 1
HD223352 # 2
Δδ (mas)
Δα (mas)

Appendix B

Contrast limits for individual observations of two-belt targets

Here we present contrast limits for each individual observation in Chapter 3. Orange and blue lines represent data from the SPHERE/IRDIS and SPHERE/IFS subsystems respectively. The contrasts are calculated by injecting fake planets, with full details given in Section 3.4.4 in the main text.

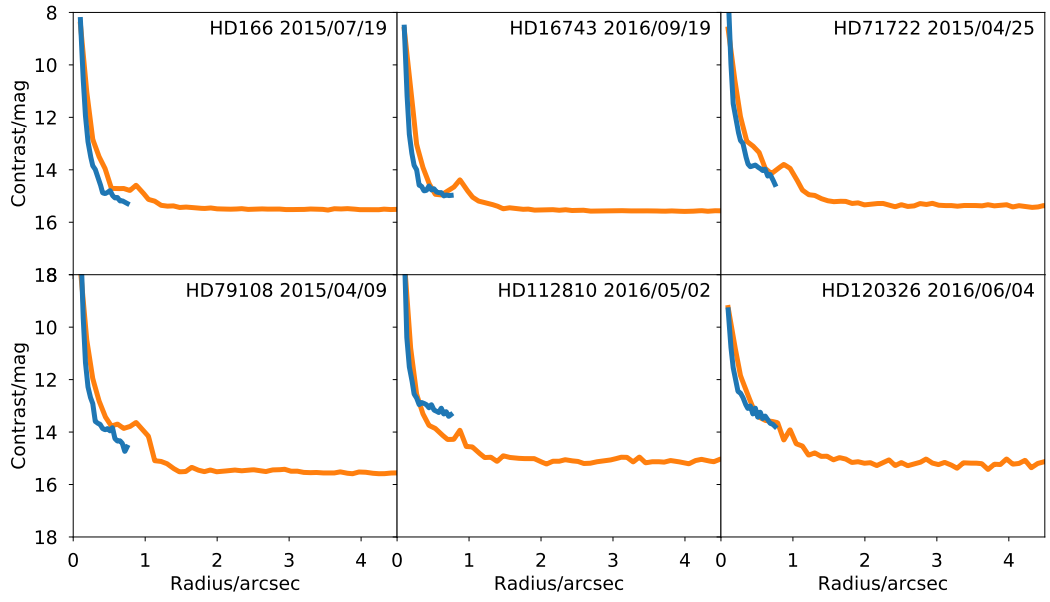

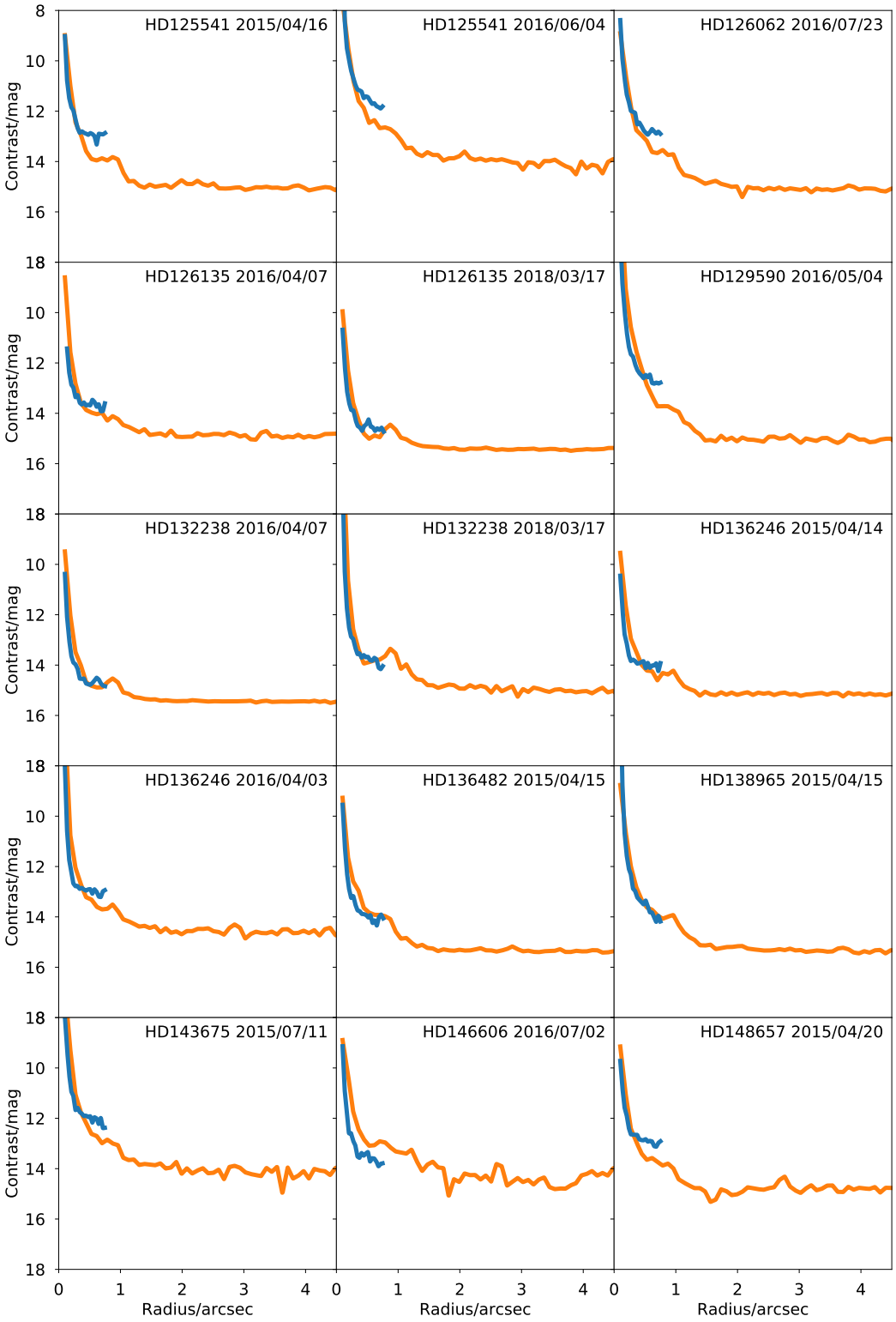
HD125541 2015/04/16
HD125541 2016/06/04
HD126062 2016/07/23
HD126135 2016/04/07
HD126135 2018/03/17
HD129590 2016/05/04
HD132238 2016/04/07
HD132238 2018/03/17
HD136246 2015/04/14
HD136246 2016/04/03
HD136482 2015/04/15
HD138965 2015/04/15
HD143675 2015/07/11
HD146606 2016/07/02
HD148657 2015/04/20
Contrast/mag
Radius/arcsec

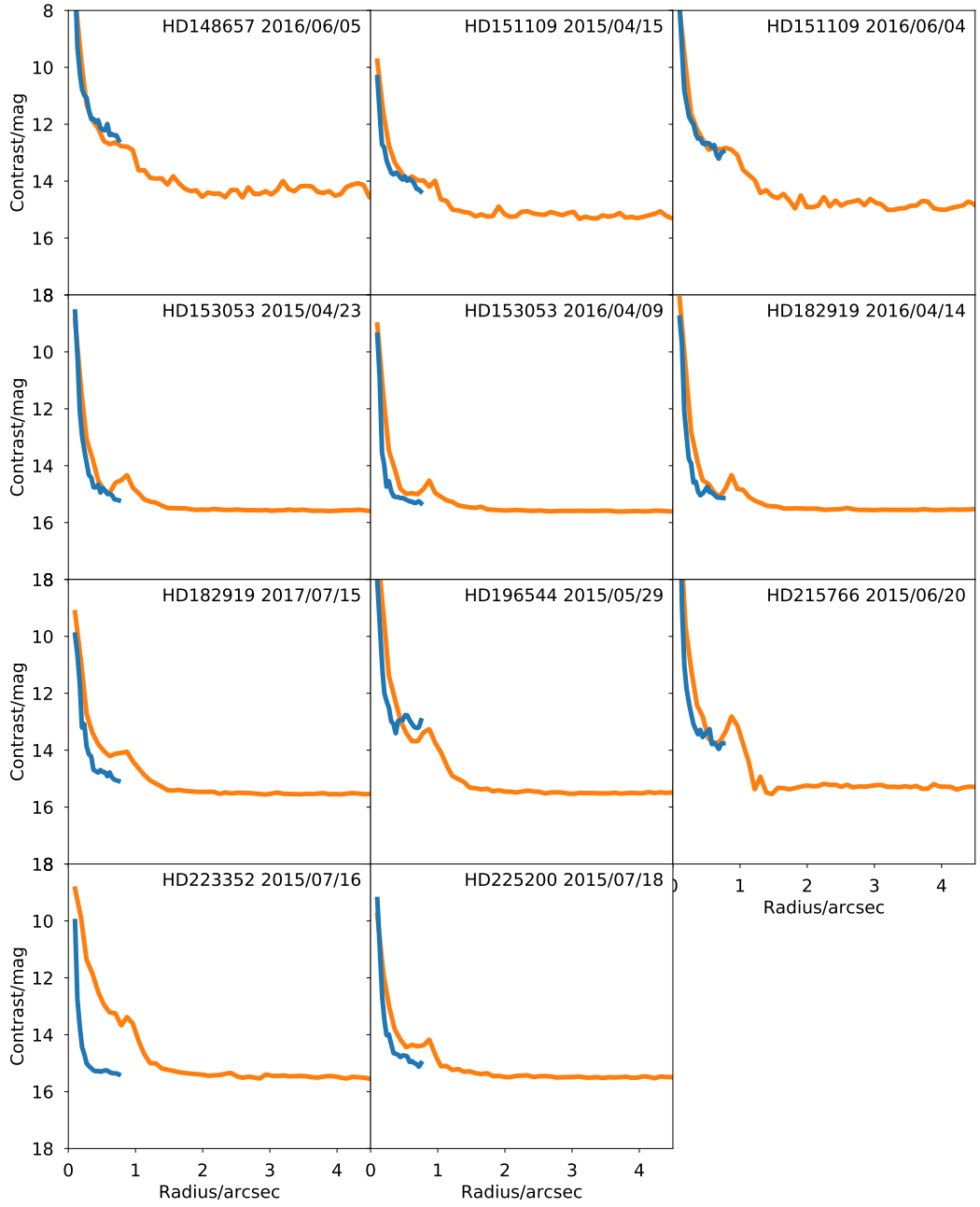
HD148657 2016/06/05
HD151109 2015/04/15
HD151109 2016/06/04
HD153053 2015/04/23
HD153053 2016/04/09
HD182919 2016/04/14
HD182919 2017/07/15
HD196544 2015/05/29
HD215766 2015/06/20
HD223352 2015/07/16
HD225200 2015/07/18
Contrast/mag
Radius/arcsec

Appendix C

Astrometry for all candidates identified in Chapter 3

In this appendix we present the full version of Table 3.4. 178 candidates were detected in this survey, of which 157 are background (BG) and a further 18 are likely background objects (?BG) based on their separation from the host star and color analysis. 2 objects are previously detected companions (C) and one object is a likely speckle (S?). Further detail on candidate designation is given in Section 3.4.3.

Note. TF = candidate too faint to be redetected, OS = candidate off-screen in this epoch.

References. (B17) Bonnefoy et al. 2017; (dR11) De Rosa et al. 2011; (G16) Galicher et al. 2016; (J13) Janson et al. 2013b; (N13) Nielsen et al. 2013; (R13) Rameau et al. 2013.

Star	Epoch Date	No.	ΔH (mag)	Sep(″)	σ_{sep}	PA	σ_{PA}	Reference	Status
HD 71722	2015-04-25	1	11.4	2818.2	6.0	260.37	0.15	N13	BG
HD 71722	2015-04-25	2	11.2	5915.2	10.8	3.47	0.14	N13	BG
HD 79108	2015-04-09	1	13.3	5248.5	9.7	89.50	0.14	–	?BG
HD 112810	2016-05-02	1	14.6	3512.9	7.0	262.04	0.15	–	?BG
HD 112810	2016-05-02	2	7.8	5682.9	10.4	311.36	0.14	–	?BG
HD 112810	2016-05-02	3	11.3	5788.2	10.6	357.93	0.14	–	?BG
HD 112810	2016-05-02	4	13.8	5859.7	10.7	126.75	0.14	–	?BG
HD 112810	2016-05-02	5	–	6188.0	11.2	284.11	0.14	–	?BG
HD 120326	2016-06-04	1	13.9	1086.7	3.9	185.43	0.23	B17	?BG
HD 120326	2016-06-04	2	13.2	4011.7	7.7	292.86	0.14	B17	?BG

HD 120326	2016-06-04	3	14.7	4256.7	8.1	71.67	0.14	B17	?BG
HD 120326	2016-06-04	4	13.8	5375.2	9.9	351.32	0.14	B17	?BG
HD 120326	2016-06-04	5	10.1	5621.4	10.3	100.05	0.14	B17	?BG
HD 120326	2016-06-04	6	14.4	5736.9	10.5	279.58	0.14	B17	?BG
HD 120326	2016-06-04	7	–	6398.9	11.6	155.53	0.14	B17	?BG
HD 125541	2015-04-16	1	8.6	2073.3	5.0	185.48	0.16	J13	BG
HD 125541	2016-06-04			2065.0	5.0	185.22	0.17		
HD 125541	2015-04-16	2	12.0	3228.0	6.6	88.03	0.15	–	?BG
HD 125541	2016-06-04			3248.8	6.6	88.09	0.15		
HD 125541	2015-04-16	3	14.0	4862.8	9.1	28.17	0.14	–	BG
HD 125541	2016-06-04			TF					
HD 125541	2015-04-16	4	13.0	5535.2	10.2	55.03	0.14	–	BG
HD 125541	2016-06-04			5565.5	10.2	55.03	0.14		
HD 126062	2016-07-23	1	15.4	4990.1	9.3	100.43	0.14	–	BG
HD 126062	2016-07-23	2	13.6	6122.1	11.1	293.3	0.14	–	BG
HD 126062	2016-07-23	3	14.2	6285.2	11.4	170.89	0.14	–	BG
HD 126135	2016-04-07	1	8.5	135.9	3.5	290.08	1.47	–	S?
HD 129590	2016-05-04	1	11.5	5672.1	10.4	28.30	0.14	–	?BG
HD 132238	2016-04-07	1	14.7	4290.5	8.2	105.03	0.14	–	BG
HD 132238	2018-03-17			4307.9	8.2	104.49	0.14	–	
HD 136246	2015-04-16	1	14.5	3431.9	6.9	143.10	0.15	–	BG
HD 136246	2016-04-03			3450.3	6.9	142.52	0.15		
HD 136246	2015-04-16	2	12.8	5085.3	9.4	246.44	0.14	–	BG
HD 136246	2016-04-03			5054.3	9.4	246.59	0.14		
HD 136482	2015-04-15	1	11.4	775.6	3.7	245.74	0.29	N13	BG
HD 136482	2015-04-15	2	12.1	2864.5	6	153.69	0.15	N13	BG
HD 136482	2015-04-15	3	14.8	3620.1	7.1	179.87	0.14	N13	BG
HD 136482	2015-04-15	4	14.6	5051.2	9.4	143.73	0.14	N13	BG
HD 136482	2015-04-15	5	10.3	5344.3	9.8	253.25	0.14	N13	BG
HD 136482	2015-04-15	6	15.8	5952.5	10.8	155.66	0.14	–	BG
HD 138965	2015-04-15	1	13.4	1240.7	4.1	20.53	0.21	–	BG
HD 138965	2015-04-15	2	10.6	2094.9	5	56.38	0.16	N13	BG
HD 138965	2015-04-15	3	12.5	3706.6	7.3	247.86	0.14	N13	BG
HD 138965	2015-04-15	4	15.1	4097.8	7.9	273.81	0.14	N13	BG
HD 143675	2015-07-11	1	13.5	3893.5	7.6	36.26	0.14	–	BG
HD 143675	2015-07-11	2	13.3	4863.4	9.1	141.17	0.14	–	BG
HD 143675	2015-07-11	3	13.0	5032.4	9.3	220.16	0.14	–	BG
HD 143675	2015-07-11	4	11.2	5388.6	9.9	118.05	0.14	–	?BG
HD 146606	2016-07-02	1	13.3	4673.0	8.8	129.30	0.14	–	?BG
HD 148657	2015-04-20	1	13.3	975.4	3.9	262.07	0.24	–	BG
HD 148657	2016-06-05			TF					
HD 148657	2015-04-20	2	10.8	1368.3	4.2	113.77	0.20	–	BG

HD 148657	2016-06-05			1383.2	4.2	112.26	0.20		
HD 148657	2015-04-20	3	8.8	1584.2	4.4	119.07	0.18	–	BG
HD 148657	2016-06-05			1593.5	4.4	117.75	0.18		
HD 148657	2015-04-20	4	13.2	1723.3	4.6	148.52	0.18	–	BG
HD 148657	2016-06-05			1707.6	4.5	147.26	0.18		
HD 148657	2015-04-20	5	13.6	2191.8	5.1	100.33	0.16	–	BG
HD 148657	2016-06-05			2217.4	5.2	99.23	0.16		
HD 148657	2015-04-20	6	10.8	2697.7	5.8	195.16	0.15	–	BG
HD 148657	2016-06-05			2659.8	5.8	194.78	0.16		
HD 148657	2015-04-20	7	13.8	2780.4	5.9	19.28	0.15	–	BG
HD 148657	2016-06-05			2812.1	6.0	19.39	0.15		
HD 148657	2015-04-20	8	12.0	3232.4	6.6	225.36	0.15	–	BG
HD 148657	2016-06-05			3198.7	6.5	225.37	0.15		
HD 148657	2015-04-20	9	14.0	3301.8	6.7	153.83	0.15	–	BG
HD 148657	2016-06-05			TF					
HD 148657	2015-04-20	10	9.5	3490.5	6.9	82.11	0.15	–	BG
HD 148657	2016-06-05			3528.2	7.0	81.61	0.15		
HD 148657	2015-04-20	11	14.0	3610.7	7.1	20.97	0.14	–	BG
HD 148657	2016-06-05			3649.6	7.2	20.94	0.15		
HD 148657	2015-04-20	12	12.5	3961.6	7.7	136.02	0.14	–	BG
HD 148657	2016-06-05			3961.7	7.7	135.36	0.14		
HD 148657	2015-04-20	13	13.0	4225.9	8.1	284.58	0.14	–	BG
HD 148657	2016-06-05			4229.0	8.1	284.97	0.14		
HD 148657	2015-04-20	14	10.5	4441.9	8.4	188.73	0.14	–	BG
HD 148657	2016-06-05			4410.5	8.3	188.48	0.14		
HD 148657	2015-04-20	15	11.4	4645.7	8.7	303.32	0.14	–	BG
HD 148657	2016-06-05			4656.2	8.7	303.77	0.14		
HD 148657	2015-04-20	16	13.5	4740.7	8.9	269.93	0.14	–	BG
HD 148657	2016-06-05			4719.2	8.8	270.13	0.14		
HD 148657	2015-04-20	17	13.0	4802.9	9.0	42.11	0.14	–	BG
HD 148657	2016-06-05			4852.4	9.1	41.98	0.14		
HD 148657	2015-04-20	18	11.5	4816.6	9.0	50.65	0.14	–	BG
HD 148657	2016-06-05			4857.3	9.1	50.57	0.14		
HD 148657	2015-04-20	19	14.3	4826.1	9.0	156.72	0.14	–	BG
HD 148657	2016-06-05			TF					
HD 148657	2015-04-20	20	11.1	4908.9	9.2	246.38	0.14	–	BG
HD 148657	2016-06-05			4888.0	9.1	246.48	0.14		
HD 148657	2015-04-20	21	12.9	4912.6	9.2	41.54	0.14	–	BG
HD 148657	2016-06-05			4956.7	9.2	41.54	0.14		
HD 148657	2015-04-20	22	13.7	4926.6	9.2	230.66	0.14	–	BG
HD 148657	2016-06-05			4892.5	9.1	230.68	0.14		
HD 148657	2015-04-20	23	10.9	5094.0	9.4	278.06	0.14	–	BG

HD 148657	2016-06-05			5078.2	9.4	278.28	0.14		
HD 148657	2015-04-20	24	13.4	5145.7	9.5	50.16	0.14	–	BG
HD 148657	2016-06-05			5182.5	9.6	49.97	0.14		
HD 148657	2015-04-20	25	13.7	5264.2	9.7	277.81	0.14	–	BG
HD 148657	2016-06-05			5246.6	9.7	278.15	0.14		
HD 148657	2015-04-20	26	13.9	5282.5	9.7	78.12	0.14	–	BG
HD 148657	2016-06-05			5291.9	9.8	77.73	0.14		
HD 148657	2015-04-20	27	12.6	5358.7	9.9	179.43	0.14	–	BG
HD 148657	2016-06-05			5341.2	9.8	179.16	0.14		
HD 148657	2015-04-20	28	11.6	6068.7	11.0	6.65	0.14	–	BG
HD 148657	2016-06-05			6105.0	11.1	6.78	0.14		
HD 148657	2015-04-20	29	–	6236.8	11.3	181.86	0.14	–	BG
HD 148657	2016-06-05			6220.3	11.3	181.53	0.14		
HD 151109	2015-04-15	1	14.6	1827.4	4.7	6.59	0.17	–	BG
HD 151109	2015-04-15			1841.6	4.7	6.67	0.17		
HD 151109	2015-04-15	2	12.9	1857.4	4.7	276.38	0.17	–	BG
HD 151109	2015-04-15			1859.7	4.7	276.82	0.17		
HD 151109	2015-04-15	3	14.9	1921.2	4.8	206.59	0.17	–	BG
HD 151109	2015-04-15			TF					
HD 151109	2015-04-15	4	13.3	1945.7	4.8	50.94	0.17	–	BG
HD 151109	2015-04-15			1958.9	4.8	50.92	0.17		
HD 151109	2015-04-15	5	11.7	1982.5	4.9	167.80	0.17	–	BG
HD 151109	2015-04-15			1972.1	4.9	167.63	0.17		
HD 151109	2015-04-15	6	14.6	2218.5	5.2	240.67	0.16	–	BG
HD 151109	2015-04-15			2242.5	5.2	240.73	0.16		
HD 151109	2015-04-15	7	11.8	2320.5	5.3	199.40	0.16	–	BG
HD 151109	2015-04-15			2311.8	5.3	199.47	0.16		
HD 151109	2015-04-15	8	14.4	2395.2	5.4	1.29	0.16	–	BG
HD 151109	2015-04-15			2430.2	5.4	1.55	0.16		
HD 151109	2015-04-15	9	15.0	2405.1	5.4	173.39	0.16	–	BG
HD 151109	2015-04-15			TF					
HD 151109	2015-04-15	10	12.3	2459.8	5.5	263.93	0.16	–	BG
HD 151109	2015-04-15			2457.7	5.5	264.14	0.16		
HD 151109	2015-04-15	11	13.3	2656.5	5.7	242.16	0.15	–	BG
HD 151109	2015-04-15			2650.5	5.7	242.26	0.16		
HD 151109	2015-04-15	12	12.1	2691.5	5.8	134.88	0.15	–	BG
HD 151109	2015-04-15			2687.8	5.8	134.53	0.15		
HD 151109	2015-04-15	13	13.6	2691.7	5.8	338.12	0.15	–	BG
HD 151109	2015-04-15			2703.5	5.8	338.22	0.15		
HD 151109	2015-04-15	14	13.4	2742.3	5.9	167.34	0.15	–	BG
HD 151109	2015-04-15			2732.7	5.9	167.25	0.15		
HD 151109	2015-04-15	15	14.4	2888.2	6.1	92.04	0.15	–	BG

HD 151109	2015-04-15			2908.2	6.1	91.73	0.15		
HD 151109	2015-04-15	16	11.4	2959.1	6.2	51.84	0.15	–	BG
HD 151109	2015-04-15			2978.7	6.2	51.72	0.15		
HD 151109	2015-04-15	17	14.1	2968.2	6.2	230.78	0.15	–	BG
HD 151109	2015-04-15			2955.9	6.2	230.73	0.15		
HD 151109	2015-04-15	18	13.8	3009.6	6.2	106.91	0.15	–	BG
HD 151109	2015-04-15			3017.0	6.3	106.62	0.15		
HD 151109	2015-04-15	19	14.8	3149.0	6.4	258.36	0.15	–	BG
HD 151109	2015-04-15			TF					
HD 151109	2015-04-15	20	13.7	3156.7	6.5	250.65	0.15	–	BG
HD 151109	2015-04-15			3151.4	6.4	250.76	0.15		
HD 151109	2015-04-15	21	15.0	3259.6	6.6	9.19	0.15	–	BG
HD 151109	2015-04-15			3289.5	6.6	8.78	0.15		
HD 151109	2015-04-15	22	14.2	3443.1	6.9	282.34	0.15	–	BG
HD 151109	2015-04-15			3435.9	6.9	282.41	0.15		
HD 151109	2015-04-15	23	10.6	3621.1	7.1	41.76	0.14	–	BG
HD 151109	2015-04-15			3634.3	7.2	41.62	0.15		
HD 151109	2015-04-15	24	14.9	3743.5	7.3	29.83	0.14	–	BG
HD 151109	2015-04-15			TF					
HD 151109	2015-04-15	25	12.5	3757.7	7.4	83.72	0.14	–	BG
HD 151109	2015-04-15			3765.7	7.4	83.35	0.15		
HD 151109	2015-04-15	26	13.4	4126.6	7.9	280.56	0.14	–	BG
HD 151109	2015-04-15			4137.6	7.9	280.65	0.14		
HD 151109	2015-04-15	27	12.4	4247.8	8.1	227.07	0.14	–	BG
HD 151109	2015-04-15			4240.7	8.1	227.15	0.14		
HD 151109	2015-04-15	28	12.8	4430.0	8.4	328.02	0.14	–	BG
HD 151109	2015-04-15			4439.0	8.4	328.15	0.14		
HD 151109	2015-04-15	29	14.2	4665.5	8.8	230.91	0.14	–	BG
HD 151109	2015-04-15			4657.2	8.7	230.82	0.14		
HD 151109	2015-04-15	30	13.2	4917.4	9.2	108.73	0.14	–	BG
HD 151109	2015-04-15			4931.0	9.2	108.41	0.14		
HD 151109	2015-04-15	31	11.8	5222.1	9.7	97.22	0.14	–	BG
HD 151109	2015-04-15			5233.0	9.7	96.98	0.14		
HD 151109	2015-04-15	32	11.7	5274.7	9.7	45.72	0.14	–	BG
HD 151109	2015-04-15			5297.7	9.8	45.57	0.14		
HD 151109	2015-04-15	33	11.3	5501.4	10.1	201.20	0.14	–	BG
HD 151109	2015-04-15			5491.2	10.1	201.19	0.14		
HD 151109	2015-04-15	34	12.6	5537.4	10.2	320.88	0.14	–	BG
HD 151109	2015-04-15			5552.5	10.2	320.98	0.14		
HD 151109	2015-04-15	35	14.1	5587.8	10.2	359.34	0.14	–	BG
HD 151109	2015-04-15			5603.8	10.3	359.37	0.14		
HD 151109	2015-04-15	36	13.6	5624.8	10.3	291.77	0.14	–	BG

HD 151109	2015-04-15			5637.9	10.3	291.84	0.14		
HD 151109	2015-04-15	37	12.8	5646.2	10.3	13.34	0.14	–	BG
HD 151109	2015-04-15			5681.3	10.4	13.27	0.14		
HD 151109	2015-04-15	38	13.5	5687.0	10.4	322.02	0.14	–	BG
HD 151109	2015-04-15			5707.7	10.4	322.12	0.14		
HD 151109	2015-04-15	39	10.2	5697.1	10.4	190.38	0.14	–	BG
HD 151109	2015-04-15			5688.2	10.4	190.32	0.14		
HD 151109	2015-04-15	40	12.5	5707.8	10.4	337.45	0.14	–	BG
HD 151109	2015-04-15			5737.7	10.5	337.58	0.14		
HD 151109	2015-04-15	41	13.1	5727.4	10.5	317.45	0.14	–	BG
HD 151109	2015-04-15			5743.4	10.5	317.58	0.14		
HD 151109	2015-04-15	42	12.1	5776.2	10.5	327.96	0.14	–	BG
HD 151109	2015-04-15			5793.7	10.6	328.00	0.14		
HD 151109	2015-04-15	43	12.7	5816.8	10.6	82.03	0.14	–	BG
HD 151109	2015-04-15			5835.1	10.6	81.89	0.14		
HD 151109	2015-04-15	44	12.0	5823.8	10.6	334.11	0.14	–	BG
HD 151109	2015-04-15			5839.4	10.7	334.11	0.14		
HD 151109	2015-04-15	45	14.6	5870.7	10.7	85.94	0.14	–	BG
HD 151109	2015-04-15			5898.3	10.7	85.76	0.14		
HD 151109	2015-04-15	46	11.9	5898.5	10.7	188.95	0.14	–	BG
HD 151109	2015-04-15			5895.1	10.7	188.92	0.14		
HD 151109	2015-04-15	47	15.3	5989.1	10.9	358.76	0.14	–	BG
HD 151109	2015-04-15			TF					
HD 151109	2015-04-15	48	13.8	6113.6	11.1	139.97	0.14	–	BG
HD 151109	2015-04-15			6112.1	11.1	139.72	0.14		
HD 151109	2015-04-15	49	–	6185.6	11.2	150.94	0.14	–	BG
HD 151109	2015-04-15			6178.1	11.2	150.83	0.14		
HD 153053	2015-04-23	1	15.6	1579.1	4.4	331.02	0.18	–	BG
HD 153053	2016-04-09			1633.8	4.5	332.15	0.18		
HD 153053	2015-04-23	2	15.0	2117.2	5.0	30.67	0.16	–	BG
HD 153053	2016-04-09			2195.1	5.1	29.58	0.16		
HD 153053	2015-04-23	3	13.7	2527.7	5.6	243.59	0.16	–	BG
HD 153053	2016-04-09			2496.5	5.5	245.00	0.16		
HD 153053	2015-04-23	4	13.9	3197.6	6.5	83.34	0.15	–	BG
HD 153053	2016-04-09			3212.1	6.5	82.02	0.15		
HD 153053	2015-04-23	5	11.8	3438.8	6.9	48.47	0.15	–	BG
HD 153053	2016-04-09			3497.8	7.0	47.49	0.15		
HD 153053	2015-04-23	6	16.6	3466.0	6.9	83.34	0.15	–	BG
HD 153053	2016-04-09			3402.6	6.8	82.02	0.15		
HD 153053	2015-04-23	7	16.4	3870.9	7.5	238.99	0.14	–	BG
HD 153053	2016-04-09			3839.0	7.5	239.72	0.15		
HD 153053	2015-04-23	8	16.0	4085.2	7.9	107.06	0.14	–	BG

HD 153053	2016-04-09			4026.9	7.8	106.28	0.14		
HD 153053	2015-04-23	9	12.1	4283.4	8.2	85.01	0.14	–	BG
HD 153053	2016-04-09			4300.4	8.2	84.02	0.14		
HD 153053	2015-04-23	10	15.0	4703.2	8.8	31.74	0.14	–	BG
HD 153053	2016-04-09			4767.5	8.9	31.20	0.14		
HD 153053	2015-04-23	11	17.1	5351.9	9.9	292.50	0.14	–	BG
HD 153053	2016-04-09			5388.3	9.9	292.99	0.14		
HD 153053	2015-04-23	12	13.5	5499.7	10.1	16.05	0.14	–	BG
HD 153053	2016-04-09			5569.5	10.2	15.72	0.14		
HD 153053	2015-04-23	13	–	5597.2	10.3	69.87	0.14	–	?BG
HD 153053	2016-04-09			OS					
HD 153053	2015-04-23	14	14.1	6016.6	10.9	107.06	0.14	–	BG
HD 153053	2016-04-09			6006.7	10.9	106.28	0.14		
HD 182919	2016-04-14	1	13.0	1102.7	4.0	341.04	0.23	–	BG
HD 182919	2017-07-15			1129.2	4.0	341.33	0.22		
HD 182919	2016-04-14	2	14.7	1252.5	4.1	173.94	0.21	–	BG
HD 182919	2017-07-15			1218.3	4.1	173.81	0.21		
HD 182919	2016-04-14	3	15.0	1338.2	4.2	211.83	0.20	–	BG
HD 182919	2017-07-15			1313.4	4.1	212.42	0.20		
HD 182919	2016-04-14	4	11.4	2065.6	5.0	211.53	0.17	–	BG
HD 182919	2017-07-15			2043.1	4.9	211.82	0.17		
HD 182919	2016-04-14	5	15.2	2433.4	5.4	183.40	0.16	–	BG
HD 182919	2017-07-15			2401.8	5.4	183.49	0.16		
HD 182919	2016-04-14	6	13.6	2669.9	5.8	186.07	0.16	–	BG
HD 182919	2017-07-15			2635.3	5.7	186.07	0.16		
HD 182919	2016-04-14	7	15.9	2684.2	5.8	65.76	0.15	–	BG
HD 182919	2017-07-15			2724.5	5.8	64.88	0.15		
HD 182919	2016-04-14	8	16.3	2703.1	5.8	323.88	0.15	–	BG
HD 182919	2017-07-15			TF					
HD 182919	2016-04-14	9	15.7	2928.9	6.1	32.39	0.15	–	BG
HD 182919	2017-07-15			2958.8	6.2	31.97	0.15		
HD 182919	2016-04-14	10	13.5	3163.9	6.5	319.53	0.15	–	BG
HD 182919	2017-07-15			3184.7	6.5	319.81	0.15		
HD 182919	2016-04-14	11	16.5	3413.4	6.8	277.50	0.15	–	BG
HD 182919	2017-07-15			3391.4	6.8	277.79	0.15		
HD 182919	2016-04-14	12	15.8	3599.9	7.1	119.78	0.15	–	BG
HD 182919	2017-07-15			3589.9	7.1	119.33	0.15		
HD 182919	2016-04-14	13	13.3	3734.2	7.3	73.95	0.15	–	BG
HD 182919	2017-07-15			3745.6	7.3	73.35	0.15		
HD 182919	2016-04-14	14	15.2	4000.9	7.7	339.98	0.14	–	BG
HD 182919	2017-07-15			4025.0	7.8	340.11	0.14		
HD 182919	2016-04-14	15	11.7	4228.9	8.1	77.51	0.14	–	BG

HD 182919	2017-07-15			4238.9	8.1	77.00	0.14		
HD 182919	2016-04-14	16	15.3	4415.8	8.4	90.41	0.14	–	BG
HD 182919	2017-07-15			4426.6	8.4	89.77	0.14		
HD 182919	2016-04-14	17	16.0	4431.6	8.4	144.43	0.14	–	BG
HD 182919	2017-07-15			4404.2	8.4	144.13	0.14		
HD 182919	2016-04-14	18	16.1	4446.4	8.4	51.46	0.14	–	BG
HD 182919	2017-07-15			4477.6	8.5	51.11	0.14		
HD 182919	2016-04-14	19	14.7	4506.7	8.5	279.36	0.14	–	BG
HD 182919	2017-07-15			4511.7	8.5	279.68	0.14		
HD 182919	2016-04-14	20	12.9	4690.8	8.8	228.32	0.14	–	BG
HD 182919	2017-07-15			4679.5	8.8	228.44	0.14		
HD 182919	2016-04-14	21	16.5	4736.0	8.9	278.78	0.14	–	BG
HD 182919	2017-07-15			4739.9	8.9	278.95	0.14		
HD 182919	2016-04-14	22	16.9	4854.6	9.1	58.73	0.14	–	BG
HD 182919	2017-07-15			4893.2	9.1	58.46	0.14		
HD 182919	2016-04-14	23	16.1	5021.0	9.3	81.90	0.14	–	BG
HD 182919	2017-07-15			5036.2	9.4	81.38	0.14		
HD 182919	2016-04-14	24	14.0	5061.0	9.4	221.76	0.14	–	BG
HD 182919	2017-07-15			5043.5	9.4	221.83	0.14		
HD 182919	2016-04-14	25	14.8	5072.3	9.4	129.64	0.14	–	BG
HD 182919	2017-07-15			5058.1	9.4	129.26	0.14		
HD 182919	2016-04-14	26	16.4	5111.5	9.5	89.59	0.14	–	BG
HD 182919	2017-07-15			5120.4	9.5	88.96	0.14		
HD 182919	2016-04-14	27	12.3	5185.3	9.6	162.91	0.14	–	BG
HD 182919	2017-07-15			5155.0	9.5	162.65	0.14		
HD 182919	2016-04-14	28	13.9	5219.0	9.6	79.70	0.14	–	BG
HD 182919	2017-07-15			5228.3	9.7	79.23	0.14		
HD 182919	2016-04-14	29	17.1	5221.8	9.7	146.77	0.14	–	BG
HD 182919	2017-07-15			5187.7	9.6	146.37	0.14		
HD 182919	2016-04-14	30	16.0	5329.6	9.8	23.01	0.14	–	BG
HD 182919	2017-07-15			5359.9	9.9	22.80	0.14		
HD 182919	2016-04-14	31	13.2	5337.5	9.8	9.80	0.14	–	BG
HD 182919	2017-07-15			5371.8	9.9	9.70	0.14		
HD 182919	2016-04-14	32	16.2	5407.2	10.0	7.20	0.14	–	BG
HD 182919	2017-07-15			5444.9	10.0	7.15	0.14		
HD 182919	2016-04-14	33	11.3	5420.8	10.0	326.86	0.14	–	BG
HD 182919	2017-07-15			5445.5	10.0	326.93	0.14		
HD 182919	2016-04-14	34	14.8	5444.9	10.0	345.53	0.14	–	BG
HD 182919	2017-07-15			5479.2	10.1	345.58	0.14		
HD 182919	2016-04-14	35	11.8	5492.2	10.1	269.28	0.14	–	BG
HD 182919	2017-07-15			5491.2	10.1	269.43	0.14		
HD 182919	2016-04-14	36	–	5567.3	10.2	90.41	0.14	–	BG

HD 182919	2017-07-15			5569.7	10.2	89.98	0.14		
HD 182919	2016-04-14	37	13.8	5606.3	10.3	188.81	0.14	–	BG
HD 182919	2017-07-15			5580.2	10.2	188.74	0.14		
HD 182919	2016-04-14	38	15.9	5964.4	10.9	131.72	0.14	–	BG
HD 182919	2017-07-15			OS					
HD 182919	2016-04-14	39	14.2	6066.0	11.0	307.88	0.14	–	BG
HD 182919	2017-07-15			6082.9	11.1	308.02	0.14		
HD 182919	2016-04-14	40	–	6223.3	11.3	191.67	0.14	–	BG
HD 182919	2017-07-15			6196.9	11.2	191.62	0.14		
HD 196544	2015-05-29	1	12.5	4203.1	8.0	93.15	0.14	N13	BG
HD 196544	2015-05-29	2	11.4	4600.4	8.7	90.24	0.14	N13	BG
HD 223352	2015-07-18	1	5.2	3373.8	6.8	239.13	0.15	dR11, R13, G16	C
HD 223352	2015-07-18	2	4.4	3714.1	7.3	238.06	0.14	dR11, R13, G16	C

Appendix D

Common proper motion plots for highly dusty targets

Here we present the Common Proper Motion plots for each of the candidates in Chapter 4 with multiple epochs of data. Color Schemes are as for Figure 3.3 in Chapter 3.

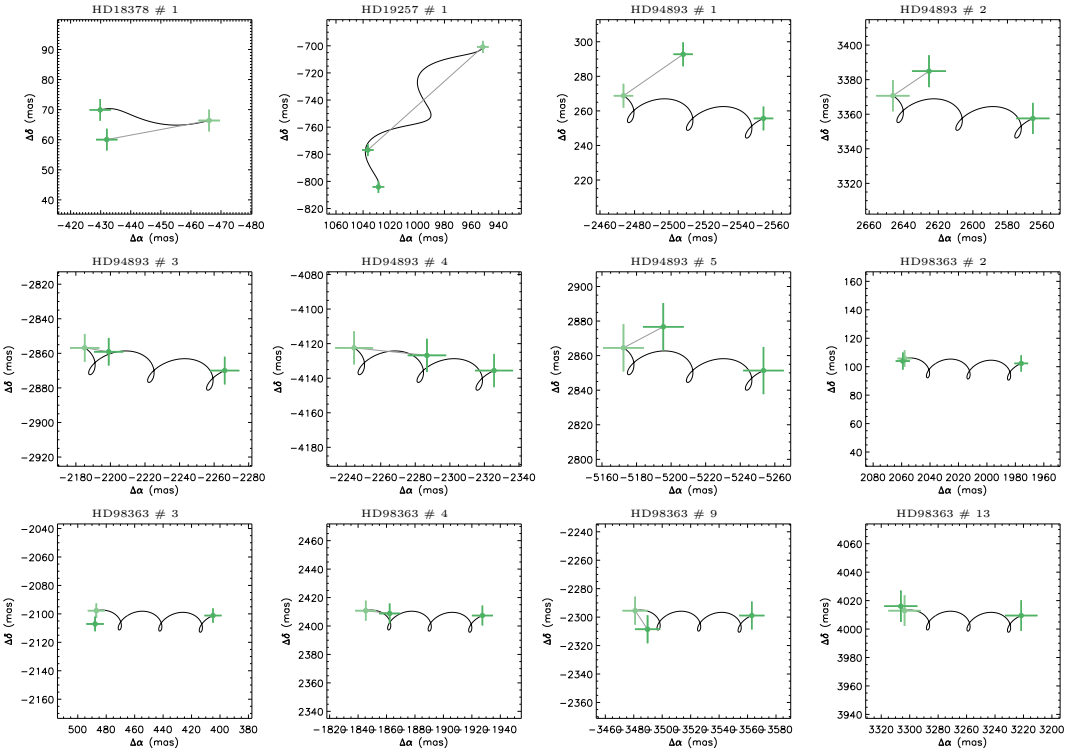

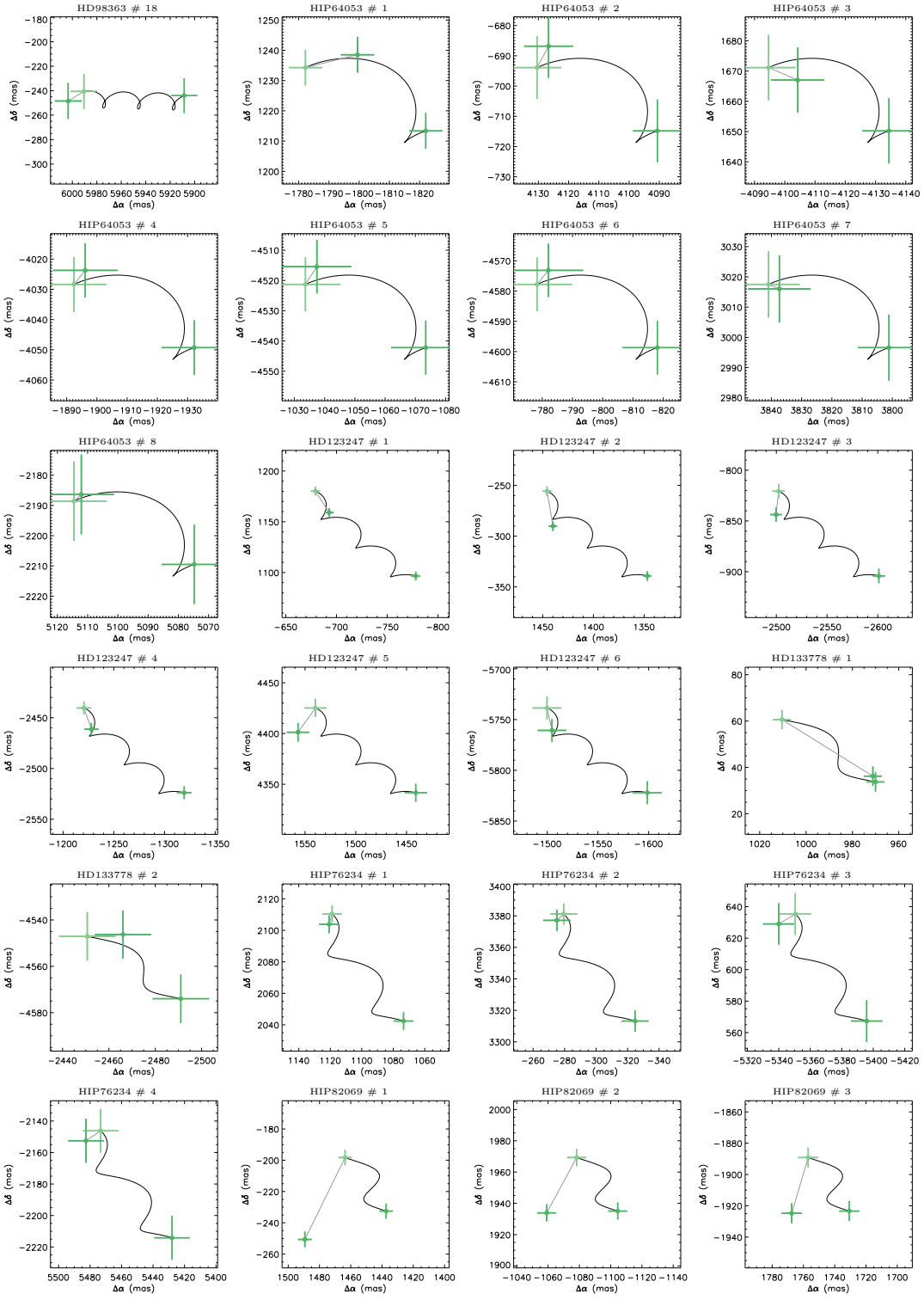
HD98363 # 18
HIP64053 # 1
HIP64053 # 2
HIP64053 # 3
HIP64053 # 4
HIP64053 # 5
HIP64053 # 6
HIP64053 # 7
HIP64053 # 8
HD123247 # 1
HD123247 # 2
HD123247 # 3
HD123247 # 4
HD123247 # 5
HD123247 # 6
HD133778 # 1
HD133778 # 2
HIP76234 # 1
HIP76234 # 2
HIP76234 # 3
HIP76234 # 4
HIP82069 # 1
HIP82069 # 2
HIP82069 # 3
Δδ (mas)
Δα (mas)

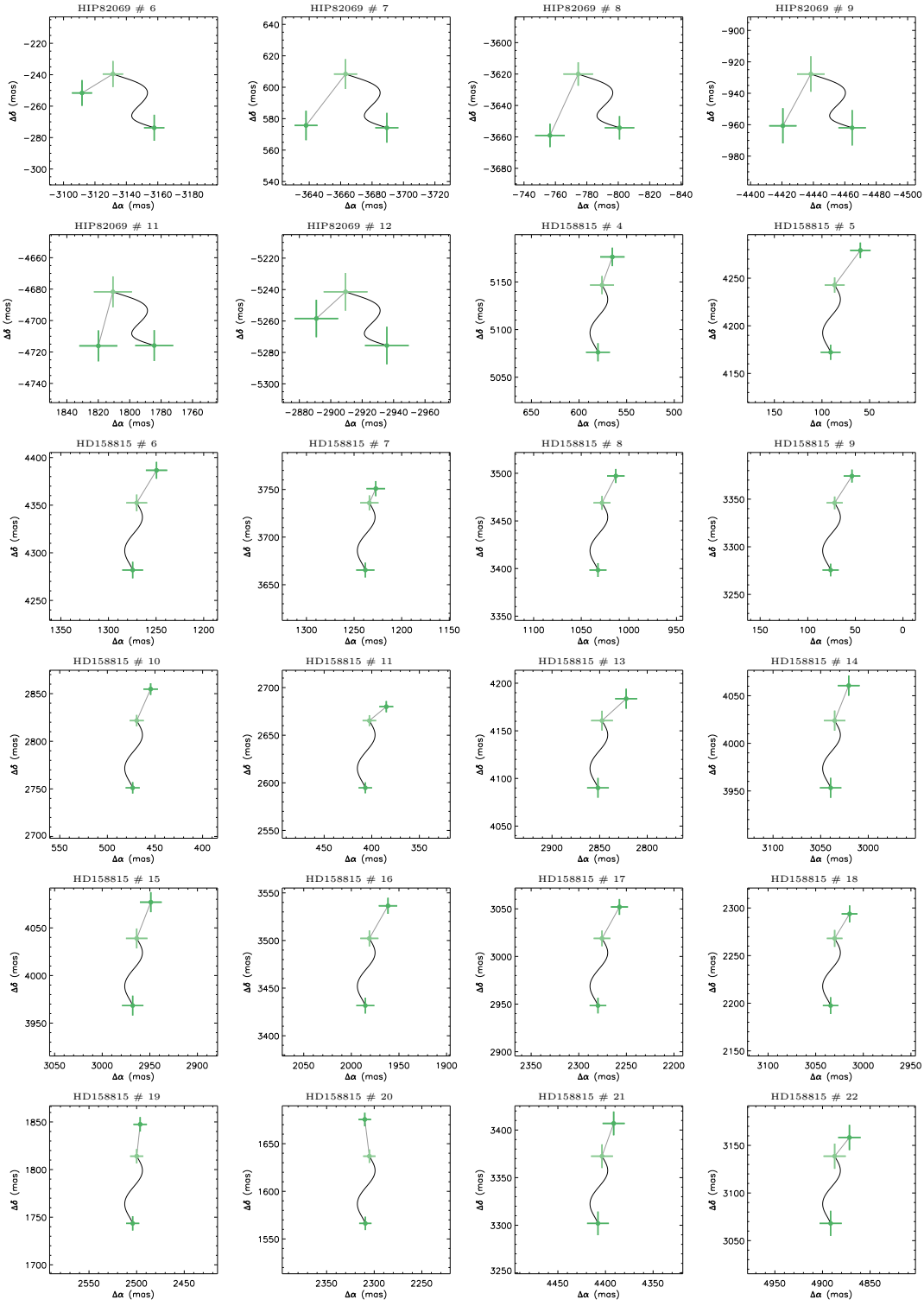
HIP82069 # 6
HIP82069 # 7
HIP82069 # 8
HIP82069 # 9
HIP82069 # 11
HIP82069 # 12
HD158815 # 4
HD158815 # 5
HD158815 # 6
HD158815 # 7
HD158815 # 8
HD158815 # 9
HD158815 # 10
HD158815 # 11
HD158815 # 13
HD158815 # 14
HD158815 # 15
HD158815 # 16
HD158815 # 17
HD158815 # 18
HD158815 # 19
HD158815 # 20
HD158815 # 21
HD158815 # 22
Δδ (mas)
Δα (mas)

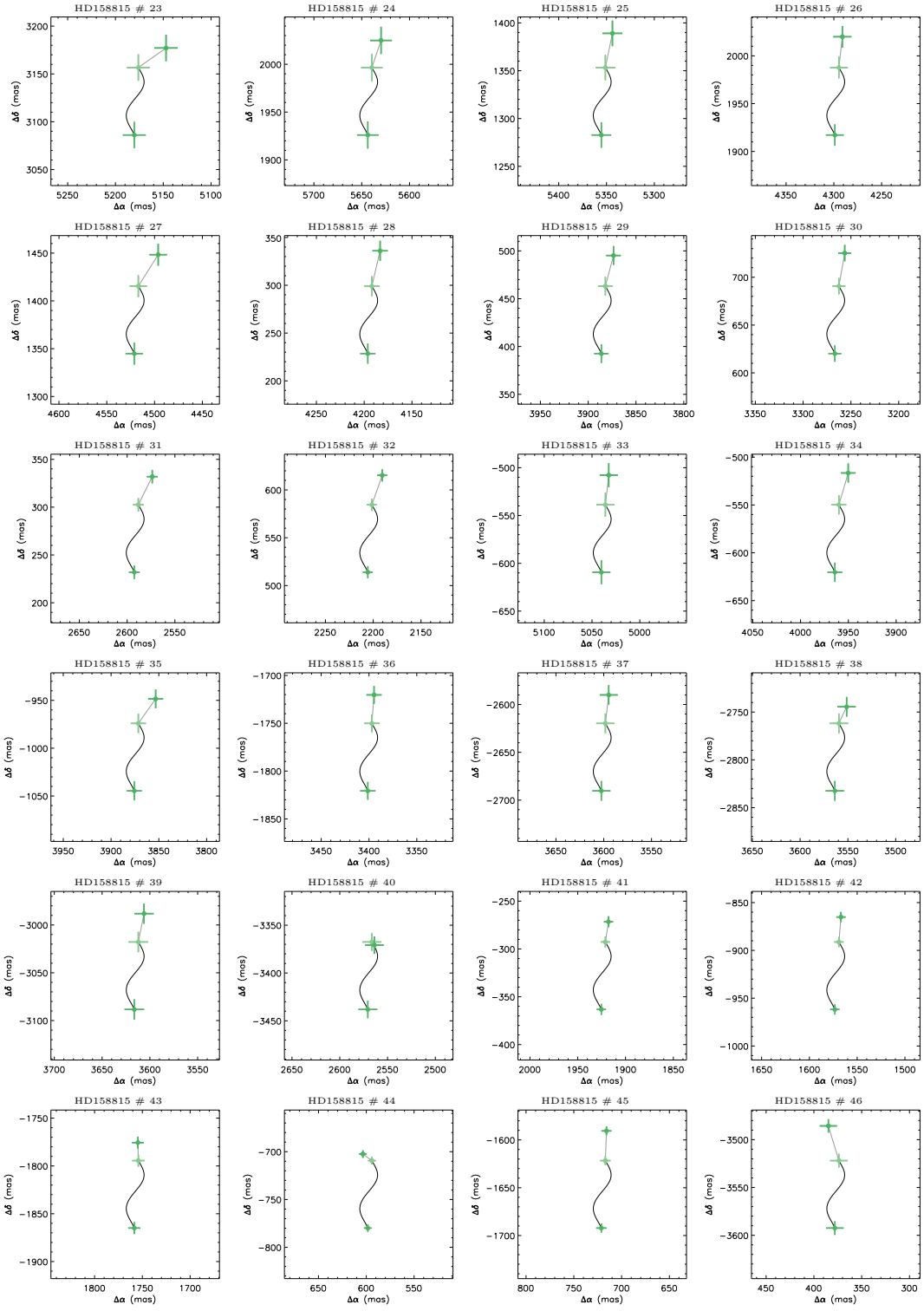
HD158815 # 23
HD158815 # 24
HD158815 # 25
HD158815 # 26
HD158815 # 27
HD158815 # 28
HD158815 # 29
HD158815 # 30
HD158815 # 31
HD158815 # 32
HD158815 # 33
HD158815 # 34
HD158815 # 35
HD158815 # 36
HD158815 # 37
HD158815 # 38
HD158815 # 39
HD158815 # 40
HD158815 # 41
HD158815 # 42
HD158815 # 43
HD158815 # 44
HD158815 # 45
HD158815 # 46
Δδ (mas)
Δα (mas)

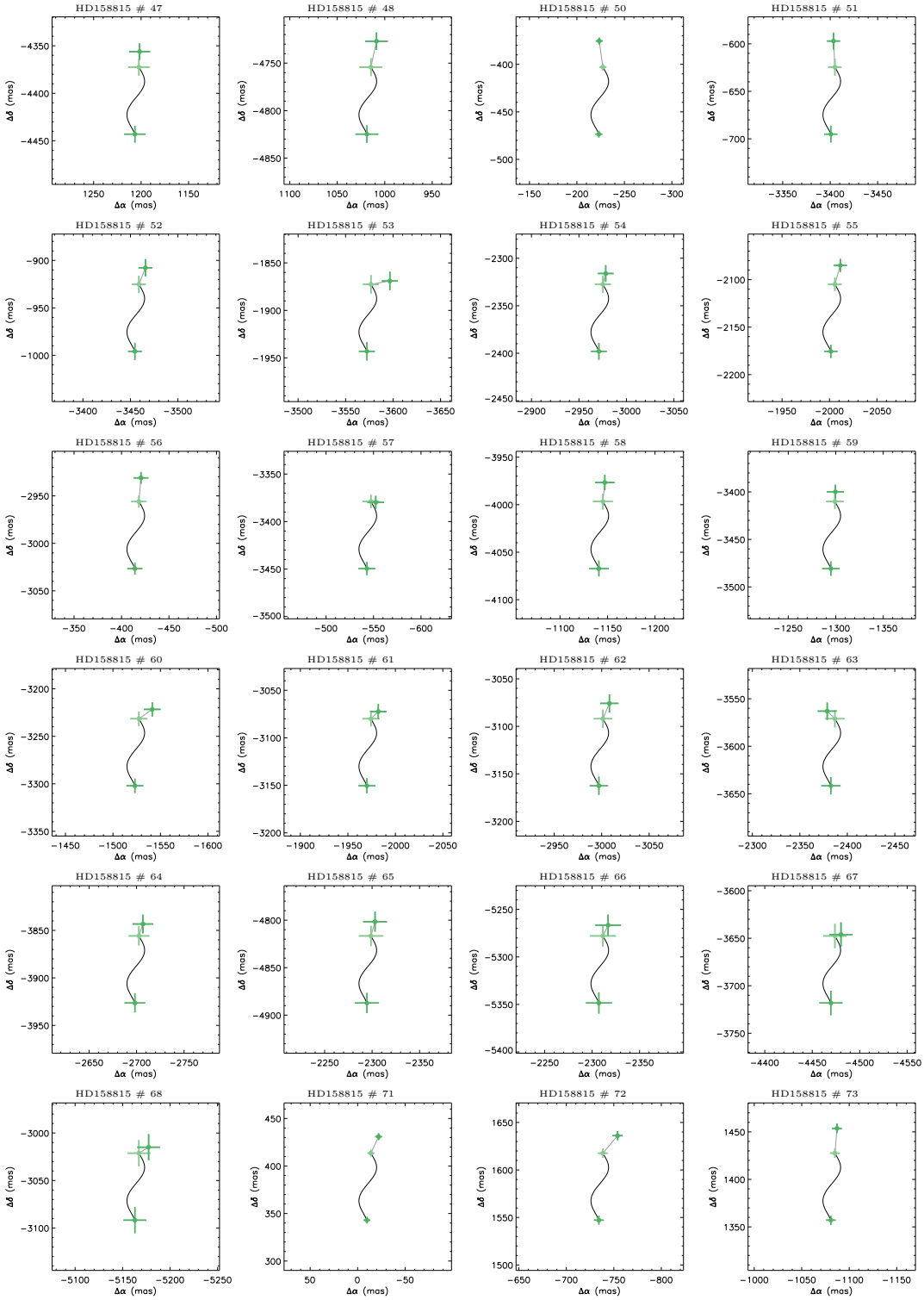
HD158815 # 47
HD158815 # 48
HD158815 # 50
HD158815 # 51
HD158815 # 52
HD158815 # 53
HD158815 # 54
HD158815 # 55
HD158815 # 56
HD158815 # 57
HD158815 # 58
HD158815 # 59
HD158815 # 60
HD158815 # 61
HD158815 # 62
HD158815 # 63
HD158815 # 64
HD158815 # 65
HD158815 # 66
HD158815 # 67
HD158815 # 68
HD158815 # 71
HD158815 # 72
HD158815 # 73
Δδ (mas)
Δα (mas)

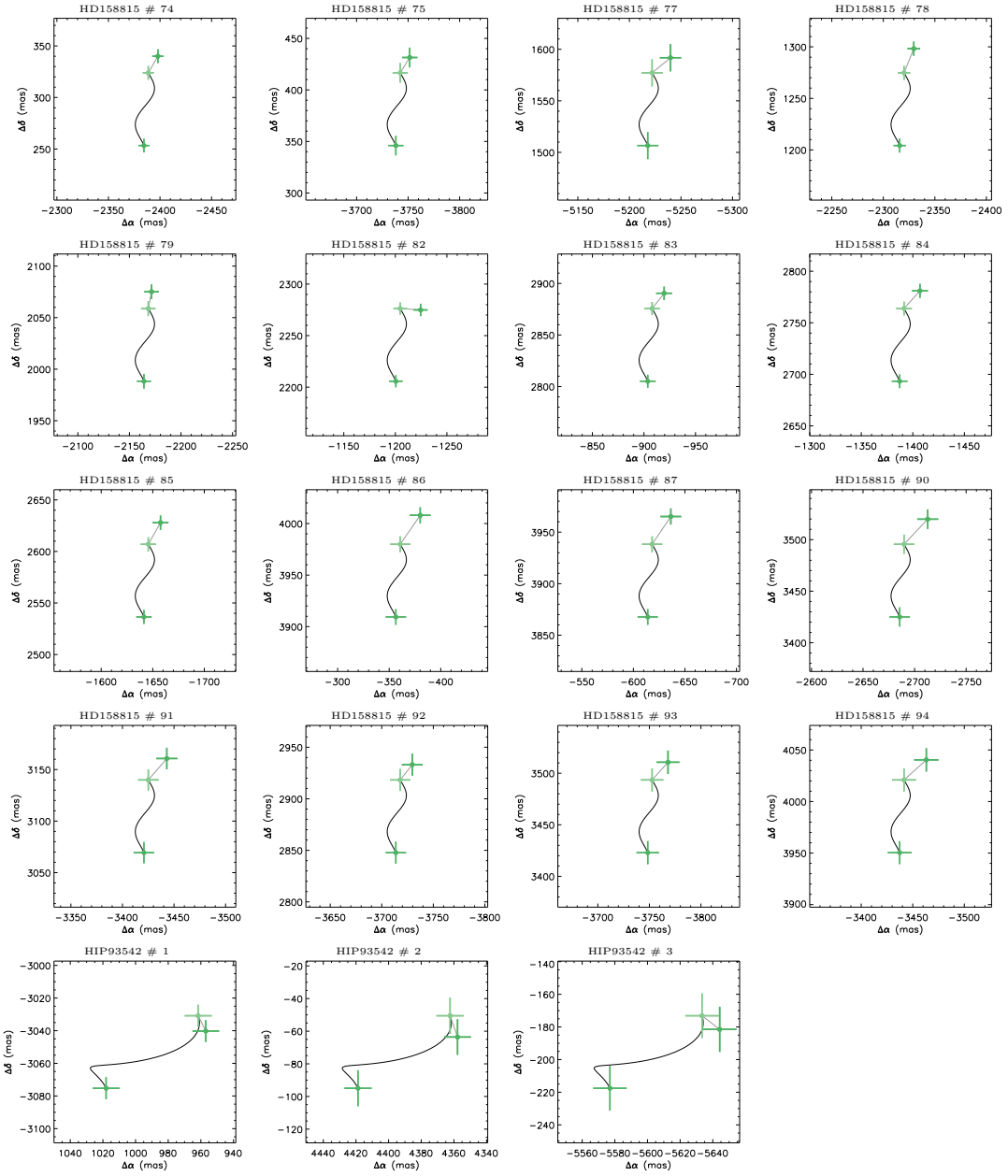
HD158815 # 74
HD158815 # 75
HD158815 # 77
HD158815 # 78
HD158815 # 79
HD158815 # 82
HD158815 # 83
HD158815 # 84
HD158815 # 85
HD158815 # 86
HD158815 # 87
HD158815 # 90
HD158815 # 91
HD158815 # 92
HD158815 # 93
HD158815 # 94
HIP93542 # 1
HIP93542 # 2
HIP93542 # 3
Δδ (mas)
Δα (mas)

Appendix E

Contrast limits for initial observations of highly dusty targets

Here we present contrast limits for each individual observation in Chapter 4. Orange and blue lines represent data from the SPHERE/IRDIS and SPHERE/IFS subsystems respectively. The contrasts are calculated by injecting fake planets, with full details given in Section 3.4.4 in the main text.

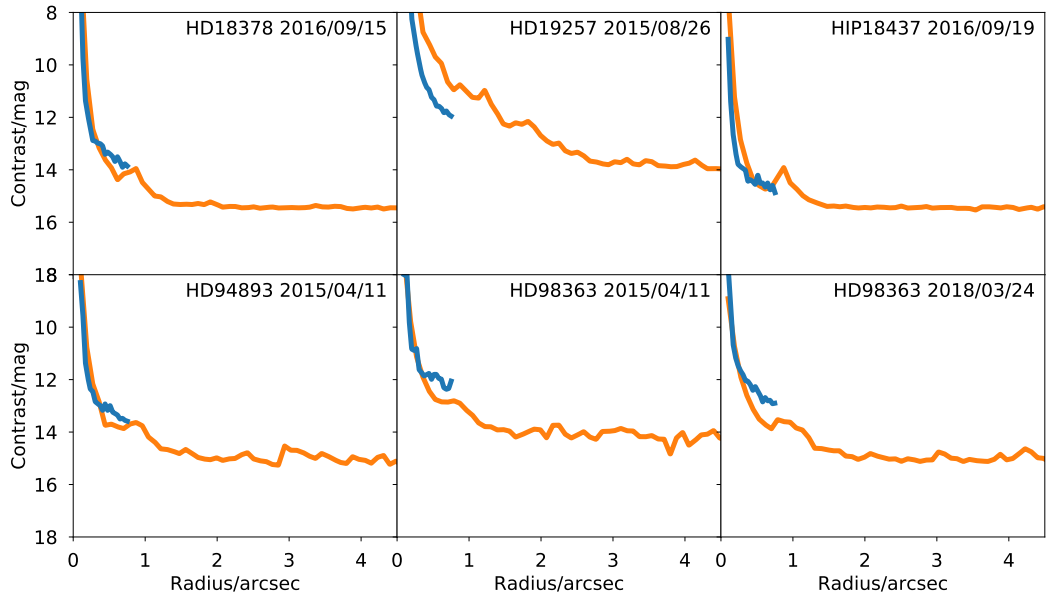

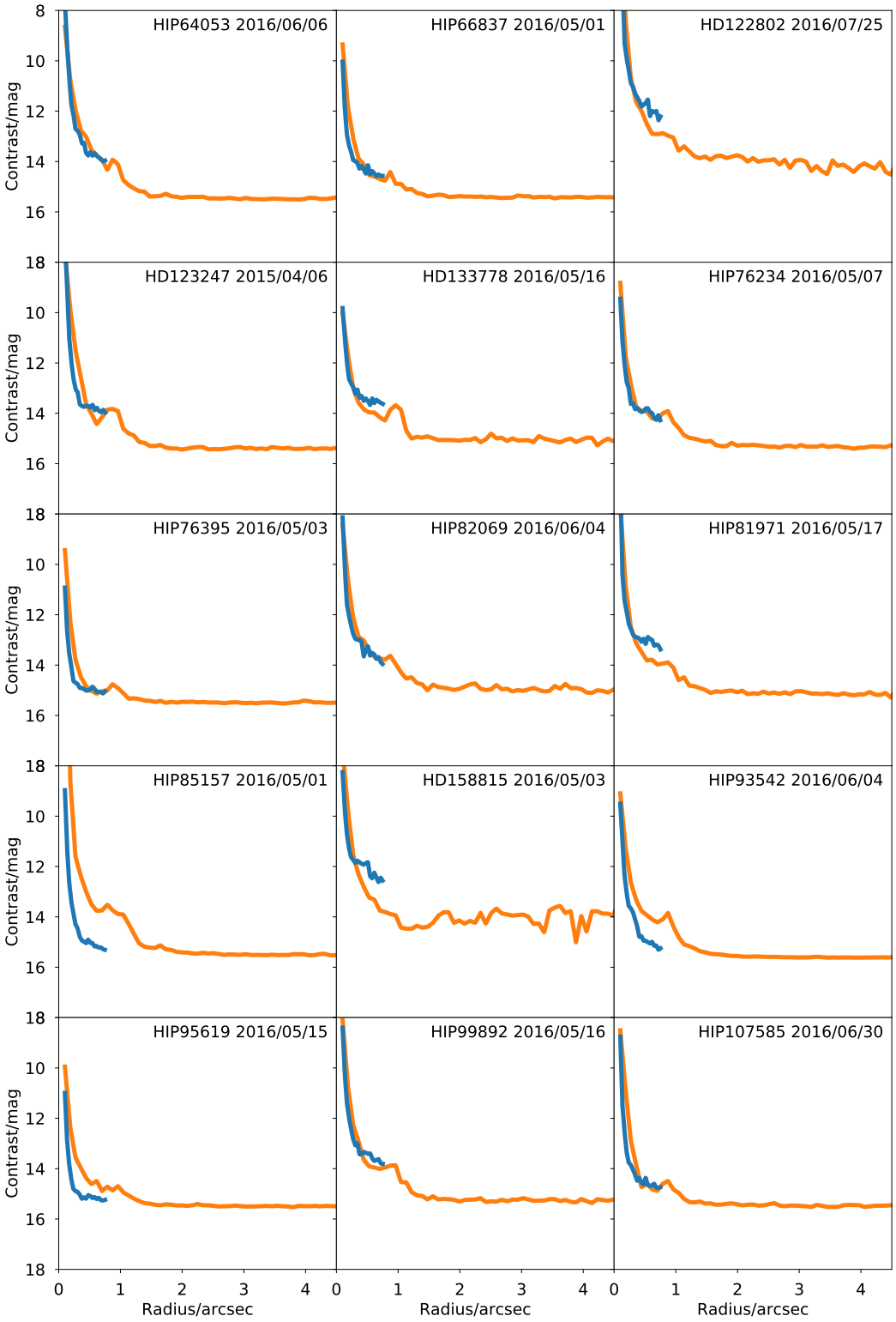
HIP64053 2016/06/06
HIP66837 2016/05/01
HD122802 2016/07/25
HD123247 2015/04/06
HD133778 2016/05/16
HIP76234 2016/05/07
HIP76395 2016/05/03
HIP82069 2016/06/04
HIP81971 2016/05/17
HIP85157 2016/05/01
HD158815 2016/05/03
HIP93542 2016/06/04
HIP95619 2016/05/15
HIP99892 2016/05/16
HIP107585 2016/06/30
Contrast/mag
Radius/arcsec

Appendix F

Astrometry for all candidates identified in Chapter 4

In this appendix we present full astrometry for all of the candidates discussed in Chapter 4. The candidates are classified as background objects (BG), companions (C) or requiring further work (tbc).

Note. TF = candidate too faint to be redetected, OS = candidate off-screen in this epoch.

Star	Epoch Date	No.	Sep(″)	σ_{sep}	PA	σ_{PA}	Status
HD18378	2016-09-15	1	435.5	3.5	279.24	0.48	C
HD18378	2017-08-29		436.2	3.5	277.91	0.48	
HD19257	2015-08-26	1	1305.7	4.1	128.01	0.20	C
HD19257	2017-09-01		1295.3	4.1	126.80	0.20	
HIP94893	2015-04-11	1	2567.4	5.6	275.71	0.15	BG
HIP94893	2018-01-07		2525.2	5.6	276.66	0.16	
HIP94893	2015-04-11	2	3656.8	7.2	218.29	0.14	BG
HIP94893	2018-01-07		3606.9	7.1	217.56	0.15	
HIP94893	2015-04-11	3	4225.4	8.1	37.38	0.14	BG
HIP94893	2018-01-07		4283.7	8.2	37.80	0.14	
HIP94893	2015-04-11	4	4744.6	8.9	209.35	0.14	BG
HIP94893	2018-01-07		4718.0	8.8	208.99	0.14	
HIP94893	2015-04-11	5	5977.4	10.9	298.49	0.14	BG
HIP94893	2018-01-07		5938.7	10.8	298.97	0.14	
HD98363	2015-04-11	1	1455.9	4.3	277.48	0.19	tbc
HD98363			–				

HD98363	2015-04-11	2	1978.5	4.9	87.04	0.17	BG
HD98363	2018-03-24		2061.8	5.0	87.11	0.17	
HD98363	2015-04-11	3	2139.8	5.1	169.09	0.16	BG
HD98363	2018-03-24		2162.8	5.1	166.96	0.16	
HD98363	2015-04-11	4	2439.4	5.5	234.72	0.16	tbc
HD98363			–				
HD98363	2015-04-11	5	3083.9	6.3	321.32	0.15	BG
HD98363	2018-03-24		3044.7	6.3	322.29	0.15	
HD98363	2015-04-11	6	3755.9	7.3	200.55	0.15	tbc
HD98363			–				
HD98363	2015-04-11	7	3828.5	7.5	83.78	0.15	tbc
HD98363			–				
HD98363	2015-04-11	8	4188.1	8.0	307.66	0.14	tbc
HD98363			–				
HD98363	2015-04-11	9	4240.3	8.1	237.17	0.14	BG
HD98363	2018-03-24		4184.2	8.0	236.51	0.14	
HD98363	2015-04-11	10	4654.8	8.7	250.75	0.14	tbc
HD98363			–				
HD98363	2015-04-11	11	4931.0	9.2	300.22	0.14	tbc
HD98363			–				
HD98363	2015-04-11	12	5104.1	9.5	120.45	0.14	tbc
HD98363			–				
HD98363	2015-04-11	13	5143.4	9.5	38.78	0.14	BG
HD98363	2018-03-24		5201.9	9.6	39.46	0.14	
HD98363	2015-04-11	14	5145.4	9.5	333.33	0.14	tbc
HD98363			–				
HD98363	2015-04-11	15	5353.4	9.9	269.77	0.14	tbc
HD98363			–				
HD98363	2015-04-11	16	5447.4	10.0	215.43	0.14	tbc
HD98363			–				
HD98363	2015-04-11	17	5517.5	10.1	31.81	0.14	tbc
HD98363			–				
HD98363	2015-04-11	18	5913.6	10.8	92.37	0.14	BG
HD98363	2018-03-24		6008.6	10.9	92.37	0.14	
HD98363	2015-04-11	19	6222.7	11.3	22.08	0.14	tbc
HIP64053	2016-06-06	1	2189.1	5.1	303.66	0.16	BG
HIP64053	2017-06-23		2184.5	5.1	304.54	0.16	
HIP64053	2016-06-06	2	4152.6	8.0	99.91	0.14	BG
HIP64053	2017-06-23		4183.4	8.0	99.45	0.14	
HIP64053	2016-06-06	3	4451.6	8.4	291.76	0.14	BG
HIP64053	2017-06-23		4429.9	8.4	292.11	0.14	
HIP64053	2016-06-06	4	4486.6	8.5	205.51	0.14	BG

HIP64053	2017-06-23		4448.1	8.4	205.23	0.14	
HIP64053	2016-06-06	5	4667.3	8.8	193.30	0.14	BG
HIP64053	2017-06-23		4633.1	8.7	192.94	0.14	
HIP64053	2016-06-06	6	4670.9	8.8	190.09	0.14	BG
HIP64053	2017-06-23		4639.5	8.7	189.70	0.14	
HIP64053	2016-06-06	7	4840.3	9.0	51.75	0.14	BG
HIP64053	2017-06-23		4880.8	9.1	51.83	0.14	
HIP64053	2016-06-06	8	5534.9	10.2	113.53	0.14	BG
HIP64053	2017-06-23		5560.0	10.2	113.16	0.14	
HD122802	2016-07-25	1	6339.4	11.5	229.63	0.14	tbc
HD123247	2015-04-06	1	1344.6	4.2	324.64	0.20	BG
HD123247	2018-03-22		1350.3	4.2	329.13	0.20	
HD123247	2015-04-06	2	1388.9	4.2	104.14	0.20	BG
HD123247	2018-03-22		1468.9	4.3	101.39	0.19	
HD123247	2015-04-06	3	2753.8	5.9	250.83	0.15	BG
HD123247	2018-03-22		2638.3	5.7	251.35	0.15	
HD123247	2015-04-06	4	2847.9	6.0	207.60	0.15	BG
HD123247	2018-03-22		2750.6	5.9	206.52	0.15	
HD123247	2015-04-06	5	4574.5	8.6	18.36	0.14	BG
HD123247	2018-03-22		4668.5	8.8	19.48	0.14	
HD123247	2015-04-06	6	6037.6	11.0	195.35	0.14	BG
HD123247	2018-03-22		5953.9	10.8	194.64	0.14	
HD133778	2016-05-16	1	970.6	3.8	88.01	0.25	C
HD133778	2017-06-22		971.9	3.9	87.86	0.25	
HD133778	2016-05-16	2	5208.3	9.6	208.57	0.14	BG
HD133778	2017-06-22		5172.1	9.6	208.48	0.14	
HIP76234	2016-05-07	1	2307.3	5.3	27.73	0.16	BG
HIP76234	2018-03-17		2383.7	5.4	28.05	0.16	
HIP76234	2016-05-07	2	3329.1	6.7	354.40	0.15	BG
HIP76234	2018-03-17		3388.3	6.8	355.34	0.15	
HIP76234	2016-05-07	3	5425.6	10.0	276.00	0.14	BG
HIP76234	2018-03-17		5376.9	9.9	276.72	0.14	
HIP76234	2016-05-07	4	5862.2	10.7	112.19	0.14	BG
HIP76234	2018-03-17		5890.0	10.7	111.44	0.14	
HIP76395	2016-05-03	1	3993.1	7.7	228.84	0.14	tbc
HIP82069	2016-06-04	1	1456.0	4.3	99.19	0.19	tbc
HIP82069	2017-07-15		1510.3	4.3	99.55	0.19	
HIP82069	2016-06-04	2	2228.1	5.2	330.28	0.16	tbc
HIP82069	2017-07-15		2204.9	5.1	331.29	0.16	
HIP82069	2016-06-04	3	2587.4	5.7	138.02	0.16	tbc
HIP82069	2017-07-15		2613.2	5.7	137.44	0.16	
HIP82069	2016-06-04	4	2746.0	5.9	90.62	0.15	tbc

HIP82069	2017-07-15		TF				
HIP82069	2016-06-04	5	2906.3	6.1	93.77	0.15	tbc
HIP82069	2017-07-15		TF				
HIP82069	2016-06-04	6	3169.6	6.5	265.05	0.15	tbc
HIP82069	2017-07-15		3121.9	6.4	265.38	0.15	
HIP82069	2016-06-04	7	3733.8	7.3	278.85	0.15	tbc
HIP82069	2017-07-15		3683.2	7.2	278.99	0.15	
HIP82069	2016-06-04	8	3740.9	7.3	192.36	0.15	tbc
HIP82069	2017-07-15		3736.4	7.3	191.68	0.15	
HIP82069	2016-06-04	9	4567.1	8.6	257.84	0.14	tbc
HIP82069	2017-07-15		4523.8	8.5	257.74	0.14	
HIP82069	2016-06-04	10	4643.9	8.7	105.72	0.14	tbc
HIP82069	2017-07-15		TF				
HIP82069	2016-06-04	11	5042.2	9.4	159.27	0.14	tbc
HIP82069	2017-07-15		5055.1	9.4	158.90	0.14	
HIP82069	2016-06-04	12	6037.4	11.0	209.09	0.14	tbc
HIP82069	2017-07-15		6000.7	10.9	208.80	0.14	
HD158815	2016-05-03	1	5872.0	10.7	1.58	0.14	tbc
HD158815	2017-06-29		OS				
HD158815	2016-05-03	2	6119.3	11.1	17.06	0.14	tbc
HD158815	2017-06-29		OS				
HD158815	2016-05-03	3	6258.3	11.3	31.63	0.14	tbc
HD158815	2017-06-29		OS				
HD158815	2016-05-03	4	5109.2	9.5	6.52	0.14	BG
HD158815	2017-06-29		5207.0	9.6	6.23	0.14	
HD158815	2016-05-03	5	4173.2	8.0	1.25	0.14	BG
HD158815	2017-06-29		4279.6	8.2	0.80	0.14	
HD158815	2016-05-03	6	4467.6	8.5	16.58	0.14	BG
HD158815	2017-06-29		4561.1	8.6	15.90	0.14	
HD158815	2016-05-03	7	3868.9	7.5	18.66	0.15	BG
HD158815	2017-06-29		3946.5	7.6	18.12	0.15	
HD158815	2016-05-03	8	3551.8	7.0	16.90	0.15	BG
HD158815	2017-06-29		3641.1	7.2	16.16	0.15	
HD158815	2016-05-03	9	3276.5	6.6	1.33	0.15	BG
HD158815	2017-06-29		3374.7	6.8	0.91	0.15	
HD158815	2016-05-03	10	2791.6	5.9	9.76	0.15	BG
HD158815	2017-06-29		2890.7	6.1	9.05	0.15	
HD158815	2016-05-03	11	2626.4	5.7	8.91	0.16	BG
HD158815	2017-06-29		2707.4	5.8	8.17	0.15	
HD158815	2016-05-03	12	5346.3	9.9	36.56	0.14	tbc
HD158815	2017-06-29		TF				
HD158815	2016-05-03	13	4986.2	9.3	34.89	0.14	BG

HD158815	2017-06-29		5046.6	9.4	34.00	0.14	
HD158815	2016-05-03	14	4986.7	9.3	37.56	0.14	BG
HD158815	2017-06-29		5060.9	9.4	36.64	0.14	
HD158815	2016-05-03	15	4955.5	9.2	36.79	0.14	BG
HD158815	2017-06-29		5031.7	9.3	35.88	0.14	
HD158815	2016-05-03	16	3964.6	7.7	30.05	0.14	BG
HD158815	2017-06-29		4044.0	7.8	29.02	0.14	
HD158815	2016-05-03	17	3727.0	7.3	37.71	0.15	BG
HD158815	2017-06-29		3796.0	7.4	36.49	0.15	
HD158815	2016-05-03	18	3746.5	7.3	54.09	0.15	BG
HD158815	2017-06-29		3787.9	7.4	52.73	0.15	
HD158815	2016-05-03	19	3051.3	6.3	55.15	0.15	BG
HD158815	2017-06-29		3105.6	6.4	53.49	0.15	
HD158815	2016-05-03	20	2790.4	5.9	55.85	0.15	BG
HD158815	2017-06-29		2853.6	6.0	54.05	0.15	
HD158815	2016-05-03	21	5507.5	10.1	53.16	0.14	BG
HD158815	2017-06-29		5558.1	10.2	52.19	0.14	
HD158815	2016-05-03	22	5774.0	10.5	57.90	0.14	BG
HD158815	2017-06-29		5805.9	10.6	57.05	0.14	
HD158815	2016-05-03	23	6029.9	11.0	59.22	0.14	BG
HD158815	2017-06-29		6048.7	11.0	58.31	0.14	
HD158815	2016-05-03	24	5963.2	10.9	71.16	0.14	BG
HD158815	2017-06-29		5982.9	10.9	70.22	0.14	
HD158815	2016-05-03	25	5506.9	10.1	76.53	0.14	BG
HD158815	2017-06-29		5521.4	10.1	75.43	0.14	
HD158815	2016-05-03	26	4707.1	8.8	65.96	0.14	BG
HD158815	2017-06-29		4742.8	8.9	64.79	0.14	
HD158815	2016-05-03	27	4717.0	8.8	73.43	0.14	BG
HD158815	2017-06-29		4723.7	8.9	72.14	0.14	
HD158815	2016-05-03	28	4202.4	8.0	86.88	0.14	BG
HD158815	2017-06-29		4196.8	8.0	85.41	0.14	
HD158815	2016-05-03	29	3906.0	7.6	84.23	0.15	BG
HD158815	2017-06-29		3905.1	7.6	82.71	0.15	
HD158815	2016-05-03	30	3325.1	6.7	79.25	0.15	BG
HD158815	2017-06-29		3336.2	6.7	77.44	0.15	
HD158815	2016-05-03	31	2602.9	5.7	84.89	0.16	BG
HD158815	2017-06-29		2595.0	5.7	82.65	0.16	
HD158815	2016-05-03	32	2264.7	5.2	76.88	0.16	BG
HD158815	2017-06-29		2275.3	5.2	74.31	0.16	
HD158815	2016-05-03	33	5076.9	9.4	96.89	0.14	BG
HD158815	2017-06-29		5058.0	9.4	95.76	0.14	
HD158815	2016-05-03	34	4012.4	7.7	98.89	0.14	BG

HD158815	2017-06-29		3983.8	7.7	97.45	0.14	
HD158815	2016-05-03	35	4014.0	7.7	105.08	0.14	BG
HD158815	2017-06-29		3968.3	7.7	103.83	0.14	
HD158815	2016-05-03	36	3857.9	7.5	118.16	0.15	BG
HD158815	2017-06-29		3805.7	7.4	116.87	0.15	
HD158815	2016-05-03	37	4496.2	8.5	126.75	0.14	BG
HD158815	2017-06-29		4430.6	8.4	125.77	0.14	
HD158815	2016-05-03	38	4552.2	8.6	128.48	0.14	BG
HD158815	2017-06-29		4488.2	8.5	127.70	0.14	
HD158815	2016-05-03	39	4755.6	8.9	130.50	0.14	BG
HD158815	2017-06-29		4683.2	8.8	129.65	0.14	
HD158815	2016-05-03	40	4292.9	8.2	143.21	0.14	BG
HD158815	2017-06-29		4235.1	8.1	142.74	0.14	
HD158815	2016-05-03	41	1959.3	4.8	100.69	0.17	BG
HD158815	2017-06-29		1937.0	4.8	98.06	0.17	
HD158815	2016-05-03	42	1844.0	4.7	121.44	0.17	BG
HD158815	2017-06-29		1789.9	4.6	118.90	0.18	
HD158815	2016-05-03	43	2563.2	5.6	136.68	0.16	BG
HD158815	2017-06-29		2496.3	5.5	135.34	0.16	
HD158815	2016-05-03	44	983.0	3.9	142.50	0.24	BG
HD158815	2017-06-29		926.2	3.8	139.33	0.25	
HD158815	2016-05-03	45	1839.5	4.7	156.92	0.17	BG
HD158815	2017-06-29		1744.3	4.6	155.77	0.18	
HD158815	2016-05-03	46	3612.3	7.1	173.99	0.15	BG
HD158815	2017-06-29		3506.8	7.0	173.70	0.15	
HD158815	2016-05-03	47	4603.9	8.7	164.81	0.14	BG
HD158815	2017-06-29		4518.8	8.5	164.58	0.14	
HD158815	2016-05-03	48	4931.1	9.2	168.08	0.14	BG
HD158815	2017-06-29		4833.4	9.0	167.95	0.14	
HD158815	2016-05-03	49	5773.0	10.5	167.23	0.14	tbc
HD158815	2017-06-29		OS				
HD158815	2016-05-03	50	523.4	3.6	205.24	0.40	BG
HD158815	2017-06-29		436.9	3.5	210.77	0.47	
HD158815	2016-05-03	51	3471.1	6.9	258.45	0.15	BG
HD158815	2017-06-29		3455.5	6.9	260.05	0.15	
HD158815	2016-05-03	52	3595.4	7.1	253.92	0.15	BG
HD158815	2017-06-29		3582.7	7.1	255.32	0.15	
HD158815	2016-05-03	53	4066.7	7.8	241.46	0.14	BG
HD158815	2017-06-29		4053.2	7.8	242.54	0.14	
HD158815	2016-05-03	54	3818.0	7.4	231.09	0.15	BG
HD158815	2017-06-29		3772.8	7.4	232.13	0.15	
HD158815	2016-05-03	55	2956.1	6.2	222.61	0.15	BG

HD158815	2017-06-29		2897.1	6.1	223.97	0.15	
HD158815	2016-05-03	56	3054.7	6.3	187.79	0.15	BG
HD158815	2017-06-29		2961.1	6.2	188.16	0.15	
HD158815	2016-05-03	57	3492.0	6.9	188.95	0.15	BG
HD158815	2017-06-29		3424.7	6.8	189.28	0.15	
HD158815	2016-05-03	58	4224.2	8.1	195.67	0.14	BG
HD158815	2017-06-29		4138.8	7.9	196.09	0.14	
HD158815	2016-05-03	59	3713.7	7.3	200.41	0.15	BG
HD158815	2017-06-29		3639.8	7.2	200.92	0.15	
HD158815	2016-05-03	60	3636.4	7.2	204.76	0.15	BG
HD158815	2017-06-29		3571.4	7.1	205.57	0.15	
HD158815	2016-05-03	61	3715.7	7.3	212.02	0.15	BG
HD158815	2017-06-29		3656.2	7.2	212.83	0.15	
HD158815	2016-05-03	62	4357.1	8.3	223.46	0.14	BG
HD158815	2017-06-29		4302.2	8.2	224.36	0.14	
HD158815	2016-05-03	63	4351.8	8.3	213.20	0.14	BG
HD158815	2017-06-29		4284.1	8.2	213.73	0.14	
HD158815	2016-05-03	64	4764.2	8.9	214.50	0.14	BG
HD158815	2017-06-29		4700.8	8.8	215.16	0.14	
HD158815	2016-05-03	65	5399.0	9.9	205.15	0.14	BG
HD158815	2017-06-29		5325.3	9.8	205.62	0.14	
HD158815	2016-05-03	66	5824.9	10.6	203.33	0.14	BG
HD158815	2017-06-29		5753.7	10.5	203.75	0.14	
HD158815	2016-05-03	67	5813.9	10.6	230.24	0.14	BG
HD158815	2017-06-29		5776.4	10.6	230.86	0.14	
HD158815	2016-05-03	68	6017.9	10.9	239.09	0.14	BG
HD158815	2017-06-29		5991.3	10.9	239.79	0.14	
HD158815	2016-05-03	69	6304.3	11.4	248.17	0.14	tbc
HD158815	2017-06-29		TF				
HD158815	2016-05-03	70	6106.8	11.1	252.08	0.14	tbc
HD158815	2017-06-29		TF				
HD158815	2016-05-03	71	343.1	3.5	358.37	0.59	BG
HD158815	2017-06-29		431.5	3.5	357.07	0.48	
HD158815	2016-05-03	72	1712.6	4.6	334.61	0.18	BG
HD158815	2017-06-29		1801.5	4.7	335.26	0.18	
HD158815	2016-05-03	73	1734.8	4.6	321.47	0.18	BG
HD158815	2017-06-29		1815.3	4.7	323.21	0.17	
HD158815	2016-05-03	74	2397.8	5.4	276.07	0.16	BG
HD158815	2017-06-29		2421.9	5.4	278.07	0.16	
HD158815	2016-05-03	75	3754.1	7.3	275.29	0.15	BG
HD158815	2017-06-29		3776.3	7.4	276.56	0.15	
HD158815	2016-05-03	76	4664.5	8.8	284.95	0.14	tbc

HD158815	2017-06-29		TF				
HD158815	2016-05-03	77	5431.0	10.0	286.11	0.14	BG
HD158815	2017-06-29		5476.3	10.1	286.90	0.14	
HD158815	2016-05-03	78	2610.2	5.7	297.47	0.16	BG
HD158815	2017-06-29		2666.9	5.8	299.13	0.16	
HD158815	2016-05-03	79	2938.8	6.1	312.58	0.15	BG
HD158815	2017-06-29		3003.5	6.2	313.70	0.15	
HD158815	2016-05-03	80	3128.4	6.4	313.94	0.15	tbc
HD158815	2017-06-29		TF				
HD158815	2016-05-03	81	2124.4	5.0	325.26	0.17	tbc
HD158815	2017-06-29		TF				
HD158815	2016-05-03	82	2511.3	5.5	331.44	0.16	BG
HD158815	2017-06-29		2583.6	5.6	331.71	0.16	
HD158815	2016-05-03	83	2947.1	6.2	342.14	0.15	BG
HD158815	2017-06-29		3033.2	6.3	342.35	0.15	
HD158815	2016-05-03	84	3029.5	6.3	332.75	0.15	BG
HD158815	2017-06-29		3116.6	6.4	333.17	0.15	
HD158815	2016-05-03	85	3021.3	6.3	327.09	0.15	BG
HD158815	2017-06-29		3107.0	6.4	327.76	0.15	
HD158815	2016-05-03	86	3925.6	7.6	354.79	0.15	BG
HD158815	2017-06-29		4026.0	7.8	354.58	0.14	
HD158815	2016-05-03	87	3916.1	7.6	350.98	0.15	BG
HD158815	2017-06-29		4015.9	7.7	350.88	0.14	
HD158815	2016-05-03	88	5048.4	9.4	356.38	0.14	tbc
HD158815	2017-06-29		TF				
HD158815	2016-05-03	89	5987.3	10.9	356.92	0.14	tbc
HD158815	2017-06-29		OS				
HD158815	2016-05-03	90	4352.3	8.3	321.90	0.14	BG
HD158815	2017-06-29		4443.9	8.4	322.38	0.14	
HD158815	2016-05-03	91	4596.0	8.7	311.90	0.14	BG
HD158815	2017-06-29		4673.8	8.8	312.55	0.14	
HD158815	2016-05-03	92	4679.8	8.8	307.48	0.14	BG
HD158815	2017-06-29		4744.8	8.9	308.18	0.14	
HD158815	2016-05-03	93	5076.2	9.4	312.40	0.14	BG
HD158815	2017-06-29		5150.1	9.5	312.97	0.14	
HD158815	2016-05-03	94	5236.5	9.7	318.97	0.14	BG
HD158815	2017-06-29		5321.5	9.8	319.40	0.14	
HD158815	2016-05-03	95	5450.7	10.0	320.00	0.14	tbc
HD158815	2017-06-29		OS				
HD158815	2016-05-03	96	OS				tbc
HD158815	2017-06-29		6042.1	11.0	115.44	0.14	
HD158815	2016-05-03	97	OS				tbc

HD158815	2017-06-29		5613.6	10.3	123.70	0.14	
HD158815	2016-05-03	98	5816.8	10.6	157.87	0.14	tbc
HD158815	2017-06-29		OS				
HIP93542		1	3239.4	6.6	161.68	0.15	BG
HIP93542			3187.3	6.5	162.53	0.15	
HIP93542		2	4419.8	8.4	91.23	0.14	BG
HIP93542			4358.2	8.3	90.84	0.14	
HIP93542		3	5581.2	10.2	267.77	0.14	BG
HIP93542			5647.1	10.3	268.16	0.14	
HIP95619		1	4595.9	8.7	253.82	0.14	tbc

Bibliography

Allard, F. , Homeier, D. & Freytag, B., 2012, *Philosophical Transactions of the Royal Society of London Series A* , 370:2765–2777.

Allard, F., Homeier, D. & Freytag, B., 2011, *Astronomical Society of the Pacific Conference Series,* Astronomical Society of the Pacific Conference Series, , 448:91.

Amara, A. & Quanz, S. P., 2012, MNRAS , 427:948–955.

Amara, A., Quanz, S. P. & Akeret, J., 2015, *Astronomy and Computing* , 10:107–115.

Andrews, S. M., Rosenfeld, K. A., Kraus, A. L. & Wilner, D. J., 2013, ApJ , 771:129.

Apai, D., Janson, M., Moro-Martín, A., et al., 2008, ApJ , 672:1196–1201.

Artymowicz, P., Burrows, C. & Paresce, F., 1989, ApJ , 337:494–513.

Astraatmadja, T. L. & Bailer-Jones, C. A. L., 2016, ApJ , 833:119.

Augereau, J. C., Lagrange, A. M., Mouillet, D., Papaloizou, J. C. B. & Grorod, P. A., 1999, A&A , 348:557–569.

Aumann, H. H., 1985, PASP , 97:885–891.

Ballering, N. P., Rieke, G. H., Su, K. Y. L. & Gáspár, A., 2017, ApJ , 845:120.

Ballering, N. P., Rieke, G. H., Su, K. Y. L. & Montiel, E., 2013, ApJ , 775:55.

Baraffe, I., Chabrier, G., Barman, T. S., Allard, F. & Hauschildt, P. H., 2003, A&A , 402:701–712.

Barclay, T., Pepper, J. & Quintana, E. V., 2018, *ArXiv e-prints.*

Barenfeld, S. A., Bubar, E. J., Mamajek, E. E. & Young, P. A., 2013, ApJ , 766:6.

Bate, M. R., Bonnell, I. A. & Bromm, V., 2003, MNRAS , 339:577–599.

Bell, C. P. M., Mamajek, E. E. & Naylor, T., 2015, MNRAS , 454:593–614.

Beuzit, Jean-Luc, Feldt, Markus, Dohlen, Kjetil, et al., 2008, *Proc. SPIE* , 7014:701418.

Biller, B. A., Liu, M. C., Wahhaj, Z., et al., 2013, ApJ , 777:160.

Bonavita, M., Desidera, S., Thalmann, C., et al., 2016, A&A , 593:A38.

Bonnefoy, M., Milli, J., Ménard, F., et al., 2017, A&A , 597:L7.

Boss, A. P., 1986, ApJS , 62:519–552.

Boss, A. P. & Bodenheimer, P., 1979, ApJ , 234:289–295.

Bowler, B. P., 2016, PASP , 128 (10): 102001.

Bowler, B. P., Liu, M. C., Mawet, D., et al., 2017, AJ , 153:18.

Bowler, B. P., Liu, M. C., Shkolnik, E. L. & Dupuy, T. J., 2013, ApJ , 774:55.

Bowler, B. P., Liu, M. C., Shkolnik, E. L., et al., 2012, ApJ , 753:142.

Brandt, T. D. & Huang, C. X., 2015, ApJ , 807:58.

Brandt, T. D., McElwain, M. W., Turner, E. L., et al., 2014, ApJ , 794:159.

Brogi, M., de Kok, R. J., Birkby, J. L., Schwarz, H. & Snellen, I. A. G., 2014, A&A , 565:A124.

Brogi, M., Snellen, I. A. G., de Kok, R. J., et al., 2012, Nature , 486:502–504.

Brott, I. & Hauschildt, P. H., 2005, ESA Special Publication, , 576:565.

Burrows, A., Marley, M., Hubbard, W. B., et al., 1997, ApJ , 491:856–875.

Campante, T. L., Lund, M. N., Kuszlewicz, J. S., et al., 2016, ApJ , 819:85.

Cantalloube, F., Mouillet, D., Mugnier, L. M., et al., 2015, A&A , 582:A89.

Carpenter, J. M., Bouwman, J., Mamajek, E. E., et al., 2009, ApJS , 181:197–226.

Casagrande, L., Schönrich, R., Asplund, M., et al., 2011, A&A , 530:A138.

Chabrier, G., Baraffe, I., Allard, F. & Hauschildt, P., 2000, ApJ , 542:464–472.

Chauvin, G., Desidera, S., Lagrange, A.-M., et al., 2017, A&A , 605:L9.

Chauvin, G., Vigan, A., Bonnefoy, M., et al., 2015, A&A , 573:A127.

Chen, C. H., Mamajek, E. E., Bitner, M. A., et al., 2011, ApJ , 738:122.

Chen, C. H., Mittal, T., Kuchner, M., et al., 2014, ApJS , 211:25.

Chen, C. H., Pecaut, M., Mamajek, E. E., Su, K. Y. L. & Bitner, M., 2012, ApJ , 756:133.

Chiang, H.-F., Looney, L. W., Tassis, K., Mundy, L. G. & Mouschovias, T. C., 2008, ApJ , 680:474–482.

Choquet, É., Bryden, G., Perrin, M. D., et al., 2018, ApJ , 854:53.

Choquet, É., Milli, J., Wahhaj, Z., et al., 2017, ApJL , 834:L12.

Choquet, É., Perrin, M. D., Chen, C. H., et al., 2016, ApJL , 817:L2.

Cieza, L. A., Padgett, D. L., Allen, L. E., et al., 2009, ApJL , 696:L84–L88.

Claudi, R. U., Turatto, M., Gratton, R. G., et al., 2008, *Proc. SPIE* , 7014:70143.

Correia, A. C. M., Udry, S., Mayor, M., et al., 2005, A&A , 440:751–758.

Crepp, J. R., Johnson, J. A., Howard, A. W., et al., 2012, ApJ , 761:39.

Crepp, J. R., Johnson, J. A., Howard, A. W., et al., 2014, ApJ , 781:29.

Currie, T., Burrows, A., Itoh, Y., et al., 2011, ApJ , 729:128.

Currie, T., Cloutier, R., Brittain, S., et al., 2015a, ApJL , 814:L27.

Currie, T., Lisse, C. M., Kuchner, M., et al., 2015b, ApJL , 807:L7.

Currie, T., Muto, T., Kudo, T., et al., 2014, ApJL , 796:L30.

Cutri, R. M., Skrutskie, M. F., van Dyk, S., et al., 2003, *VizieR Online Data Catalog* , 2246.

David, T. J. & Hillenbrand, L. A., 2015, ApJ , 804:146.

Davies, R. & Kasper, M., 2012, ARA&A , 50:305–351.

de Bruijne, J. H. J., 1999, MNRAS , 310:585–617.

de Geus, E. J., Lub, J. & van de Grift, E., 1990, A&AS , 85:915–970.

de Kok, R. J., Stam, D. M. & Karalidi, T., 2011, ApJ , 741:59.

De Rosa, R. J., Bulger, J., Patience, J., et al., 2011, MNRAS , 415:854–866.

De Rosa, R. J., Nielsen, E. L., Blunt, S. C., et al., 2015, ApJL , 814:L3.

de Zeeuw, P. T., Hoogerwerf, R., de Bruijne, J. H. J., Brown, A. G. A. & Blaauw, A., 1999, AJ , 117:354–399.

Debes, J. H., Ygouf, M., Choquet, E., et al., 2016, *Journal of Astronomical Telescopes, Instruments, and Systems* , 2 (1): 011010.

Deming, D., Wilkins, A., McCullough, P., et al., 2013, ApJ , 774:95.

Dohlen, Kjetil, Langlois, Maud, Saisse, Michel, et al., 2008, *Proc. SPIE* , 7014:70143.

Doyle, L. R., Carter, J. A., Fabrycky, D. C., et al., 2011, *Science* , 333:1602.

Draper, Z. H., Duchêne, G., Millar-Blanchaer, M. A., et al., 2016, ApJ , 826:147.

Duchêne, G., 2010, ApJL , 709:L114–L118.

Dupuy, T. J. & Kraus, A. L., 2013, *Science* , 341:1492–1495.

Durisen, R. H., Boss, A. P., Mayer, L., et al., 2007, *Protostars and Planets V:* 607–622.

Fabrycky, D. C., Ford, E. B., Steffen, J. H., et al., 2012, ApJ , 750:114.

Fabrycky, D. C. & Murray-Clay, R. A., 2010, ApJ , 710:1408–1421.

Fang, J. & Margot, J.-L., 2013, ApJ , 767:115.

Feldt, M., Olofsson, J., Boccaletti, A., et al., 2017, A&A , 601:A7.

Foreman-Mackey, D., Hogg, D. W., Lang, D. & Goodman, J., 2013, PASP , 125:306.

Frémat, Y., Lampens, P., van Cauteren, P., et al., 2007, A&A , 471:675–686.

Fressin, F., Torres, G., Charbonneau, D., et al., 2013, ApJ , 766:81.

Gaia Collaboration, Brown, A. G. A., Vallenari, A., et al., 2016a, A&A , 595:A2.

Gaia Collaboration, Brown, A. G. A., Vallenari, A., et al., 2018, *ArXiv e-prints.*

Gaia Collaboration, Prusti, T., de Bruijne, J. H. J., et al., 2016b, A&A , 595:A1.

Galicher, R., Marois, C., Macintosh, B., et al., 2016, A&A , 594:A63.

Gerbaldi, M., Faraggiana, R., Burnage, R., et al., 1999, A&AS , 137:273–292.

Girardi, L., Groenewegen, M. A. T., Hatziminaoglou, E. & da Costa, L., 2005, A&A , 436:895–915.

Gomez Gonzalez, C. A., Absil, O., Absil, P.-A., et al., 2016, A&A , 589:A54.

Goździewski, K. & Migaszewski, C., 2014, MNRAS , 440:3140–3171.

Graham, J. R., Kalas, P. G. & Matthews, B. C., 2007, ApJ , 654:595–605.

Guyon, O., Pluzhnik, E. A., Kuchner, M. J., Collins, B. & Ridgway, S. T., 2006, ApJS , 167:81–99.

Hedman, M. M. & Stark, C. C., 2015, ApJ , 811:67.

Helling, C., Woitke, P. & Thi, W.-F., 2008, A&A , 485:547–560.

Helou, G. & Walker, D. W., 1988, , 7:1–265.

Herczeg, G. J. & Hillenbrand, L. A., 2015, ApJ , 808:23.

Hines, D. C., Schneider, G., Hollenbach, D., et al., 2007, ApJL , 671:L165–L168.

Hinkley, S., Bowler, B. P., Vigan, A., et al., 2015a, ApJL , 805:L10.

Hinkley, S., Kraus, A. L., Ireland, M. J., et al., 2015b, ApJL , 806:L9.

Hinkley, S., Oppenheimer, B. R., Soummer, R., et al., 2007, ApJ , 654:633–640.

Hinkley, S., Oppenheimer, B. R., Soummer, R., et al., 2009, ApJ , 701:804–810.

Høg, E., Fabricius, C., Makarov, V. V., et al., 2000, A&A , 357:367–386.

Hoogerwerf, R., 2000, MNRAS , 313:43–65.

Houk, N. & Cowley, A. P., 1975,

Howard, A. W., Marcy, G. W., Johnson, J. A., et al., 2010, *Science* , 330:653.

Huitson, C. M., Sing, D. K., Pont, F., et al., 2013, MNRAS , 434:3252–3274.

Ireland, M. J., Kraus, A., Martinache, F., Law, N. & Hillenbrand, L. A., 2011, ApJ , 726:113.

Jang-Condell, H., Chen, C. H., Mittal, T., et al., 2015, ApJ , 808:167.

Janson, M., Brandt, T. D., Kuzuhara, M., et al., 2013a, ApJL , 778:L4.

Janson, M., Brandt, T. D., Moro-Martín, A., et al., 2013b, ApJ , 773:73.

Jensen, A. G., Redfield, S., Endl, M., et al., 2011, ApJ , 743:203.

Kalas, P. G., Rajan, A., Wang, J. J., et al., 2015, ApJ , 814:32.

Kalas, P., Liu, M. C. & Matthews, B. C., 2004, *Science* , 303:1990–1992.

Kasper, M., Apai, D., Wagner, K. & Robberto, M., 2015, ApJL , 812:L33.

Kennedy, G. M. & Wyatt, M. C., 2010, MNRAS , 405:1253–1270.

Kennedy, G. M., Wyatt, M. C., Bryden, G., Wittenmyer, R. & Sibthorpe, B., 2013, MNRAS , 436:898–903.

Kennedy, G. M. & Wyatt, M. C., 2014a, MNRAS , 444:3164–3182.

Kennedy, G. M. & Wyatt, M. C., 2012, MNRAS , 426:91–107.

Kennedy, G. M. & Wyatt, M. C., 2014b, MNRAS , 444:3164–3182.

Kennedy, G. M. & Wyatt, M. C., 2013, MNRAS , 433:2334–2356.

Kenworthy, M. A., Mamajek, E. E., Hinz, P. M., et al., 2009, ApJ , 697:1928–1933.

Kenyon, S. J. & Bromley, B. C., 2002, AJ , 123:1757–1775.

Kenyon, S. J. & Bromley, B. C., 2010, ApJS , 188:242–279.

Keppler, M., Benisty, M., Müller, A., et al., 2018, *ArXiv e-prints.*

Knutson, H. A., Fulton, B. J., Montet, B. T., et al., 2014, ApJ , 785:126.

Konopacky, Q. M., Barman, T. S., Macintosh, B. A. & Marois, C., 2013, *Science* , 339:1398–1401.

Kratter, K. & Lodato, G., 2016, ARA&A , 54:271–311.

Kraus, A. L., Ireland, M. J., Hillenbrand, L. A. & Martinache, F., 2012, ApJ , 745:19.

Lafrenière, D., Doyon, R., Marois, C., et al., 2007, ApJ , 670:1367–1390.

Lafrenière, D., Jayawardhana, R., van Kerkwijk, M. H., Brandeker, A. & Janson, M., 2014, ApJ , 785:47.

Lagrange, A.-M., Bonnefoy, M., Chauvin, G., et al., 2010, *Science* , 329:57.

Lagrange, A.-M., Gratadour, D., Chauvin, G., et al., 2009, A&A , 493:L21–L25.

Lagrange, A.-M., Langlois, M., Gratton, R., et al., 2016, A&A , 586:L8.

Lambrechts, M. & Johansen, A., 2012, A&A , 544:A32.

Lannier, J., Delorme, P., Lagrange, A. M., et al., 2016, A&A , 596:A83.

Lazzoni, C., Desidera, S., Marzari, F., et al., 2018, A&A , 611:A43.

Leconte, J., Soummer, R., Hinkley, S., et al., 2010, ApJ , 716:1551–1565.

Lee, E. J. & Chiang, E., 2016, ApJ , 827:125.

Lieman-Sifry, J., Hughes, A. M., Carpenter, J. M., et al., 2016, ApJ , 828:25.

Lindegren, L., Hernandez, J., Bombrun, A., et al., 2018, *ArXiv e-prints.*

Lisse, C. M., Wyatt, M. C., Chen, C. H., et al., 2012, ApJ , 747:93.

López-Santiago, J., Montes, D., Crespo-Chacón, I. & Fernández-Figueroa, M. J., 2006, ApJ , 643:1160–1165.

Luhman, K. L. & Jayawardhana, R., 2002, ApJ , 566:1132–1146.

Lynga, G. & Wramdemark, S., 1984, A&A , 132:58–74.

Lyot, B., 1939, MNRAS , 99:580.

Macintosh, B., Graham, J. R., Barman, T., et al., 2015, *Science* , 350:64–67.

Macintosh, B., Graham, J. R., Ingraham, P., et al., 2014, *PNAS* , 111:12661–12666.

Maire, A.-L., Langlois, M., Dohlen, K., et al., 2016, *Proc. SPIE,* Proc. SPIE, , 9908:990834.

Maldonado, J., Martínez-Arnáiz, R. M., Eiroa, C., Montes, D. & Montesinos, B., 2010, A&A , 521:A12.

Mamajek, E. E., 2016, *IAU Proc.* IAU Symposium, , 314:21–26.

Marley, M. S. & Sengupta, S., 2011, MNRAS , 417:2874–2881.

Marois, C., Macintosh, B., Barman, T., et al., 2008, *Science* , 322:1348.

Marois, C., Macintosh, B. & Véran, J.-P., 2010a, in *Adaptive Optics Systems II,* vol. 7736, 77361J, Proc. SPIE.

Marois, C., Zuckerman, B., Konopacky, Q. M., Macintosh, B. & Barman, T., 2010b, Nature , 468:1080–1083.

Marois, Christian, Lafrenière, David, Doyon, René, Macintosh, Bruce & Nadeau, Daniel, 2006, ApJ , 641 (1): 556.

Matrà, L., Marino, S., Kennedy, G. M., et al., 2018, ApJ , 859:72.

Matthews, B., Kennedy, G., Sibthorpe, B., et al., 2014, ApJ , 780:97.

Matthews, E., Hinkley, S., Vigan, A., et al., 2017, ApJL , 843:L12.

Matthews, E., Hinkley, S., Vigan, A., et al., 2018, *ArXiv e-prints.*

Mawet, D., Milli, J., Wahhaj, Z., et al., 2014, ApJ , 792:97.

Mayor, M. & Queloz, D., 1995, Nature , 378:355–359.

McDonald, I., Zijlstra, A. A. & Boyer, M. L., 2012, MNRAS , 427:343–357.

Mesa, D., Gratton, R., Zurlo, A., et al., 2015a, A&A , 576:A121.

Mesa, D., Gratton, R., Zurlo, A., et al., 2015b, A&A , 576:A121.

Meshkat, T., Bailey, V. P., Su, K. Y. L., et al., 2015, ApJ , 800:5.

Meshkat, T., Mawet, D., Bryan, M. L., et al., 2017, AJ , 154:245.

Milli, J., Mouillet, D., Lagrange, A.-M., et al., 2012, A&A , 545:A111.

Mittal, T., Chen, C. H., Jang-Condell, H., et al., 2015, ApJ , 798:87.

Mohanty, S., Greaves, J., Mortlock, D., et al., 2013, ApJ , 773:168.

Morales, F. Y., Bryden, G., Werner, M. W. & Stapelfeldt, K. R., 2013, ApJ , 776:111.

Morales, F. Y., Rieke, G. H., Werner, M. W., et al., 2011, ApJL , 730:L29.

Morales, F. Y., Bryden, G., Werner, M. W. & Stapelfeldt, K. R., 2016, ApJ , 831:97.

Moro-Martín, A., 2013, in *Planets, Stars and Stellar Systems. Volume 3: Solar and Stellar Planetary Systems*, 431.

Morrison, S. & Malhotra, R., 2015, ApJ , 799:41.

Morton, T. D., Bryson, S. T., Coughlin, J. L., et al., 2016, ApJ , 822:86.

Mustill, A. J. & Wyatt, M. C., 2009, MNRAS , 399:1403–1414.

Mustill, A. J. & Wyatt, M. C., 2012, MNRAS , 419:3074–3080.

Nakajima, T. & Morino, J.-I., 2012, AJ , 143:2.

Nesvold, E. R. & Kuchner, M. J., 2015, ApJ , 798:83.

Ngo, H., Knutson, H. A., Hinkley, S., et al., 2015, ApJ , 800:138.

Nielsen, E. L., Liu, M. C., Wahhaj, Z., et al., 2013, ApJ , 776:4.

Nordström, B., Mayor, M., Andersen, J., et al., 2004, A&A , 418:989–1019.

Olsen, E. H., 1994, A&AS , 104:429–472.

Padgett, D. & Stapelfeldt, K., 2016, *IAU Proc.* IAU Symposium, , 314:175–178.

Panagi, P. M. & O'dell, M. A., 1997, A&AS , 121.

Pavlov, A., Möller-Nilsson, O., Feldt, M., et al., 2008, *Proc. SPIE*, Proc. SPIE, , 7019:701939.

Pawellek, N. & Krivov, A. V., 2015, MNRAS , 454:3207–3221.

Pecaut, M. J. & Mamajek, E. E., 2013, ApJS , 208:9.

Pecaut, M. J., Mamajek, E. E. & Bubar, E. J., 2012, ApJ , 746:154.

Pecaut, M. J. & Mamajek, E. E., 2016, MNRAS , 461:794–815.

Perrin, M. D., Duchene, G., Millar-Blanchaer, M., et al., 2015, ApJ , 799:182.

Perryman, M. A. C., Hartman, J., Bakos, G. Á. & Lindegren, L., 2014, ApJ , 797:14.

Perryman, M. A. C., Lindegren, L., Kovalevsky, J., et al., 1997, A&A , 323.

Phillips, N. M., 2011, PhD diss., Institute for Astronomy, The University of Edinburgh.

Pueyo, L., 2016, ApJ , 824:117.

Quillen, A. C., 2006, MNRAS , 372:L14–L18.

Rameau, J., Chauvin, G., Lagrange, A.-M., et al., 2013, ApJL , 779:L26.

Raymond, S. N., Armitage, P. J., Moro-Martín, A., et al., 2012, A&A , 541:A11.

Redfield, S., Endl, M., Cochran, W. D. & Koesterke, L., 2008, ApJL , 673:L87.

Reidemeister, M., Krivov, A. V., Schmidt, T. O. B., et al., 2009, A&A , 503:247–258.

Rhee, J. H., Song, I., Zuckerman, B. & McElwain, M., 2007, ApJ , 660:1556–1571.

Rieke, G. H., Su, K. Y. L., Stansberry, J. A., et al., 2005, ApJ , 620:1010–1026.

Rizzuto, A. C., Ireland, M. J. & Robertson, J. G., 2011, MNRAS , 416:3108–3117.

Rodet, L., Beust, H., Bonnefoy, M., et al., 2017, A&A , 602:A12.

Rodigas, T. J., Weinberger, A., Mamajek, E. E., et al., 2015, ApJ , 811:157.

Rodriguez, D. R. & Zuckerman, B., 2012, ApJ , 745:147.

Sacco, G. G., Kastner, J. H., Forveille, T., et al., 2014, A&A , 561:A42.

Seager, S., 2003, *Earth and Planetary Science Letters* , 208:113–124.

Sengupta, S. & Marley, M. S., 2009, ApJ , 707:716–726.

Sengupta, S. & Marley, M. S., 2010, ApJL , 722:L142–L146.

Shannon, A., Bonsor, A., Kral, Q. & Matthews, E., 2016, MNRAS , 462:L116–L120.

Shannon, A., Clarke, C. & Wyatt, M., 2014, MNRAS , 442:142–147.

Sing, D. K., Fortney, J. J., Nikolov, N., et al., 2016, Nature , 529:59–62.

Sirbu, D., Thomas, S., Belikov, R. & Bendek, E., 2017, ApJ , 849:142.

Sivaramakrishnan, A., Koresko, C. D., Makidon, R. B., Berkefeld, T. & Kuchner, M. J., 2001, ApJ , 552:397–408.

Smith, B. A. & Terrile, R. J., 1984, *Science* , 226:1421–1424.

Snellen, I. A. G., de Kok, R. J., de Mooij, E. J. W. & Albrecht, S., 2010, Nature , 465:1049–1051.

Soummer, R., Perrin, M. D., Pueyo, L., et al., 2014, ApJL , 786:L23.

Soummer, R., Pueyo, L. & Larkin, J., 2012, ApJL , 755:L28.

Stark, C. C., Schneider, G., Weinberger, A. J., et al., 2014, ApJ , 789:58.

Su, K. Y. L., Morrison, S., Malhotra, R., et al., 2015, ApJ , 799:146.

Su, K. Y. L. & Rieke, G. H., 2014, IAU Symposium, , 299:318–321.

Su, K. Y. L., Rieke, G. H., Stansberry, J. A., et al., 2006, ApJ , 653:675–689.

Su, K. Y. L., Rieke, G. H., Stapelfeldt, K. R., et al., 2009, ApJ , 705:314–327.

Sudol, J. J. & Haghighipour, N., 2012, ApJ , 755:38.

Tetzlaff, N., Neuhäuser, R. & Hohle, M. M., 2011, MNRAS , 410:190–200.

Thalmann, C., Desidera, S., Bonavita, M., et al., 2014, A&A , 572:A91.

Thébault, P. & Wu, Y., 2008, A&A , 481:713–724.

Thilliez, E. & Maddison, S. T., 2017, MNRAS , 464:1434–1448.

Thomas, S., Belikov, R. & Bendek, E., 2015, ApJ , 810:81.

Thureau, N. D., Greaves, J. S., Matthews, B. C., et al., 2014, MNRAS , 445:2558–2573.

Torres, C. A. O., Quast, G. R., da Silva, L., et al., 2006, A&A , 460:695–708.

Trilling, D. E., Bryden, G., Beichman, C. A., et al., 2008, ApJ , 674:1086–1105.

Urban, L. E., Rieke, G., Su, K. & Trilling, D. E., 2012, ApJ , 750:98.

Veras, D., Crepp, J. R. & Ford, E. B., 2009, ApJ , 696:1600–1611.

Vigan, A., Bonavita, M., Biller, B., et al., 2017, A&A , 603:A3.

Vigan, A., Bonnefoy, M., Ginski, C., et al., 2016, A&A , 587:A55.

Vigan, A., Gry, C., Salter, G., et al., 2015, MNRAS , 454:129–143.

Vigan, A., Moutou, C., Langlois, M., et al., 2010, MNRAS , 407:71–82.

Wahhaj, Z., Liu, M. C., Nielsen, E. L., et al., 2013, ApJ , 773:179.

Wahhaj, Z., Milli, J., Kennedy, G., et al., 2016, A&A , 596:L4.

Wahhaj, Zahed, Liu, Michael C., Biller, Beth A., et al., 2014, A&A , 567:A34.

Wolszczan, A. & Frail, D. A., 1992, Nature , 355:145–147.

Wright, E. L., Eisenhardt, P. R. M., Mainzer, A. K., et al., 2010, AJ , 140:1868–1881.

Wyatt, M. C., 2008, ARA&A , 46:339–383.

Wyatt, M. C., Smith, R., Su, K. Y. L., et al., 2007, ApJ , 663:365–382.

Zorec, J. & Royer, F., 2012a, A&A , 537:A120.

Zorec, J. & Royer, F., 2012b, A&A , 537:A120.

Zuckerman, B., Rhee, J. H., Song, I. & Bessell, M. S., 2011, ApJ , 732:61.

Zurlo, A., Vigan, A., Mesa, D., et al., 2014, A&A , 572:A85.